J. Bangladesh Acad. Sci. Volume 50, Issue 1, March 2026

ISSN 2224-7270 (Online), 0378-8121 (Print)

Journal of Bangladesh Academy of Sciences is published four times a year (March, June, September and December comprising one volume) in English. Original research articles, review articles, and short communications of all branches of Science and Technology are considered for publication in this journal. Review articles are generally by invitation.

Disclaimer

The opinions, analysis and conclusions expressed or implied in this journal are those of the authors and do not represent the views of Bangladesh Academy of Sciences.

Submission

All correspondence regarding contributions for publication in the journal should be addressed to the *Editor, Journal of Bangladesh Academy of Sciences* <jbas.editor@yahoo.com>. Authors should consult the contributor's guideline at the back of the journal before submitting their manuscripts.

Published by

Bangladesh Academy of Sciences, National Science and Technology Complex, Agargaon, Dhaka-1207.

Design and Printed by

Sucharu Desktop Publishing, 1/E/1, Paribagh, Dhaka-1000, Bangladesh

Annual Subscription: Tk. 500.00 (Bangladesh); US $ 60.00; £ 21.50 plus postage.
Single Copy: Tk. 250.00 (Bangladesh); US $ 30.00; £ 11.25 plus postage.

J. Bangladesh Acad. Sci. 48(1); 1-25: June 2024 DOI:https://doi.org/10.3329/jbas.v48i1.73005

Journal of Bangladesh Academy of Sciences

Journal homepage: http://www.bas.org.bd/publications/jbas.html

Review Article

New wonder materials - exciting technological horizon

A.K.M. Azharul Islam

Professor Emeritus & Former Vice Chancellor, International Islamic University Chittagong;
Professor (Retd.), Rajshahi University, Bangladesh

ARTICLE INFO

Article History

Received: 15 April 2024
Revised: 16 May 2024
Accepted: 18 May 2024

Keywords: 3D MAX Phases, Superconducting and magnetic MAX, Properties & application, 2D MXenes, Synthesis, Structure of MXenes, Electrochemical energy storage, Li-S battery, Wearable electronics, Biomedical applications, Sensitive gas sensor, Drug delivery, Phototherapy, Antimicrobial.

ABSTRACT

A significant advancement in materials science has been made with the 2D MXene nanomaterials that were etched from their parent 3D MAX phases. Layered ternary carbide, nitride, and boride compounds with the general formula $M_{n+1}AX_n$ (n=1,2, 3,4 ...) make up the 3D MAX phase materials, where A is an element of Group IIA or IIIA, M is an early transition metal, and X is either C, N, or B. MXene's chemical formula is $M_{n+1}X_n$, whereas that of the precursor is $M_{n+1}AX_n$. The MAX materials have a distinct set of properties that are similar to those of metal and ceramic. They are helpful in the development of high-efficiency engines, thermal systems that can withstand damage, fatigue resistance enhancement, and high-temperature rigidity retention technologies. The 2D MXenes are potentially described as a 'wonder material' in the class of nanomaterials. Because of their intriguing mechanical properties resulting from their atomically thin dimensions, as well as their unusual electrical and optical properties, these have become the focus of materials research in recent years. These nanomaterials are multilayer electrically conductive materials that are comparable to multilayer graphene. They have been discovered to be beneficial for a variety of applications, such as energy storage materials, composite reinforcement, chemical, environmental, and biological sensors, and electronic devices. The recent advancements in the use of nanomaterials in optoelectronics, field-effect transistors, transparent conductive electrodes and shielding against electromagnetic interference, energy storage, and other fields have been extensively documented. The potential of nanomaterials as a novel ceramic photothermal agent employed in cancer therapy has been revealed by a very recent study on Ti_3C_2 MXene. The same 2D nanomaterial can be used in water desalination and purification membranes since it has antibacterial qualities and is resistant to bio fouling. The MXene-based piezoresistive sensor is also capable of detecting weak pressures and the slight bending-release actions of humans. It can be applied to recover lost frictional energy from, say, walking or typing-related muscular contractions. Since MAX phases are precursors to MXenes, the former are valuable due to the growing interest in the latter. This review provides an overview of the literature, including the author's own work, from the groundbreaking MXene publication to the present. It provides information on the characteristics, synthesis, crystal structure, and current and future uses of the new wonder materials as well as the MAX phases.

Introduction

Today's technological advancements dictates the search for new nanomaterials for a wide range of applications, including energy storage, optoelectronics, and medicine. An atom from the group of early transition metals and an atom from A-group elements (Al, Si, etc.) chemically combine with carbon or nitrogen or boride to give rise to a new type of compounds known as MAX phases. There is a technique to eliminate A-group element, mainly

---

[*] Corresponding author:<azi46@ru.ac.bd>

Al from the MAX phase to form exfoliated layered structured MXene, which creates a potential role in many applications. Recent years have seen a significant increase in interest in both the 3D MAX materials and the derived 2D MXene materials due to their exceptional mechanical, chemical, and physical qualities as well as their wide range of potential applications.

MAX phases are new ceramics with a layered structure that are both structural and functional. MAX phases are exfoliated to create 2D materials called MXenes, which have structures like graphene. MXene materials have a high specific surface area, good chemical stability, biocompatibility, tunable physical properties, and other characteristics that allow their surface to interact with more functional atoms and molecules. The MAX phase is typically etched, among other techniques, in the preparation of MXene materials. Physical qualities including electrical conductivity, magnetism, and optics can be tuned by varying the chemical composition and structure of MXene materials. These wonder materials through their current exciting applications and prospects for future applications show promising technological horizon, e.g. among others in the delivery of drug, treatment of cancer etc., which are popular topics these days.

MAX phase materials

The 3D MAX phase materials are layered ternary carbide, nitride and boride nanolaminated compounds with general formula $M_{n+1}AX_n$ (n = 1, 2, 3, 4 ...), where M is an early transition metal, A is a Group IIA or IIIA element and X is C, N, B and/or P. While the precursor has $M_{n+1}AX_n$ chemical formula MXene has $M_{n+1}X_n$ formula. The number of phases has expanded from the initial 50 or so to over 300 in recent years due to advancements in phase research. Following 2018, half of the 342 MAX phases were found. At the moment, alloys including 28 M, 28 A, and 6 X elements have been integrated into the MAX phases. Furthermore, using phase stability predictions 182 new theoretically stable MAX phases are awaiting experimental confirmation, according to Dahlqvist et al. (2024). Notably, MAX phases are even more important because they are predecessors to MXenes, and there is a growing interest in the latter due to a wide range of possible uses. The MAX materials possess unique set of both ceramic- and metal-like properties. They are useful in technologies involving high efficiency engines, damage tolerant thermal systems, increasing fatigue resistance, and retention of rigidity at high temperatures.

Discovery of MAX phases

MAX phases were discovered first by crystal chemist Hans Nowotny and his coworkers during the 1960s. The phases, called H-phases at that time, included more than thirty 211 phases (Ti_2AlC, Ti_2AlN, V_2AlC, etc.) and two 312 phases (Ti_3SiC_2 and Ti_3GeC_2) (Jeitschko et al., 1963; Jeitschko and Nowotny 1967; Jeitschko et al., 1964). In the 1980s, another important 312 phase, Ti_3AlC_2, was found by Schuster and Nowotny (1980).

However, until the mid1990s, these MAX phases received little attention from the scientific community because of their unstable and impure performance. Predominately single-phase, dense samples of Ti_3SiC_2 were prepared by Barsoum and his group at Drexel University in 1996 and their mechanical and oxidation behaviors were evaluated (Barsoum et al., 1997). Later, several bulk MAX phases (Ti_2AlC, V_2AlC, Ti_2SnC, Nb_2AlC, etc.) were fabricated successfully by them and it was observed that they possessed similar properties like those of Ti_3SiC_2 (Barsoum and El-Raghy, 1996). Barsoum et al. (1999) further discovered Ti_4AlN_3 in 1999, which yields the first prototype of 413 phase and led to the the formula $M_{n+1}AX_n$ or MAX for short.

The ternary phases typically crystallize in space group $P6_3/mmc$ and follow the notation $M_{n+1}AX_n$ for describing their stoichiometry (Fig. 1). Commonly used short notations for composition are: 211 ($n = 1$) for M_2AX, 312 ($n = 2$) for M_3AX_2, 413 ($n = 3$) for M_4AX_3 etc. $M_{n+1}X_n$ layers with ceramic properties are formed in the crystal structure of MAX phases by the near-closed packing of M atoms and the X atoms filling the edge-shared M_6X octahedral sites. A layers with metal properties separate the $M_{n+1}Xn$ layers. MAX phases thus combine the metal and ceramic properties. Like metals, MAX phases have high strength, excellent high temperature strength, and thermal stability. They are also easily machined with conventional tools, thermally and electrically conductive, and resistant to thermal shock (Zhou et al. 2021).

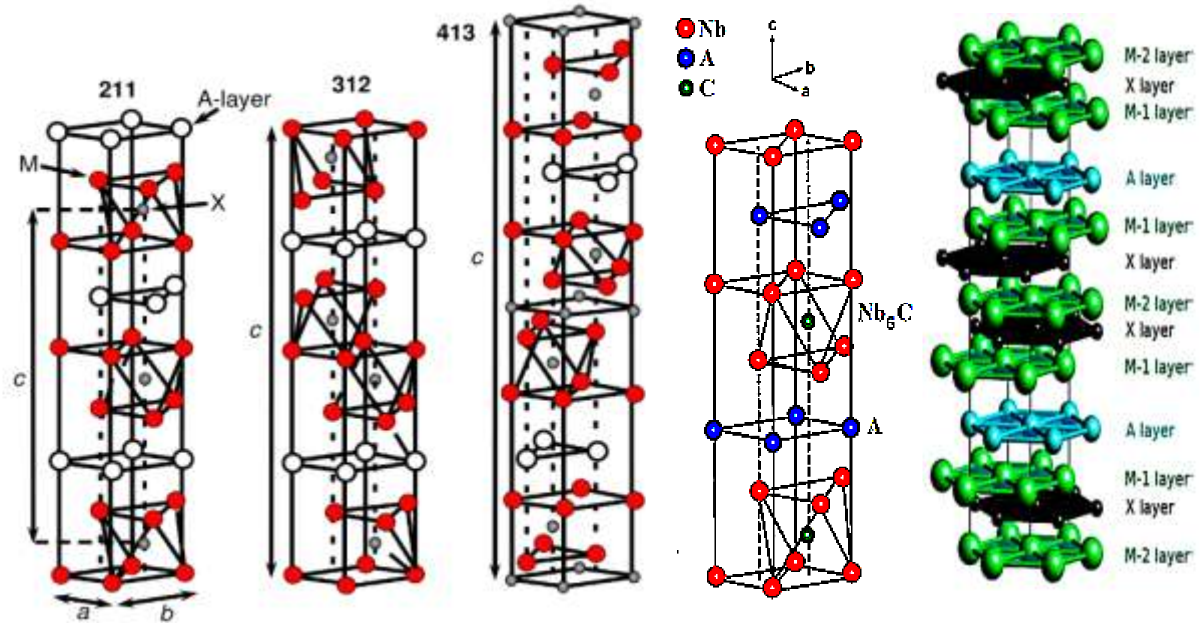

(a) (b) (c)

Fig. 1. Several ternary MAX phase structures. (a) Conventional phases crystallize in space group *P6₃/mmc* with a general $M_{n+1}AX_n$ composition. (b) Hexagonal crystal structure of Nb_2AC (A: Al, S, Ge, As, and Sn), in which A atomic sheets are sandwiched between blocks of Nb-carbides [NbC] formed by edge-shared Nb_6C octahedra. (c) Crystal structure of the 312 MAX phase (Fillipatos et al., 2019). For the 312 structure, there are two different M sites denoted M-1 and M-2.

Superconducting MAX phases

In 1967 Mo_2GaC was the first MAX phase to exhibit superconducting characteristics with transition temperature T_c~4.0 K (Toth, 1967). According to the BCS theory, superconductivity is attributed to a phonon-mediated attraction between mobile electrons near Fermi surface (called Fermi electrons). The attraction is sometimes referred to as a residual Coulomb interaction that can glue Cooper pair together to cause superconductivity. MAX materials are expected to be possible superconductors because of the metallic-like characteristics of the phases. Indeed in such remarkable class of materials there are ten low-temperature superconductors studied from about 70 MAX phases reported till 2015 (Islam, 2021, Hadi et al., 2014; Hadi et al., 2013, Karaca et al., 2021). The superconducting transition temperatures (T_c in K) of the experimentally proven MAX superconductors along with their theoretically obtained parameters are presented in Table 1. The number of reported superconductors shows that a vast majority of the MAX phases are not superconductors and all superconducting MAX phases belong to the 211 subfamily of MAX phases. The reason is due to the difference in repetition of the A-layers, the 211 structure has more metallic and better electrical and thermal conducting properties than the 312 and 413 phases that have more carbide- or nitride-like properties (Magnuson and Mattesini, 2017).

The conductivity, elasticity, magnetism, and other material properties can be altered by changing the elements at the M, A, or X-sites in the crystal structure. This allows for the manipulation of the chemical bond strengths, which in turn allows for the customization of this class of materials' properties (Magnuson and Mattesini, 2017).

Table 1. DOS at the Fermi level (N_F in states/eV)), frequency (ω_{ln} in K), the average e-ph coupling constant (λ), and T_c (K) for the MAX phases. E= Expt. T= Theoret.

MAX	$N(E_F)$ (states/eV)	ω_{ln}(K)	λ	T_c(K)	References
Nb_2SC	3.452	249.124	0.739^T	7.72^T	Karaca et al., 2021
				7.78^E, 7.2^E	Bortoloza et al., 2006, Romero et al., 2013
				5.0^E	Sakamaki et al., 1999
Nb_2GeC	3.992	298.347	0.685^T	9.83^T	Karaca et al., 2021
				10.0^E	Bortolozo et al., 2017
Nb_2AsC	3.005	300.906	0.44^T	2.09^T	Karaca et al., 2021
	3.00		0.34^E	2.0^E	Lofland et al., 2006
Nb_2SnC	3.843	258.14	0.614^T	6.31^T	Karaca et al., 2021
				7.8^E, 7.2^E	Bortolozo et al., 2006, Romero et al., 2013
Nb_2InC	-	-	-	7.5^E	Bortolozo et al., 2009
Mo_2GaC	4.79	-	-	4^E	Toth, 1967
Ti_2InN	-	-	-	7.3^E	Bortolozo et al., 2010
			0.62^T	-	Roknuzzaman and Islam, 2013
Ti_2InC	-	-	-	3.1^E	Bortolozo et al., 2007
			0.49^T	-	Roknuzzaman and Islam, 2013
Ti_2GeC				9.5^E	Bortolozo et al., 2012
Lu_2SnC				5.2^E	Kuchida et al., 2013
Ti_2AlN				13^T	Karaca et al., 2022

The structural parameters, elastic, electronic, thermodynamic and optical properties of the MAX superconductors have been studied by several researchers. Variety of such theoretical and experimental studies have revealed the structural, electronic, mechanical and vibrational, thermodynamic, thermal, magnetic, transport and optical properties including machinability, brittle/ductile behavior, radiation resistance and damage tolerance of the materials (Shein and Ivanovvskii., 2010, 2011; Nasir and Islam, 2012; Hadi et al., 2013; Roknuzzaman and Islam, 2013; Hadi et al., 2014; Hadi et al., 2019; Karaca et al., 2021).

The transition temperatures T_c of hexagonal Nb_2AC (A: Al, S, Ge, As and Sn) have been studied using DFT (perturbation) to model the e–ph interaction (Karaca et al., 2021). These theoretical results - DOS at the Fermi level N_F, logarithmic frequency ω_{ln}, the average e-ph coupling constant λ and the superconducting transition temperature T_c are also shown in the table for comparison with the experimental T_c.

Magnetic MAX phases

DFT was first used to predict magnetic MAX phases by evaluating phase stability. These were then synthesized as heteroepitaxial thin films. A nanolaminated magnetic MAX compound which has only one M-element, namely Mn_2GaC was predicted theoretically and subsequently synthesized first by Ingason et al. (2014). According to Ingason et al. (2016), all magnetic MAX phases that have been described thus far, whether in bulk or thin-film form, are based on Cr and/or Mn. The list includes $(Cr,Mn)_2AlC$, $(Cr,Mn)_2GeC$, $(Cr,Mn)_2GaC$, $(Mo,Mn)_2GaC$, and $(V,Mn)_3GaC_2$, Cr_2AlC, Cr_2GeC and Mn_2GaC.

Numerous magnetic characteristics have been discovered, including structural alterations connected to magnetic anisotropy and ferromagnetic reactivity much above room temperature. The techniques, findings, and conclusions of the theoretical and experimental work done on these materials up to this point are critically examined by Ingasan et al. (2016). An outlook centered on new materials, superstructures, property tailoring, and more synthesis and characterization is offered, along with questions about magnetic properties that are examined.

The discovery of novel magnetic phases and compositions, as well as the foundations of magnetic properties, have been the exclusive focus of research efforts thus far. However, potential uses have been noted thus far for everything from refrigeration to spintronics (Ingasan et al., 2016).

Synthesis, properties and applications

Synthesis

Many techniques for bulk solid-state synthesis have been developed to yield a range of MAX phases. However, since 2002, there has been a growing interest in potential applications due to the growth of MAX phases, particularly in its high quality epitaxial thin-films form (Palmquist et al., 2002).

Among these are bond coatings on sapphire fibers, low friction and oxidation-resistant contacts, and protective and oxidation-resistant coatings for turbine blades. In the latter cases, the main objective is to produce high density single-phase films, and since 2010, most efforts have been made to produce single crystal samples of superior quality. Chemical vapor deposition (CVD), magnetron sputtering, cathodic arc deposition, and pulsed laser deposition (PLD) are the primary growth techniques that have been employed for the deposition of MAX phases thin films. Biswas et al. (2021) have provided an overview of the advancements achieved thus far in the assessment of the properties and epitaxial growth of MAX phase thin films cultivated using diverse deposition methods. Dahlqvist et al. (2024) published a review paper in which MAX phase classification based on their synthesis method was introduced (Fig. 2). The distinct elemental compositions of the two synthesis routes, bottom-up and top-down, inspired the idea of dividing the MAX phases according to how they were synthesized. Adding magnetic elements and noble metals to the A-layer of MAX phases via top-down synthesis is a sophisticated method of creating more exotic MAX phases. We would now go over to their classification system.

Bottom-up synthesis

The first category consists of the `classic' MAX phases with space group $P6_3/mmc$. A is an element of the A-group (groups 12 to 16), M is the early transition metal, and X is C, N, B and/or P. In this case, `classic' does not imply `old', but rather refers to Nowotny's discoveries, where n = 1, 2, 3, and so on to 4, 5, or 6. Similarly, for recent discoveries of B-containing MAX phases (Rackl et al., 2019). The ability to be created directly through synthesis, for example, by thin film deposition or powder metallurgy routes (powder synthesis) (Dahlqvist et al., 2024) is another significant characteristic of bottom-up synthesized MAX phases. Accordingly, this group comprises high-entropy MAX phases and ternary MAX phases, as well as matching alloys that go up to multi-element solids with significant disorder on the M-sites (Dahlqvist et al., 2024), provided that they can be synthesized in a single step and follow the hexagonal $P6_3/mmc$ space group symmetry.

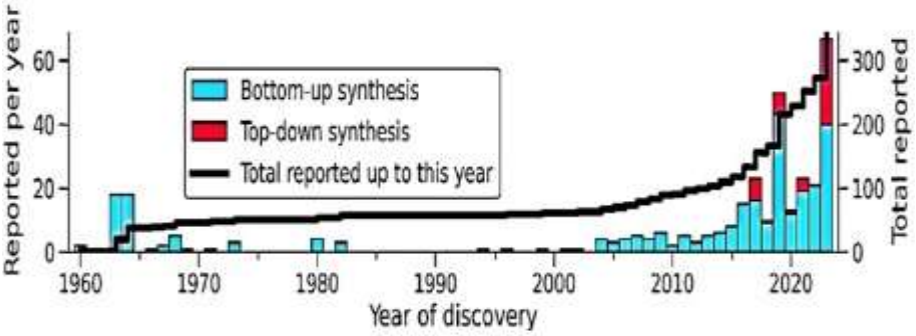

Fig. 2. Discovery histogram for synthesized MAX phases. Credit: Permission from Dahlqvist et al. (2024). Copyright © 2023 The Authors. Published by Elsevier Ltd.

Top-down synthesis

The only difference between this one and the first category is that we now include A-site elements outside of groups 12 to 16 (Dahlqvist et al., 2024). The modification of the A-group layers is what distinguishes a top-down synthesized MAX phase from other types. This is more important than its chemistry. These phases are typically obtained through post-synthesis procedures from a bottom-up MAX phase precursor in which the A-layer is either partially or completely replaced. Here, we discuss two approaches:

1. the molten salt method, which substitutes a more varied group of elements, such as transition metals like Mn, Fe, Co, Ni, Cu, Zn, (Li et al. , 2019) and
2. the replacement of noble metals in MAX phase thin films by thermally induced exchange reactions, e.g. Al, Si, and Ga layers with layers of Au or Ir. In-plane order within the A-layers among top-down synthesized phases is also found (Lai et al., 2017).

Properties and application

Physical and chemical characteristics of MAX phases is provided here. In fact a very brief survey is discussed on the possible domains of use of MAX phases, including MXene precursors, nuclear materials, and materials at high temperatures.

Interesting characteristics of MAX phase compositions include oxidation resistance, damage tolerance, crack healing, machinability, irradiation tolerance, relatively high temperature stability, and resistance to liquid metal corrosion. They are suitable options for electrical contacts, sensors, connectors, etc. because of their good electrical and thermal properties. Furthermore, some of the MAX phases are used in protective coatings, micro-mechanical systems, and even commonplace items like drill bits and non-stick cookware because of their superior mechanical properties. Ultimately, they are good options for high-temperature structural and non-structural applications, such as gas burning and heating elements, due to their exceptional high temperature properties and resistance to oxidation (Barsoum, 2013).

a. Fracture toughness and damage tolerance

One important characteristic that gauges a material's resistance to crack propagation is fracture toughness. It sheds light on a material's capacity to tolerate the propagation of pre-existing fissures under stress. In general, ceramic materials exhibit brittle mechanical properties. They do not have energy-absorbing systems like dislocation motion of metals. As a result, most ceramics have a modest fracture toughness (K_{IC}) due to their low resistance to crack propagation. However, this characteristic is required for designing a structural component in the majority of engineering applications, which restricts the usage of ceramic materials. The inclusion of extra energy-absorbing processes, which may make MAX phase materials several times harder than their comparable binary carbides, is one of their distinctive characteristics. The damage resistance mechanism is related to the fact that it is nanolayered, but this structure alone cannot explain it (Goossens et al., 2021) .

b. Oxidation resistance and crack healing

Some MAX phases possess excellent oxidation resistance (Goossens et al., 2021). The formation of a protective oxide layer that adheres well to the underlying material is essential for the material's stability in oxidative environments. MAX phase compounds that exhibit strong resistance to oxidation (i.e. stable above 1000°C) are Ti_3SiC_2, Ti_2AlC, Ti_3AlC_2, and Cr_2AlC. Ti_3SiC_2 exhibits a stable oxidation behavior up to roughly 1100°C, forming a duplex oxide layer consisting of an outer rutile (TiO_2) layer followed by a mixture of TiO_2 and silica (SiO_2) (Barsoum et al., 1997; Sun et al., 2001). The three additional compounds primarily depend on the creation of a stable layer of α-Al_2O_3. Tallman et al. (2013) provide a thorough overview of their oxidation behavior in which the most oxidation-resistant MAX phase is said to be Ti_2AlC.

The capacity of MAX phases to `heal' cracks has been demonstrated by research on their oxidation behavior in the Ti-Al-C system. In order to partially restore the material's strength, Ti_2AlC or Ti_3AlC_2 must be heat treated in an oxidative environment to produce TiO_2 and Al_2O_3 oxidation products that fill the crack (Song et al., 2016; Yang et al., 2011).

c. Corrosion and radiation resistance

The candidate structural/functional MAX phase based materials for some applications in the Gen-IV lead-cooled Fast Reactor (LFR) must be compatible with the heavy liquid metal (HLM) primary coolant, such as lead (Pb) and lead-bismuth eutectic (LBE) (Goossens et al., 2021).

Under operational circumstances where traditional stainless steels are severely hampered by dissolution corrosion (Lambrinou et al., 2017) in contact with liquid LBE, most MAX phases remain inert due to factors like high temperatures (> 450°C) and low HLM oxygen concentrations (<10 mass%).

$M_{n+1}AX_n$ phases due to their unusual characteristics have been proposed for application in both fission and fusion nuclear reactors, where they will be subjected to high temperatures and harsh radiation conditions. The electronic structures, bonding types, and defect processes of Sn-based 211 MAX phases have been studied by Hadi et al. (2019). A detailed theoretical study of the intrinsic defect processes, Nb_2SnC is predicted to have better radiation tolerance of the M_2SnC MAX phases (M = Lu, Ti, Zr, Hf, Nb). A more or less similar studies of a newly synthesized 211 MAX phase V_2SnC has been made by Hadi et al. (2020). The new phase V_2SnC when included in the systems of 5-member of Sn-based 211 MAX phases, Nb_2SnC remains in the same position. Compared to the other M_2SnC phases, the radiation resistance of V_2SnC is better than Lu_2SnC and lower than the remaining phases.

The effects of radiation on the $M_{n+1}AX_n$ phases have recently been the subject of numerous other studies, which have revealed complex behavior induced by ion or neutron irradiation over a range of temperatures, including phase transformations, surface modification, and mechanical property changes. Wang et al. (2020) examine the intrinsic controls on the radiation tolerance of these materials and summarize recent experimental and theoretical work on the response of the $M_{n+1}AX_n$ phases to irradiation. This article develops a thorough understanding of the mechanisms underlying the structural modification and defect evolution caused by irradiation in $M_{n+1}AX_n$ phases. It also suggests strategies for creating new $M_{n+1}AX_n$ phases that perform better under extreme irradiation scenarios.

d. Stability at elevated temperature

Transition metal carbides are referred to as refractory carbides because of their superior strength at elevated temperatures. It has been reported that the MAX phases exhibit good stability at high temperatures. Phase stability is the primary lens through which to interpret this thermal stability. The MAX phases separate at high temperatures, and depending on the particular MAX phase and the surrounding circumstances, the precise dissociation temperature can range from roughly 1000°C to 1700°C. Low (2019) published a summary of the various factors influencing the breakdown and deterioration of Ti-based MAX phases.

The mechanical behavior of the MAX phases under high temperature and mechanical loads is also of interest. The current state of knowledge on this mechanical behavior is based mainly on experiments with Ti_2SiC_2, with some reports on Ti_2GeC_2 and Al containing phases. A detailed description can be found in Barsoum (2013). Generally speaking, MAX phases have a BPTT (Brittle-to-Plastic transition temperature).

e. Machinability

The machinability of MAX phase compounds is a key technical feature for the manufacturing and shape of components. Because they can be machined with standard high-speed steel and hard metal tools, shaping of the MAX phases can be accomplished with traditional machining techniques including milling, turning, and drilling. As oxide or carbide phases that are parasitic might harm the tools, excellent phase purity is an essential requirement for machining.

MXenes

Introduction

2D materials are among the most interesting scientific research materials of the 21st century. The `First Wonder Material' is 2D Graphene which was discovered in 2004 for which 2010 Nobel Prize was awarded to Andre Geim and Kostya Novoselov both of the University of Manchester. It is considered as a miracle material for scientists and engineers owing to its outstanding physical properties. Graphene and its nano-composites are promising multifunctional materials with improved tensile strength and elastic modulus.

MXenes are potentially described as a ‘wonder material’ in the class of 2D nanomaterials. These 2D-layered MXenes, mostly derived from MAX phases, have the suffix ‘ene’ to indicate that they are similar to grapheme. The credit for the groundbreaking discovery in 2011 goes to researchers led by Yury Gogotsi and Michel Barsoum at Drexel University, USA. They achieved this feat by selectively etching the A layer from bulk MAX phases, resulting in the creation of multilayered MXenes. (Naguib et al., 2011; Naguib et al., 2012). The fields of MXene development, synthesis, and application are expanding quickly. This material family has demonstrated superior performance compared to materials utilized in numerous applications and holds the potential to revolutionize the integration of nanotechnology in daily life (MXenes, Drexel Nanomaterials Institute). Ever since the discovery of the first MXene in 2011, about 40 MXenes have been successfully synthesized, with many of these originating from Linköping University, Sweden, and many more are predicted till date.

MXenes are a fascinating class of materials that have captured the imagination of scientists and their efforts continue to unfold as researchers delve deeper into their properties and applications. The flurry of scientific activity on MXenes has been remarkable. Not seen since the discovery of Graphene was there such a proliferation of research articles and intense interest in a class of materials in such a short period of time. From fundamental properties to applications in batteries, catalysis, optoelectronics, medicine and telecommunications, MXenes have had a meteoric rise in materials science.

MXene is considered superior to graphene because MXene is inherently hydrophilic, yet exhibits higher conductivity than solution-treated graphene (Dillon et al., 2016). Furthermore, their remarkable electrochemical characteristics hold significant potential for flexible electronics and planar devices.

Since 2015, MXenes research has grown significantly on a worldwide scale, with more publications, including many groundbreaking papers, coming from countries other than the USA. Approximately 70,000 scientists from over 7600 institutions across 100 countries on all six continents have done MXene research so far. Since that this statistic is based on data from the Web of Science, which has a high barrier for adding publications to the database, the total numbers are believed to be 20-30% higher. (Anasori and Gogotsi, 2023). So MXenes global expansion may further be realized if one checks the holding of conferences in 2024 only. The third MXene conference, which will take place at MXenes' birthplace of Drexel University in Philadelphia, PA, on August 5-7, 2024, is planned. It is anticipated that Xi'an, China will host the Fifth International Conference on MXenes in October 2024. The first MXene conference specifically in Europe, called EUROMXENE, is likewise slated for June 2024 in Valencia.

Brief review of synthesis of MXenes

Naguib et al. (2011; 2012) developed and reported the synthesis of MXene phases. The 2D layers that remain after the A group layer is removed from the MAX phases are called MXenes to signify the absence of the A element and highlight their structural resemblances to graphene.

The family of 2D transition metal carbides, nitrides, and carbonitrides (MXenes) has grown significantly since the initial publication on $Ti_3C_2T_x$ in 2011.

MXenes now comprise both single and multi-element compounds, and many more have not yet been synthesized but are expected to have desirable features. A more thorough mechanistic knowledge of the precursors, etching-exfoliation, and final intercalation-delamination stages of the known MXene synthesis methods is required in order to synthesize these elusive compounds as well as to enhance and increase the production of known MXenes (Lim et al., 2022).

There are now two distinct methods for obtaining MXenes through the `bottom-up’ and `top-down’ ways (Fig. 3). The primary distinction between these two approaches is that, whereas the bottom-up technique forms the material from the bottom to the top using MXene deposition technology, the top-down synthesis method separates bulk materials, like MAX phases into several layers. It should be noted that the characteristics of the MXenes might vary depending on the synthesis process used. Moreover, the starting material including non MAX layered materials and different surface modification techniques employed in their preparation determinethe properties of 2D transition metal Carbides/nitrides/carbonitrides etc. For more details and to identify the advantages and disadvantages of various strategies see the review articles (Pogorielov et al., 2021; Lim et al., 2022; Panda et al., 2022; Oyehan et al., 2023; Akhtar and Maktedar, 2023). An overview of fabrication techniques is shown in Fig. 3.

The top-down method involves the exfoliation of thin layers of MXene films from their MAX phase/non-MAX phase precursors, while the bottom-up method combines different elements to create MXene thin films. The flowchart that shows the various top-down and bottom-up synthesis approaches of MXenes will be useful in providing a general understanding of the various techniques that will be further developed.

A top-down solution synthesis method of Nb_2C MXene to create fine 2D sheets using hydrofluoric (HF) acid through chemical etching is illustrated in Fig. 4 (Babar et al., 2020a).

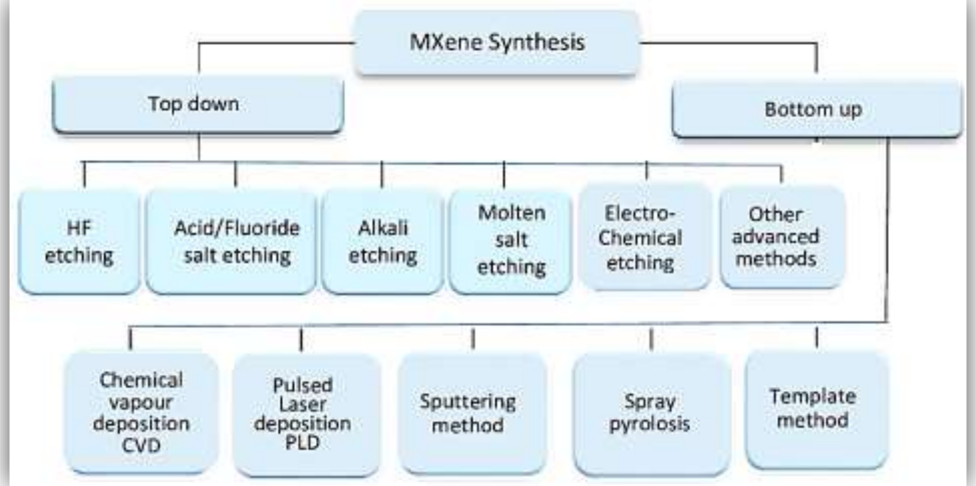

Fig. 3. Flow chart of MXene synthesis techniques.

$M_{n+1}X_nT_x$ (n = 1, 2, and 3) is the generic formula for MXenes, where M is a transition metal (such as Ti, Mo, Cr, Nb, and V), X is nitrogen or carbon, and T_x is a variety of surface functional groups (such as –OH, –O, and –F). The chemical interacts with acids during the etching process, and it forms the functional groups. Hexagonal crystal cells are layered to create MXenes. Wherever the M atoms are arranged hexagonally, the X atoms occupy the octahedral interstitial spaces. (Jiang et al., 2020).

Approximately thirty stoichiometric MXene family representatives have been produced experimentally in the ten years since their discovery, and more than 100 are theoretically predicted. Furthermore, reports of over 20 solid solutions and high-entropy MXenes have been made (Pogorielov et al., 2021).

The Al planes from the MAX phases were selectively etched to produce the majority of MXenes (25 out of 30). Thus far, only Ti_3SiC_2, a non-Al containing MAX phase, has been effectively etched into MXene. Notably, MXenes can also be produced from precursors of non-MAX phases; for example, Mo_2CT_z was produced by etching Ga layers from Mo_2Go_2C, $Zr_2C_2T_z$ was produced by etching Al_3C_3 layers from $Zr_3Al_3C_5$, and $Hf_3C_2T_Z$ was produced by etching $(Al,Si)_4C_4$ layers from $Hf_3(Al,Si)_4C_6$ (Champagne and Charlier, 2021).

Although hydrofluoric acid (HF) treatment is still the most widely used production process, it is hazardous and often requires a delamination step in order to separate the MXene sheets by the intercalation of metallic cations or organic molecules. Consequently several alternatives have been used, namely electrochemical etching, NH_4HF_2, and in situ HF production through the combination of HCl and LiF solutions. For more details see Champagne and Charlier (2021).

Structure and properties of MXenes

MXenes are produced in the MAX phase of the precursor material by selectively etching Group A elements. Etching can be used to remove the more chemically reactive Group A elements while maintaining the layered structure of $M_{n+1}X_n$ because the MX bonds are stronger than the MA bonds. As was previously mentioned, T_x stands for a variety of surface functional groups, including -OH, -O, and -F, in the formula for MXenes $M_{n+1}X_nT_x$. Wherever the X atoms occupy the octahedral interstitial sites, the M atoms are grouped hexagonally (Ampong et al., 2023).

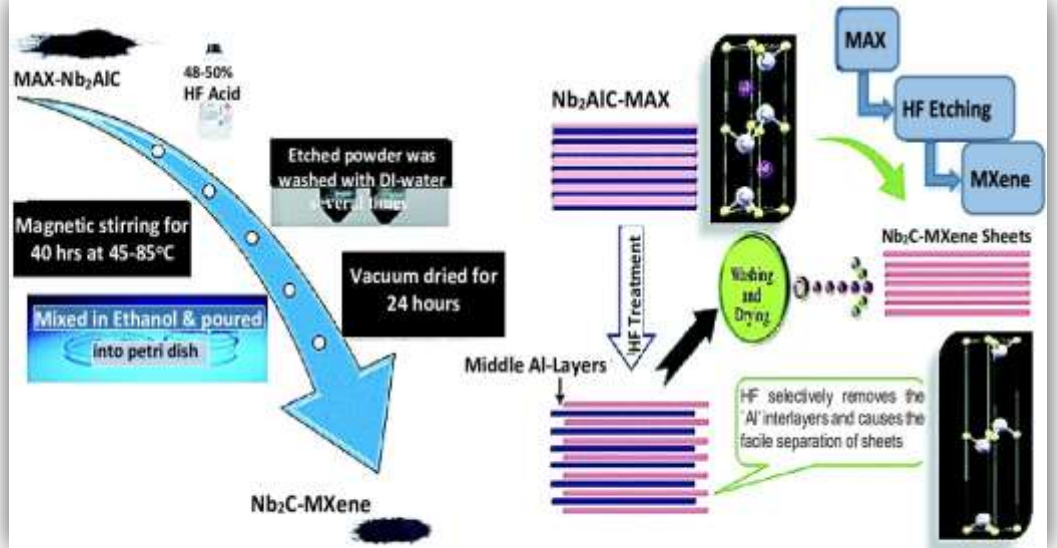

Fig. 4. The etching technique and synthesis schematics for the production of 2D MXene. Slightly modified from the original. Reproduced from Babar et al. (2020b) with permission. Copyright the Royal Society of Chemistry.

Extensive computational simulation studies are employed to comprehend the structures of MXenes and identify novel potentially stable compounds. This in reality aids experimental developments. These studies have yielded six distinct forms, namely Mo_2TiC_2 and $Mo_2Ti_2C_3$, and mono-M elements Ti_2C and Nb_4C_3 and ordered in-plane double-M elements such as ($Mo_{2/3}$), in which discrete M elements are placed in the basal plane. The vacancies might be randomly dispersed, as in $Nb_{1.33}CT_x$, or ordered, as in $Mo_{1.33}CT_x$ and $W_{1.33}CT_x$. These investigations support the search for new and stable MXene compounds and provide insights about the structural characteristics of MXenes (Akhter et al., 2023).

Numerous theoretical and experimental investigations have been conducted to learn more about the chemical and physical characteristics of MXenes since their discovery in 2011. High thermal and electrical conductivities, a variable electronic band gap, different magnetic ordering, and a high Young's modulus are among the special qualities of MXene (Champagne and Charlier, 2021).

The first member of the MXene family, Ti_3C_2, has been the subject of most research because of its wide range of applications. These are energy storage, sensors, photocatalysis, purification of water, electrodes (including flexible electronics), tribology, biomedicine, and SERS (Surface-Enhanced Raman Spectroscopy) substrates. Its exceptional hydrophilic nature, active surface area, and electrical and optical qualities make it stand out among other MXenes representatives, such as Nb_2C, Mo_2C, Ta_4C_3, Mo_2TiC_2, etc. over the past five years, have been actively investigated for a variety of applications (Pogorielov et al., 2021).

Zhu et al. (2021) observed that MXene's ability to control material properties make it more appealing than Graphene. This can be accomplished through processing, doping, and functionalization, while Graphene permits only functionalization.

According to DFT simulations bandgap of MXenes can be tailored by changing the surface terminations. The OH or F terminated MXenes, Ti_3C_2 in this example, behave as semiconductors with bandgap values of 0.05 eV and 0.1 eV, respectively, while the non-terminated (Pristine) MXenes behave as metallic conductors in nature. By changing their bandgap, these materials can therefore be used in applications ranging from semiconductors to field-effect transistors (Salim et al., 2019).

Babar et al. (2020b) reported that superconductivity was first observed in as-prepared powdered Nb_2C, with the MXene family having the highest onset transition temperature ($T_{c,onset}$= 12.5 K). Spin-polarized generalized gradient approximation (sp-GGA) was used in Wein2K to perform a first principles calculation of density functional theory (DFT) in order to investigate the magnetic nature. The compound's magnetic moment is calculated to be -0.00485; this value is significant despite being small because it indicates the presence of diamagnetism in Nb_2C as it is negative. Because the sample was powdered, it was impossible to measure its transport properties. The work is a major step forward in the study of superconductivity and magnetism in 2D MXene, and it may be investigated further in the future to measure the transport properties.

Breakthrough applications and future prospects of MXenes

a. Recent trends of applications of MXenes

MXenes have hydrophilic surfaces, bio-compatibility, reversible surface redox reaction capacity, high electronic conductivity (up to 20,000 S/cm), and visible and infrared optical absorption bands. As a result, the MXenes materials have been investigated for applications in optoelectronics, communication, electro-catalysis, water and gas purification, electrical energy storage, electromagnetic interference (EMI) shielding, flexible electronics, sensors, catalysis, additive manufacturing, biomedical and healthcare fields, etc.

The special issue MXenes: From Discovery to Applications (Xu and Gagotsi, 2020) features an editorial and articles that highlight the latest developments in the field of MXenes, extending their applications beyond energy and catalysis to include the biomedical sciences, optics, and other fields. Naguib et al. (2021) offer a synopsis of the first ten years of MXene research history as well as an outlook on their synthesis and future advancement.

Pogorielov et al. (2021) have reported that a variety of fields, including environmental pollution removal, water desalination, energy storage and harvesting, quantums, sensors, electrodes, and optical devices, have seen a rise in the use of MXene applications recently. Additionally, they have concentrated on the three most significant medical applications: antibacterial therapy, diagnostics, and photothermal cancer therapy. The initial findings regarding the acquisition and examination of high-entropy MXene structures.

EMI (Electromagnetic Interference) shielding is one of the MXenes application sectors that is expanding fast (Iqbal et al., 2020). It is truly dominated by MXenes these days with record performances of $Ti_3C_2T_x$. In biomedical applications, MXenes' flexibility and transparency enable their use in the engineering of tunable intraocular lenses. The spin-coating of $Ti_3C_2T_x$ over a hydrophobic acrylate intraocular lens has been reported by Ward et al. (2020). This leads to a decreased sheet resistance with visible region transmission. MXene's potential in optics is demonstrated by the MXenes coated lens, which showed no biotoxicity towards epithelial cells or release of inflammatory cytokines, suggesting that cataract sufferers may have enhanced eyesight.

We show below in Table 2 the investigated applications and properties of MXenes since 2011 till date. First ten rows of the second column of the table show the year in which the first papers had been reported on each application (Gogotsi and Anasori, 2019). Second column of the next seven rows show the year of recent development and applications of MXene-based films (MFs) (Iqbal et al., 2022). Energy storage was the first area in which MXenes was investigated. It makes up a sizable amount of MXene's operations. Since its introduction into the biomedical area in 2017, the use of MXenes has grown to become one of the most popular study subjects in the domains of theranostics, biosensors, dialysis, photothermal therapy of cancer, and neural electrodes. In areas like electromagnetic applications - such as printed antennas and electromagnetic interference shielding - MXene research is also taking over from other nanomaterials (Gogotsi and Anasori, 2019). They observed that the majority of published works are theoretical, and many predicted properties, like ferromagnetism or topological insulators, have not yet been experimentally validated. There are also very few experimental articles in other disciplines, like electrical and structural applications.

The widespread application of several promising electrochemical processes, such as CO_2 reduction reaction (CO_2RR), nitrogen reduction reaction (NRR), oxygen evolution reaction (OER), hydrogen evolution reaction (HER), and oxygen reduction reaction (ORR), is contingent upon the utilization of capable electrocatalysts. A surface-sensitive method known as surface-enhanced Raman spectroscopy (SERS) or surface-enhanced Raman scattering (SERS) increases Raman scattering by molecules adsorbed on abrasive metal surfaces or by nanostructure. Photocatalysis is a potential, currently among the most important topics for addressing environmental and energy problems (Sun et al., 2022).

b. Some breakthrough applications

We now discuss and provide some breakthrough and diverse applications of the wonder material MXenes below. Both current and future prospects will also be mentioned.

(i) Electrochemical energy storage

MXenes are efficient electrochemical energy storage materials and have thus shown a prominent role as electrodes in rechargeable Li- and Na-ion batteries, Li-S batteries and supercapacitors and ionic batteries. MXenes are characterized by a large specific surface area, a high number of active sites, a variety of surface functional groups, and an adjustable interlayer distance. The photocatalytic fuel production, such as hydrogen evolution from water splitting, and CO_2 reduction have exciting potential in terms of energy conversion (Pang et al., 2019).

Table 2. Explored applications of MXenes since 2011 till date.

MXenes	Year	Explored applications
$Ti_3C_3T_x$	2011	Synthesis, Stability, Intercalation, Other Processing.
$Ti_3C_3T_x$	2012	Energy: Electrochemical Capacitors, Micro-supercapacitors. Bateries: Li-ion, Na-Ion, Mg-Ion, Li-Sulfur. Energy Harvesting, Textile, Flexible energy storage.
$Ti_3C_3T_x$+other MXenes	2012	Structural: Mechanical, Composites.
Other MXenes	2013	Electronics: Electrical, Thermal, High Electrical Conductivity, Topological Insulators, Magnetic.
$Ti_3C_3T_x$	2015	Environment: Clean Air, Clean Water, Membrane.
Other MXenes	2015	Optical: SERS, Laser, Photo Detectors.
$Ti_3C_3T_x$	2016	Electromagnetic: EMI Shielding, Antenna, Microwave Absorption.
Other MXenes	2016	Catalysis: HER, OER, NRR, CO_2RR.
$Ti_3C_3T_x$	2017	Sensors: Gas, Humidity, Strain.
$Ti_3C_3T_x$	2017	Biomedical: Cancer Treatment, Dialysis Disorder, Neural Electrodes.
MXene-based films (MFs)	2016	Spray coating and Laser cutting.
	2017	Electrospinning, Spray coating, Vacuum filtration.
	2018	Stamping, Mechanical cutting, Screen printing.
	2019	3D printing, Inkjet printing, Electrochemical process.
	2020	Ion-beam cutting.
	2021	Vacuum filtration, Laser cutting fabrication, Screen printing.
	2022	Templating and Injection, Vacuum filtration.

(ii) MXene: A breakthrough for fast battery charging

Maintaining the energy density and power density (the pace at which the device can charge) of a charge-storing material involves making sure that ion channels stay clear. The Drexel team propped the MXene flakes in the electrodes vertically to avoid the stacking problem, which prevents ion diffusion. In this design, MXene is able to create additional pathways for ions to travel through the material quickly, in contrast to Traditional Battery (Adapted from Xia et al., 2018). A Model drawing of ion transport in such system using $Ti_3C_2T_x$ MXene films (MF) is shown in Fig. 5.

(iii) Emerging battery beyond Li-ion battery

In recent years, there has been a huge increase in research into next-generation battery technology beyond Li-ion batteries, or LIBs. The lack of suitable electrode materials has been a major obstacle that has significantly limited their development. Due to their many beneficial properties, MXenes are in demand as electrode materials for these emerging batteries (Ming et al., 2021). The electrolyte, or polyethylene oxide, has better ionic conductivity when Nb_2CT_x MXene is added. By incorporating Nb_2CT_x MXene, the ionic conductivity of the electrolyte (PEO, polyethylene oxide) is improved. Additionally, the nanosheets efficiently adsorb polysulfides on forming Nb-S bonds which inhibits the shuttle effect of polysulphides within the PEO framework.

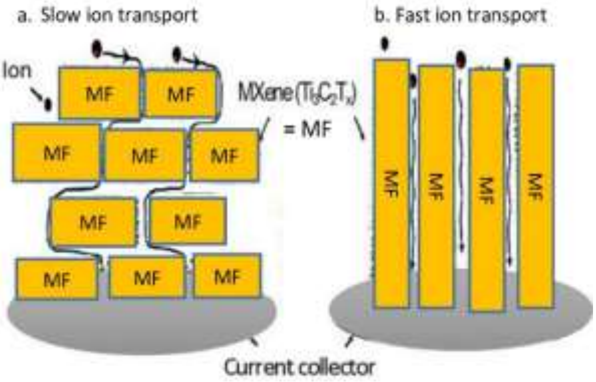

Fig. 5. Ion transport in $Ti_3C_2T_x$ MXene films stacked horizontally and vertically, respectively (a, b). The pathways for ion transport are shown by the vertically curved lines.

PEO is compatible with Li-S batteries, has strong lithium salt dissociation capability, and is well processable. Natural abundant sulfur with high capacity, and high specific energy density of lithium-sulfur (Li-S) batteries make them one of the most desirable candidates for next generation energy storage systems (1675 $mAhg^{-1}$ and 2600 $Whkg^{-1}$, respectively) (Huang et al., 2022). Lithium-sulfur batteries with up to 1,500 charge and discharge cycles have been demonstrated.

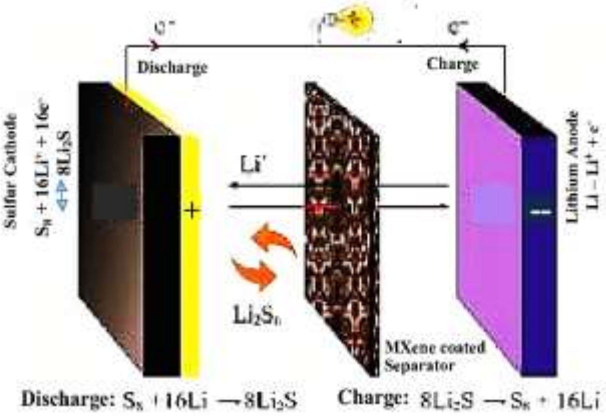

Fig. 6. Design of the Li-S cells using MXene PP (MPP) separator (Adapted from Song et al., 2016).

Lithium-sulfur (Li-S) batteries are considered to be among the most promising options to overcome the specific energy constraints of commercial lithium-ion batteries due to their low cost, high theoretical specific energy, and environmental credentials.

With a minimal mass loading of 0.1 mg cm^{-2} and a thickness of just 522 nm, the $Ti_3C_2T_x$ MXene can create a homogeneous coating layer in favor of the ultrathin 2D structure. The lithium-sulfur batteries with MXene-functionalized separators (Fig. 6) operate better than other lithium-sulfur batteries, exhibiting high specific capacities and cycling stability, due to their enhanced electric conductivity and efficient polysulfide trapping (Song et al., 2016).

▪ Promising results and future applications

Laser modified Leap: In order to improve MXene's electrode characteristics, researchers from KAUST, KSA, recently employed laser pulses. This could result in a breakthrough in rechargeable battery technology that could outperform conventional lithium-ion batteries (Bayhan et al., 2023). A lithium-ion battery was used to evaluate an anode made from this laser-scribed material through a total of 1000 charge-discharge cycles. Surprisingly, the material demonstrated a four-fold increase in electrical storage capacity with the nanodots compared to the unaltered MXene, almost matching the theoretical peak capacity of graphite. Furthermore, during the testing phase, laser modified material maintained its maximum potential. The promise of MXene-based hybrid materials for high-performance energy storage applications has thus been highlighted by the laser-induced synthesis method.

An anode composed of this laser-scribed material was tested through a total of 1000 charge-discharge cycles using a lithium-ion battery. Remarkably, as compared to the unaltered (Pristine) MXene, the material showed a four-fold incease in electrical storage capacity with the nanodots. Moreover, during the testing phase, the material changed by laser maintained its maximum potential. Thus, laser-induced synthesis technique highlights the potential of MXene-based hybrid materials for high-performance energy storage applications.

(iv) MXenes as electrocatalysts for HER

Hydrogen has drawn a lot of attention because of the global issues of environmental degradation and energy scarcity. Numerous benefits of hydrogen include its high energy density, low emissions of pollutants or greenhouse gases, recycling potential, and more. There are several ways to create hydrogen, such as burning biomass or fossil fuels, fermenting marsh gas, or using organic waste. Among which, the hydrogen evolution reaction (HER) based on water splitting has proven to be a cost-effective and ecologically sustainable method.

In order to obtain hydrogen in HER, the electrocatalyst is important. Electrocatalysts based on precious metals, including Pt and Ru, show efficiency and stability in this regard. However, a lack of resources and growing costs have made it difficult to meet the growing demand for electrocatalysts based on precious metals. In addition there are some problems of electrocatalysis in the existing methods.

With the advances of materials, MXenes show the ability to solve the issues listed above. MXenes have been considered a class of promising HER electrocatalysts due to their intrinsic layered structure and high carrier mobility (Bai et al., 2021).

(v) MXene: Best-ever protection against EM interference

Electromagnetic interference shielding is one of the MXenes application domains that is expanding fast. These days, MXenes really dominate it with record performances of $Ti_3C_2T_x$ and Ti_3CNT_x. Recent progress of the MXene family which entered the field in 2016 for protection against electromagnetic jamming, including EMI shielding and microwave absorption is noteworthy.

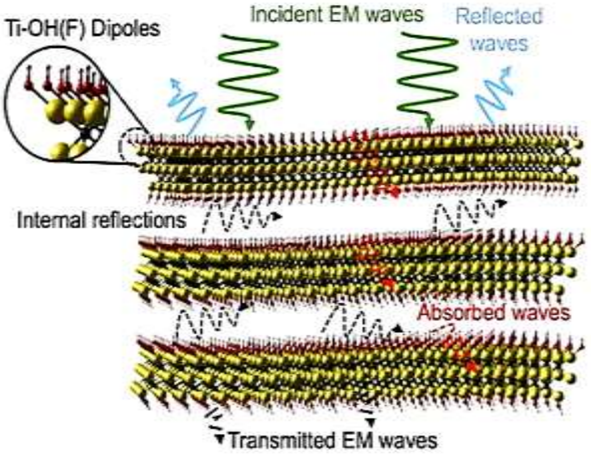

Fig. 7. EMI shielding mechanism of MXene-SA composite films. Reproduced with permission from Shahzad et al.(2016). Copyright 2016, the American Association for the Advancement of Science.

MXenes may contain “electromagnetic pollution” such as buzzing sound/EM. Radio noise can come from anything that generates, transmits, or uses electrical power, including televisions, Internet cables, cell phones, tablets, and laptops. Figure 7 shows that MXene protects against electromagnetic interference by absorbing and trapping waves between its layers (Shahzad et al., 2016). MXene works by both reflecting and absorbing electromagnetic fields. Waves. Some bounce of the coating surface immediately. Others pass through but lose energy in atomically thin layers of material. Lower energy EM waves are reflected by the inner layers until they are completely absorbed.

Remarkable advancements in communication technology coincide with the introduction of 5G technology. Compared to 4G cellular networks, it offers improved data-carrying capacities and transfer speeds that are about 100 times faster. Due to the wide frequency range of electromagnetic waves (EMWs) that these systems generate, receive, and/or transmit, EMI is prone to intensify, impairing device performance and jeopardizing system security (Iqbal et al., 2021). This review demonstrates how MXenes' inherent qualities such as their excellent metallic conductivity, 2D sheet morphology, tunable surface chemistry, light weight, and ease of solution processing offer them a promising future for EMI shielding applications. Ti_3C_2Tx MXene sheets with thicknesses in the nanometer to submicron range showed the best shielding efficiency. Through external modifications such as metastructure formation, Ti_3CNT_x MXene films demonstrated industry-leading shielding performance, superior to highly conductive $Ti_3C_2T_x$ MXene films and metallic films of comparable thickness.

(vi) Spintronic devices - 2D information superhighway

Spintronics is one of the emerging areas where next-generation nanoelectronic devices can reduce power consumption and increase storage and processing capabilities. MXenes or other nanomaterial-based devices exploit the spin degrees of freedom of electrons and/or holes, which can also interact with their orbital moments.

The ability to dynamically alter the spin of an electron presents opportunities for the development of new quantum-mechanical devices, including spin valves, spin transistors, and high-density memory. Particularly interesting are spintronic devices in the fields of quantum data processing, computing, and sensing.

(vii) MXenes in Nanogenerators

A device that transforms mechanical energy into electrical energy at the nanoscale is called a nanogenerator. Piezoelectric and triboelectric effects are the two underlying principles of nanogenerator operation. MXenes are frequently used to create effective nanogenerators in combination with other active materials. Both piezoelectric and triboelectric energy harvesting applications can make use of these nanocomposites. According to reports, a blue energy solution that transforms mechanical energy into electrical power is the piezoelectric nanogenerator (PENG).

▪ Piezoelectric Nanogenerators (PENGs)

The applied mechanical stress causes a displacement of the positive and negative charge centers within the material's crystal structure, resulting in the piezoelectric effect at the microscopic level. An electric potential, or voltage, is created across the material as a result of this displacement, which also causes electric polarization.

According to the most recent studies, Pt-infiltrated MXene on a paper substrate serves as a starting of the development of the flexible piezoresistive sensor. The sensitivity has increased from 0.08 to 0.5 kPa^{-1}, the detection limit has been extended from 5 to 9 kPa, the response time has decreased from 200 ms to 20 ms, and the recovery time has decreased from 230 ms to 50 ms (Qi et al., 2023).

Due to their low cost of fabrication, simple signal collection, and numerous useful applications-including smart displays, skin-inspired electronics, and portable healthcare monitors - these sensors have attracted a lot of attention.

Fig. 8. MXene-based TENG mounted on different parts of the body for harvesting energy from human muscle movements and from feet pressure.

- **Triboelectric Nanogenerators (TENG)**

TENGs generate electricity from friction. When two dissimilar materials come into contact and then separate, charge transfer occurs due to the triboelectric effect.

MXenes are helpful as constituents of TENG, which converts mechanical motion into electrical power. According to research, wearable technology, computers, mobile phones, and portable gadgets may all eventually be powered by these cutting-edge materials.

The ability to power electronic devices utilizing waste mechanical energy from the environment has been made possible by the quick development of energy harvesting employing nanogenerators. The development of TENG has advanced to the point of large-scale, scalable manufacture, and it is beginning to get commercialized.

The integration of wearable technology in clinical settings shows promise in enhancing diagnosis, enabling real-time monitoring of disease progression, and tailoring treatment to individuals.

In recent years, researchers have focused on harnessing environmental energy to generate electricity, addressing the need for a cleaner and more sustainable power supply (Jeewandara, 2019). The conversion of mechanical energy from the environment offers a green approach that is crucial in the development of wearable electronics and sensor networks for the Internet of Things (IoT).

- **TENG for Mars exploration**

This project is to field-test the in-house developed TENG that can harvest energy from the wind and all kinds of vibrations and motions. By rubbing two sheets of material together, the triboelectric effect and electrostatic induction combine to transform mechanical energy from the environment - such as wind and other motion or vibration - into electrical energy. This device is known as a harvesting device for energy. Because of its advantages in terms of launching and propulsion costs, this is an incredibly lightweight substitute for traditional electromagnetic motors, which are heavy. NASA states that this makes it a perfect fit for Mars exploration.

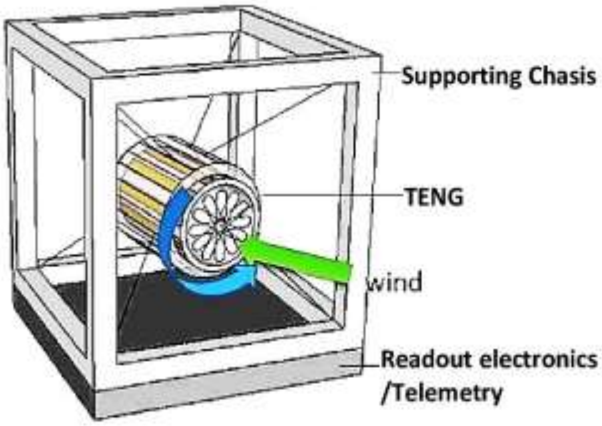

Fig. 9. Developed TENG for Mars exploration.

One day, using TENG for wind power generation on Mars will require overcoming a number of known and unknown technical obstacles. The next step in the process is to create a functional test bed in a balloon flight (Meyyappan and Kang, NASA).

(viii) Printed structures

Due to the hydrophilicity and extremely negative charge of MXene flakes, which have a zeta potential of about -30 mV, MXene can be uniformly dispersed in water, which has led to a rapid increase in the number of printed electronic products based on MXene. These properties of MXene also contribute to the process of producing colloidal particle dispersions in a variety of organic and aqueous solvents. (Ahmed et al., 2022).

Furthermore, recent advances in the field of MXene inks have led to promising results in the development of additive-free devices. This process is considered an innovative strategy due to its environmental impact, especially when compared to previous printing techniques that used additives.

- **Wearable sensors in smart fabrics**

Wearable sensors can be described as smart electronic devices that are worn on the body as an accessory or part of a garment. Sensors embedded in wearable devices can be used to continuously monitor physiological and motion variables.

In addition to data transmission, textile sensors in the form of a computer device worn on the body can also be used as intelligent sensor technology for accessing the mobile Internet. The next generation of human-machine interfaces can be built on these sensors. One of the main drivers of the development of textile sensors is the continuous discovery of new conductive materials. Recently a 2D MXene material that performs exceptionally well has drawn a lot of attention because of its strong conductivity, processability, and mechanical stability (Jin and Bai., 2022).

c. Versatile biomedical and related applications

MXenes represent a fascinating frontier in biomedical research, bridging the gap between nanotechnology and healthcare. Their multifaceted properties make them suitable for drug delivery, phototherapy, diagnostic imaging, biosensing, antimicrobial, biosafety evaluations and tissue engineering (Lin et al., 2018; Lu et al., 2021; Garg and Vitale, 2023; Lee et al., 2024).

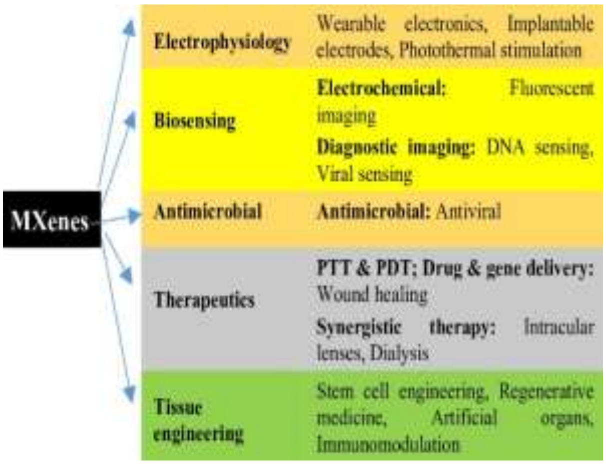

Electrophysiology	Wearable electronics, Implantable electrodes, Photothermal stimulation
Biosensing	**Electrochemical:** Fluorescent imaging **Diagnostic imaging:** DNA sensing, Viral sensing
Antimicrobial	**Antimicrobial:** Antiviral
Therapeutics	**PTT & PDT; Drug & gene delivery:** Wound healing **Synergistic therapy:** Intracular lenses, Dialysis
Tissue engineering	Stem cell engineering, Regenerative medicine, Artificial organs, Immunomodulation

Table 10. Emerging and novel areas of applications of MXenes e.g., in bioelectronics, tissue engineering, immunotherapy, therapeutics.

(i) MXene as sensitive gas sensor

The human body is a chemical metabolism factory, dogs are able to detect volatile organic compounds (VOCs) that are expelled by humans. The presence of certain compounds or the distinct chemical signatures of these VOCs can offer crucial hints about our health.

When a gas interacts with the MXene surface, it leads to changes in electrical conductivity. These conductivity variations are correlated with gas concentration, enabling sensitive detection. MXenes can form composite materials with other nanomaterials, enhancing their gas sensing capabilities. Composite structures increase surface area, interlayer spacing, and active sites for gas adsorption. MXenes are used for detecting various gases, including: Volatile Organic Compounds (VOCs): Such as acetone, ethanol, and benzene.

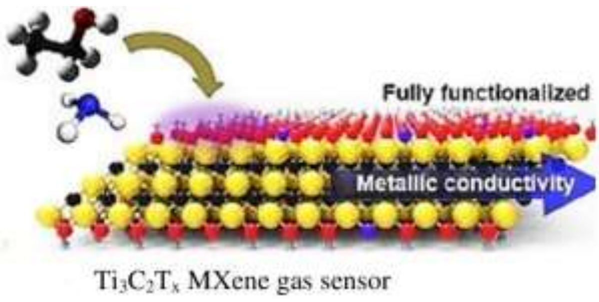

Fig. 11. Ultrahigh signal-to-noise ratio metallic $Ti_3C_2T_x$ MXene gas sensors. Reproduced with pemission from Kim et al. (2018). Copyright © 2018 American Chemical Society.

Solid-state gas sensors that achieve great sensitivity may be able to precisely identify chemical substances. Specifically, early illness diagnosis depends on the detection of VOCs at the parts per billion (ppb) level. Two conditions must be met at the same time in order to achieve great sensitivity: Existing sensor materials are unable to fulfill (i) low electrical noise and (ii) strong signal requirements. Existing sensor materials are unable to fulfill these two requirements (Kim et al., 2018).

Gas sensors must be able to precisely identify acetone molecules in breath at concentrations of between 300 and 1,800 parts per billion in order to identify diabetes. Gas sensors need to identify ammonia molecules in breath at 50–200 parts per billion in order to identify peptic ulcers. MXenes are an ideal gas sensor due to their great sensitivity and low noise, as demonstrated by theoretical work that has been verified by expt. These unique properties make $Ti_3C_2T_x$ superior gas-sensor over previously studied materials. Their versality, stability, and sensitivity contribute to the development of advanced sensors for environmental monitoring, safety, and health (Kim et al., 2018).

(ii) Targeted delivery of anticancer drugs or Nanomaterials

A cancer treatment called photothermal therapy (PTT) uses heat produced in tumor tissue that is exposed to near-infrared (NIR-II, 1000–1350 nm) light to cause the death of cancer cells. Utilizing NIR absorbents helps to produce heat more effectively. MXenes are great candidates for PTT because of their high absorbance in the near- infrared-II (NIR-II) region (An et al., 2021; Wu et al., 2023).

Nomura et al. (2020) has shown that PTT is an extremely dependable cancer treatment when it combines thermal dosimetry with an NIR absorbent.

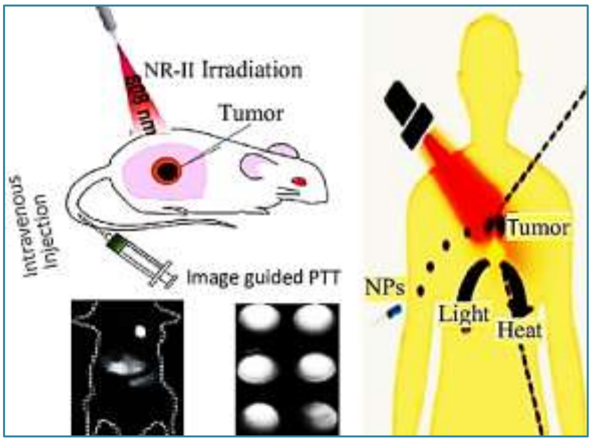

Fig. 12. PTT and NIR-II/MR imaging of cancer/ tumor using the MXene nanocomposites (collected from several sources and modified).

(iii) Antibacterial activity of $Ti_3C_2T_x$ MXene

In a colloidal solution, the antibacterial qualities of monolayer and multilayer $Ti_3C_2T_x$ MXene flakes were examined (Rasool et al., 2016). Initially, they proposed MXene's antimicrobial mechanism as a `nanoknife'. $Ti_3C_2T_x$ demonstrates stronger antibacterial activity against Gram-negative *E. coli* and Gram-positive *B. subtilis* than graphene oxide, which is widely reported as an antibacterial agent.

Fig. 13 illustrates the observed conc-dependent anti-bacterial activity. Photographs of agar plates onto which *E. coli* bacterial cells were recultivated after treatment for 4 h with 0 µg/mL (A), 10 µg/mL (B), 20 µg/mL (C), 50 µg/mL (D), 100 µg/mL (E), and 200 µg/mL (F) of $Ti_3C_2T_x$, respectively. Bacterial suspensions in deionized water without $Ti_3C_2T_x$ MXene material were used as control (Rasool et al., 2016).

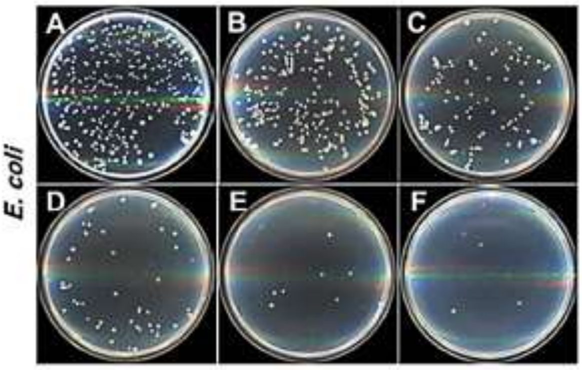

Fig. 13. Concentration dependent antibacterial activities of the $Ti_3C_2T_x$ in aqueous suspensions. Reproduced with permission from Rasool et al. (2016). Copyright © 2018 American Chemical Society.

In addition to having strong antibacterial, anti-inflammatory, and cell proliferation and migration-promoting qualities, MXene-based dressings also somewhat enhance their mechanical or physico-chemical qualities (Li et al., 2024). MXenes are now being deeveloped and used in a variety of wound dressings, including hydrogels, films, scaffolds, and sponges.

The excellent antibacterial, anti-inflammatory, and antioxidant properties of MXenes materials have been demonstrated in several recent studies. This has greatly aided in the development of MXenes in the fields of tissue engineering and skin regeneration. The development of novel wound dressings has advanced considerably as a result of several recent studies on the addition of MXenes.

(iv) Self-powered cardiovascular electronic devices (CED)

Cardiovascular disease is a leading cause of death worldwide. Current therapeutic approaches (such as drugs, cell-based therapy, and heart transplantation) have limitations in terms of efficacy and practical availability. MXenes play a crucial role to the development of self-powered CEDs. They are perfect for mediator-free biosensors because they allow direct electron flow between bioreceptors and electrodes. Additionally, MXenes act as frameworks for the immobilization of biomolecules, maintaining the activity of proteins.

Millions of patients with cardiovascular disease now experience lower rates of morbidity and death thanks to the development of wearable or implantable electronic devices, which have completely changed cardiovascular medicine's diagnostic and therapeutic approaches. This kind of self-powered technology produces electricity by converting energy from the environment or the human body. It can be used as a sustainable power source to augment or replace battery technology.

By providing continuous health monitoring both inside and outside of the clinical setting, wearable or portable CEDs have completely changed digital and mobile health monitoring. Wearable electronics have a plethora of potential uses in cardiovascular care, including monitoring vital signs and aiding in the diagnosis of both acute and chronic cardiovascular illness. Based on their functions, wearable cardiac electrodes can be categorized into four primary groups: heart rate monitors, hemodynamic monitors, daily activity monitors, and electrocardiography and heart rhythm monitors. Wearable electronics for cardiovascular health are available in a variety of styles, such as T-shirts, vests, smart watches, rings, wrist bands (cuffs), and chest patches (Amani et al., 2024).

Futuristic look

Even though MXene applications have advanced greatly, a few difficult problems still need to be fixed before new MXene-based products are released into the market. The first technological issue is from the manufacture of MXene using largely acidic chemicals including fluorine, which are hazardous to the biological environment. This problem might be partially resolved by bottom-up synthesis, but it requires technological advancement and scaling up. There have only been preliminary efforts made in this regard. If efficient delamination of salt-etched MXenes can be accomplished, molten salt etching holds great potential. MXene's cost has dropped dramatically in recent years, although it is still costly, primarily due to the materials' continued scarcity for large-scale manufacturing.

MXenes might oxidize while being stored. This could have a substantial impact on their characteristics, leading to further deterioration under specific application circumstances. MXenes, on the other hand, are stable for months in suspension and for many years in dry films due to enhanced stoichiometry and flake perfection. The synthesis and post-production processes of MXene have significantly improved in recent years due to the application of new technologies and solutions, which have dramatically improved the compound's characteristics and opened up new application opportunities (Pogorielov et al., 2021).

In the field of energy storage, MXenes show promise, and research is still being done to fully realize their potential. This fascinating topic is still being shaped by viewpoints and challenges for the future.

Acknowledgements

The author gratefully thanks Prof Yuri Gogotsi (Distinguished University Professor; Director, A.J. Drexel Nanomaterials Institute, USA) and Prof Martin Dahlqvist (Linköping University, Sweden) and all the authors of published works reported in this review.

References

Ahmed A, Sharma S, Adak B, Hossain MM, LaChance AM, Mukhopadhyay S and Sun L. Two-dimensional MXenes: New frontier of wearable and flexible electronics. *InfoMat*. 2022; 4: e12295.

Akhter R and Maktedar SS. MXenes: A comprehensive review of synthesis, properties, and progress in supercapacitor applications. *J. Mater.* 2023; 9(6):1196-1241.

Amani AM, Abbasi LTM, Vaez A, Kamyab H, Chelliapan S and Vafa E. The Need for smart materials in an expanding smart world: MXene-based wearable electronics and their advantageous applications. *ACS Omega*, 2024; 9(3): 3123-3142.

Ampong DN, Agyekum E, Agyemang FO, Mensah-Darkwa K, Andrews A, Kumar A and Gupta RK. MXene: fundamentals to applications in electrochemical energy storage. *Discover Nano*. 2023;18: 3.

An D, Fu J, Zhang B, Xie N, Nie G, Ågren H, Qiu M and Zhang H. NIR-II responsive inorganic 2D nanomaterials for cancer photothermal therapy: Recent advances and future challenges. *Adv. Funct. Mater.* 2021; 31(32):2101625

Anasori B and Gogotsi Y. *The global expansion of MXenes*. Graphene and 2D mater. 2023; 8: 39-41.

Anasori B, Shi C, Moon EJ, Xie Y, Voigt CA, Kent PRC, May SJ, Billinge SJL, Barsoum MW and Gogotsi Y. Control of electronic properties of 2D carbides (MXenes) by manipulating their transition metal layers. Nanoscale Horiz. 2016; 1: 227-234.

Babar ZUD, Anwar MS, Mumtaz M, Iqbal M, Zheng R-K, Akinwande D and Rizwan S. *Peculiar* magnetic behaviour and Meissner effect in two-dimensional layered Nb_2C MXene. *2D Mater.* 2020a; 7: 035012.

Babar ZUD, Fatheema J, Arif N, Anwar MS, Gul S, Iqbal M, and Rizwan S. Magnetic phase transition from paramagnetic in Nb_2AlC-MAX to superconductivity-like diamagnetic in Nb_2C-MXene: an experimental and computational analysis. *RSC Adv.* 2020b; 10: 43: 25669-25678.

Bai S, Yang M, Jiang J He X, Zou J, Xiong Z, Liao G and Liu S. Recent advances of MXenes as electrocatalysts for hydrogen evolution reaction. *npj 2D Mater. Appl.* 2021; 5: 78.

Barsoum MW and El-Raghy T. Synthesis and characterization of a remarkable ceramic: Ti_3SiC_2. *J. Am. Ceram. Soc*. 1996; 79: 1953-1956.

Barsoum MW, El-Raghy T and Ogbuji LUJT. Oxidation of Ti_3SiC_2 in air. *J. Electrochem. Soc.* 1997; 144: 2508-2516.

Barsoum MW, Farber L, Levin I, Procopio A, El-Raghy T and Berner A. High-resolution transmission electron microscopy of Ti_4AlN_3, or $Ti_3Al_2N_2$ revisited. *J. Am. Ceram. Soc*. 1999; 82: 2545-2547.

Barsoum MW. MAX phases: properties of machinable ternary carbides and nitrides. *Wiley-VCH Verlag GmbH & Co*. 2013. p. 436.

Barsoum MWand El-Raghy T. A progress report on Ti_3SiC_2, Ti_3GeC_2, and the H-phases, M_2BX. *J. Mater. Synth. Process.* 1997; 5: 197-216.

Bayhan Z, El-Demellawi JK, Yin J, Khan Y, Lei Y, Alhajji E, Wang Q, Hedhili MN and Alshareef HN. A laser-induced Mo_2CT_x MXene hybrid anode for high-performance li-ion batteries. *Small*, 2023; 19(36): 2208253.

Biswas A, Natu V and Puthirath AB. Thin-film growth of MAX phases as functional materials. *Oxford Open Mater. Sci.* 2021; 1(1): itab020.

Bortolozo AD, Sant'Anna OH, Dos Santos CAM and Machado AJS. Superconductivity in the hexagonal-layered nanolaminates Ti_2InC compound. *Solid State Commun.* 2007; 144: 419-421.

Bortolozo AD, Sant'Anna OH, Dos Santos CAM and Machado AJS. Superconductivity at 9.5 K in the Ti_2GeC compound. *Mater. Sci-Pol*, 2012; 30: 92-97.

Bortolozo AD, Fisk Z, Sant'Anna OH, Dos Santos CAM and Machado AJS. Superconductivity in Nb_2InC. *Physica C: Supercond*. 2009; 469: 256-258.

Bortolozo AD, Osorio WR, de Lima BS, Dos Santos CAM and Machado AJS. Superconducting evidence of a processed Nb_2GeC compound under a microwave heating. *Mater. Chem. Phys.* 2017; 194: 219-223.

Bortolozo AD, Sant'Anna OH, da Luz MS, dos Santos CAM, Pereira AS, Trentin KS and Machado AJS. Superconductivity in the Nb_2SnC compound. *Solid State Commun*. 2006; 139: 57-59.

Bortolozo AD, Serrano G, Serquis A, Rodrigues D Jr, dos Santos CAM, Fisk Z and Machado AJS. Superconductivity at 7.3 K in Ti_2InN. *Solid State Commun.* 2010; 150: 1364-1366.

Champagne A and Charlier J-C. Physical properties of 2D MXenes: from a theoretical perspective. *J. Phys. Mater.* 2021; 3: 3: 032006.

Dahlqvist M, Barsoum MW and Rosen J. MAX phases - Past, present, and future. *Mater. Today.* 2024; 72: 1-24.

Dillon AD, Ghidiu MJ, Krick AL, Griggs J, May SJ, Gogotsi Y, Barsoum MW and Fafarman AT. Highly conductive optical quality solution-processed films of 2D titanium carbide. *Adv. Funct. Mater.* 2016; 26: 4162-4168.

Filippatos PP, Hadi MA, Christopoulos S-RG, Kordatos Kelaidis AN, Fitzpatrick ME, Vasilopoulou M, and Chroneos A. 312 MAX Phases: Elastic Properties and Lithiation. *Materials,* 2019; 12(24): 4098.

Garg R and Vitale F. Latest advances on MXenes in biomedical research and health care. *MRS Bull.* 2023; 48(3): 283-290.

Gogotsi Y and Anasori B. The Rise of MXenes. *ACS Nano* 2019; 13: 8: 8491-8494.

Goossens N, Tunca B, Lapauw T, Lambrinou K and Vleugels J. MAX Phases, Structure, Processing, and Properties. In: Encyclopedia of Materials: Technical Ceramics and Glasses. M. Pomeroy (ed.), *Elsevier, Oxford,* 2021; pp. 182-199.

Hadi MA, Ali MS, Naqib SH and Islam AKMA. Band structure, Hardness, Thermodynamic and Optical properties of Superconducting Nb_2AsC, Nb_2InC and Mo_2GaC. *Int. J. Comp. Mater. Sci. Eng.* 2013; 2: 2: 1350007.

Hadi MA, Dahlqvist M, Christopoulos S-RG, Naqib SH, Chroneosc A and Islam AKMA. Chemically stable new MAX phase V_2SnC: A damage and radiation tolerant TBC material. *RSC Adv.* 2020; 10: 43783-43798.

Hadi MA, Kelaidis N, Naqib SH, Chroneos A and Islam AKMA. Electronic structures, bonding natures and defect processes in Sn-based 211 MAX phases. *Comput. Mater. Sci*. 2019; 168: 203-212.

Hadi MA, Roknuzzaman Md, Parvin F, Naqib SH, Islam AKMA and Aftabuzzaman Md. New MAX phase superconductor Ti_2GeC: A first-principles study. *J. Sci. Res.* 2014; 6: 1: 11-27.

Huang Y, Lin L, Zhang C, Liu L, Li Y, Qiao Z, Lin J, Wei Q, Wang L, Xie Q and Peng D-L. Recent advances and strategies toward polysulfides shuttle inhibition for high-performance li-s batteries. *Adv. Sci*. 2022; 9(12): 2106004.

Ingason AS, Dahlqvist M and Rosén J, Magnetic MAX phases from theory and experiments; a review. *J. Phys. Condens. Matter,* 2016; 28(43): 433003.

Ingason AS, Petruhins A, Dahlqvist M, Magnus F, Mockute A, Alling B, Hultman L, Abrikosov IA, Persson POÅ and Rosén J. A Nanolaminated Magnetic Phase: Mn_2GaC. Mater. *Res. Lett.* 2014; 2: 89-93.

Iqbal A, Kwon J, Kim M-K and Koo CM. MXenes for electromagnetic interference shielding: Experimental and theoretical perspectives. *Mater. Today Adv.* 2021; 9: 100124.

Iqbal A, Sambyal P and Koo CM. 2D MXenes for Electromagnetic Shielding: A Review. *Adv. Funct. Mater*. 2020; 30(47): 2000883.

Iqbal N, Ghani U, Liao W, He X, Lu Y, Wang Z and Li T. Synergistically engineered 2D MXenes for metal-ion/Li-S batteries: Progress and outlook. *Mater. Today Adv.* 2022; 16: 100303.

Islam AKMA. Remarkable class of materials: Band structures and optical properties of non superconducting and superconducting MAX phases. *J. Phys.: Conf. Ser.* 2021 (conf. 2015); 1718: 012002.

Jeewandara T. A next-generation triboelectric nanogenerator (TENG) to realize constant current from electrostatic breakdown. *Phys .Org.* April 15, 2019. http://phys.org/news/2019-04-

next-generation-triboelectric-nanogenerator-teng-constant.html

Jeitschko W and Nowotny H. Die Kristallstruktur von Ti_3SiC_2-ein neuer Komplexcarbid-Typ. *Monatshefte Für Chemie Chem Mon.* 1967;

98: 329-337.

Jeitschko W, Nowotny H and Benesovsky F. Carbides of formula T_2MC. *J Less Common Met.* 1964; 7(2): 133-138.

Jeitschko W, Nowotny H and Benesovsky F. *Kohlenstoffhaltige ternäre verbindungen (H-phase).* Monatshefte Für Chemie Und Verwandte Teile Anderer Wissenschaften. 1963; 94: 672-676.

Jiang X, Kuklin AV, Baev A, Ge Y, Ågren H, Zhang H and Prasad PN. Two-dimensional MXenes: From morphological to optical, electric, and magnetic properties and applications. *Phys. Rep.* 2020; 848: 1-58.

Jin C and Bai Z. MXene-based textile sensors for wearable applications. *ACS Sens.* 2022; 7(4): 929-950.

Karaca E, Byrne PJP, Hasnip PJ and Probert MIJ. Prediction of phonon-mediated superconductivity in new Ti-based M_2AX phases. *Sci. Rep.* 2022; 12: 13198.

Karaca E, Byrne PJP, Hasnip PJ, Tutuncu HM and Probert MIJ. Electron–phonon interaction and superconductivity in hexagonal ternary carbides Nb_2AC (A: Al, S, Ge, As and Sn). *Electron. Struct.* 2021; 3: 045001.

Kim SJ, Koh H-J, Ren CE, Kwon O, Maleski K, Cho S-Y, Anasori B, Kim C-K, Choi Y-K, Kim J, Gogotsi Y and Jung H-T. Metallic $Ti_3C_2T_x$ MXene gas sensors with ultrahigh signal-to-noise ratio. *ACS Nano*, 2018; 12(2): 986-993.

Kuchida S, Muranaka T, Kawashima K, Inoue K and Yoshikawa M. Superconductivity in Lu_2SnC. *Physica C: Supercond.* 2013; 494: 77-79.

Lai C-C, Fashandi H, Lu J, Palisaitis J, Persson POÅ, Hultman L, Eklund P and Rosen R. Phase formation of nanolaminated Mo_2AuC and $Mo_2(Au_{1-x}Ga_x)_2C$ by a substitutional reaction within Au-capped Mo_2GaC and Mo_2Ga_2C thin films. *Nanoscale,* 2017; 9: 17681-17687.

Lambrinou K, Charalampopoulou E, Van der Donck T, Delville R and Schryvers S. Dissolution corrosion of 316L austenitic stainless steels in contact with static liquid lead-bismuth eutectic (LBE) at 500°C. *J. Nucl. Mater.* 2017; 490: 9-27.

Lee I-C, Li Y-C E, Thomas JL, Lee M-H and Lin H-Y. Recent advances using MXenes in biomedical applications. *Mater. Horiz.* 2024; 11: 876-902.

Li H, Mu M, Chen B, Zhou L, Han B and Guo G. MXene-based nanomaterials for antibacterial and wound healing, *Mater. Res. Lett.* 2024; 12: 2: 67-87.

Li M, Lu J, Luo K, Li Y, Chang K, Chen K, Zhou J, Rosen J, Hultman L, Eklund P, Persson POÅ, Du S, Chai Z, Huang Z and Huang Q. Element replacement approach by reaction with lewis acidic molten salts to synthesize nanolaminated MAX phases and MXenes. *J. Am. Chem. Soc.* 2019; 141: 11: 4730-4737.

Lim KRG, Shekhirev M, Wyatt BC, Anasori B, Gogotsi Y and She ZW. Fundamentals of MXene synthesis. *Nat. Synth.* 2022; 1: 601-614.

Lin H, Chen Y, and Shi J. Insights into 2D MXenes for versatile biomedical applications: Current advances and challenges ahead. *Adv. Sci.* 2018; 5(10): 1800518.

Lofland SE, Hettinger JD, Meehan T, Bryan A, Finkel P, Gupta S, Barsoum MW and Hug G. Electron-phonon coupling in $M_{n+1}AX_n$-phase carbides. *Phys. Rev. B.* 2006; 74: 174501.

Low IT. An Overview of Parameters Controlling the Decomposition and Degradation of Ti-Based $M_{n+1}AX_n$ Phases *Materials*. 2019; 12: 3: 473.

Lu B, Zhu Z, Ma B, Wang W, Zhu R and Zhang J. 2D MXene Nanomaterials for Versatile Biomedical Applications: Current Trends and Future Prospects. *Small.* Nov 2021; 17: 46: e2100946.

Magnuson M and Mattesini M. Chemical bonding and electronic-structure in MAX phases as viewed by X-ray spectroscopy and density functional theory. *Thin Solid Films*. 2017; 621: 108-130.

Meyyappan M and Kang JH. Triboelectric Nano Generator (TENG) for Mars Exploration and High Altitude Power Generation on Earth.

NASA/Ames Research Center, NASA/Langley Research Center, USA. T0222-B. NASA sponsored.

Ming F, Liang H, Huang G, Bayhan Z and Alshareef HN. MXenes for Rechargeable Batteries Beyond the Lithium-Ion. *Adv. Mater*. 2021; 33(1) 2004039.

Naguib M, Barsoum MW and Gogotsi Y. Ten years of progress in the synthesis and development of MXenes. *Adv. Mater.* 2021; 33(39): 2103393.

Naguib M, Kurtoglu M, Presser V, Lu J, Niu J, Heon M, Hultman L, Gogotsi Y, and Barsoum MW. Two-Dimensional nanocrystals produced by exfoliation of Ti_3AlC_2. *Adv. Mater.* 2011; 23: 4248-4253.

Naguib M, Mashtalir O, Carle J, Presser V, Lu J, Hultman L, Gogotsi Y and Barsoum MW. Two-Dimensional transition metal carbides. *ACS Nano,* 2012; 6(2):1322-1331.

Nasir MT and Islam AKMA. MAX phases Nb_2AC (A = S, Sn): An ab initio study. *Comput. Mater. Sci*. 2012; 65: 365-371.

Nomura S, Morimoto Y, Tsujimoto H, Arake M, Harada M, Saitoh D, Hara I, Ozeki E, Satoh A, Takayama E, Hase K, Kishi Y and Ueno H. Highly reliable, targeted photothermal cancer therapy combined with thermal dosimetry using a near-infrared absorbent. *Sci Rep.* 2020; 10(1): 9765.

Oyehan TA, Salami BA, Abdulrasheed AA, Hambali HU, Gbadamosi A, Valsami-Jones E and Saleh TA. MXenes: Synthesis, properties, and applications for sustainable energy and environment. *Appl. Mater. Today*. 2023; 35: 101993.

Palmquist JP, Jansson U, Seppänen T, Persson POÅ, Birch J, Hultman L, and Isberg P. Magnetron sputtered epitaxial single-phase Ti_3SiC_2 thin films. *Appl.Phys.Lett.* 2002; 81(5): 835-837.

Panda S, Deshmukh K, Pasha SKK, Theerthagiri J, Manickam JS and Choi MY. MXene based emerging materials for supercapacitor applications: recent advances, challenges, and future perspectives. *Coord. Chem. Rev*. 2022; 462: 214518.

Pang J, Mendes RG, Bachmatiuk A. Zhao L, Ta HQ, Gemming T, Liu H, Liu Z, and Rummeli MH. Applications of 2D MXenes in energy conversion and storage systems. *Chem. Soc. Rev*. 2019; 48: 72-133.

Pogorielov M, Smyrnova K, Kyrylenko S, Gogotsi O, Zahorodna V and Pogrebnjak A. MXenes-A new class of two-dimensional materials: structure, properties and potential applications. *Nanomater*. 2021; 11(12): 3412.

Qi Z, Zhang T, Zhang X-D, Xu Q, Cao K and Chen R. MXene-based flexible pressure sensor with piezoresistive properties significantly enhanced by atomic layer infiltration. *Nano Mater. Sci.* 2023; 5(4): 439-446.

Rackl T, Eisenburger L, Niklaus R and Johrendt D. Syntheses and physical properties of the MAX phase boride Nb_2SB and the solid solutions $Nb_2SB_xC_{1-x}$ (x=0-1). *Phys. Rev. Mater.* 2019; 3(5): 054001.

Rasool K, Helal M, Ali A, Ren CE, Gogotsi Y and Mahmoud KA. Antibacterial Activity of $Ti_3C_2T_x$ MXene. *ACS Nano,* 2016: 10(3): 3674-3684.

Roknuzzaman M and Islam AKMA. Ab initio investigation of superconducting MAX phases Ti_2InX (X =C, N). *ISRN Cond. Matter Phys.* 2013; 2013: 646042.

Romero M, Huerta L, Akachi T, Llamazares JLS and Escamilla R. X-ray photoelectron spectroscopy studies of the electronic structure of superconducting Nb_2SnC and Nb_2SC J. *Alloys Compd*. 2013; 579: 516-520.

Sakamaki K, Wada H, Nozaki, H Ōnuki Y and Kawai M. Carbosulfide superconductor. *Solid State Commun*. 1999; 112: 323-327.

Salim O, Mahmoud KA, Pant KK and Joshi RK. Introduction to MXenes: synthesis and characteristics. *Mater. Today Chem.* 2019; 14: 100191.

Schuster JC and Nowotny H. Investigations of the ternary systems (Z r, Hf, Nb, Ta)-Al-C and studies on complex carbides. *Int. J. Mater. Res.* 1980; 71: 341-346.

Shahzad F, Alhabeb M, Hatter CB, Anasori B, Man Hong S, Koo CM and Gogotsi Y. Electromagnetic interference shielding with 2D transition metal carbides (MXenes). *Science,* 2016; 353(6304): 1137-1140.

Shein IR and Ivanovskii AL. Elastic properties of superconducting MAX phases from first-principles calculations. *Phy. Stat. Soli. B.* 2011; 248(1): 228-232.

Shein R and Ivanovskii AL. Structural, elastic, electronic properties and Fermi surface for superconducting Mo_2GaC in comparison with V_2GaC and Nb_2GaC from first principles. *Physica C: Supercond.* 2010; 470(13-14): 533-537.

Song J, Su D, Xie X, Guo X, Bao W, Shao G, and Wang G. Immobilizing Polysulfides with MXene-Functionalized Separators for Stable Lithium-Sulfur Batteries. *ACS Appl. Mater. Interf.* 2016; 8(43): 29427-29433.

Sun Y, Dall'Agnese C, Zhang C, Yang L, Jin X, Dall'Agnese Y and Wang X-F. Applications of MXenes and their composites in catalysis and photoelectrocatalysis. In: *MXenes and their Composites: Synthesis, Properties and Potential Applications.* Chapter 14, Sadasivuni KK, Deshmukh K, Pasha SKK and Kovari KT, (eds.*)* *Elsevier.* 2022; pp. 449-498.

Sun ZM, Zhou Y and Li M. Oxidation behaviour of Ti_3SiC_2-based ceramic at 900-1300°C in air. *Corros. Sci.* 2001; 43(6): 1095-1109.

Tallman DJ, Anasori B and Barsoum MW. A critical review of the oxidation of Ti_2AlC, Ti_3AlC_2 and Cr_2AlC in air. *Mater. Res. Lett*. 2013; 1(3): 115-125.

Toth LE. High superconducting transition temperatures in the molybdenum carbide family of compounds*. J. Less Common Met.* 1967; 13(1): 129-131.

Wang C, Tracy CL, and Ewing RC. Radiation effects in $M_{n+1}AX_n$ phases. *Appl. Phys. Rev*. 2020; 7(4): 041311.

Ward EJ, Lacey J, Crua C, Dymond M, Maleski K, Hantanasirisakul K, Gogotsi Y and Sandeman SR. 2D titanium carbide ($Ti_3C_2T_x$) in accommodating intraocular lens design. *Adv. Funct. Mater*. 2020; 30(47): 2000841.

Wu Z-H, Peng M, Ji C, Kardasis P, Tzourtzouklis l, Baumgarten M, Wu H, Basché T, Floudas G, Yin M and Müllen K. A Terrylene–Anthraquinone dyad as a chromophore for photothermal therapy in the NIR-II window. *J. Am. Chem. Soc.* 2023; 145(48): 26487-26493.

Xia Y, Mathis TS, Zhao M-Q, Anasori B, Dang A, Zhou Z, Cho H, Gogotsi Y and Yang S. Thickness-independent capacitance of vertically aligned liquid-crystalline MXenes. *Nature* 2018*;* 557: 409-412.

Xu B and Gogotsi Y. MXenes: from discovery to applications. *Adv. Funct. Mater*, 2020; 30(47): 2007011.

Yang HJ, Pei YT, Song GM, De Hosson JTM, Comments on "microstructural evolution during high-temperature oxidation of Ti_2AlC ceramics", *Scr. Mater*. 2011; 65(10): 930-932.

Zhou A, Liu Y, Li S, Wang X, Ying G, Xia Q, Zhang P. From structural ceramics to 2D materials with multi-applications: A review on the development from MAX phases to MXenes. *J. Adv. Ceram*. 2021; 10(6): 1194-1242.

Zhu X, Liu P, Xue T, Ge Y, Ai S, Sheng Y, Wu R, Xu L, Tang K, Wen Y. A novel graphene-like titanium carbide MXene/Au-Ag nanoshuttles bifunctional nanosensor for electrochemical and SERS intelligent analysis of ultra-trace carbendazim coupled with machine learning. *Ceram. Int*. 2021; 47(1): 173-184.

J. Bangladesh Acad. Sci. 48(1); 27-34: June 2024 DOI:https://doi.org/10.3329/jbas.v48i1.68708

Journal of Bangladesh Academy of Sciences

Journal homepage: http://www.bas.org.bd/publications/jbas.html

Research Article

Effect of *p*-type doped buffer layer on the structural and magnetic properties of (Zn, Fe)Te dilute magnetic semiconductor

Indrajit Saha* and Shinji Kuroda[1]

Department of Physical and Mathematical Sciences, Chottogram Veterinary and Animal Sciences University, Khulshi, Chottogram, Bangladesh

ARTICLE INFO

Article History

Received: 10 September 2023
Revised: 19 November 2023
Accepted: 27 December 2023

Keywords: Molecular beam epitaxy, Tellurites, Magnetic materials, van-Vleck paramagnetism, Ordinary paramagnetism, Zinc-blende.

.

ABSTRACT

We have studied the structural and magnetic properties of Zn $_{1\text{-}x}$Fe$_x$Te thin films grown under Te-rich flux conditions with almost the same Fe composition, x =1.3%, on both undoped and nitrogen (N) acceptor doped ZnTe buffer layer by molecular beam epitaxy (MBE). Structural analysis by XRD and XAFS reveals that Zn $_{0.987}$Fe$_{0.013}$Te films have a pure diluted phase of Zinc-blende structure having Fe atoms in the substitutional position on the Zn-site in both cases. However, the magnetization measurement using SQUID shows distinctly different *M-H* curves for these films; the linear nature of magnetization on magnetic field (*M-H*), namely, van-Vleck paramagnetic behavior of Zn $_{0.987}$Fe$_{0.013}$Te film grown over undoped ZnTe turns into ordinary paramagnetic behavior with S-shape *M-H* curve for film grown on N-doped ZnTe buffer layer, [N] ≈10^{20} cm^{-3} which may reflect the impact of interfacial holes provided by N-acceptors on the valence state of substitutional Fe.

Introduction

Diluted Magnetic Semiconductors (DMSs) comprise a group of semiconductor materials in which a considerable amount of host atoms are substituted by transition metals or rare earths (lanthanides) having incomplete 3d or 4f shells, respectively. Among most of the studied DMSs, the impurity band developed from these open d or f shells has been observed to be located in the mid-gap region of the host material and, hence, supplies only the magnetic moment but no extra carriers (Dietl, 1981; Vonsovskii, 1974; Sato and Katayama-Yoshida, 2002). (Zn, Fe) Te belongs to the same category of DMS with Fe$^{2+/3+}$ impurity level residing at 150 me Vin the band gap region of ZnTe, as confirmed by experimental observations (Jantsch and Hendorfer, 1990; Szadkowski, 1990). First-principle calculations for substitutional Fe on the Zn-site of the ZnTe matrix have evidenced that the interaction between the Fe ions is antiferromagnetic in nature and the stable magnetic state of (Zn,Fe)Te is paramagnetic (Sato and Katayama-Yoshida, 2002). This theoretical observation has later been experimentally verified for both bulk crystals and epitaxial layers grown by MBE (Twardowski, 1990; Malguth et al., 2008; Ishitsuka et al., 2014; Nakamura et al., 2017). The magnetization results have confirmed van-Vleck paramagnetic behavior as the intrinsic magnetic properties of (Zn, Fe)Te with very low Fe composition (Fe ≈1.6%) (Twardowski, 1990). Accordingly, Zn$_{1\text{-}x}$Fe$_x$Te thin films maintain the pure dilute zinc-blende (ZB) phase of ZnTe and exhibit van-Vleck type paramagnetic behavior for Fe composition, $x \leq 0.02$ (Ishitsuka et al., 2014; Nakamura et al., 2017).

However, for such DMSs, engineering the Fermi level position with additional charge co-doping or

---

*Corresponding author:<indrajits.cvasu@gmail.com>

[1] *Institute of Materials Science, University of Tsukuba, Tennoudai, Tsukuba, Japan*

controlled deviations of stoichiometry has remained an efficient way to change the valence state of magnetic ions, and hence, modify the magnetic properties (Kuroda et al., 2007; Dietl and Ohno, 2006; Dietl et al., 2015; Dietl, 2006).We have already performed similar experimental studies on N-acceptor co-doped $Zn_{1-x}Fe_xTe$ thin films with Fe composition, $x \leq 0.02$, grown under different growth conditions (Saha et al., 2019; Saha et al., 2020). Since the position of N acceptor levels is just below the $Fe^{2+/3+}$ deep donor levels in the band gap region of ZnTe (Jantsch and Hendorfer, 1990; Szadkowski, 1990; Grun et al., 1996), the capturing of holes supplied by N acceptor can alter the valence state of isoelectronic Fe^{2+}, which has indeed been evidenced in our studies (Saha et al., 2019; Saha et al., 2020). The van-Vleck paramagnetic behavior of (Zn, Fe)Te thin films has transformed to room temperature ferromagnetic behavior in N-doped (Zn, Fe)Te films for $[N] = 10^{18}$ cm^{-3} (Saha et al., 2020). This modification of magnetic properties has been explained based on the deviation of the Fe valence state from isoelectronic Fe^{2+} to $Fe^{2+/3+}$ mixed states due to N-doping. As a result, Fe ions can produce finite magnetic moments even without applying an external magnetic field and hence, the exchange interaction among the magnetic ions may change (Saha et al., 2020). We have also verified the impact of stoichiometry deviation on the magnetic properties of (Zn, Fe)Te thin films experimentally by varying the Te/Zn flux ratios during the growth (Saha et al., 2022).

DMSs that have ferromagnetic properties above room temperature are of great interest to spintronics applications (Ohno, 1998). Since future spintronics devices are expected to be composite heterostructures, the growth of (Zn, Fe)Te on *n*- or *p*-type doped buffer layer is necessary for any spin injection devices. The magnetic and transport properties of $Ga_{1-x}Mn_xAs$ thin films grown on Be (*p*-type) doped GaAs buffer layer have shown significant differences from those grown on an undoped GaAs buffer layer (Yoon et al., 2004). The magnetic properties of $Ga_{1-x}Mn_xAs$ thin film have been significantly improved by using *p*-type doped buffer layer. However, the magnetic properties of $Zn_{1-x}Fe_xTe$ thin films grown on either *n*- or *p*-type buffer layer have yet to be studied. The ionization energy of N in ZnTe has been measured at 53.4 ±1 meV, which decreases rapidly with the increase of the doping level (Baron et al., 1998). For ZnTe, by bringing the radio frequency (rf) or direct current (DC) glow plasma source closer to the substrate, hole density up to 10^{20} cm^{-3} can be achieved for N-doping concentrations, $[N] \approx 1.5 \times 10^{20}$ cm^{-3} (Baron et al., 1998; Han et al., 1993; Baron et al., 1995). At this doping level, ZnTe shows metallic behavior with resistivity down to $\rho \approx 5 \times 10^{-3} \Omega$ cm and mobility, $\mu_h \approx 10$ cm^2/ Vs at 10 K (Baron et al., 1998). These exciting properties of the heavily N-doped ZnTe layer, together with the remarkable enhancement of magnetic properties of (Zn, Fe)Te due to N-acceptor (*p*-type) co-doping (Saha et al., 2019; Saha et al., 2020), has inspired us to investigate the impact of interfacial holes on the structural and magnetic properties of $Zn_{1-x}Fe_xTe$ thin films grown on N-acceptor doped ZnTe buffer layer which are expected to be different from those grown on undoped ZnTe buffer layer.

Materials and Methods

$Zn_{1-x}Fe_xTe$ thin films are grown with Fe composition almost fixed at $x \approx 0.013$ in ultra-high vacuum condition of 10^{-10} Torr inside a molecular beam epitaxy (MBE) chamber having Zn, Te and Fe elemental solid sources. Films are grown on GaAs (001) substrate. In the case of conventional sample (#1) ($Zn_{0.987}Fe_{0.013}Te$ on ZnTe), a thick buffer layer of ZnTe (~600 nm) is grown before the growth of $Zn_{0.987}Fe_{0.013}Te$ layer (~40 nm) to relax the large lattice mismatch. However, in the case of modulation doped sample (#2) ($Zn_{0.987}Fe_{0.013}Te$ on *p*-type ZnTe), The N-doped ZnTe layer (~300 nm) is additionally grown in between the ZnTe (~600 nm) and $Zn_{0.987}Fe_{0.013}Te$ (~40 nm) layer. During the growth of the ZnTe: N layer, radio frequency (rf) plasma has been employed to excite a nitrogen plasma source filled with N_2 gas at 300 W and a flow rate of 0.3

cm^3/min. We have kept the shutter of the plasma source positioned at 2 cm from the substrate fully open during the growth of the N-doped layer. In both cases, we deposited a thin ZnTe cap layer (~2 nm) on the magnetic layer to avoid surface oxidation during air exposure. All epitaxial layers are grown at substrate temperature of 260°C except the cap layer, which is grown at low temperature. The Beam Equivalent Pressures (BEPs) of Zn and Te during the growth of both the buffer layer and magnetic layer have been kept at 2.0×10^{-7} and 4.6×10^{-7} Torr respectively, to achieve Te-rich growth mode (Te/Zn flux ratio ≈ 2.3) for films (#1) and (#2). The BEPs are measured both before and after the growth of each epitaxial layer with the help of an ion gauge by placing it at the growth position.The flux of the effusion cells depends on the cell temperature measured by the thermocouple placed in contact with the cell crucible. Reflection high energy electron diffraction (RHEED) has been used to monitor the in-situ of the film surface during growth. The (2 × 1) streak pattern is maintained throughout $Zn_{0.987}Fe_{0.013}Te$ film (#1) growth over the ZnTe buffer layer. However, in the case of the film (#2), the (2×1) RHEED pattern changes from streak to spotty after the growth of the N-doped ZnTe layer. A similar type of spotty pattern has been observed for $Zn_{1-x}Fe_xTe$: N films with [N] > 10^{19} cm^{-3} (Saha et al., 2019; Saha et al., 2020). The Fe concentration of the films was measured by using an electron probe microanalyzer (EPMA). X-ray diffraction (XRD) θ-2θ scan has been utilized to accomplish the structural characterizations of the grown films to identify any possible precipitates of secondary phases. X-ray absorption fine structure (XAFS) measurements have been performed at the beamline BL12C of KEK-PF to investigate the surrounding environment of Fe in the films. Since the concentration of the material of interest is very low, the fluorescence-detection mode has been chosen for the Fe K-edge XAFS spectrum and measured at a low temperature of around 20 K. A Si (111) double crystal monochromator has been used to adjust the intensity of the incident X-ray monochromatic beam, and a nitrogen-filled ionization chamber has been employed for monitoring. An array of 19 Ge detector elements helps to detect the fluorescence signal. The magnetization measurements were accomplished with the help of a superconducting quantum interference device (SQUID) magnetometer with magnetic field applied normal to the film plane. The dependences of magnetization on magnetic field (M-H) and on temperature (M-T) have been performed to explain different aspects of the magnetic properties (Kuroda et al., 2007).

Results and Discussion

First, the result of XRD θ-2θ scan profiles has been discussed to analyze the structural properties of $Zn_{0.987}Fe_{0.013}Te$ films grown over undoped (#1) and N-doped (#2) ZnTe buffer layer as shown in Fig.1. In both cases, diffraction peaks only from the ZnTe buffer layer and GaAs substrate have been detected. However, for the film (#2) [$Zn_{0.987}Fe_{0.013}Te$/ZnTe: N], Peaks from the ZnTe and ZnTe: N layer have appeared separately for the (400) and (600) diffractions. A similar type of lattice parameter difference between the undoped and doped layer of ZnTe has been observed in the XRD pattern of ZnTe: N/ZnTe pseudosuperlattices for N concentrations, [N] ≈ 10^{19} cm^{-3} (Baron et al., 1998). The introduction of nitrogen atoms into the ZnTe crystal in the N_{Te} configuration with $[N_{Te}] = 10^{19}$ cm^{-3} can produce a relative change of -1.3×10^{-4} in the lattice parameter (Baron et al., 1998). This change in lattice parameter has been estimated based on the change in ionic radii, $\delta d \approx -0.062$ nm, when one N atom ($r_N = 0.07$ nm) replaces one Te atom ($r_{Te} = 0.132$ nm). As we have deposited heavily N-doped ZnTe layer above the undoped ZnTe layer for $Zn_{0.987}Fe_{0.013}Te$ film [#2], separated diffraction peaks from the ZnTe layer and ZnTe: N layer for the (400) and (600) diffractions are expected. From this deviation of lattice constant, a, the concentration of nitrogen atoms in the substitutional site on Te-site has been measured as $[N_{Te}] = 2.7\times10^{20}$ cm^{-3} following the linear relationship between a and $[N_{Te}]$ reported (Baron et al., 1998). Thus, the overall XRD results have confirmed that both films (# 1) and (# 2) have

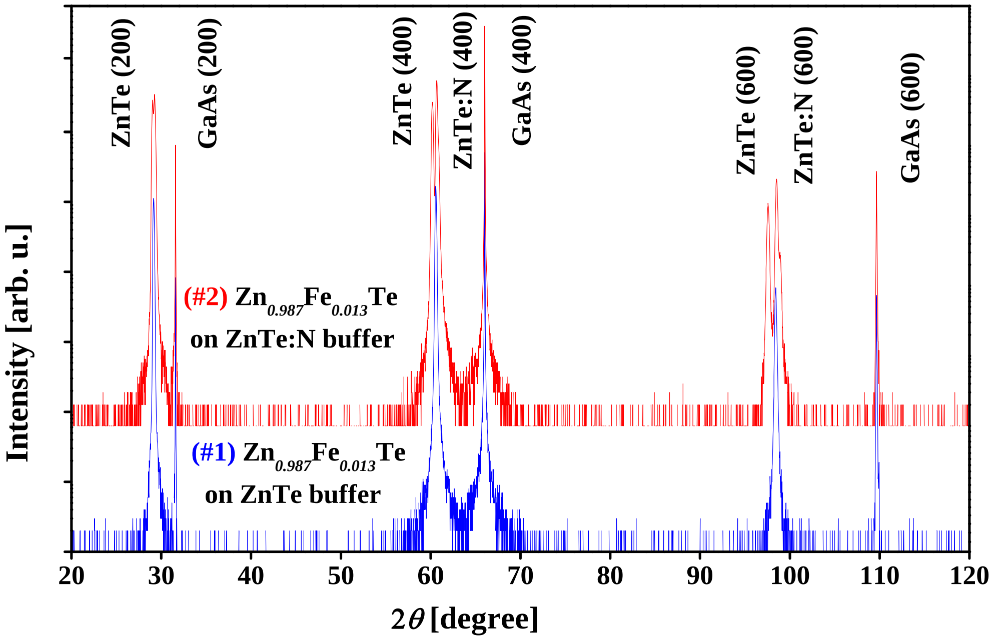

Fig. 1 The XRD θ-2θ scan profiles of $Zn_{0.987}Fe_{0.013}Te$ thin films (# 1) and (# 2) of thickness ≈ 40 nm grown over the un-doped and N-doped ZnTe buffer layer respectively.

pure diluted ZB phase of ZnTe with substitutional Fe atoms staying on the Zn site.

To examine the surrounding environment of Fe on the atomic dimension, XAFS measurements have been carried out for Fe K-edge in $Zn_{0.987}Fe_{0.013}Te$ thin films. Since the Fe concentration (1.3%) is very low in our sample, we have to choose the fluorescence-detection mode, which is very effective for low-concentrated elements of interest (Koningsberger and Prins, 1998). In this detection mode, thick samples are generally used to achieve better signal-to-noise levels. Fig. 2 represents the result of XAFS measurement of $Zn_{0.987}Fe_{0.013}Te$ films (#1) and (#2) of thickness ≈ 700nm, which clarifies the fact that Fe atoms incorporatesubstitutionally on the Zn site in ZnTe crystal for such as Fe concentration. The Fourier transforms of extended X-ray absorption fine structure (EXAFS) oscillation have been used to explain the experimental radial distribution function (RDF) curves around the Fe atom, which closely resemble the result of simulation for the substitutional Fe on the Zn-site in the zinc-blende (ZB) structure as shown in Fig. 2(a). The main peak at around 2.5 Å describes the bond length of Fe with Te atoms as the first nearest neighbor (1^{st} NN). In plotting the RDF spectra, we have weighted the oscillatory parts $\chi(k)$ of EXAFS at Fe K-edge by k^3 and transformed them into real space. In the simulation curve, the substitutional Fe on the Zn-site is assumed to produce no change in the lattice constant of the ZnTe crystal and the single scattering path has been chosen.

The X-ray absorption near edge structure (XANES) spectra of the films have been demonstrated in Fig. 2(b), along with the spectrum of an elemental Fe foil. The XANES spectra of $Zn_{0.987}Fe_{0.013}Te$ films are very different from that of elemental Fe foil, showing three absorption peaks near the Fe K-edge: the pre-edge peak at 7.1096 keV, the shoulder peak at 7.1165 keV and the main peak at 7.1238 keV. The pre-edge peak corresponds to the transitions from the 1s state to the 3d-like state (quadrupolar), while both

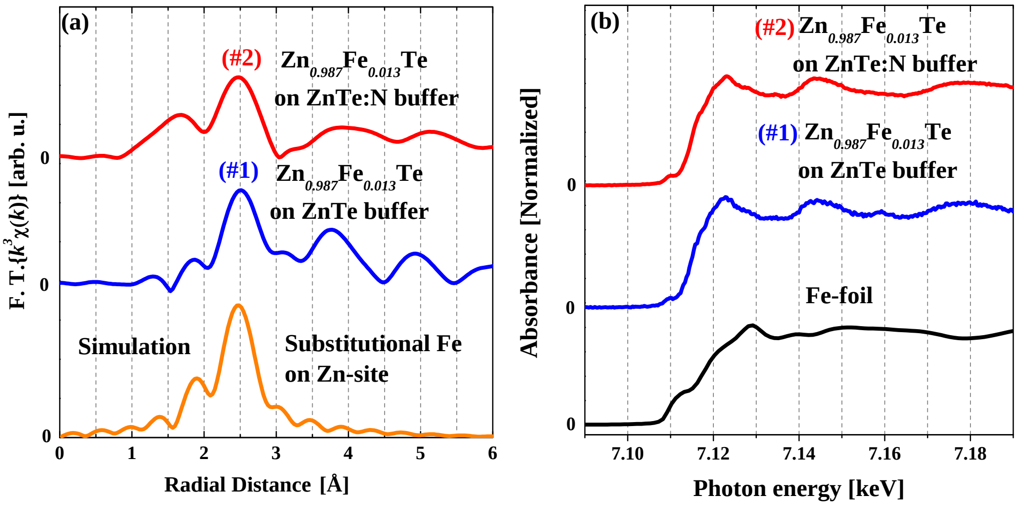

Fig. 2 shows the (a) RDF and (b) XANES spectra of Zn$_{0.987}$Fe$_{0.013}$Te (# 1) and (# 2) thin films (thickness ≈ 700 nm) grown on un-doped and N-doped ZnTe respectively. Experimental RDF and XANES spectra are compared by simulating an substitutional Fe atom on the Zn-site in the ZB structure and spectra for an elemental Fe foil as shown in Fig. 2(a) and (b) respectively.

the shoulder and main peaks explain the transition from the 1s state to the 4p-like state (dipolar) (Westre et al., 1997). Through these observed RDF and XANES spectra of Zn $_{0.987}$Fe$_{0.013}$Te films, we have confirmed the pure diluted ZB phase of ZnTe has been maintained with Fe atoms incorporated in the substitutional site on the Zn-site.

The magnetization measurements have been carried out in a SQUID magnetometer by applying external magnetic field normal to the film plane. Fig. 3 (a) shows *M-H* curves for Zn $_{0.987}$Fe$_{0.013}$Te films (#1) and (#2) grown on undoped and N-doped ZnTe respectively, at 2 K. Fig. 3 (b) shows *the M-H* curve of the film (#2) at 300 K. The magnetization results of films (#1) and (#2) are significantly different [Fig. 3(a)]. For Zn $_{0.987}$Fe$_{0.013}$Te film (#1) grown on undoped ZnTe buffer, the magnetization increases almost linearly with the external applied magnetic field without being saturated. The linear dependence of magnetization on a magnetic field signifies the characteristics of van-Vleck paramagnetism (Twardowski, 1990); the quenching form of thelocalized magnetic moment can be energized through induction by applying an external magnetic field. On the other hand, Zn $_{0.987}$Fe$_{0.013}$Te film (#2) grown on N-doped ZnTe buffer shows ordinary paramagnetic behavior with an S-shape *M-H* curve. Since ZnTe: N layer with N-doping concentrations, [N] ≈ 10^{20} cm^{-3} can have hole density as high as 10^{20} cm^{-3} and exhibit metallic behavior (Baron et al., 1998), the growth of Zn$_{0.987}$Fe$_{0.013}$Te film (#2) over heavily N-doped ZnTe buffer layer can allow delocalized holes to transfer from the buffer layer to the top of the magnetic layer. This increase in hole concentration in the magnetic layer may have deviated the valence state of substitutional Fe from isoelectronic Fe^{2+} can produce finite magnetic moments that persist even at zero external magnetic fields. Thus, we observe the ordinary paramagnetic behavior with an S-shape *M-H* curve in Zn $_{0.987}$Fe$_{0.013}$Te film (#2) grown on p-type ZnTe buffer layer instead of the conventional linear *M-H* curve of van-Vleck paramagnetism for the film (#1) grown over undoped ZnTe buffer layer. A similar type of enhancement in the magnetic properties has also been observed for GaMnAs ferromagnetic semiconductors when grown on *p*- type doped buffer layer (Yoon et al., 2004). In addition, we have already observed the Fe valence state deviation in

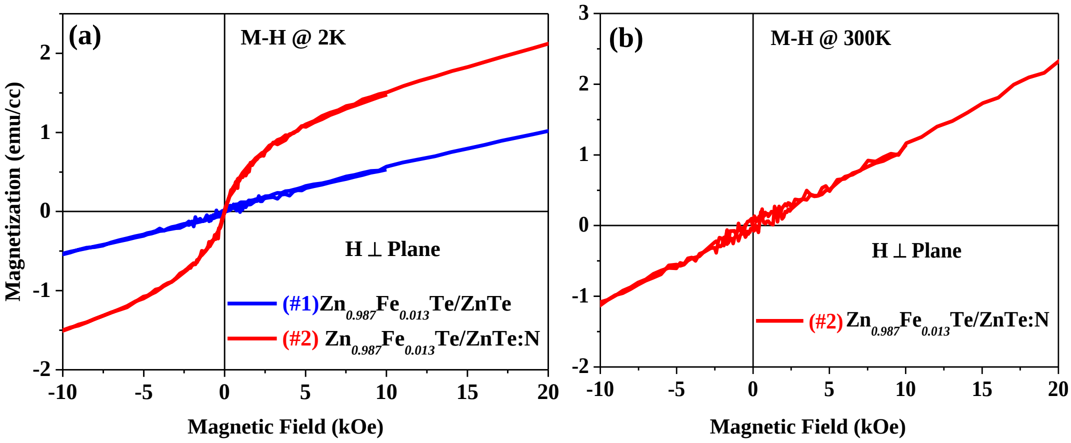

Fig. 3 (a) *M-H* curves of $Zn_{0.987}Fe_{0.013}Te$ thin films of thickness ≈ 40 nm grown over undoped (#1) and N-doped (#2) ZnTe buffer layer measured at 2 K. (b) *M-H* curve of $Zn_{0.987}Fe_{0.013}Te$ film (#2) at 300 K. Measurements are performed with magnetic field normal to the film plane.

$Zn_{1-x}Fe_xTe$ due to nitrogen acceptor co-doping and, hence, the modification of its magnetism (Saha et al., 2019; Saha et al., 2020). Thus, this finding provides evidence to modify the magnetism of $Zn_{0.987}Fe_{0.013}Te$ films indirectly (impact of interfacial holes from the *p*-type buffer). However, film (#2) has shown van-Vleck paramagnetic behavior at 300 K [Fig. 3(b)].

We have also demonstrated *M-T* curves for $Zn_{0.986}Fe_{0.014}Te$ films (#1) and (#2) grown on undoped and N-doped ZnTe buffer layers, respectively with the application of external magnetic field of 500 Oe as shown in Fig. 4. For film (#1) the cusp-like magnetic behavior termed as blocking phenomenon has beenobserved in the zero-field-cooled (ZFC) curve at low temperature of around 5 K [Fig. 4(a)], while both the field-cooled (FC) and zero-field-cooled (ZFC) curves show monotonic increase with lowering temperature without such blocking phenomena in film (#2) [Fig. 4(b)].

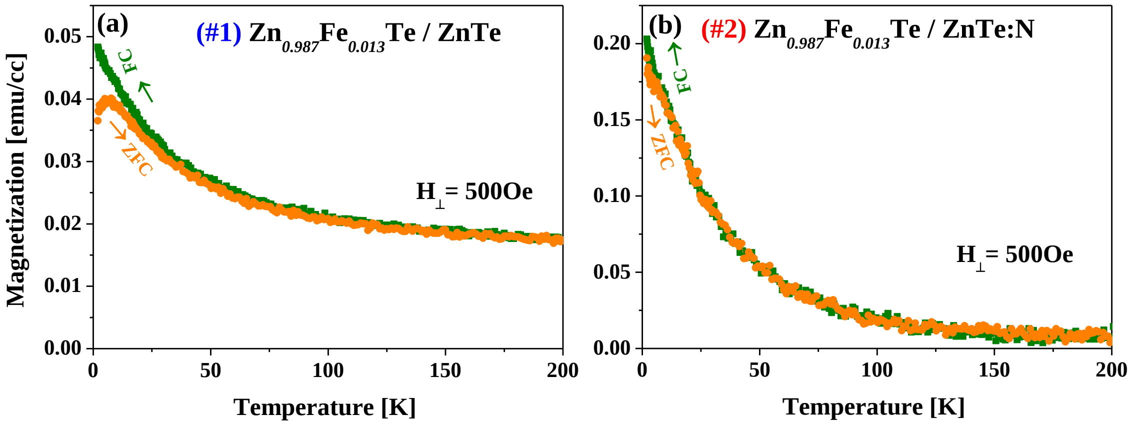

Fig. 4 *M-T* curves of $Zn_{0.987}Fe_{0.013}Te$ thin films of thickness ≈ 40 nm grown over (a) undoped (#1) and (b) N-doped (#2) ZnTe buffer layer. Field-cooled (FC) and zero-field-cooled (ZFC) magnetization have been measured by applying 500 Oe constant magnetic field normal to the film plane.

The blocking phenomenon, a feature of superparamagnetism, is usually seen in magnetically inhomogeneous systems (Dietl et al., 2015; Sato et al., 2007; Devillers et al., 2007). In such a system, the clustering of local regions may exhibit ferromagnetism inside the crystal; at low temperatures, the magnetic anisotropy can effectively inactivate the magnetic moments of these regions and suppress the resulting magnetization. Based on the result of the XAFS measurement, we can exclude the possibility of the formation of precipitates, so the clustering of substitutional Fe on the Zn-site in ZnTe may be the source of the blocking phenomenon. However, the FC and ZFC magnetization values at low-temperature regions are largely different in the *M-T* curves of these films (#1) and (#2); higher values of magnetization are observed in film (#2) grown on N-doped ZnTe buffer layer. Similar FC and ZFC magnetization tendencies have also been noticed in (Zn, Fe)Te: N thin films compared to undoped (Zn, Fe)Te thin films. (Saha et al., 2019; Saha et al., 2020).

Conclusion

We have investigated the structural and magnetic properties of $Zn_{0.987}$ $Fe_{0.013}Te$ thin films grown on undoped and N-doped ZnTe buffer layer by MBE. XRD and XAFS have ensured the zinc-blende crystal structure of the films with Fe atoms substituting the Zn-site. However, SQUID measurements reveal different magnetic behavior among these films; van-Vleck paramagnetic behavior (linear *M-H* curve) of the film grown on undoped ZnTe buffer transforms to S-shape *M-H* curve of ordinary paramagnetic behavior for the film grown over N-doped ZnTe buffer layer. This enhancement in the magnetic properties may happen; Since the heavily N-doped ZnTe layer, $[N] \approx 10^{20}$ cm^{-3}, can accommodate as high as 10^{20} cm^{-3} delocalized holes at the interface with the (Zn, Fe)Te layer, the trapping of holes by the Fe 3*d* levels alter the isoelectronic Fe^{2+} ions valence state. This deviation of valence state can introduce finite magnetic moment in (Zn, Fe)Te even without an external magnetic field. Thus, these experimental findings have opened the scope of future research studies of controlling the magnetic properties of (Zn, Fe)Te by external means, such as by applying electric field or irradiation of light, which may impact substitutional Fe ions valence state and the resultant magnetic properties of (Zn,Fe)Te.

Acknowledgment

The collaboration between the Semiconductor Spintronics laboratory, Institute of Materials Science, University of Tsukuba, Japan, and the High Energy Accelerator Research Organization (KEK), Tsukuba, Japan, is greatly acknowledged.

References

Baron T, Saminadayar K and Magnea M. Nitrogen doping of Te-based II-VI compounds during growth by molecular beam epitaxy. *J. Appl. Phys.*1998; 83: 1354-1370.

Baron T, Saminadayar K and Magnea M. Nitrogen doping of tellurium-based II-VI compounds during growth by molecular beam epitaxy. *Appl. Phys. Lett.* 1995; 67: 2972-2974.

Devillers T, Jamet M, Barski A, Poydenot V, Bayle-Guillemaud P, Belet-Amalric E, Cherifi S and Cibert J. Structure and magnetism of self-organized $Ge_{1-x}Mn_x$ nanocolumns on Ge(001). *Phys. Rev. B* 2007; 76: 205306.

Dietl T, Sato K, Fukushima T, Bonanni A, Jamet M, Barki A, Kuroda S, Tanaka M, Hai PN and Katayama-Yoshida H. Spinodal nanodecomposition in semiconductors doped with transition metals. *Rev. Mod. Phys.* 2015; 87: 1311-1377.

Dietl T and Ohno H. Engineering magnetism in semiconductors. *Materi. Today* 2006; 9: 18-26.

Dietl T. Self-organized growth controlled by charge states of magnetic impurities. *Nat. Mater.* 2006; 5: 673.

Dietl T. Semimagnetic semiconductors in magnetic fields. Chikazumi S. and Miura N. (Eds.), In: *Physics in High Magnetic Fields*. Springer, Berlin; 1981, pp. 344-354.

Grun M, Haury A, Cibert J and Wasiela A. The nitrogen acceptor energy in ZnTe measured by Hall effect and optical spectroscopy. *J. Appl. Phys.* 1996; 79: 7386-7388.

Han J, Stavrinides TS, Kobayashi M, Gunshor RL, Hageroot MM and Nurmikko AV. Heavy *p*-doping of ZnTe by molecular beam epitaxy using a nitrogen plasma source. *Appl. Phys. Lett.* 1993; 62: 840-842.

Ishitsuka S, Domon T, Akiyama R, Kanazawa K, Kuroda S and Ofuchi H. Structural and magneticcharacterization of (Zn, Fe) Te thin films grown by MBE. *Phys. Stat. Sol. (C)* 2014; 11: 1312-1315.

Jantsch W and Hendorfer G. Characterization of deep levels in CdTe by photo-EPR and related techniques. *J. Cryst. Growth.* 1990; 110: 404-413.

Koningsberger DC and Prins R. *X-ray Absorption: Principles, Applications, Techniques of EXAFS, SEXAFS and XANES.* Chemical Analysis. John Wiley and Sons, New York; 1988, p. 688.

Kuroda S, Nishizawa N, Takita K, Mitome M, Bando Y, Osuch K and Dietl T. Origin and control of high-temperature ferromagnetism in semiconductors. *Nat. Mater.* 2007; 6: 440-446.

Malguth E, Hoffmann A and Philips MR. Fe in III-V and II-VI semiconductors. *Phys. Stat. Sol. (b)* 2008; 245(3): 455-480.

Nakamura T, Sugimura Y, Domon T, Ishitsuka S, Kanazawa K, Ofuchi H and Kuroda S. Structural and magnetic properties of (Zn,Fe)Te thin films grown by MBE under Zn-rich flux condition. *J. Cryst. Growth.* 2017; 477: 123-126.

Ohno H. Making nonmagnetic semiconductors ferromagnetic. *Science.*1998 ; 281 : 951-956.

Saha I, Kanazawa K, Nitani H and Kuroda S. Impact of growth conditions on the structural and magnetic properties of (Zn, Fe)Te thin films grown by molecular beam epitaxy (MBE). *J. Cryst. Growth.* 2022; 580: 126492.

Saha I, Nakamura T, Kanazawa K, Nitani H, Mitome M, and Kuroda S. Nitrogen co-doping affects the structural and magnetic properties of (Zn, Fe)Te. *J. Cryst. Growth.* 2019; 511: 42-47.

Saha I, Tomohiro Y, Kanazawa K, Nitani H and Kuroda S. Structural and magnetic properties of nitrogen acceptor co-doped (Zn, Fe)Te thin films grown in Zn-rich condition by molecular beam epitaxy (MBE). *J. Electron. Mater.* 2020; 49(10): 5739-5749.

Sato K, Fukushima T and Katayama-Yoshida H. Super-paramagnetic blocking phenomena and roon temperature ferromagnetism in wide band-gap dilute magnetic semiconductor (Ga, Mn)N. *Jpn. J. Appl. Phys.* 2007; 46: L682.

Sato K and Katayama-Yoshida H. First principles materials design for semiconductor spintronics. *Semicond. Sci. Technol.* 2002; 17: 367-376.

Szadkowski AJ. The $Fe^{2+/3+}$ donor level in CdTe. *J. Phys. Cond. Matter.* 1990; 2: 9853-9859.

Twardowski A. Magnetic properties of Fe-based diluted magnetic semiconductors. *J. Appl. Phys.* 1990; 67: 5108-5113.

Vonsovskii SV. *Magnetism.* John Wiley and Sons, New York; 1974, p. 1256.

Westre TE, Kennepohl P, DeWitt JG, Hedman B, Hodgson KO and Solomon EI. A multiplet analysis of Fe K-edge 1s→3d pre-edge features of iron complexes. *J. Am. Chem. Soc.* 1997; 119: 6297-6314.

Yoon YJ, Chung SJ, Lee HJ, Lee S, An SY, Liu X and Furdyna J K. Effect of p-type buffer layer on the properties of GaMnAs ferromagnetic semiconductors. *J. Korean Phys. Soc.* 2004; 45: S720-S723.

J. Bangladesh Acad. Sci. 48(1); 35-43: June 2024 DOI:https://doi.org/10.3329/jbas.v48i1.68849

Journal of Bangladesh Academy of Sciences

Journal homepage: http://www.bas.org.bd/publications/jbas.html

Research Article

T_0 Separation axioms in intuitionistic topological spaces

Rajandra Chadra Bhowmik* and Md. Sahadat Hossain[1]

Department of Mathematics, Pabna University of Science and Technology, Pabna, Bangladesh

ARTICLE INFO

Article History

Received: 19 September 2023
Revised: 19 December 2023
Accepted: 28 December 2023

Keywords: Intuitionistic Set, Intuitionistic topological space, T_0 separation axioms, Hereditary, Productive, Projective.

ABSTRACT

In this paper, we aim to investigate T_0 separation axioms in intuitionistic topological spaces. After presenting some characterizations of T_0 separation axioms, we provide interrelationships among those and their non-implications in counterexamples. Furthermore, we show that our notions satisfy hereditary and topological properties. Moreover, we establish that some of these notions satisfy productive and projective properties. 2000 Mathematics Subject Classification. 54A99.

Introduction

After the grand introduction of the fuzzy Set by Zadeh (Zadeh, 1965) in 1965, Atanassov (Atanassov, 1984, 1986) proposed the notion of an intuitionistic fuzzy set as the generalization of fuzzy Set considering the degree of membership and non-membership in 1983. Later, Coker (Coker, 1996, 1997) introduced the concept of an intuitionistic set, which is, in one way, the specialization of an intuitionistic fuzzy set and, in another way, the generalization of an ordinary set. Intuitionistic set theory, as a building framework for constructive mathematics, and its logic have influenced many later researchers in developing intuitionistic topology. It has many applications in various areas, particularly computer science, formal verification, and constructive mathematics. It was Coker (2000) who first applied the notion of topology to an intuitionistic set and investigated its various topological consequences. Bayhan and Coker (Bayhan and Coker, 2001) and Prova and Hossain (Prova and Hossain, 2020, 2022) dealt with separation axioms in intuitionistic topological spaces. Selvanayaki and Ilango (Selvanayaki and Ilango, 2016, 2017) studied homeomorphisms and generators in intuitionistic topological spaces. Besides, Bayhan and Coker (Bayhan and Coker, 1996), Ahmed (Ahmed et al., 2014 a & b), and Prova and Hossain (Prova and Hossain, 2022) studied separation axioms in intuitionistic fuzzy topological spaces. Islam (Islam et al., 2018b) studied intuitionistic $L-T_0$ spaces, and Islam (Islam et al., 2018a) studied level separation on intuitionistic fuzzy T_1 spaces. Mahbub (Mahbub et al., 2019, 2021, 2022) studied a particular type of connectedness and compactness in intuitionistic fuzzy topological spaces.

In the literature on separation axioms and related outcomes in intuitionistic topological spaces, we studied and investigated as far as we didn't get T_0 separation axioms in detail. However, it is offered well for T_1, T_2, and others. In this paper, we present the T_0 separation axioms, following Bayhan and Coker (Bayhan and Coker, 2001) for T_1 separation axioms, in possibly various and modified ways with investing their interrelationships and topological consequences.

We start with listing some basic concepts and results introduced by Coker (Coker, 1996), Bayhan and Coker (Bayhan and Coker, 2001), and

---

*Corresponding author:<rajcumath@yahoo.com>

[1] *Department of Mathematics, Rajshahi University, Rajshahi, Bangladesh*

Selvanayaki and Ilango (Selvanayaki and Ilango, 2016, 2017) to construct the path for our principal purpose. Afterward, we give some new and modified notions for T_0 separation axioms and find the relationships among those, revealing some counterexamples for non-implications too. Furthermore, we show that our defined notions satisfy hereditary and topological properties. Finally, we observe that two of these notions are productive and projective.

Preliminaries

In this section, we list some basic concepts of intuitionistic Set and intuitionistic topological space.

Definition (Coker, 1996)**:** Let X be a nonempty set. An intuitionistic set (IS for short) A is an object having the form $A = \langle X, A_1, A_2 \rangle\, A2$, where A_1 and A_2 are subsets of X satisfying $A_1 \cap A_2 = \emptyset$. Set A_1 is called the Set of members of A, while $set\, A_2$ is called the Set of non-members of A.

Definition (Coker, 1996)**:** Let X be a nonempty set and let the IS's A and B be $A = \langle X, A_1,\ A_2 \rangle$ and $B = \langle X, B_1,\ B_2 \rangle$ respectively. Furthermore, let $\{A_i : i \in J\}$ be an arbitrary family of IS's in X, where $A_i = \langle X, A_i^{(1)},\ A_i^{(2)} \rangle$. Then

(a) $A \subseteq B$ if and only if $A_1 \subseteq B_1$ and $A_2 \supseteq B_2$;
(b) $A = B$ if and only if $A \subseteq B$ and $B \subseteq A$;
(c) $\bar{A} = \langle X, A_2, A_1 \rangle$;
(d) $\cup A_i = \langle X, \cup A_i^{(1)}, \cap A_i^{(2)} \rangle$;
(e) $\cap A_i = \langle X, \cap A_i^{(1)}, \cup A_i^{(2)} \rangle$;
(f) $[\quad]A = \langle X, A_1, A_1^c \rangle$;
(g) $(\quad)A = \langle X, A_2^c, A_2 \rangle$;
(h) $\underset{\sim}{\phi} = \langle X, \emptyset, X \rangle$, $\underset{\sim}{X} = \langle X, X, \emptyset \rangle$.

Definition (Coker, 1996)**:** Let X be a nonempty set and $p \in X$ be a fixed element in X. Then IS's: $\underset{\sim}{p} = \langle X, \{p\}, \{p\}^c \rangle$ and $\underset{\approx}{p} = \langle X, \emptyset, \{p\}^c \rangle$ are called an intuitionistic point (IP in short) and a vanishing intuitionistic point (VIP in short) respectively in X.

Definition (Coker, 1996)**:** Let $\underset{\sim}{p}$ be an IP, $\underset{\approx}{p}$ be a VIP, and $A = \langle X, A_1,\ A_2 \rangle$ be an IS in X. Then

(a) $\underset{\sim}{p} \in A$ if and only if $p \in A_1$;
(b) $\underset{\approx}{p} \in A$ if and only if $p \notin A_2$.

Definition (Coker, 1996)**:** Let $A = \langle X, A_1, A_2 \rangle$ and $B = \langle X, B_1, B_2 \rangle$ are IS's in X and Y respectively, then

(a) the preimage of B under f is the IS in X, defined by $f^{-1}(B) = \langle X, f^{-1}(B_1), f^{-1}(B_2) \rangle$;
(b) the image of A under f, denoted by $f(A)$, is the IS in Y, defined by $f(A) = \langle Y, f(A_1), f_{-}(A_2) \rangle$, where $f_{-}(A_2) = (f(A_2^c))^c$.

Corollary (Coker, 1996)**:** Let A, A_i $(i \in J)$ be IS in X, B, B_j $(j \in K)$ be IS in Y, and $f: X \to Y$ is a function. Then

(a) $A_1 \subseteq A_2 \Rightarrow f(A_1) \subseteq f(A_2)$;
(b) $B_1 \subseteq B_2 \Rightarrow f^{-1}(B_1) \subseteq f^{-1}(B_2)$;
(c) $A \subseteq f^{-1}\big(f(A)\big)$ and if f is one-one, then $A = f^{-1}\big(f(A)\big)$;
(d) $f(f^{-1}(B)) \subseteq B$ and if f is onto, then $f\big(f^{-1}(B)\big) = B$.

Definition (Coker, 1997)**:** An intuitionistic topology (IT for short) on a nonempty set X is a family τ of IS's in X satisfying the following axioms:

(a) $\underset{\sim}{\emptyset}, \underset{\sim}{X} \in \tau$,
(b) $G_1 \cap G_2 \in \tau$ for any $G_1, G_2 \in \tau$,
(c) $\cup G_i \in \tau$ for any arbitrary family $\{G_i : i \in J\} \subseteq \tau$.

In this case, the pair (X, τ) is called an intuitionistic topological space (ITS for short), and any IS in τ is known as an intuitionistic open set (IOS for short) in X.

Definition (Selvanayaki and Ilango, 2017)**:** Let X be a nonempty set and $A = \langle X, A_1,\ A_2 \rangle$ be an IS in X. Then

the intuitionistic generator of A, denoted as $G(A)$, is defined as the collection of IS's of the form $\langle X, A_1,\ A_2 \rangle$,$\langle X, A_2,\ A_1 \rangle$, $\langle X, \emptyset, A_1 \cup A_2 \rangle$ and $\langle X, A_1 \cup A_2, \emptyset \rangle$;

(a) the intuitionistic prime generator of A, denoted as $G_p(A)$, is the collection of IS's of the form

$\langle X, A_1, \emptyset \rangle, \langle X, \emptyset, A_2 \rangle$, $\langle X, A_1, A_2 \rangle$, $\langle X, \emptyset, A_1 \cup A_2 \rangle$ and $\langle X, A_1 \cup A_2, \emptyset \rangle$.

Definition (Selvanayaki and Ilangom, 2017)**:** Let X be a nonempty set and A be any IS in X. Then

(a) the collection $G(A)$, along with $\underset{\sim}{\emptyset}\underset{\sim}{,}$ X, forms a topology, and it is called intuitionistic generator topology generated by A and is denoted by (X, τ_G);

(b) the collection $G_p(A)$ along with $\emptyset\underset{\sim}{,} X$ forms a topology, and it is called intuitionistic prime generator topology generated by A and is denoted by (X, τ_{pG}).

Definition (Bayhan and Coker, 2001)**:** Let A and B be two IS's in X and Y, respectively. Then the product intuitionistic Set (PIS for short) of A and B on $X \times Y$ is defined by $U \times V = \langle (X,) Y, A_1 \times B_1, (A_2^c \times B_2^c)^c \rangle$, where $A = \langle X, A_1, A_2 \rangle$ and $B = \langle X, B_1, B_2 \rangle$.

Definition (Selvanayaki and Ilangom, 2016)**:** A bijection $f: (X, \tau) \to (Y, \sigma)$ is called intuitionistic homeomorphism if f is both intuitionistic continuous and intuitionistic open.

T_0 Separation Axioms in ITS's

In this section, we define six notions for T_0 separation axioms in ITSs and show some of their features and properties: hereditary, topological property, productive, and projective. We form the separation axioms for T_0 from the separation axioms for T_1 in Bayhan and Coker (Bayhan and Coker, 2001) with some necessary modifications.

Definition: Let (X, τ) be an ITS. Then (X, τ) is said to be

(a) $T_0(i)$ if for all $x, y \in X$, with $x \neq y$, there exist $U \in \tau$ such that $\underset{\sim}{x} \in U, \underset{\sim}{y} \notin U$ or $\underset{\sim}{y} \in U, \underset{\sim}{x} \notin U$ (cf. Bayhan and Coker, 2001);

(b) $T_0(ii)$ if for all $x, y \in X$, with $x \neq y$, there exist $U \in \tau$ such that $\underset{\approx}{x} \in U, \underset{\approx}{y} \notin U$ or $\underset{\approx}{y} \in U, \underset{\approx}{x} \notin U$ (cf. Bayhan and Coker, 2001);

(c) $T_0(iii)$ if for all $x, y \in X$, with $x \neq y$, there exist $U \in \tau$ such that $\underset{\sim}{x} \in U \subseteq \bar{\underset{\sim}{y}}$ or $\underset{\sim}{y} \in U \subseteq \bar{\underset{\sim}{x}}$ (cf. Bayhan and Coker, 2001);

(d) $T_0(iv)$ if for all $x, y \in X$, with $x \neq y$, there exist $U \in \tau$ such that $\underset{\approx}{x} \in U \subseteq \bar{\underset{\approx}{y}}$ or $\underset{\approx}{y} \in U \subseteq \bar{\underset{\approx}{x}}$ (cf. Bayhan and Coker, 2001);

(e) $T_0(v)$ if for all $x, y \in X$, with $x \neq y$, there exists nonempty $U \in \tau$ such that $\underset{\sim}{y} \notin U$ or $\underset{\sim}{x} \notin U$ (cf. Bayhan and Coker, 2001).

[In this case, we use the non-emptiness of U as an external restriction];1

(f) $T_0(vi)$ if for all $x, y \in X$, with $x \neq y$, there exists nonempty $U \in \tau$ such that $\underset{\approx}{y} \notin U$ or $\underset{\approx}{x} \notin U$ (cf. Bayhan and Coker, 2001).

[In this case, we use the non-emptiness of U as an external restriction].

Remarks: In the first four T_0 separation axioms [$T_0(i)$ to $T_0(iv)$] in the above definition, according to the characterization, $U \in \tau$ is nonempty by default because for any $x, y \in X$, to satisfy $T_0(i)$ to $T_0(iv)$, we have to satisfy either of these four: $\underset{\sim}{x}, \underset{\sim}{y}, \underset{\approx}{x}, \underset{\approx}{y} \in U$, which $\underset{\sim}{\emptyset}$ as a U fails to do. But in the case of the last two T_0 separation axioms ($T_0(v)$ and $T_0(vi)$), we impose non-emptiness of U externally because, otherwise, every ITS become $T_0(v)$ and $T_0(vi)$ automatically for the character of $\underset{\sim}{\emptyset}$ as a U]

Theorem: Let (X, τ) be an ITS, then the following implications are valid:

$$\begin{tikzcd}
T_0(v) & & T_0(vi) \arrow[ll] \\
T_0(i) \arrow[u] & T_0(i) + T_0(ii) \arrow[l] \arrow[r] & T_0(ii) \arrow[u] \arrow[d] \\
& T_0(iii) \arrow[u] & T_0(iv)
\end{tikzcd}$$

Proof

(i) $T_0\ (i) \Rightarrow T_0(v)$ and **(ii)** $T_0\ (ii) \Rightarrow T_0(vi)$.

Proofs of (i) and (ii) are easy to obtain and can be done directly from the corresponding definitions.

Conversely, these are untrue [see counterexamples 4 and 5 in the examples section].

(iii) $T_0\ (ii) \Rightarrow T_0(iv)$

Let (X, τ) be an ITS satisfying $T_0(ii)$. We want to show that it is $T_0(iv)$ too, i.e., for all $x, y \in X$, with $x \neq y$, there exists $U \in \tau$ such that $\underset{\approx}{x} \in U \subseteq \bar{\underset{\approx}{y}}$ or $\underset{\approx}{y} \in U \subseteq \bar{\underset{\approx}{x}}$.

Choose arbitrary $x \neq y$ in X, then by $T_0\ (ii)$, there exist $U = \langle X, U_1, U_2 \rangle \in \tau$ such that $\underset{\approx}{x} \in U, \underset{\approx}{y} \notin U$ or $\underset{\approx}{y} \in U, \underset{\approx}{x} \notin U$ is true, or, $\underset{\approx}{x} \in U, y \in U_2$ or $\underset{\approx}{y} \in U, x \in U_2$ is true, or, $\underset{\approx}{x} \in U, y \notin U_1$, or $\underset{\approx}{y} \in U, x \notin U_1$ is true, or, $\underset{\approx}{x} \in U, y \notin U_1 \subseteq \{y\}^C$ (and obviously $U_2 \supseteq \emptyset$), or $\underset{\approx}{y} \in U, x \notin U_1 \subseteq \{x\}^C$ (and obviously $U_2 \supseteq \emptyset$) is true, or, $\underset{\approx}{x} \in U \subseteq \langle X, \{y\}^c, \emptyset \rangle = \bar{\underset{\approx}{y}}$ or $\underset{\approx}{y} \in U \subseteq \langle X, \{x\}^c, \emptyset \rangle = \bar{\underset{\approx}{x}}$. Hence, it is $T_0\ (iv)$.

Conversely, this is untrue [see counterexample 1 in the examples section].

(iv) $T_0\ (vi) \Rightarrow T_0(v)$

Let (X, τ) be an ITS satisfying $T_0\ (vi)$. We want to show that it is $T_0\ (v)$ too, i.e., for all $x, y \in X$, with $x \neq y$, there exist nonempty $U \in \tau$ such that $\underset{\sim}{y} \notin U$ or $\underset{\sim}{x} \notin U$.

Choose arbitrary $x \neq y$ in X; then by $T_0\ (vi)$, there exist nonempty $U = \langle X,\ U_1, U_2 \rangle \in \tau$ such that $\underset{\approx}{y} \notin U$ or $\underset{\approx}{x} \notin U$ is true, or, $y \in\ U_2$ or $x \in\ U_2$ is true, or, $y \notin\ U_1$ or $x \notin\ U_1$ is true, or, $\underset{\sim}{y} \notin U$ or $\underset{\sim}{x} \notin U$ is true. Hence, it is $T_0(v)$.

Conversely, this is untrue [see counterexample 5 in the examples section].

(v) $T_0\ (iii) \Rightarrow T_0(i) +\ T_0(ii)$.

Let (X, τ) be an ITS satisfying $T_0\ (iii)$. We want to show that it is simultaneously $T_0\ (i)$ and $T_0\ (ii)$.

To show $T_0\ (i)$, choose arbitrary $x \neq y$ in X, then by $T_0(iii)$, there exist $U \in \tau$ such that $\underset{\sim}{x} \in U \subseteq \bar{\underset{\sim}{y}}$ or $\underset{\sim}{y} \in U \subseteq \bar{\underset{\sim}{x}}$ is true, or, $\underset{\sim}{x} \in U = \langle X, U_1, U_2 \rangle \subseteq \langle X, \{y\}^c, \{y\} \rangle$ or $\underset{\sim}{y} \in U = \langle X, U_1, U_2 \rangle \subseteq \langle X, \{x\}^c, \{x\} \rangle$ is true, or, $\underset{\sim}{x} \in U$, with $U_1 \subseteq \{y\}^c$ and $U_2 \supseteq \{y\}$ or $\underset{\sim}{y} \in U$, with $U_1 \subseteq \{x\}^c$ and $U_2 \supseteq \{x\}$ is true, or, $\underset{\sim}{x} \in U$, with $y \notin U_1$ and $y \in U_2$or $\underset{\sim}{y} \in U$, with $x \notin U_1$ and $x \in U_2$ is true, or, $\underset{\sim}{x} \in U$, with $y \notin U_1$ or $\underset{\sim}{y} \in U$, with $x \notin U_1$ is true , or, $\underset{\sim}{x} \in U$, with $\underset{\sim}{y} \notin U$ or $\underset{\sim}{y} \in U$, with $\underset{\sim}{x} \notin U_1$ is true. Hence, it is $T_0(i)$.

To show $T_0(ii)$, choose arbitrary $x \neq y$ in X, then by $T_0\ (iii)$ there exist $U \in \tau$ such that $\underset{\sim}{x} \in U \subseteq \bar{\underset{\sim}{y}}$ or $\underset{\sim}{y} \in U \subseteq \bar{\underset{\sim}{x}}$ is true, or, $\underset{\sim}{x} \in U = \langle X, U_1, U_2 \rangle \subseteq \langle X, \{y\}^c, \{y\} \rangle$ or $\underset{\sim}{y} \in U = \langle X, U_1, U_2 \rangle \subseteq \langle X, \{x\}^c, \{x\} \rangle$ is true, or, $x \in U_1$, with $U_1 \subseteq \{y\}^c$ and $U_2 \supseteq \{y\}$, or $y \in U_1$, with $U_1 \subseteq \{x\}^c$ and $U_2 \supseteq \{x\}$ is true, or, $x \notin U_2$, with $y \notin U_1$ and $y \in U_2$ or $y \notin U_2$, with $x \notin U_1$ and $x \in U_2$ is true, or, $\underset{\approx}{x} \in U$, with $y \notin U_1$ and $y \in U_2$ or $\underset{\approx}{y} \in U$, with $x \notin U_1$ and $x \in U_2$ is true, ort, $\underset{\approx}{x} \in U$, with $y \notin U_1$ or $\underset{\approx}{y} \in U$, with $x \notin U_1$ is true, or, $\underset{\approx}{x} \in U$, with $\underset{\approx}{y} \notin U$ or $\underset{\approx}{y} \in U$, with $\underset{\approx}{x} \notin U$ is true. Hence, it is $T_0(ii)$.

Conversely, this is untrue [see counterexamples 1, 2, and 3 in the examples section].

Examples

Counterexample 1:

Let $X = \{p, q\}$, and τ be a topology on X given by $\mathcal{T} = \left\{\underset{\sim}{X}, \underset{\sim}{\emptyset}, \langle X, \{p\}, \emptyset \rangle, \langle X, \{q\}, \emptyset \rangle, \langle X, \emptyset, \emptyset \rangle\right\}$. We get IOS's containing $\underset{\sim}{p}$ as $\underset{\sim}{X}$ and $\langle X, \{p\}, \emptyset \rangle$and IOS’s containing $\underset{\sim}{q}$ as $\underset{\sim}{X}$ and $\langle X, \{q\}, \emptyset \rangle$. Thus choosing $U = \langle X, \{p\}, \emptyset \rangle \in \tau$, we get $\underset{\sim}{p} \in U, \underset{\sim}{q} \notin U$. Therefore, it is $T_0(i)$. In addition, there does not exist open U to satisfy $\underset{\sim}{q} \in U \subseteq\ \bar{\underset{\sim}{p}} = \langle X, \{q\}, \{p\} \rangle$ or $\underset{\sim}{p} \in U \subseteq\ \bar{\underset{\sim}{q}} = \langle X, \{p\}, \{q\} \rangle$. Therefore, it is not $T_0(iii)$.

On the other hand, we get, IOS’s containing $\underset{\approx}{p}$ are $\underset{\sim}{X}, \langle X, \{P\} \rangle \langle \{\ p, \emptyset, X, q\}, \emptyset \rangle$ and $\langle X, \emptyset, \emptyset \rangle$, and IOS’s containing $\underset{\approx}{q}$ are $\underset{\sim}{X}, \langle X, \{q\} \rangle \langle \{\ p, \emptyset, X, q\}, \emptyset \rangle$ and $\langle X, \emptyset, \emptyset \rangle$. Therefore, however, if we choose U, we never get $\underset{\approx}{p} \in U, \underset{\approx}{q} \notin U$or $\underset{\approx}{q} \in U, \underset{\approx}{p} \notin U$. Therefore, it is not $T_0(ii)$. Furthermore, choosing $U = \langle X, \{p\}, \emptyset\rangle$, we get $\underset{\approx}{p} \in U \subseteq \underset{\approx}{\bar{q}} = \langle X, \{p\}, \emptyset\rangle$. Therefore, it is $T_0(iv)$. Moreover, for $p, q \in X$, nonempty open U does not exist to satisfy $\underset{\approx}{p} \notin U$ or $\underset{\approx}{q} \notin U$. Hence, it is not $T_0(vi)$.

Therefore, this is a topological space which is $T_0(i)$ and $T_0(iv)$, but not $T_0(ii)$, $T_0(iii)$ and $T_0(vi)$. Hence, $T_0(i)$ and $T_0(iv)$ can't assert $T_0(ii)$, $T_0(iii)$ or $T_0(vi)$.

Counterexample 2:

Let $X = \{p, q\}$, and τ be a topology on X given by $\tau = \{\underset{\sim}{X}, \underset{\sim}{\emptyset}, \langle X, \emptyset, \{p\}\rangle, \langle X, \emptyset, \{q\}\rangle, \langle X, \emptyset, \emptyset\rangle\}$. We get, IOS's containing $\underset{\sim}{p}$ is $\underset{\sim}{X}$ only, and similarly IOS's containing $\underset{\sim}{q}$ is $\underset{\sim}{X}$ only. Therefore, there does not exist open U to get $\underset{\sim}{p} \in U, \underset{\sim}{q} \notin U$ or $\underset{\sim}{q} \in U, \underset{\sim}{p} \notin U$. Therefore, it is not $T_0(i)$. Analogously, we can conclude that it is not $T_0(iii)$.

Again, we get, IOS's containing $\underset{\approx}{p}$ are $\underset{\sim}{X}, \langle X, \{\emptyset, q\}\rangle$ and $\langle X, \emptyset, \emptyset\rangle$, and IOS's containing $\underset{\approx}{q}$ are $\underset{\sim}{X}, \langle X, \emptyset, \{p\}\rangle$ and $\langle X, \emptyset, \emptyset\rangle$. Therefore, by choosing $U = \langle X, \{\emptyset, q\}\rangle$, we get $\underset{\approx}{p} \in U, \underset{\approx}{q} \notin U$. Therefore, it is $T_0(ii)$. Furthermore, choosing $U = \langle X, \{\emptyset, q\}\rangle$, we get $\underset{\approx}{p} \in U \subseteq \underset{\approx}{\bar{q}} = \langle X, \{p\}, \emptyset\rangle$. Therefore, it is $T_0(iv)$.

Therefore, this is a topological space that is $T_0(ii)$ and $T_0(iv)$, but not $T_0(i)$ and $T_0(iii)$. Hence, $T_0(ii)$ and $T_0(iv)$ can't assert $T_0(i)$ or $T_0(iii)$.

Counterexample 3:

Let $X = \{p, q\}$, and τ be a topology on X given by $\tau = \{\underset{\sim}{X}, \underset{\sim}{\emptyset}, \langle X\{P\}\rangle\langle\{X, p, \emptyset, X, \emptyset, p\}\rangle\}$; an intuitionistic generator topology generated by $A = \langle X, \{\emptyset, p\}\rangle$. We get, IOS's containing $\underset{\sim}{p}$ are $\underset{\sim}{X}$ and $\langle X, \{p\}, \emptyset\rangle$ and IOS's containing $\underset{\sim}{q}$ is $\underset{\sim}{X}$ only. Thus choosing $U = \langle X, \{p\}, \emptyset\rangle \in \tau$, we get $\underset{\sim}{p} \in U, \underset{\sim}{q} \notin U$. Therefore, it is $T_0(i)$. Furthermore, choosing $U = \langle X, \{p\}, \emptyset\rangle \in \tau$ or $U = \underset{\sim}{X} \in \tau$, we fail to get $\underset{\sim}{p} \in U \subseteq \underset{\sim}{\bar{q}} = \langle X, \{p\}, \{q\}\rangle$, and similarly, choosing $U = \underset{\sim}{X} \in \tau$, we fail to get $\underset{\sim}{q} \in U = \underset{\sim}{X} \subseteq \underset{\sim}{\bar{p}} = \langle X, \{q\}, \{p\}\rangle$. Therefore, it is not $T_0(iii)$.

On the other hand, IOS's containing $\underset{\approx}{p}$ are $\underset{\sim}{X}$ and $\langle X, \{p\}, \emptyset\rangle$, and open Set containing $\underset{\approx}{q}$ are $\underset{\sim}{X}$, $\langle X, \{p\}, \emptyset\rangle$, and $\langle X, \{\emptyset, p\}\rangle$. Choosing $U = \langle X, \{\emptyset, p\}\rangle$, we get $\underset{\approx}{q} \in U, \underset{\approx}{p} \notin U$. Therefore, it is $T_0(ii)$. Furthermore, choosing $U = \langle X, \{\emptyset, p\}\rangle$, we get $\underset{\approx}{q} \in U \subseteq \underset{\approx}{\bar{p}} = \langle X, \{q\}, \emptyset\rangle$. Therefore, it is $T_0(iv)$.

Therefore, this is a topological space that is $T_0(i)$, $T_0(ii)$, and $T_0(iv)$, but not $T_0(iii)$. Hence, $T_0(i)$, $T_0(ii)$ and $T_0(iv)$ can't assert $T_0(iii)$.

Counterexample 4:

Let $X = \{p, q, r\}$, and $\tau = \{\underset{\sim}{X}, \underset{\sim}{\emptyset}, \langle\{X, p\}, \{q, r\}\rangle, \langle x\{q, r\}, \{p\}\rangle\}$ is a topology on X; It is an intuitionistic generator topology, generated by $A = \langle X, \{p\}\{q, r\}\rangle$. We get, IOS's containing $\underset{\sim}{p}$ are $\underset{\sim}{X}$ and $\langle X, \{q, r\}\{p\}\rangle$ p, q, r, and IOS's containing $\underset{\sim}{q}$ are $\underset{\sim}{X}$ and $\langle X, \{q, r\}, \{p\}\rangle$, and IOS's containing $\underset{\sim}{r}$ are $\underset{\sim}{X}$ and $\langle X, \{q, r\}, \{p\}\rangle$. Thus for $q, r \in X$, there does not exist open U to get $\underset{\sim}{q} \in U, \underset{\sim}{r} \notin U$ or $\underset{\sim}{r} \in U, \underset{\sim}{q} \notin U$. Therefore, it is not $T_0(i)$. Analogously, it is not $T_0(iii)$. Additionally, for any pair from $p, q, r \in X$, choosing $U = \langle X, \{p\}, \{q, r\}\rangle \in \tau$, we get the necessary $\underset{\sim}{q} \notin U$ or $\underset{\sim}{r} \notin U$ as required. Hence, it is $T_0(v)$.

On the other hand, IOS's containing $\underset{\approx}{p}$ are $\underset{\sim}{X}$ and $\langle X, \{p\}, \{q, r\}\rangle$, containing $\underset{\approx}{q}$ are $\underset{\sim}{X}$ and $\langle X, \{q, r\}, \{p\}\rangle$, and containing $\underset{\approx}{r}$ are $\underset{\sim}{X}$ and $\langle X, \{q, r\}, \{p\}\rangle$. For $q, r \in X$, there does not exist open U to satisfy $\underset{\approx}{q} \in U, \underset{\approx}{r} \notin U$ or $\underset{\approx}{r} \in U, \underset{\approx}{q} \notin U$. Therefore, it is not $T_0(ii)$. Analogously, there is no open U to get $\underset{\approx}{q} \in U \subseteq \underset{\approx}{\bar{r}} = \langle X, \{p, q\}, \{r\}\rangle$ or $\underset{\approx}{r} \in U \subseteq \underset{\approx}{\bar{q}} = \langle X, \{p, r\}, \{q\}\rangle$. Therefore, it is not $T_0(iv)$ too. Additionally, for any pair from $p, q, r \in X$ and choosing $U = \langle X, \{p\}, \{q, r\}\rangle \in \tau$, we get the necessary $\underset{\approx}{q} \notin U$ or $\underset{\approx}{r} \notin U$ as required. Hence, it is $T_0(vi)$.

Therefore, this is a topological space which is $T_0(v)$, $T_0(vi)$, but not $T_0(i)$, $T_0(ii)$, $T_0(iii)$ and $T_0(iv)$.

Hence, $T_0(v)$ and $T_0(vi)$ can'nt assert $T_0(i)$ or $T_0(ii)$ or $T_0(iii)$ or $T_0(iv)$.

Counterexample 5:

Let $X = \{p, q, r\}$, and τ be a topology on X given by $\tau = \{\underset{\sim}{X}, \underset{\sim}{\emptyset}, \langle\{x,\}\rangle\langle\{p\},\rangle\langle X, p, \emptyset, X, \emptyset, p, X, \emptyset, \emptyset\rangle\}$; an intuitionistic prime generator topology generated by $A = \langle X, \{p\}, \emptyset\rangle$. We get IOS's containing $\underset{\sim}{p}$ are $\underset{\sim}{X}$ and $\langle X, \{p\}, \emptyset\rangle$, IOS's containing $\underset{\sim}{q}$ is $\underset{\sim}{X}$ only, and IOS's containing $\underset{\sim}{r}$ is $\underset{\sim}{X}$ only too. Therefore, for $q, r \in X$, there does not exist open U to get $\underset{\sim}{p} \in U, \underset{\sim}{q} \notin U$ or $\underset{\sim}{q} \in U, \underset{\sim}{p} \notin U$. Therefore, it is not $T_0(i)$ and not $T_0(iii)$ as well. In addition, for each pair from $p, q, r \in X$, choosing $U = \langle X, \emptyset, \emptyset\rangle \in \tau$, we get $\underset{\sim}{p}, \underset{\sim}{q}, \underset{\sim}{r} \notin U$. Therefore, it is $T_0(v)$.

Again IOS's containing $\underset{\approx}{p}$ are $\underset{\sim}{X}, \langle\{X, p\}, \emptyset\rangle$ and $\langle X, \emptyset, \emptyset\rangle$, IOS's not containing $\underset{\approx}{p}$ are $\langle X, \{\emptyset\, p\}\rangle$ and $\underset{\sim}{\emptyset}$; IOS's containing $\underset{\approx}{q}$ are $\underset{\sim}{X}$, $\langle X, \{p\}, \emptyset, \rangle, \langle X, \emptyset, \{p\}\rangle$ and $\langle X, \emptyset, \emptyset\rangle$, IOS's not containing $\underset{\approx}{q}$ is $\underset{\sim}{\emptyset}$ only. IOS's containing $\underset{\approx}{r}$ are $\underset{\sim}{X}$, $\langle X, \{p\}, \emptyset\rangle\langle X, \emptyset, \{p\}\rangle$ and $\langle X, \emptyset, \emptyset\rangle$, IOS's not containing $\underset{\approx}{r}$ is $\underset{\sim}{\emptyset}$ only. We see, for $q, r \in X$, there does not exist open U to satisfy $\underset{\approx}{q} \in U, \underset{\approx}{r} \notin U$ or $\underset{\approx}{r} \in U, \underset{\approx}{q} \notin U$. Therefore, it is not $T_0(ii)$ too. However, for $p, q \in X$, choosing $U = \langle X, \{p\}, \emptyset\rangle$, we get $\underset{\approx}{p} \in U \subseteq \underset{\approx}{\bar{q}} = \langle X, \{p, r\}, \emptyset\rangle$, the similar results hold for $p, r \in X$ and for $q, r \in X$ too. Therefore, it is $T_0(iv)$. Similarly, for $q, r \in X$, nonempty open U does not exist to satisfy $\underset{\approx}{q} \notin U$ or $\underset{\approx}{r} \notin U$. Hence, it is not $T_0(vi)$.

Therefore, this is a topological space which is $T_0(iv)$, $T_0(v)$, but is not $T_0(i)$, $T_0(ii)$, $T_0(iii)$ and $T_0(vi)$. Hence, $T_0(iv)$ and $T_0(v)$ can't assert $T_0(i)$ or $T_0(ii)$ or $T_0(iii)$ or $T_0(vi)$.

Properties

This section proves that our defined notions satisfy the hereditary and topological properties. Moreover, we prove that the two of these notions are productive and projective.

Theorem: A homeomorphic image of a $T_0(i)$ space is a $T_0(i)$ space.

Proof.

Let $f: (X, \tau) \to (Y, \sigma)$ be a homeomorphism, i.e., a bijection open and continuous (by definition in the primaries section). Suppose that (X, τ) is a $T_0(i)$ space. We want to show that (Y, σ) is $T_0(i)$ too.

Choose two arbitrary $y_1, y_2 \in Y$, with $y_1 \neq y_2$, then $f^{-1}(y_1), f^{-1}(y_2) \in X$, And since f is a bijection, so is f^{-1}, with its existence. In particular, as f^{-1} is one-one, $f^{-1}(y_1) \neq f^{-1}(y_2)$ in X. Suppose that $f^{-1}(y_1) = x_1$ and $f^{-1}(y_2) = x_2$. As (X, τ) is a $T_0(i)$ space, with $x_1 \neq x_2$ in X, then there exists $U \in \tau$ such that $\underset{\sim}{x_1} \in U, \underset{\sim}{x_2} \notin U$ or $\underset{\sim}{x_2} \in U, \underset{\sim}{x_1} \notin U$. Now $\underset{\sim}{x_1} \in U, \underset{\sim}{x_2} \notin U$ or $\underset{\sim}{x_2} \in U, \underset{\sim}{x_1} \notin U$ implies $f(\underset{\sim}{x_1}) \in f(U), f(\underset{\sim}{x_2}) \notin f(U)$ or $f(\underset{\sim}{x_2}) \in f(U), f(\underset{\sim}{x_1}) \notin f(U)$. As f is open, $f(U) = R(say) \in \sigma$. Since f is onto, $f\left(\underset{\sim}{x_1}\right) = f\left(f^{-1}(\underset{\sim}{y_1})\right) = \underset{\sim}{y_1}$ and $f\left(\underset{\sim}{x_2}\right) = f\left(f^{-1}(\underset{\sim}{y_2})\right) = \underset{\sim}{y_2}$ [by corollary in the preliminaries section]. Therefore, we get $R \in \sigma$ such that $\underset{\sim}{y_1} \in R, \underset{\sim}{y_2} \notin R$ and $\underset{\sim}{y_2} \in R, \underset{\sim}{y_1} \notin R$.

Theorem: Homeomorphic image of a $T_0(r)$ space is a $T_0(r)$ space for $r = i, ii, \ldots, vi$.

The proof is the same for $r = ii, iii, \ldots, vi.$ as for $r = i$ in the above theorem.

Each $T_0(r)$ separation axioms for $r = i, ii, \ldots, vi$ is a topological property.

Theorem: Inverse homeomorphic image of a $T_0(i)$ space is a $T_0(i)$ space.

Proof.

Let $f: (X, \tau) \to (Y, \sigma)$ be a homeomorphism, i.e., a bijection open and continuous. Suppose that (Y, σ) is a $T_0(i)$ space. We want to show that (X, τ) is $T_0(i)$ too. For any two arbitrary $x_1, x_2 \in X$, with $x_1 \neq x_2$, since f is a bijection, particularly one-one, therefore, $f(x_1) \neq f(x_2)$ in Y.

Choose two arbitrary $x_1, x_2 \in X$, with $x_1 \neq x_2$, then $f(x_1), f(x_2) \in Y$, And since f is a bijection, and in particular one-one, therefore, $f(x_1)\, f(x_2)$ in Y.

Suppose $f(x_1) = y_1$ and $f(x_2) = y_2$. As (Y, σ) is a $T_0(i)$ space, with this $y_1 \neq y_2$ in Y, there must exist $R \in \sigma$ such that $\underset{\sim}{y_1} \in R, \underset{\sim}{y_2} \notin R$ or $\underset{\sim}{y_2} \in R, \underset{\sim}{y_1} \notin R$. Now $\underset{\sim}{y_1} \in R, \underset{\sim}{y_2} \notin R$ or $\underset{\sim}{y_2} \in R, \underset{\sim}{y_1} \notin R$ implies $f^{-1}(\underset{\sim}{y_1}) \in f^{-1}(R), f^{-1}(\underset{\sim}{y_2}) \notin f^{-1}(R)$ or $f^{-1}(\underset{\sim}{y_2}) \in f(R),\ f^{-1}(\underset{\sim}{y_1}) \notin f^{-1}(R)$. As f is continuous, and $R \in \sigma$, therefore, $f^{-1}(R) = U(say) \in \tau$. Since f is one-one, $f^{-1}(\underset{\sim}{y_1}) = f^{-1}(f(\underset{\sim}{x_1})) = \underset{\sim}{x_1}$ and $f^{-1}(\underset{\sim}{y_2}) = f^{-1}(f(\underset{\sim}{x_2})) = \underset{\sim}{x_2}$ [By corollary in the preliminaries section]. Therefore, we get $U \in \sigma$ such that $\underset{\sim}{x_1} \in U, \underset{\sim}{x_2} \notin U$ and $\underset{\sim}{x_2} \in U, \underset{\sim}{x_1} \notin U$.

Theorem: Inverse homeomorphic image of a $T_0(r)$ space is a $T_0(r)$ space for $r = i, ii, \ldots, vi$.

The proof is the same for $r = ii, \ldots, vi.$ as for $r = i$ in the above theorem.

Theorem: If $(X,)\ \tau$ is $T_0(i)$, then for any subset $A \subseteq X$, the subspace (A, τ_A) is also $T_0(i)$.

Proof.

Let (X, τ) be a $T_0(i)$ space and $A \subseteq X$, with the subspace topology τ_A on A. We want to show that (A, τ_A) is also $T_0(i)$.

Let $x, y \in A$, with $x \neq y$, then $x, y \in X$, with $x \neq y$, hold the same. As (X, τ) is a $T_0(i)$ space, therefore, we must have $U \in \tau$ such that $\underset{\sim}{x} \in U, \underset{\sim}{y} \notin U$ or $\underset{\sim}{y} \in U, \underset{\sim}{x} \notin U$. Now, for this $U \in \tau$, we get $U_A = U \cap A$ in τ_A. This must satisfy $\underset{\sim}{x} \in U_A, \underset{\sim}{y} \notin U_A$ or $\underset{\sim}{y} \in U_A, \underset{\sim}{x} \notin U_A$. Hence, (A, τ_A) is $T_0(i)$.

Theorem: If $(X,)\ \tau$ is $T_0(r)$, then for any subset $A \subseteq X$, the subspace (A, τ_A) is also $T_0(r)$ for $r = ii, iii, \ldots, vi$.

The proof is the same for $r = ii, iii \ldots, vi.$ as for $r = i$ in the above theorem.

This shows that each of $T_0(r)$ for $r = i, ii, \ldots, vi$ is hereditary.

Theorem: If $(X,)\ \tau$, and (Y, σ) be two ITSs. If

(a) $(X,)\ \tau$, and (Y, σ) both are $T_0(i)$, then so is $(X \times Y, \sigma \times \tau)$.

(b) $(X,)\ \tau$, and (Y, σ) both are $T_0(ii)$, then so is $(X \times Y, \sigma \times \tau)$.

Proof

(a) Let (X, τ) and (Y, σ) are both $T_0(i)$. We want to prove that $(X \times Y, \sigma \times \tau)$ is $T_0(i)$ too. Choose arbitrary points (x_1, y_1) and (x_2, y_2) in $X \times Y$, with $(x_1, y_1) \neq (x_2, y_2)$. Then either $x_1 \neq x_2$ or $y_1 \neq y_2$. For $x_1 \neq x_2$ in X, as $(X, \tau)$is $T_0(i)$, there must exist $U \in \tau$ such that such that $\underset{\sim}{x_1} \in U, \underset{\sim}{x_2} \notin U$ or $\underset{\sim}{x_2} \in U, \underset{\sim}{x_1} \notin U$. Then we have IOS's $U \times \underset{\sim}{Y} = \langle X \times Y, U_1 \times Y, (U_2^c \times \phi^c)^c \rangle$ in $\tau \times \sigma$ such that $\underset{\sim}{(x_1, y_1)} \in U \times \underset{\sim}{Y}$, $\underset{\sim}{(x_2, y_2)} \notin U \times \underset{\sim}{Y}$ or $\underset{\sim}{(x_2, y_2)} \in U \times \underset{\sim}{Y}$, $\underset{\sim}{(x_1, y_1)} \notin U \times \underset{\sim}{Y}$.

Similarly, for $y_1 \neq y_2$ in Y, as (Y, σ) is $T_0(i)$, there must exist $R \in \sigma$ such that such that $\underset{\sim}{y_1} \in R, \underset{\sim}{y_2} \notin R$ or $\underset{\sim}{y_2} \in R, \underset{\sim}{y_1} \notin R$. Then we have IOS's $\underset{\sim}{X} \times R = \langle X \times Y, X \times R_1, (\phi^c \times R_2^c)^c \rangle$ in $\tau \times \sigma$ such that $\underset{\sim}{(x_1, y_1)} \in \underset{\sim}{X} \times R$, $\underset{\sim}{(x_2, y_2)} \notin \underset{\sim}{X} \times R$ or $\underset{\sim}{(x_2, y_2)} \in \underset{\sim}{X} \times R$, $\underset{\sim}{(x_1, y_1)} \notin \underset{\sim}{X} \times R$.

(b) Let (X, τ) and (Y, σ) are both $T_0(ii)$. We want to prove that $(X \times Y, \sigma \times \tau)$ is $T_0(ii)$ too. Choose arbitrary points (x_1, y_1) and (x_2, y_2) in $X \times Y$, with $(x_1, y_1) \neq (x_2, y_2)$. Then either $x_1 \neq x_2$ or $y_1 \neq y_2$. For $x_1 \neq x_2$ in X as $(X, \tau)$is $T_0(ii)$, there must exist $U \in \tau$ such that $\underset{\approx}{x_1} \in U$, $\underset{\approx}{x_2} \notin U$ or $\underset{\approx}{x_2} \in U$, $\underset{\approx}{x_1} \notin U$. Then we have IOS's $U \times \underset{\sim}{Y} = \langle X \times Y, U_1 \times Y, (U_2^c \times \phi^c)^c \rangle$ in $\tau \times \sigma$ such that $\underset{\approx}{(x_1, y_1)} \in U \times \underset{\approx}{Y}$, $\underset{\approx}{(x_2, y_2)} \notin U \times \underset{\approx}{Y}$ or $\underset{\approx}{(x_2, y_2)} \in U \times \underset{\approx}{Y}$, $\underset{\approx}{(x_1, y_1)} \notin U \times \underset{\approx}{Y}$.

Similarly, for $y_1 \neq y_2$ in Y, as (Y, σ) is $T_0(ii)$, there must exist $R \in \sigma$ such that such that $\underset{\approx}{y_1} \in R$, $\underset{\approx}{y_2} \notin R$ or $\underset{\approx}{y_2} \in R$, $\underset{\approx}{y_1} \notin R$. Then we have IOS's $\underset{\approx}{X} \times R = \langle X \times Y, X \times R_1, (\phi^c \times R_2^c)^c \rangle$ in $\tau \times \sigma$ such that $\underset{\approx}{(x_1, y_1)} \in \underset{\approx}{X} \times R$, $\underset{\approx}{(x_2, y_2)} \notin \underset{\approx}{X} \times R$ or $\underset{\approx}{(x_2, y_2)} \in \underset{\approx}{X} \times R$, $\underset{\approx}{(x_1, y_2)} \notin \underset{\approx}{X} \times R$.

Hence, $T_0(i)$ and $T_0(ii)$ are productive.

Theorem: If $(X,)$ τ, and (Y,σ) be two ITS's. If

(a) $(X\times Y,\sigma\times\tau)$ is $T_0(i)$, then $(X,)$τ, and (Y,σ) both are $T_0(i)$.

(b) $(X\times Y,\sigma\times\tau)$ is $T_0(ii)$, then $(X,)$τ, and (Y,σ) both are $T_0(ii)$.

Proof.

(a) Let $(X\times Y,\sigma\times\tau)$ is $T_0(i)$. We want to show that (X,τ) and (Y,σ) are $T_0(i)$.

To show (X,τ) follows $T_0(i)$, choose arbitrary points $x_1,x_2\in X$, with $x_1\neq x_2$, and fix $y\in Y$, then in $X\times Y$, $(x_1,y)\neq(x_2,y)$, and as $(X\times Y,\sigma\times\tau)$ is $T_0(i)$, we must have $U\times R\in\tau\times\sigma$ such that $(\underset{\sim}{x_1},y)\in U\times R$, $(\underset{\sim}{x_2},y)\notin U\times R$ or $(\underset{\sim}{x_2},y)\in U\times R$, $(\underset{\sim}{x_1},y)\notin U\times R$. This implies that $(x_1,y)\in U_1\times R_1$, $(x_2,y)\notin U_1\times R_1$ or $(x_2,y)\in U_1\times R_1$, $(x_1,y)\notin U_1\times R_1$. More specifically, we get $x_1\in U_1$, $x_2\notin U_1$ or $x_2\in U_1$, $x_1\notin U_1$. Therefore, for $x_1,x_2\in X$, with $x_1\neq x_2$, we get $U\in\tau$ such that $\underset{\sim}{x_1}\in U$, $\underset{\sim}{x_2}\notin U$ or $\underset{\sim}{x_2}\in U$, $\underset{\sim}{x_1}\notin U$. This shows that (X,τ) is $T_0(i)$.

Now, to show (Y,σ) is $T_0(i)$, choose arbitrary points $y_1,y_2\in Y$, with $y_1\neq y_2$, and fix $x\in X$. Then in $X\times Y$, $(x,y_1)\neq(x,y_2)$ and as $(X\times Y,\sigma\times\tau)$ is $T_0(i)$, we must have $U\times R\in\tau\times\sigma$ such that $(x,\underset{\sim}{y_1})\in U\times R$, $(x,\underset{\sim}{y_2})\notin U\times R$ or $(x,\underset{\sim}{y_2})\in U\times R$,$(x,\underset{\sim}{y_1})\notin U\times R$. This implies that $(x,y_1)\in U_1\times R_1$, $(x,y_2)\notin U_1\times R_1$ or $(x,y_2)\in U_1\times R_1$, $(x,y_1)\notin U_1\times R_1$. More specifically, we get $y_1\in R_1$, $y_2\notin R_1$ or $y_2\in R_1$, $y_1\notin R_1$. Therefore, for $y_1,y_2\in Y$, with $y_1\neq y_2$, we get $R\in\sigma$ such that $\underset{\sim}{y_1}\in R$, $\underset{\sim}{y_2}\notin R$ or $\underset{\sim}{y_2}\in R$, $\underset{\sim}{y_1}\notin R$. This shows that (Y,σ) is $T_0(i)$.

(b) Let $(X\times Y,\sigma\times\tau)$ is $T_0(ii)$. We want to show that (X,τ) and (Y,σ) are $T_0(ii)$.

To show (X,τ) follows $T_0(ii)$, choose arbitrary points $x_1,x_2\in X$, with $x_1\neq x_2$, and fix $y\in Y$ then in $X\times Y$, $(x_1,y)\neq(x_2,y)$ and as $(X\times Y,\sigma\times\tau)$ is $T_0(ii)$, we must have $U\times R\in\tau\times\sigma$ such that $(\underset{\approx}{x_1},y)\in U\times R$, $(\underset{\approx}{x_2},y)\notin U\times R$ or $(\underset{\approx}{x_2},y)\in U\times R$,$(\underset{\approx}{x_1},y)\notin U\times R$. This implies that $(x_1,y)\notin U_2\times R_2$,$(x_2,y)\in U_2\times R_2$ or $(x_2,y)\notin U_2\times R_2$, $(x_1,y)\in U_2\times R_2$. we get $x_1\notin U_2$, $x_2\in U_2$ or $x_2\notin U_2$, $x_1\in U_2$. Therefore, for $x_1,x_2\in X$, with $x_1\neq x_2$, we get $U\in\tau$ such that $\underset{\approx}{x_1}\in U$, $\underset{\approx}{x_2}\notin U$ or $\underset{\approx}{x_2}\in U$, $\underset{\approx}{x_1}\notin U$. This shows that (X,τ) is $T_0(ii)$.

Now, to show (Y,σ) is $T_0(ii)$, choose arbitrary points $y_1,y_2\in Y$, Y, $y_1\neq,y_2$, and Fix $x\in X$. Then in $X\times Y$, $(x,y_1)\neq(x,y_2)$ and as $(X\times Y,\sigma\times\tau)$ is $T_0(ii)$, we must have $U\times R\in\tau\times\sigma$ such that $(x,\underset{\approx}{y_1})\in U\times R$, $(x,\underset{\approx}{y_2})\notin U\times R$ or $(x,\underset{\approx}{y_2})\in U\times R$, $(x,\underset{\approx}{y_1})\notin U\times R$. This implies that $(x,y_1)\notin U_2\times R_2$, $(x,y_2)\in U_2\times R_2$ or $(x,y_2)\notin U_2\times R_2$, $(x,y_1)\in U_2\times R_2$. More specifically, we get $y_1\notin R_2$, $y_2\in R_2$ or $y_2\notin R_2$, $y_1\in R_2$. Hence, for $y_1,y_2\in Y$, with $y_1\neq y_2$, we get $R\in\sigma$ such that $\underset{\approx}{y_1}\in R$, $\underset{\approx}{y_2}\notin R$ or $\underset{\approx}{y_2}\in R$, $\underset{\approx}{y_1}\notin R$. This shows that (Y,σ) is $T_0(ii)$. Hence, $T_0(i)$ and $T_0(ii)$ are projective.

Conclusions

In this paper, we provide some new and modified notions for T_0 separation axioms, analyze interrelationships among them, and give necessary counter examples for non-implications. We show that our defined notions satisfy hereditary and topological properties, and two of these given notions are productive and projective. These results are very encouraging for further study in this area, especially for other higher separation axioms.

Credit authorship contribution statement

Rajendra Chandra Bhowmik:

Conceptualization, Investigation, Methodology, Formal analysis, Writing-original draft, Writing review editing;

Md. Sahadat Hossain: Validation, Supervision.

Conflict of interest

The authors declare that they have no conflict of interest.

References

Ahmed E, Hossain MS and Ali DM. On intuitionistic fuzzy T_0 spaces. *J. Bangladesh Acad. Sci.* 2014a; 38(2): 197-207.

Ahmed E, Hossain MS and Ali DM. On intuitionistic fuzzy T_1 spaces. *J. Phys. Sci*. 2014b; 19: 59-66.

Atanassov KT. Intuitionistic fuzzy sets. *Fuzzy Sets Syst.* 1986; 20(1): 87-96.

Atanassov KT. Intuitionistic fuzzy sets. *Int. J. Bioautomation,* 2016; 20(S1): S1-S6.

Bayhan S and Coker D. On fuzzy separation axioms in intuitionistic fuzzy topological spaces. *BUSEFAL.* 1996; 67: 77-87.

Bayhan S and Coker D. On separation axioms in intuitionistic topological space. *Int. J. Math. Math. Sci.* 2001; 27(10): 621-630.

Coker D and Demirci M. On intuitionistic fuzzy points. *Notes on Intuitionistic Fuzzy Sets.* 1995; 1(2): 79-84.

Coker D. A note on intuitionistic sets and intuitionistic points. *Turkish J. Math.* 1996; 20(3): 343-351.

Coker D. An introduction to intuitionistic fuzzy topological spaces. *Fuzzy Sets Syst.* 1997; 88 (1): 81-89.

Coker D. An introduction to intuitionistic topological spaces. *BUSEFAL*. 2000; 81: 51-56.

Islam MS, Hossain MS and Asaduzzaman M. Level separation on intuitionistic fuzzy T_1 spaces. *J. Bangladesh Acad. Sci.* 2018a; 42(1): 73-85.

Islam R, Hossain MS and Amin SR. Some properties of intuitionistic $L-T_0$ spaces. *J. fuzzy Set. Valued Anal.* 2018b; 2018(2): 77-85.

Mahbub MA, Hossain MS and Hossain MA. Connectedness concept in intuitionistic fuzzy topological spaces. *Notes on Intuitionistic Fuzzy Sets*. 2021; 27(1): 72-82.

Mahbub MA, Hossain MS and Hossain MA. On (r,s)–connectedness in intuitionistic fuzzy topological spaces. *Notes on Intuitionistic Fuzzy Sets*. 2022; 28 (1): 23-36.

Mahbub MA, Hossain MS and Hossain MA. On Q-compactness in intuitionistic fuzzy topological spaces. *J. Bangladesh Acad. Sci.* 2019; 43(2): 197-230.

Prova TT and Hossain MS. Intuitionistic fuzzy based regular and normal spaces. *Notes on Intuitionistic Fuzzy Sets*. 2020; 26(4):53-63.

Prova TT and Hossain MS. Separation axioms in intuitionistic topological spaces. *Ital. J. Pure Appl. Math.* 2022; 48: 986-995.

Selvanayaki S and Ilango G. Generators in intuitionistic topological spaces. *Int. J. Pure Appl. Math*. 2017; 116 (12): 209-218.

Selvanayaki S and Ilango G. Homeomorphism on intuitionistic topological spaces. *Ann. Fuzzy Math. Inform*. 2016; 11 (6): 957-966.

Zadeh LA. Fuzzy sets. *Information and Control.* 1965; 8(3): 338-353.

J. Bangladesh Acad. Sci. 48(1); 45-50: June 2024 DOI:https://doi.org/10.3329/jbas.v48i1.69202

Journal of Bangladesh Academy of Sciences

Journal homepage: http://www.bas.org.bd/publications/jbas.html

Research Article

Responses of tiba on growth, yield and biochemical components of BARI Maize-6

A M M Golam Adam*, Shirajum Munira and Hasna Hena Brgum

Department of Botany, Jagannath University, Dhaka, Bangladesh

ARTICLE INFO

Article History

Received: 2 October 2023
Revised: 17 January 2024
Accepted: 23 January 2024

Keywords: Growth, Yield, Biochemical components, Maize, TIBA.

ABSTRACT

A field trial was carried out to investigate the responses of TIBA (0, 25, 50, 75, and 100 ppm) on growth, yield, and biochemical components of BARI Maize-6. Results revealed that plant height gradually reduced with the rising levels of TIBA but non-significantly. The application of 75 ppm TIBA resulted in the highest number of leaves and maximum dry weight of leaves and stems, whereas the dry weight of leaves was significantly higher than that of the control. Plants treated with 50 ppm TIBA resulted in maximum dry weight of roots, absolute growth rate, and relative growth rate, but statistically, they were at par with the rest of the treatments. The total number of cobs per plant was noted to be the highest at 50 ppm, followed by 75 ppm TIBA. Application of 75 ppm TIBA produced the highest fresh (127.10 g) and dry (111.51 g) weight of cobs, the longest cob (17.07 cm), the maximum number of kernels per row (31.81) and cob (408.17), dry weight of tassel (3.75 g), yield per plant (107.07 g) yield per hectare (7138.08 kg) and harvest index (89.72%). Significantly higher values were noted in the case of fresh and dry weight of cobs, number of kernels per cob, yield per plant, and yield per hectare. Yield per plant due to 75 ppm TIBA increased by 65.72% over control. Pigment contents of leaves responded positively following most of the TIBA treatments except chl. a content at the tassel initiation stage. Positive responses of TIBA in the protein content of leaves were also obtained in most cases. The maximum protein content of seeds was recorded from 50 ppm (94.88 mg/g) followed by 75 ppm (83.94 mg/g) TIBA but with a similar statistical identity. Among five treatments, 75 ppm TIBA produced better stimulations.

Introduction

Rice, wheat, and maize comprise a chief factor of the human diet, representing 42 and 37% of the world's calories and protein intake, respectively (FAOSTAT, 2021). Among cereals, the worldwide annual production of maize (*Zea mays* L.) is greater than 1 billion metric tons (García-Lara and Serna-Saldivar, 2019). Comparatively, maize is a more versatile crop than wheat and rice used as a feed crop and plays a pivotal role in global food security (Grote et al., 2020; Poole et al., 2021).

Maize is a crucial task in our country's agri-based economy. It is consumed in many forms across the country and has become a good source of nutrition for the escalating population of Bangladesh. Farmers could not obtain higher yields in Bangladesh due to diverse constraints, and the country needed to import a large amount of maize annually to mitigate its rising demand. Among the various methods of improving crop production, using plant growth regulators (PGRs) is the best technique for such an attempt. Insufficiency of these magical substances

---

*Corresponding author:<adamammg@bot.jnu.ac.bd>

may generate an obstacle in attaining the desired yield. Additionally, these hormones can develop physiological efficacy, photosynthetic capability, and suitable partitioning in various crops.

Previous findings indicated that TIBA (2,3,5 tri-iodo benzoic acid) at minute dose had inducing effect in promoting physiological parameters, yield attributes and biochemical components of various important crop plants *viz*. chickpea (Islam and Jahan, 2019), soybean (Basuchaudhuri, 2016), papaya (Mutum et al., 2021), rice (Adam et al., 2015, Doel et al., 2021). However, no investigation has been completed in Bangladesh regarding applying TIBA for maize. Thus, the current investigation was conducted to assess the responses of TIBA to some growth parameters, yield attributes, and biochemical components of maize var. BARI Maize-6.

Materials and Methods

A trial was carried out in the research field of the botanical garden at Jagannath University, Dhaka, Bangladesh. The trial was laid out in RBD and had three replications. The size of the investigational area was 40.0 m^2, which was divided into three plots. Each plot consisted of 5 rows, maintaining a distance of 75 cm between two rows and 20 cm between plant to plant. Preparation of the experimental field was done conventionally. Cow dung was mixed homogenously, and chemical fertilizers were applied as described by Chowdhury and Hassan (2013). One-third of urea and a full dose of other fertilizers were given during final plowing. The remaining doses of urea were applied at tassel initiation and before the silking stage. Calcium hypochlorite (0.5%) was used for seed sterilization. Cultural practices were maintained following methods described by Chowdhury and Hassan (2013) in the Handbook of Agricultural Technology. This experiment comprised control, 25, 50, 75, and 100 ppm foliar TIBA treatments. The foliar spray was done in the early morning of the sunny day. Height of plant, number of leaves, dry weight of leaves, stem and root, shoot-root ratio, biomass duration (BMD), absolute growth rate (AGR), and relative growth rate (AGR) were recorded after harvest following standard methods. Yield contributing parameters and yield were estimated after harvest. Leaf pigment and protein content were recorded at tassel initiation and grain filling stages, whereas the protein content of seed after harvest as per approved procedures (Mckinney, 1940; Lowry et al., 1951; von Wettstein, 1957; Maclachalan and Zalik, 1963).

Six plants from each treatment were arbitrarily selected to collect data on different parameters. Collected data were subjected to statistical analysis, and LSD test treatment was done at a 5% level of significance for the comparison of treatment means (Steel et al., 1997).

Results and Discussion

Findings indicated that the plant height of BARI Maize-6 reduced gradually with the increasing concentration of TIBA (Table 1). The maximum decrease due to 100 ppm TIBA was 6.08% higher than the control. The leaf number of BARI Maize-6 was positively influenced by the application of TIBA but non-significantly. A maximum number of leaves, 11.83, was noted from 75 ppm TIBA followed by 100 ppm (11.67) treatment. Findings on the height of plant and leaf number are in harmony with the results of other investigations (Adam et al., 2015; Basuchaudhuri, 2016; Islam and Jahan, 2019; Doel et al., 2021).

Table 1 indicated that foliar application of TIBA as foliar treatment produced a higher amount of biomass, i.e., dry weight of leaves, stem, and root, than control, where 75 ppm TIBA resulted in maximum dry weight of leaves (39.99 g) and stem (73.47 g). The dry weight of leaves was recorded at 50, 75, and 100 ppm. Even though they produced significantly superior weights to the control, they were identical to the 25 ppm treatment. Results also showed that the highest dry weight of roots was recorded from 50 ppm (14.02 g) but not statistically dissimilar from other treatments. This result is very similar to the findings of Adam and Jahan (2014) on BARI Mung-5 and Jahan and Khan (2014) on soybean.

TIBA as foliar spray had retarding responses on the shoot-root ratio of BARI Maize-6. However, BMD, AGR, and RGR were positively influenced due to TIBA treatments (Table 1).

Table 1. Effect of TIBA on growth parameters of BARI Maize-6 at harvest.

Treatments	Height (cm)	No. of leaves/ plant	Dry weight of leaves (g)	Dry weight of stem (g)	Dry weight of roots (g)	Shoot-root ratio	BMD	AGR (g/day)	RGR (g/g/day)
Control	243.83	10.50	23.40 ^{b}	48.83	8.52 ^{a}	7.91	1286.00	-0.803	-0.007
25 ppm TIBA	241.00	11.17	35.54 ^{ab}	51.37	11.62 ^{a}	4.19	1362.80	-0.660	-0.002
50 ppm TIBA	239.33	11.00	39.16 ^{a}	58.69	14.02 ^{a}	2.49	1320.18	0.503	0.015
75 ppm TIBA	236.50	11.83	39.99 ^{a}	73.47	12.91 ^{a}	6.03	1463.30	-0.023	-0.006
100 ppm TIBA	229.00	11.67	39.01 ^{a}	71.48	9.49 ^{a}	4.82	1298.50	0.433	0.011
CV (%)	6.53	11.83	29.83	17.05	11.43	5.61	25.44	27.46	17.31
LSD (0.05)	NS	NS	14.52	NS	10.56	NS	NS	NS	NS

The mean followed by an identical letter (vertically) or without a letter is statistically similar at a 5% level.

Outcomes are reasonably in harmony with the conclusion of Islam and Jahan (2016) on chickpeas. Table 2 revealed that spraying of TIBA had inducing effects on yield components of BARI Maize-6. A total number of cobs per plant was positively responded to due to TIBA application, where 50 ppm TIBA produced a maximum number of cobs (1.50) followed by 75 ppm (1.33) and both 25 and 100 ppm (1.17) treatments, respectively. A higher number of cobs per plant following TIBA treatments has also been reported by Mutum et al., (2021). Results showed that TIBA as foliar spray did not influence the number of productive cobs per plant, whereas all the treatments produced a similar number of productive cobs (1.0). Several non-productive cobs per plant due to TIBA treatment augmented but with non-significant variations.

On the other hand, the report of Adam et al. (2018) revealed positive responses of TIBA on the number of productive tillers per plant. The experiment's findings showed that the fresh and dry weight of cobs was enhanced significantly due to all applications of TIBA treatments, with an exception. The maximum fresh (127.10 g) and dry weight of cobs (111.51 g) was

The highest dry weights were obtained from 75 ppm TIBA, followed by 50, 25, and 100 ppm TIBA treatments, respectively. Several researchers also obtained increases in dry weight of pods due to TIBA application in different crops (Adam et al., 2018; Doel et al., 2021).

TIBA treatments positively responded to the length of the cob, and the application of 75 ppm resulted in the longest cob in BARI Maize-6. Many researchers have observed the stimulating effects of TIBA on pod length in different crops (Adam et al., 2018; Doel et al., 2021). Thus, the findings are fairly similar to those of earlier workers.

Outcomes presented in Table 2 indicated that the number of kernels per row, kernels per cob, dry weight of tassel, 1000-grains weight, yield per plant, and hectare were remarkably influenced by TIBA application where a significantly higher number of kernels per cob was noted from 75 ppm but statistically similar to other treatments. A foliar spray of 75 ppm TIBA also produced maximum cob length, number of kernels per row, yield, and harvest index. The weight of 1000-grain due to 25 ppm TIBA treatment was recorded as a superior value but statistically at par with other treatments.

various authors on diverse plants, viz. chickpea (Islam and Jahan, 2019), papaya (Mutum et al., 2021), mungbean (Adam and Jahan, 2014). Hence, the current results concur with the outcomes for many workers.

Findings revealed that TIBA as a foliar spray had mostly inducing effects on the leaf pigment of BARI Maize-6 at both the tassel initiation and grain-filling stages.

At the tassel initiation phase, 25, 50, and 75 ppm TIBA resulted in higher chlorophyll b and carotenoid content of leaves than the control with an exception.

Table 2. Effect of TIBA on yield attributes and yields of BARI Maize-6 at harvest.

Treatments	Total no. of cobs /plant	No. of productive cobs/ plant	No. of non-productive,cos/ plant	Fresh weight of Cob (g)	Dry weight of Cob (g)	Length of cob (cm)	No. of Karnels rows/ cob	No. of kerns/row	No. of kernels/ cob	Dry weight of tassel (g)	1000-grain weight (g)	Yield/ plant (g)	Yield /hectare (kg)	Harvest Index (%)
Control	1.00	1.00	0.00	83.48 ^{b}	70.43 ^{b}	14.15	12.83	21.42	273.33 ^{b}	1.78	236.73^{b}	64.61 ^{b}	4306.89 ^{b}	84.56
25 ppm TIBA	1.17	1.00	0.17	108.56 ^{ab}	95.71 ^{a}	16.20	12.83	24.69	318.17 ^{ab}	2.48	283.70 ^{a}	88.57 ^{ab}	5904.34 ^{ab}	88.26
50 ppm TIBA	1.50	1.00	0.50	124.48 ^{a}	109.40 ^{a}	16.62	12.50	28.46	355.00 ^{ab}	3.24	279.23 ^{ab}	99.43 ^{a}	6628.83 ^{a}	83.66
75 ppm TIBA	1.33	1.00	0.33	127.10 ^{a}	111.51 ^{a}	17.07	12.83	31.81	408.17 ^{a}	3.75	262.80 ^{ab}	107.07 ^{a}	7138.08 ^{a}	89.72
100 ppm TIBA	1.17	1.00	0.17	104.32 ^{a}	95.86 ^{a}	15.50	12.17	24.63	293.50 ^{b}	3.44	276.73 ^{ab}	82.39 b	5492.35 ^{ab}	65.43
CV (%)	14.88	0.00	8.36	22.06	23.07	12.02	9.63	7.18	23.26	43.52	11.65	24.30	24.30	31.73
LSD (0.05)	NS	-	NS	33.41	29.52	NS	NS	NS	102.89	NS	42.03	27.36	1824.18	NS

The maximum yield per plant due to 75 ppm TIBA was 65.72% higher than the control, followed by 50 ppm (53.89%), 25 ppm (37.14%), and 100 ppm (27.52%), respectively. Results also showed that 75 ppm, although producing a significantly superior yield than the control and 100 ppm TIBA, was statistically equal to the 25 and 50 ppm treatments.

The stimulating responses of TIBA on yield attributes and yield have also been observed by

Chlorophyll content decreased due to all concentrations of TIBA (Table 3). At the grain-filling stage, a higher quantity of chlorophyll a, b, and carotenoid content was noted from TIBA treatments except chlorophyll content due to 100 ppm treatment. The results also revealed that 50 ppm TIBA at the tassel initiation stage and 25 ppm TIBA at the grain filling stage resulted in maximum pigment content except for chlorophyll content in the case of the tassel initiation stage.

Similar results of increases were observed by Adam et al., 2018).

Leaf protein at both tassel initiation and grain filling stages were positively influenced by TIBA application except due to 75 and 100 ppm treatments at the grain filling stage (Table 4). Findings also indicated that the protein content of the seed increased by 14.31% and 1.13% due to 75 and 100 ppm treatment, respectively. However, applying 25 ppm and 100 ppm TIBA reduced the protein content of seeds by 33.06% and 21.13%, respectively. The outcome of this investigation contradicts the results of Doel et al. (2021), where they obtained higher protein content from 25 ppm TIBA in BRRI Dhan-55, but is in compliance with the findings of Ridge (1991).

Table 3. Responses of TIBA on the photosynthetic pigment of leaves (mg/g) of BARI Maize-6 at tassel initiation and grain filling stages.

Treatments	Tassel initiation stage			Grain filling stage		
	Chl a	Chl b	Carotenoids	Chl a	Chl b	Carotenoids
Control	0.252 a	0.121	6.803 ab	0.235 b	0.088 b	2.600 bc
25 ppm TIBA	0.170 b	0.159	7.036 a	0.424 a	0.142 a	3.477 a
50 ppm TIBA	0.166 b	0.300	7.722 a	0.366 a	0.111 ab	3.175 ab
75 ppm TIBA	0.213 ab	0.215	7.114 a	0.384 a	0.123 a	2.813 abc
100 ppm TIBA	0.077 c	0.135	5.782 b	0.226 b	0.089 b	1.517 d
CV (%)	6.87	8.03	21.57	7.86	6.64	6.27
LSD (0.05)	0.063	NS	1.090	0.090	0.031	0.701

The mean followed by an identical letter (vertically) or without a letter is statistically similar at a 5% level.

Table 4. Responses of TIBA on the protein content of leaves and seeds (mg/g) of BARI Maize-6.

Treatments	Leaves		Seeds
	Tassel initiation stage	Grain filling stage	At harvest
Control	6.50	3.25b	83.00 ab
25 ppm TIBA	8.13	7.70a	55.56 b
50 ppm TIBA	8.70	4.50ab	94.88 a
75 ppm TIBA	7.08	1.48b	83.94 ab
100 ppm TIBA	10.53	1.23b	65.46 ab
CV (%)	12.73	16.74	33.27
LSD (0.05)	NS	3.29	29.57

The mean followed by an identical letter (vertically) or without a letter is statistically similar at the 5% level.

Conclusion

The overall findings indicated that TIBA as a foliar spray had promoting responses regarding growth, yield, photosynthetic pigment, and protein content of leaves and seeds. Among the 25, 50, 75, and 100 ppm TIBA treatments, the application of 75 ppm produced better stimulation for obtaining higher yield.

References

Adam AMMG and Jahan N. Growth and yield of BARI Mung-5 (*Vigna radiata* L. Wilczek) following TIBA application. *Dhaka Univ. J. Biol. Sci.* 2014. 23(2): 179-185.

Adam AMMG, Islam R and Begum HH. Yield and biochemical attributes of BRRI Dhan-44 (*Oryza Sativa* L.) as affected by TIBA application. *J. Asiat. Soc. Bangladesh, Sci.* 2018; 44(2): 117-125.

Adam AMMG, Islam R, Begum HH and Naher MK. Growth analysis of BRRI Dhan-44 (*Oryza sativa* L.) following 2,3,5-Triiodobenzoic (TIBA) acid application. *J. Asiat. Soc. Bangladesh Sci.* 2015; 41(1): 67-74.

Basuchaudhuri P. Influences of growth regulators on yield of soybean. *Indian J. Plant. Sci.* 2016; 5(4):25-38.

Chowdhury MAH and Hassan MS. *Hand Book of Agricultural Technology.* Bangladesh Agric. Res. Council 2013; Farmgate, Dhaka. p. 230.

Doel NA, Adam AMMG, Khan FI and Begun HH. Effect of TIBA and *Rhizobium* application on growth, yield and biochemical components of BRRI Dhan-55. *Bangladesh J. Bot.* 2021; 50(4): 1181-1189.

FAOSTAT. FAO Statistical Yeabook-World food and Agriculture 2021, Rome. P. 353.

García-Lara S and Serna-Saldivar SO. Corn history and culture. In: *Corn: Chemistry and Technology, 3rd ed., Chapter 1.* AACC International Press, Oxford; 2019; pp. 1-18.

Grote U, Fasse A, Nguyen TT and Erenstein O. Food security and the dynamics of wheat and maize value chains in Africa and Asia. Front. Sustain. Food Syst. 2021; 4: 617009.

Islam S and Jahan N. Growth analysis of chickpea var. BARI Chola-7 following application of TIBA (2,3,5- triiodobenzoic acid). *J. Bangladesh Acad. Sci.* 2016; 40(2): 199-205.

Islam S and Jahan N. Growth and yield responses of chickpea var. BARI Chhola-7 following application of TIBA. *Bangladesh J. Bot.* 2019; 48(3): 603-608.

Jahan N and Khan S. Effect of TIBA on growth, yield and yield component of soybean. *J. Asiat. Soc. Bangladesh Sci.* 2014; 40(1): 89-96.

Lowry OH, Rosebrough NJ, Farr AL and Randall RJ. Protein measurement with folin phenol reagent. *J. Boil. Chem.* 1951; 193: 265-275.

Maclachalan S and Zalik S. Plastid structure, chlorophyll concentration and free amino acid composition of a chlorophyll mutant of barley. *Can. J. Bot.* 1963; 41: 1053-1062.

Mckinney G. Criteria for purity of chlorophyll preparations. *J. Biol. Chem.* 1940; 132: 91-107.

Mutum B, Maity U, Basak S, Laya B and Singh SD. Effect of plant growth regulator on flowering and yield attributes of papaya. *Biological Forum*. 2021; 13(3a): 627-630.

Poole N, Donovan J and Erenstein O. Agri-nutrition research: Revisiting the contribution of maize and wheat to human nutrition and health. *Food Policy*, 2021; 100(3): 1-13.

Ridge I. Plant cells and growth. In: *Plant Physiology*. The Open University, Hodder and Stoghton. U.K. 1991; pp. 225-281.

Steel RGD, Torrie JH and Dickey DA. Principles and Procedures of Statistics. McGraw Hill Book Co. Inc. New York 1997; p. 666.

von Wettstein D. Chlorophyll-lethal und der submikroskopische formwechsel der plastiden. *Expt. Cell Res*. 1957; 12: 427-506.

J. Bangladesh Acad. Sci. 48(1); 51-59: June 2024 DOI:https://doi.org/10.3329/jbas.v48i1.69329

Journal of Bangladesh Academy of Sciences

Journal homepage: http://www.bas.org.bd/publications/jbas.html

Research Article

Study on intutionistic fuzzy Hausdorff (T_2) bitopological spaces: theoretical insights

Saikh Shahjahan Miah* and Homayra Kabir

Department of Mathematics, Faculty of Science, Mawlana Bhashani Science and Technology University, Tangail, Bangladesh

ARTICLE INFO

Article History

Received: 12 October 2023
Revised: 2 January 2024
Accepted: 9 January 2024

Keywords: Fuzzy topological space; Fuzzy bitopological space; Intuitionistic fuzzy topology; Intuitionistic fuzzy Hausdorff bitopological space; Good extension.

ABSTRACT

In this paper, we offer the concepts of some notions of Hausdorff (T_2) property in intuitionistic fuzzy Bitopological spaces. We demonstrate that each notion satisfies good extension property and establish that these notions satisfy hereditary properties. All the concepts of intuitionistic fuzzy Hausdorff topological spaces are preserved under one-one, onto fuzzy mappings.

Introduction

The root of fuzzy logic is the paper "Fuzzy Sets" by Zadeh (1965). Zadeh developed the idea of fuzzy sets in this research article 1965 as a mechanism to express and deal with vagueness and uncertainty in mathematical and computer systems. In contrast to classical set theory, which assumes that an element either belongs to a set or does not, fuzzy sets enable the representation of partial membership within a set. In the late 1960s, Chang (1968) made significant contributions to the study of fuzzy topological spaces. In his 1968 research, he formulated the notion of fuzzy topology. He pioneered the introduction of fuzzy topological spaces, a collection of fuzzy sets satisfied by the three conditions. Since Chang integrated fuzzy set theory with topology, many operations and properties were introduced within the fuzzy framework. The concept of separation axioms has significance in fuzzy topological spaces.

As a broader development of fuzzy topological space and as an extended generalization of bitopological spaces, which was initially introduced in the research article of Kelly (1963) named "Bitopological Spaces", Kandil and El-Shafee (1989) established various forms of separation axioms on fuzzy bitopological spaces in the research paper named "Biproximities and fuzzy bitopological spaces" in 1989. The theoretical foundation of fuzzy topological and bitopological spaces has undergone extensive research in several directions (Miah et al., 2017; Miah et al., 2018) in particular among those axioms, by the concepts of Hausdorff topological space, separations on bitopological spaces, fuzzy bitopological spaces, the concept of T_2-bitopological spaces has been established from the research articles of Sufiya et al. (1994), Nouh (1996), Miah and Amin (2017) and Amin et al. (2014). Again, as a generalized concept of fuzzy sets, in 1986, Atanosov (Atanassov and Stoeva, 1986; Atanassov, 1988) first put forward the idea of intuitionistic fuzzy sets, which expand the concept of the classical fuzzy set by introducing two membership functions, one that represents the degree of membership and the another that of non-membership. With the further advancement and development of this concept, Coker

---

*Corresponding author:<skhshahjahan@gmail.com>

(Coker, 1996a, 2000, 1997; Coker and Demirci 1995) and his colleagues pioneered the notions of intuitionistic fuzzy topological spaces in his research articles named "A note on intuitionistic sets and intuitionistic points," "On intuitionistic fuzzy points," "An introduction to intuitionistic fuzzy topological spaces," "An introduction to intuitionistic topological spaces ."According to the after approach, in 2014, Ahmed et al. (2014) introduced and conducted an exploration of the intuitionistic fuzzy T_2-spaces and established some relationships among them. The main focus of this paper is new developments and contributions to the expansion of intuitionistic fuzzy Hausdorff bitopological spaces. In this research paper's context, we define intuitionistic fuzzy Hausdorff bitopological spaces and illustrate their fundamental criteria, including the mappings, suitable extension property, and hereditary property.

Basic Notions and Preliminary Results

To attain our main result, defining specific terms and notions is necessary.

Definition 2.1 (Coker, 1996a, 2000; Bayhan and Coker, 2001)**:** Let us suppose that the object M has the form $M = (x, M_1, M_2)$ such that X has the subsets M_1 and M_2 that satisfy $M_1 \cap M_2 = \emptyset$. Then, we refer to M_1 as the set of M members and M_2 as the set of M non-members. Throughout this piece of writing, we will refer to the intuitionistic set as $M = (M_1, M_2)$.

Definition 2.2 (Coker 1996a; Coker 2000; Bayhan and Coker 2001) Let us Consider $M = (M_1, M_2)$ and $N = (N_1, N_2)$ to represent the intuitionistic sets on X. let $\{M_j : j \in J\}$ be an any family of intuitionistic sets in X where $M_j = ({M_j}^{(1)}, {M_j}^{(2)})$. Then

(a) $M \subseteq N$ if and only if $M_1 \subseteq N_1$ and $M_2 \supseteq N_2$.

(b) $M = N$ if and only if $M \subseteq N$ and $N \supseteq M$.

(c) $\bar{M} = (M_1,\ M_2)$, the complement of M.

(d) $\cap M_j = (\cap {M_j}^{(1)}, \cup {M_j}^{(2)})$.

(e) $\cup M_j = (\cup {M_j}^{(1)}, \cap {M_j}^{(2)})$.

(f) $\phi_\sim = (\phi, X)$ and $X_\sim = (X, \phi)$.

Definition 2.3 (Coker, 2000; Bayhan and Coker, 2001) An intuitionistic topology defined on a non-empty set X is a family τ of intuitionistic sets in X which satisfies the axioms listed following:

(1) $\phi_\sim, X_\sim \in \tau$.

(2) $G_1 \cap G_2 \in \tau$ for any $G_1, G_2 \in \tau$. $\cup G_i \in \tau$ for any arbitrary family $G_i \in \tau$.

In this situation, the pair (X, τ) is referred to as an intuitionistic topological space, and every subset of X that possesses an intuitionistic set τ is called an intuitionistic open set in X.

Definition 2.4 (Atanassov, 1986; Coker, 1996a, 1997; Bayhan and Coker, 1996) Let us assume that X is a non-empty set and $I = [0,1]$. Let $M = \{(x, \mu_M(x), \vartheta_M(x))\}$ be the intuitionistic fuzzy set in X where x belongs to X and $\mu_M : X \to I$ represents the degree of membership and $\vartheta_M : X \to I$ represents the degree of non-membership; $\mu_M(x) + \vartheta_M(x) \leq 1$.

The set of all intuitionistic fuzzy sets in X is defined as $I(X)$. Notably, the simpler notation $(\mu_M, 1 - \mu_M)$ represents every fuzzy set μ_M in X as an intuitionistic fuzzy set.

In this work, instead of using $M = \{(x, \mu_M(x), \vartheta_M(x)), x \in X\}$,we shall use shorter notation $M = (\mu_M, \vartheta_M)$.

Definition 2.5 (Atanassov, 1986; Coker, 1996, 1997; Bayhan and Coker, 1996) Let us assume that the intuitionistic fuzzy sets in X are $M = (\mu_M, \vartheta_M)$ and $N = (\mu_N, \vartheta_N)$. Then

(1) $M \subseteq N$ if and only if $\mu_M \leq \mu_N$ and $\vartheta_M \geq \vartheta_N$.

(2) $M = N$ if and only if $M \subseteq N$ and $N \subseteq M$.

(3) $M^C = (\vartheta_M, \mu_M)$.

(4) $M \cap N = (\mu_M \cap \mu_N;\ \vartheta_M \cup \vartheta_N)$.

(5) $M \cup N = (\mu_M \cup \mu_N; \vartheta_M \cap \vartheta_N)$.

(6) $0_\sim = (0^\sim, 1^\sim)$ and $1_\sim = (1^\sim, 0^\sim)$.

Definition 2.6 (Coker, 1996b, 1997; Bayhan and Coker, 1996) An intuitionistic fuzzy topology on a non-empty set X is the collection t of intuitionistic fuzzy sets on X if it satisfies the following principles:

(1) $0_{\sim}, 1_{\sim} \in t$.

(2) If $M_1, M_2 \in t$, then$M_1 \cap M_2 \in t$.

(3) If $M_i \in t$ for each i, then $\cup M_i \in t$.

The pair (X, t) is an intuitionistic fuzzy topological space, and every intuitionistic fuzzy set in t possesses an intuitionistic fuzzy open set in X.

Definition 2.7 (Ahmed et al., 2014) An intuitionistic fuzzy topological space (X, t) is called

(a) IF-T_2(i) if for all $x_1, x_2 \in X$, $x_1 \neq x_2$ there exist $M = (\mu_M, \vartheta_M), N = (\mu_N, \vartheta_N) \in t$ such that $\mu_M(x_1) = 1, \vartheta_M(x_1) = 0; \mu_N(x_2) = 1$, $\vartheta_N(x_2) = 0$ and $M \cap N = 0_{\sim}$.

(b) IF-T_2(ii) if for all $x_1, x_2 \in X, x_1 \neq x_2$ there exist $M = (\mu_M, \vartheta_M), N = (\mu_N, \vartheta_N) \in t$ such that $\mu_M(x_1) = 1$, $\vartheta_M(x_1) = 0; \mu_N(x_2) > 1$, $\vartheta_N(x_2) = 0$ and $M \cap N = (0^{\sim}, \gamma^{\sim})$ where $\gamma \in (0,1]$.

(c) IF-T_2(iii) if for all $x_1, x_2 \in X$, $x_1 \neq x_2$, there exist $M = (\mu_M, \vartheta_M), N = (\mu_N, \vartheta_N) \in t$ such that $\mu_M(x_1) > 0$, $\vartheta_M(x_1) = 0; \mu_N(x_2) = 1$, $\vartheta_N(x_2) = 0$ and $M \cap N = (0^{\sim}, \gamma^{\sim})$ where $\gamma \in (0,1]$.

(d) IF-T_2(iv) if for all $x_1, x_2 \in X, x_1 \neq x_2$ there exist $M = (\mu_M, \vartheta_M), N = (\mu_N, \vartheta_N) \in t$ such that $\mu_M(x_1) > 1$, $\vartheta_M(x_1) = 0; \mu_N(x_2) > 0$, $\vartheta_N(x_2) = 0$ and $M \cap N = (0^{\sim}, \gamma^{\sim})$ where $\gamma \in (0,1]$.

Definition 2.8 (Kelly, 1963**):** Let us consider two general topologies, S and T, which are defined on any non-empty set X. The combination (X, S, T) is referred to as a bitopological space.

Definition 2.9 (Kandil and El-Shafee, 1989) The triple (X, s, t) is known as fuzzy bitopological space where s and t stand for two distinct fuzzy topologies defined on X.

3. Characteristics and Attributes of Intuitionistic Fuzzy Hausdorff (T_2) Bitopological Spaces

Definition: An intuitionistic fuzzy bitopological space (X, s, t) is called

(a) IFB-T_2(i) if for all $x_1, x_2 \in X$, $x_1 \neq x_2$ there exist $M = (\mu_M, \vartheta_M), N = (\mu_N, \vartheta_N) \in (s \cup t)$ such that $\mu_M(x_1) = 1$, $\vartheta_M(x_1) = 0$; $\mu_N(x_2) = 1$, $\vartheta_N(x_2) = 0$ and $M \cap N = 0_{\sim}$.

(b) IFB-T_2(ii) if for all $x_1, x_2 \in X, x_1 \neq x_2$ there exist $M = (\mu_M, \vartheta_M), N = (\mu_N, \vartheta_N) \in (s \cup t)$ such that $\mu_M(x_1) = 1$, $\vartheta_M(x_1) = 0$; $\mu_N(x_2) > 1$, $\vartheta_N(x_2) = 0$ and $M \cap N = (0^{\sim}, \gamma^{\sim})$ where $\gamma \in (0,1]$.

(c) IFB-T_2(iii) if for all $x_1, x_2 \in X$, $x_1 \neq x_2$ there exist $M = (\mu_M, \vartheta_M), N = (\mu_N, \vartheta_N) \in (s \cup t)$ such that $\mu_M(x_1) > 0$, $\vartheta_M(x_1) = 0$; $\mu_N(x_2) = 1$, $\vartheta_N(x_2) = 0$ and $M \cap N = (0^{\sim}, \gamma^{\sim})$ where $\gamma \in (0,1]$.

(d) IFB-T_2(iv) if for all $x_1, x_2 \in X$, $x_1 \neq x_2$ there exist $M = (\mu_M, \vartheta_M), N = (\mu_N, \vartheta_N) \in (s \cup t)$ such that $\mu_M(x_1) > 1$, $\vartheta_M(x_1) = 0$; $\mu_N(x_2) > 0$, $\vartheta_N(x_2) = 0$ and $M \cap N = (0^{\sim}, \gamma^{\sim})$ where $\gamma \in (0,1]$.

Definition: Let us assume that $\alpha \in (0,1)$. Then, an intuitionistic fuzzy bi-topological space (X, s, t) is referred to as

(a) α-IFB-T_2(i) if for all $x_1, x_2 \in X$, $x_1 \neq x_2$ there exist $M = (\mu_M, \vartheta_M), N = (\mu_N, \vartheta_N) \in (s \cup t)$ such that $\mu_M(x_1) = 1$, $\vartheta_M(x_1) = 0$; $\mu_N(x_2) \geq \alpha$, $\vartheta_N(x_2) = 0$ and $M \cap N = 0_{\sim}$.

(b) α-IFB-T$_2$(ii) if for all $x_1, x_2 \in X$, $x_1 \neq x_2$ there exist $M = (\mu_M, \vartheta_M), N = (\mu_N, \vartheta_N) \in (s \cup t)$ such that $\mu_M(x_1) \geq \alpha$, $\vartheta_M(x_1) = 0; \mu_N(x_2) \geq \alpha$, $\vartheta_N(x_2) = 0$ and $M \cap N = (0^{\sim}, \gamma^{\sim})$ where $\gamma \in (0,1]$.

(c) α-IFB-T$_2$(iii) if for all $x_1, x_2 \in X$, $x_1 \neq x_2$ there exist $M = (\mu_M, \vartheta_M), N = (\mu_N, \vartheta_N) \in (s \cup t)$ such that $\mu_M(x_1) > 0$, $\vartheta_M(x_1) = 0$; $\mu_N(x_2) \geq \alpha$, $\vartheta_N(x_2) = 0$ and $M \cap N = (0^{\sim}, \gamma^{\sim})$ where $\gamma \in (0,1]$.

Theorem: Let the bitopological space $(X,)$ s, t be defined as an intuitionistic fuzzy bitopological space. Subsequently, the following consequences follow.

$$\begin{tikzcd}
& \text{IFBT}_2\text{(ii)} \arrow[dr] & \\
\text{IFBT}_2\text{(i)} \arrow[ur] \arrow[rr] \arrow[dr] & & \text{IFBT}_2\text{(iv)} \\
& \text{IFBT}_2\text{(iii)} \arrow[ur] &
\end{tikzcd}$$

Proof: Given that (X,s,t) is IFB-T_2(i), then for all $x_1,x_2 \in X, x_1 \neq x_2$ there exist $M=(\mu_M,\vartheta_M), N=(\mu_N,\vartheta_N) \in (s \cup t)$ such that $\mu_M(x_1)=1$, $\vartheta_M(x_1)=0$; $\mu_N(x_2)=1$, $\vartheta_N(x_2)=0$ and $M \cap N = 0_\sim$

$\Rightarrow \mu_M(x_1)>0$, $\vartheta_M(x_1)=0$; $\mu_N(x_2)>0$, $\vartheta_N(x_2)=0$ and $M \cap N = (0^\sim,\gamma^\sim)$ where $\gamma \in (0,1]$.

Which is IFBT$_2$ (iv).

Hence, IFB-T_2(i) $\Rightarrow$ IFBT$_2$ (iv).

Furthermore, let (X,s,t) is IFB-T$_2$ (ii), then for all $x_1,x_2 \in X, x_1 \neq x_2$ there exist $M=(\mu_M,\vartheta_M), N=(\mu_N,\vartheta_N) \in (s \cup t)$ such that $\mu_M(x_1)=1$, $\vartheta_M(x_1)=0$;$\mu_N(x_2)>0$, $\vartheta_N(x_2)=0$ and $M \cap N=(0^\sim,\gamma^\sim)$ where $\gamma \in (0,1]$

$\Rightarrow \mu_M(x_1)>0$, $\vartheta_M(x_1)=0$;$\mu_N(x_2)>0$, $\vartheta_N(x_2)=0$ and $M \cap N=(0^\sim,\gamma^\sim)$ where $\gamma \in (0,1]$.

Which is also IFB-T$_2$(iv).

Hence, IFB-T$_2$ (ii) $\Rightarrow$ IFB-T$_2$ (iv).

Again, let (X,s,t) is IFB-T$_2$ (iii), then for all $x_1,x_2 \in X, x_1 \neq x_2$ there exist $M=(\mu_M,\vartheta_M)$, $N=(\mu_N,\vartheta_N) \in (s \cup t)$ such that $\mu_M(x_1) \geq 0$, $\vartheta_M(x_1)=0$; $\mu_N(x_2)=1$, $\vartheta_N(x_2)=0$ and $M \cap N = (0^\sim,\gamma^\sim)$ where $\gamma \in (0,1]$

$\Rightarrow \mu_M(x_1)>0$, $\vartheta_M(x_1)=0$;$\mu_N(x_2)>0$, $\vartheta_N(x_2)=0$ and $M \cap N=(0^\sim,\gamma^\sim)$ where $\gamma \in (0,1]$.

Which is also IFB-T$_2$(iv).

Hence, IFB-T$_2$ (iii) $\Rightarrow$ IFB-T$_2$ (iv).

Furthermore, it can easily verify that IFB-T_2(i) $\Rightarrow$ IFB-T_2(ii), IFB-T_2(i) $\Rightarrow$ IFB-T_2(iii).

We give a counter example following to show that none of the reverse implications exist.

Counterexample: For IFB-T_2(iv) $\nRightarrow$ IFB-T$_2$ (i), let us assume that s and t are intuitionistic fuzzy topologies on $X=\{x_1,x_2\}$ generated by $M=\{x_1,0.3,0\}$ and $N=\{x_2,0.2,0\}$ respectively and the corresponding intuitionistic fuzzy bitopological space (X,s,t) which is IFB-T$_2$(iv) but not IFB-T_2(i).

For IFB-T_2(iv) $\nRightarrow$ IFB-T$_2$ (ii), let us assume that s and t are intuitionistic fuzzy topologies on $X=\{x_1,x_2\}$ generated by $M=\{x_1,0.4,0\}$ and $N=\{x_2,0.1,0\}$ respectively and the corresponding intuitionistic fuzzy bitopological space (X,s,t) which is IFB-T$_2$(iv) but not IFB-T_2(ii).

For IFB-T_2(iv) $\nRightarrow$ IFBT$_2$ (iii), let us assume that s and t are intuitionistic fuzzy topologies defined on $X=\{x_1,x_2\}$ generated by $M=\{x_1,0.9,0\}$ and $N=\{x_2,0.5,0\}$ respectively and the corresponding intuitionistic fuzzy bitopological space (X,s,t) which is IFB-T$_2$ (iv) but not IFB-T$_2$ (iii).

Theorem: The bitopological space (X,s,t) is an intuitionistic fuzzy bitopological space. Consider the following implications.

$$\begin{tikzcd}
 & \alpha\text{- IFBT}_2\text{(iii)} \\
\alpha\text{- IFBT}_2\text{(i)} \arrow[ur] \arrow[dr] & \\
 & \alpha\text{- IFBT}_2\text{(ii)} \arrow[uu]
\end{tikzcd}$$

Proof: Let us assume that (X,s,t) is α-IFB-T_2(i). We shall prove that (X,s,t) is α-IFB-T_2(i). Since (X,s,t) is α-IFB-T_2(i) then for all $x_1,x_2 \in X, x_1 \neq x_2$ there exist $M=(\mu_M,\vartheta_M), N=(\mu_N,\vartheta_N) \in (s \cup t)$ such that $\mu_M(x_1)=1$, $\vartheta_M(x_1)=0$; $\mu_N(x_2) \geq \alpha$, $\vartheta_N(x_2)=0$ and $M \cap N = 0_\sim$

$\Rightarrow \mu_M(x_1) \geq \alpha$, $\vartheta_M(x_1)=0$;$\mu_N(x_2) \geq \alpha$, $\vartheta_N(x_2)=0$ for any $\alpha \in (0,1)$ and $M \cap N=(0^\sim,\gamma^\sim)$.

Which is also α-IFB-T$_2$ (ii) space.

Hence α-IFB-T_2(i) $\Rightarrow$ α-IFB-T$_2$ (ii)

Again, suppose (X,s,t) is α-IFB-T$_2$ (ii). We will prove that (X,s,t) is α-IFB-T$_2$ (ii). Now, Since (X,s,t) is α-IFB-T$_2$ (ii), then for all $x_1,x_2 \in X, x_1 \neq x_2$ there exist $M=(\mu_M,\vartheta_M), N=(\mu_N,\vartheta_N) \in (s \cup t)$ such that $\mu_M(x_1) \geq \alpha$, $\vartheta_M(x_1)=0$;$\mu_N(x_2) \geq \alpha$, $\vartheta_N(x_2)=0$ and $M \cap N=(0^\sim,\gamma^\sim)$ where $\gamma \in (0,1]$

$\Rightarrow \mu_M(x_1)>0$, $\vartheta_M(x_1)=0$;$\mu_N(x_2) \geq \alpha$, $\vartheta_N(x_2)=0$ for any $\alpha \in (0,1)$ and $M \cap N=(0^\sim,\gamma^\sim)$ where $\gamma \in (0,1]$.

Which is also α-IFB-T$_2$ (iii) space.

Hence α-IFB-T$_2$ (ii) $\Rightarrow$ α-IFB-T$_2$ (iii)

Hence it is verified that α-IFB-T_2(i) ⇒ α-IFB-T_2 (ii) ⇒ α-IFB-T_2 (iii)

Again, suppose that (X,s,t) is α-IFB-T_2(i) space. We will establish the proof that (X,s,t) is α-IFB-T_2 (iii). Since, (X,s,t) is α-IFB-T_2(i), then for all $x_1,x_2 \in X, x_1 \neq x_2$ there exist $M=(\mu_M,\vartheta_M), N=(\mu_N,\vartheta_N) \in (s \cup t)$ such that $\mu_M(x_1)=1$, $\vartheta_M(x_1)=0$; $\mu_N(x_2) \geq \alpha$, $\vartheta_N(x_2)=0$ and $M \cap N = 0_\sim$

⇒ $\mu_M(x_1) > 0$, $\vartheta_M(x_1)=0$; $\mu_N(x_2) \geq \alpha$, $\vartheta_N(x_2)=0$ for any $\alpha \in (0,1)$ and $M \cap N = 0^\sim, \gamma^\sim)$ where $\gamma \in (0,1]$.

Which is also α-IFB-T_2 (iii) space.

Hence α-IFB-T_2(i) ⇒ α-IFB-T_2 (iii).

We give a counter example following to show that none of the reverse implications exist.

Counterexample: For α-IFB-T_2(iii) ⇏ α-IFB-T_2(i), let us assume that s and t are intuitionistic fuzzy topologies on $X = \{x_1, x_2\}$ generated by $M = \{x_1, 0.5, 0\}$ and $N = \{x_2, 0.6, 0\}$ respectively. The corresponding intuitionistic fuzzy bitopological space on X defined by $\{M, N\}$ is (X,s,t). For $\alpha = 0.3$, the IFBTS (X,s,t) is α-IFB-T_2(iii) but not α-IFB-T_2(i).

For α-IFB-T_2(iii) ⇏ α-IFBT$_2$ (ii), let us assume that s and t are intuitionistic fuzzy topologies on $X = \{x_1, x_2\}$ generated by $M = \{x_1, 0.1, 0\}$ and $N = \{x_2, 0.4, 0\}$ respectively and the corresponding intuitionistic fuzzy bitopological space on X defined by $\{M, N\}$ is (X,s,t). For $\alpha = 0.3$, the IFBTS (X,s,t) is α-IFB-T_2(iii) but not α-IFB-T_2(ii).

Theorem: Let us consider an intuitionistic fuzzy bitopological space defined by (X,s,t), and $0 < \alpha \leq \beta < 1$. Then

(a) β-IFB-T_2(i) ⇒ α-IFB-T_2(i)
(b) β-IFB-T_2(ii) ⇒ α-IFB-T_2(ii)
(c) β-IFB-T_2(iii) ⇒ α-IFB-T_2(iii)

Proof: **(b)** Let (X,s,t) be an intuitionistic fuzzy bitopological space and is defined as β-IFB-T_2(ii). Then for all $x_1, x_2 \in X, x_1 \neq x_2$ there exist $M=(\mu_M,\vartheta_M), N=(\mu_N,\vartheta_N) \in (s \cup t)$ such that $\mu_M(x_1) \geq$ β, $\vartheta_M(x_1)=0$; $\mu_N(x_2) \geq$ β, $\vartheta_N(x_2)=0$ and $M \cap N = (0^\sim, \gamma^\sim)$

⇒ $\mu_M(x_1) \geq \alpha$, $\vartheta_M(x_1)=0$;$\mu_N(x_2) \geq \alpha$, $\vartheta_N(x_2)=0$ and $M \cap N = (0^\sim, \gamma^\sim)$ since $0 < \alpha \leq \beta < 1$.

Which is α-IFB-T_2 (ii) space.

Hence β-IFB-T_2 (ii) ⇒ α-IFB-T_2 (ii).

Similarly, we can prove that β-IFB-T_2(i) ⇒ α-IFB-T_2(i) and β-IFB-T_2(iii) ⇒ α-IFB-T_2(iii).

To show that none of the reverse implication exist, we give a counter example following

Counterexample: For β-IFB-T_2(i) ⇏ α-IFB-T_2(i), let us assume that s and t are intuitionistic fuzzy topologies defined on $X = \{x_1, x_2\}$ generated by $M = \{x_1, 1, 0\}$ and $N = \{x_2, 0.5, 0\}$ respectively and the corresponding intuitionistic fuzzy bitopological space on X is (X,s,t) defined by $\{M,\}$ N. For $\alpha = 0.4$ and $\beta = 0.6$, we can say that the IFBTS (X,s,t) is α-IFB-T_2(i) but not β-IFB-T_2(i).

For β-IFB-T_2(ii) ⇏ α-IFB-T_2(ii), let us assume that s and t are intuitionistic fuzzy topologies defined on $X = \{x_1, x_2\}$ generated by $M = \{x_1, 0.6, 0\}$ and $N = \{x_2, 0.3, 0\}$ respectively and the corresponding intuitionistic fuzzy bitopological space on X is (X,s,t) defined by $\{M, N\}$. For $\alpha = 0.3$ and $\beta = 0.7$, we can say that the IFBTS (X,s,t) is α-IFB-T_2(ii) but not β-IFB-T_2(ii).

For β-IFB-T_2(iii) ⇏ α-IFB-T_2(iii), let us assume that s and t are intuitionistic fuzzy topologies defined on $X = \{x_1, x_2\}$ generated by $M = \{x_1, 0.2, 0\}$ and $N = \{x_2, 0.3, 0\}$ respectively and the corresponding intuitionistic fuzzy bitopological space on X is (X,s,t) defined by $\{M, N\}$. For $\alpha = 0.2$ and $\beta = 0.4$, we can say that the IFBTS (X,s,t) is α-IFB-T_2(iii) but not β-IFB-T_2(iii).

Theorem: Consider an intuitionistic fuzzy bitopological space which is defined (X,s,t), characterized with $U \subseteq X$ and $s_U = \{M \mid U : M \in s\}$; $t_U = \{N \mid U : M \in t\}$; $\alpha \in (0,1)$.Then

(a) (X,s,t) *is* IFB-T_2(i) ⇒ (U, s_U, t_U) is IFB-T_2(i)
(b) (X,s,t) *is* IFB-T_2(ii) ⇒ (U, s_U, t_U) is IFB-T_2(ii)
(c) (X,s,t) *is* IFB-T_2(iii) ⇒ (U, s_U, t_U) is IFB-T_2(iii)

(d) (X,s,t) is IFB-T_2(iv) ⇒ (U,s_U,t_U) is IFB-T_2(iv)

(e) (X,s,t) is α-IFB-T_2(i) ⇒ (U,s_U,t_U) is α-IFB-T_2(i)

(f) (X,s,t) is α-IFB-T_2(ii) ⇒ (U,s_U,t_U) is α-IFB-T_2(ii)

(g) (X,s,t) is α-IFB-T_2(iii) ⇒ (U,s_U,t_U)) is α-IFB-T_2(iii)

Proof: (a) Consider an intuitionistic fuzzy bitopological space defined (X,s,t) as IFB-T_2(i). We will establish the proof that $(U,\ s_U,\ t_U)$ is IFB-T_2(i). Let $x_1, x_2 \in U,\ x_1 \neq x_2$, then $x_1, x_2 \in X,\ x_1 \neq x_2$ as $U \subseteq X$. Since (X,s,t) is IFB-T_2(i), then there exist $M_U = (\mu_{M_U}, \vartheta_{M_U}), N_U = (\mu_{N_U}, \vartheta_{M_U}) \in (s_U \cup t_U)$ such that $\mu_{M_U}(x_1) = 1,\ \vartheta_{M_U}(x_1) = 0;\ \mu_{N_U}(x_2) = 1,\ \vartheta_{N_U}(x_2) = 0$ and $M_U \cap N_U = 0_\sim$

$\Rightarrow\ \mu_{M_U}|U(x_1) = 1,\quad \vartheta_{M_U}|U(x_1) = 0; \mu_{N_U}|U(x_2) = 1, \vartheta_{N_U}|U(x_2) = 0$ and $M_U \cap N_U = 0_\sim$.

Since $\{(\mu_{M_U}|U, \vartheta_{M_U}|U),\ (\mu_{N_U}|U, \vartheta_{N_U}|U)\} \in (s_U \cup t_U)$.

Therefore, the intuitionistic fuzzy bitopological space $(U,\quad sU, t_U)$ is IFB-T_2(i).

Similarly, we can prove (b), (c), (d), (e), (f), and (g).

Definition: An intuitionistic bitopological space (IBTS) $(X, \tau_{1,} \tau_{2,})$ is called IB-T_2 Space if for all $x, y \in X, x \neq y$ there exists $C = (C_{1,}\ C_2),\ D = (D_{1,}\ D_2) \in (\tau_{1,} \tau_{2,})$ such that $x_1 \in C_{1,} x_2, \in D_{1,}\ and\ C \cap D = \phi_\sim$.

Good Extension Property

Theorem: Let an intuitionistic bitopological space is defined by the triple $(X, \tau_{1,} \tau_{2,})$ and an intuitionistic fuzzy bitopological space is defined by the triple (X, t_1, t_2). Then,

(a) $(X, \tau_{1,} \tau_{2,})$ is IB-T_2⇔$(X, t_{1,} t_{2,})$ is IFB-T_2(i)

(b) $(X, \tau_{1,} \tau_{2,})$ is IB-T_2⇒$(X, t_{1,} t_{2,})$ is IFB -T_2(ii)

(c) $(X, \tau_{1,} \tau_{2,})$ is IB-T_2⇒$(X, t_{1,} t_{2,})$ is IFB -T_2(iii) $(X, \tau_{1,} \tau_{2,})$ is IB-T_2⇒$(X, t_{1,} t_{2,})$ is IFB -T_2(iv).

Proof: (b) suppose that $(X, \tau_{1,} \tau_{2,})$ is an IB-T_2 Space. We prove that $(X, t_{1,} t_2)$ is IFB-T_2(ii). Given that (X, t_1, τ_2) is IB-T_2. So, for all $x_1,\ x_2 \in X,\ x_1 \neq x_2$ there exist $C = (C_{1,} C_2),\ D = (D_{1,} D_2) \in (\tau_1 \cup \tau_{2,})$ such that $x_1 \in C_{1,},\ x_2 \in D_{1,}\ and\ C \cap D = \phi_\sim$

$\Rightarrow 1_{C_1}(x_1) = 1; 1_{D_1}(x_2) = 1$ and $C \cap D = \phi_\sim$

$\Rightarrow 1_{C_1}(x_1) = 1,\quad 1_{C_2}(x_1) = 0;\quad 1_{D_1}(x_2) > 0,\ 1_{D_2}(x_2) = 0$ and $C \cap D = \phi_\sim$.

Let $1_{C_1} = \mu_M,\ 1_{C_2} = \vartheta_M,\ 1_{D_1} = \mu_N,\ 1_{D_2} = \vartheta_N$, then $\mu_M(x_1) = 1,\ \ \vartheta_M(x_1) = 0;\ \ \mu_N(x_2) > 0,\ \vartheta_N(x_2) = 0$ and $M \cap N = (0^\sim, \gamma^\sim)$ where $\gamma \in (0,1]$.

Since $\{(\mu_M, \vartheta_M), (\mu_N, \vartheta_N)\}\ \in (t_{1,} \cup t_2)$

$\Rightarrow (X, t_1, t_2)$ is IFB-T_2 (ii).

Hence, IB-T_2 ⇒ IFB-T_2(ii)

(c) Suppose, $(X, \tau_{1,} \tau_{2,})$ is an IB-T_2 Space. We must prove that $(X, t_{1,} t_2)$ is IFB- T_2(iii). Given that $(X, \tau_{1,} \tau_{2,})$ is IB-T_2 then for all $x_1, x_2 \in X,\ x_1 \neq x_2$ there exist $C = (C_{1,} C_2),\ D = (D_{1,} D_2) \in (\tau_1 \cup \tau_{2,})$ such that $x_1 \in C_{1,}, x_2 \in D_{1,}$ and $C \cap D = \phi_\sim$

$\Rightarrow 1_{C_1}(x_1) = 1; 1_{D_1}(x_2) = 1$ and $C \cap D = \phi_\sim$

$\Rightarrow 1_{C_1}(x_1) > 0,\quad 1_{C_2}(x_1) = 0;\quad 1_{D_1}(x_2) = 1,\ 1_{D_2}(x_2) = 0$ and $C \cap D = \phi_\sim$.

Let $1_{C_1} = \mu_M,\ 1_{C_2} = \vartheta_M,\ 1_{D_1} = \mu_N,\ 1_{D_2} = \vartheta_N$, then $\mu_M(x_1) > 0,\ \ \vartheta_M(x_1) = 0;\ \ \mu_N(x_2) = 1,\ \vartheta_N(x_2) = 0$ and $M \cap N = (0^\sim, \gamma^\sim)$ where $\gamma \in (0,1]$.

Since $\{(\mu_M, \vartheta_M), (\mu_N, \vartheta_N)\}\ \in (t_{1,} \cup t_2)$

$\Rightarrow (X, t_1, t_2)$ is IFB-T_2 (iii).

Hence, IB-T_2 ⇒ IFB-T_2(iii)

Similarly, we can show IB-T_2 ⇔ IFB-T_2(i) and IB-T_2⇒IFB -T_2(iv).

We give a counterexample following to show that none of the reverse implications exists.

Counterexample: For IFB-T_2(ii) ⇏ IB-T_2, let us assume that t_1 and t_2 are intuitionistic fuzzy topologies on X = $\{x_1, x_2\}$ generated by $M = \{x_1, 1,0\}$ and $N = \{x_2, 0.2,0\}$ respectively. They form the intuitionistic fuzzy bitopological space (X, t_1, t_2) on X defined by $\{M, N\}$. So, the IFBTS (X, t_1, t_2) is IFB-T_2(ii) but not IB-T_2.

For IFB-T_2(iii) ⇏ IB-$T_{2,}$ let us assume that t_1 and t_2 are intuitionistic fuzzy topologies on X =

$\{x_1,x_2\}$ generated by $M=\{x_1,0.2,0\}$ and $N=\{x_2,1,0\}$ respectively. They form the intuitionistic fuzzy bitopological space (X,t_1,t_2) on X defined by $\{M,\}$ N. So, the IFBTS (X,t_1,t_2) is IFB-T_2(iii) but not IB-T_2.

For IFB-T_2(iv) $\nRightarrow$ IB-$T_{2,}$ let us assume that t_1 and t_2 are intuitionistic fuzzy topologies on $X=\{x_1,x_2\}$ generated by $M=\{x_1,0.3,0\}$ and $N=\{x_2,0.2,0\}$ respectively. They form the intuitionistic fuzzy bitopological space (X,t_1,t_2) on X defined by $\{M,\}$ N. So, the IFBTS (X,t_1,t_2) is IFB-T_2(ii) but not IB-T_2.

Theorem: Let us consider that an intuitionistic bitopoloical space is defined by $(X,\tau_{1,}\tau_{2,})$ and an intuitionistic fuzzy bitopoloical space is defined by $(X,\mathrm{t}_{1,}\mathrm{t}_{2,})$. Then we consider the implications given below:

(a) IB-$T_2 \Rightarrow \alpha$-IFB-T_2(i)
(b) IB-$T_2 \Rightarrow \alpha$-IFB-T_2(ii)
(c) IB-$T_2 \Rightarrow \alpha$-IFB-T_2(iii)

Proof: (b) Suppose (X,t_1,τ_2) is an IB-T_2 Space. We shall prove that $(X,\mathrm{t}_{1,}\mathrm{t}_2)$ is α-IFB-T_2(ii). Since $(X,t_1,\tau_{2,})$ is IB-T_2, then for all $x_1,\ x_2\in X, x_1\neq x_2$ there exist $C=(C_{1,}\ C_2), D=(D_{1,}\ D_2)\in(\tau_1\cup\tau_{2,})$ such that $x_1\in C_1,\ x_2\in D_1$ and $C\cap D=\phi_{\sim}$

$\Rightarrow\ 1_{C_1}(x_1)=1; 1_{D_1}(x_2)=1$ and $C\cap D=\phi_{\sim}$

$\Rightarrow\ 1_{C_1}(x_1)=1; 1_{D_1}(x_2)\geq\alpha$ for any $\alpha\in(0,1)$ and $C\cap D=\phi_{\sim}$

$\Rightarrow 1_{C_1}(x_1)\geq\alpha,\quad 1_{C_2}(x_1)=0;\quad 1_{D_1}(x_2)\geq\alpha,\ 1_{D_2}(x_2)=0$ for any $\alpha\in(0,1)$ and $C\cap D=\phi_{\sim}$.

Let $1_{C_1}=\mu_M,\ 1_{C_2}=\vartheta_M,\ 1_{D_1}=\mu_N,\ 1_{D_2}=\vartheta_N$, then $\mu_M(x_1)\geq\alpha, \vartheta_M(x_1)=0; \mu_N(x_2)\geq\alpha,\ \vartheta_N(x_2)=0$ for any $\alpha\in(0,1)$ and $M\cap N=(0^{\sim},\gamma^{\sim})$ where $\gamma\in(0,1]$.

Since $\{(\mu_M,\vartheta_M),(\mu_N,\vartheta_N)\}\in(\mathrm{t}_{1,}\cup\mathrm{t}_2)$

$\Rightarrow (X,t_1,t_2)$ is α-IFB-T_2 (ii).

Hence, IB-$T_2 \Rightarrow \alpha$-IFB-T_2(ii).

Similarly, we can show that IB-$T_2 \Rightarrow \alpha$-IFB-T_2(ii) and IB-$T_2 \Rightarrow \alpha$-IFB-T_2(iii).

We give a counterexample following to show that none of the reverse implications exists.

Counterexample: For α-IFB-T_2(i)$\nRightarrow$IB-T_2, let us assume that t_1 and t_2 are intuitionistic fuzzy topologies defined on $X=\{x_1,x_2\}$ generated by $M=\{x_1,1,0\}$ and $N=\{x_2,0.4,0\}$ respectively and they form the intuitionistic fuzzy bitopological space (X,t_1,t_2) on X defined by $\{M,N\}$. For $\alpha=0.3$, we can say that the IFBTS (X,t_1,t_2) is α-IFB-T_2(i) but not IB-T_2.

For α-IFB-T_2(ii)$\nRightarrow$IB-T_2**,** let us assume that t_1 and t_2 are intuitionistic fuzzy topologies defined on $X=\{x_1,x_2\}$ generated by $M=\{x_1,0.4,0\}$ and $N=\{x_2,0.6,0\}$ respectively and they form the intuitionistic fuzzy bitopological space (X,t_1,t_2) on X defined by $\{M,N\}$. For $\alpha=0.4$, we can say that the IFBTS (X,t_1,t_2) is α-IFB-T_2(ii) but not IB-T_2.

For α-IFB-T_2(iii)$\nRightarrow$IB-$T_{2,}$ let us assume that t_1 and t_2 are intuitionistic fuzzy topologies defined on $X=\{x_1,x_2\}$ generated by $M=\{x_1,0.1,0\}$ and $N=\{x_2,0.7,0\}$ respectively and they form the intuitionistic fuzzy bitopological space (X,t_1,t_2) on X defined by $\{M,N\}$. For $\alpha=0.2$, we can say that the IFBTS (X,t_1,t_2) is α-IFB-T_2(iii) but not IB-T_2.

Theorem: Let us consider the two triples (X,t_1,t_2) and (Y,s_1,s_2) define two intuitionistic fuzzy bitopological spaces on X and Y respectively and $f\colon X\to Y$ be one- one, onto and continuous open mapping, then

(a) (X,t_1,t_2) is IFB-T_2(i) $\Leftrightarrow$ (Y,s_1,s_2) is IFB-T_2(i)
(b) (X,t_1,t_2) is IFB-T_2(ii) $\Leftrightarrow$ (Y,s_1,s_2) is IFB-T_2(ii)
(c) (X,t_1,t_2) is IFB-T_2(iii) $\Leftrightarrow$ (Y,s_1,s_2) is IFB-T_2(iii)
(d) (X,t_1,t_2) is IFB-T_2(iv) $\Leftrightarrow$ (Y,s_1,s_2) is IFB-T_2(iv)
(e) (X,t_1,t_2) is α-IFB-T_2(i) $\Leftrightarrow$ (Y,s_1,s_2) is α- IFB-T_2(i)
(f) (X,t_1,t_2) is α-IFB-T_2(ii) $\Leftrightarrow$ (Y,s_1,s_2) is α-IFB-T_2(ii)
(g) (X,t_1,t_2) is α-IFB-T_2(iii) $\Leftrightarrow$ (Y,s_1,s_2) is α-IFB-T_2(iii)

Proof: (a) Let (X, t_1, t_2), which defines an intuitionistic fuzzy topological space on X, be IFB-T_2(i). We shall prove that (Y, s_1, s_2), which defines the intuitionistic fuzzy bitopological space on Y, is also IFB-T_2(i).

Let $y_1, y_2 \in Y$, $y_1 \neq y_2$ and $Z = (\mu_Z, \vartheta_Z) \in (s_1 \cup s_2)$ such that $Z(y_1) \neq Z(y_2)$.

Since f is onto, there exists $x_1, x_2 \in X$ such that $x_1 = f^{-1}(y_2)$ and $x_2 = f^{-1}(y_2)$. Again, since $y_1 \neq y_2$, $f^{-1}(y_1) \neq f^{-1}(y_2)$ as f is one-one and onto.

Hence $x_1 \neq x_2$.

We have, $W = (\mu_W, \vartheta_W) \in (t_1 \cup t_2)$ such that $W = f^{-1}(Z)$ i.e., $(\mu_W, \vartheta_W) = (f^{-1}(\mu_Z), f^{-1}(\vartheta_Z))$ as f is Intuitionistic Fuzzy-continuous. Now,

$W(x_1) = \{\mu_W(x_1) = \left(f^{-1}(\mu_Z)\right)(x_1) = \mu_Z\left(f(x_1)\right) = \mu_Z(y_1), \vartheta_W(x_1) = (f^{-1}(\vartheta_Z))(x_1) = \vartheta_Z\left(f(x_1)\right) = \vartheta_Z(y_1)\}$ and $W(x_2) = \{\mu_W(x_2) = \left(f^{-1}(\mu_Z)\right)(x_2) = \mu_Z\left(f(x_2)\right) = \mu_Z(y_2), \vartheta_W(x_2) = (f^{-1}(\vartheta_Z))(x_2) = \vartheta_Z\left(f(x_2)\right) = \vartheta_Z(y_2)\}$.

Which implies that $W(x_1) \neq W(x_2)$ since $Z(y_1) \neq Z(y_2)$.

Therefore, since (X, t_1, t_2) is IFB-T_2(i), then there exist $M = (\mu_M, \vartheta_M), N = (\mu_N, \vartheta_N) \in (t_1 \cup t_2)$ such that $\mu_M(x_1) = 1$, $\vartheta_M(x_1) = 0$; $\mu_N(x_2) = 1$, $\vartheta_N(x_2) = 0$ and $M \cap N = 0_\sim$.

Let us put $A = f(M)$ and $B = f(N)$ where $A = (\mu_A, \vartheta_A), B = (\mu_B, \vartheta_B) \in (s_1 \cup s_2)$ as f is Intuitionistic Fuzzy-continuous. Now we can write,

$\{\mu_A(y_1) = \left(f(\mu_M)\right)(y_1) = \mu_M\left(f^{-1}(y_1)\right) = \mu_M(x_1) = 1, \vartheta_A(y_1) = \left(f(\vartheta_M)\right)(y_1) = \vartheta_M\left(f^{-1}(y_1)\right) = \vartheta_M(x_1) = 0\}$;$\{\mu_B(y_2) = \left(f(\mu_N)\right)(y_2) = \mu_N\left(f^{-1}(y_2)\right) = \mu_N(x_2) = 1, \vartheta_B(y_2) = \left(f(\vartheta_2)\right)(y_2) = \vartheta_N\left(f^{-1}(y_2)\right) = \vartheta_N(x_2) = 0\}$ and $A \cap B = 0_\sim$.

Hence $(A, B) \in (s_1 \cup s_2)$.

Therefore, (Y, s_1, s_2) is IFB-T_2(i).

Conversely, let the intuitionistic fuzzy topological space (Y, s_1, s_2) be IFB-T_2(i). Let $x_1, x_2 \in X$, $x_1 \neq x_2$ and $W = (\mu_W, \vartheta_W) \in (t_1 \cup t_2)$ such that $W(x_1) \neq W(x_2)$.

Since f is one-one, then there exist $y_1, y_2 \in (s_1 \cup, and\ y2s_2)$ such that $y_1 = f(x_1)$ and $y_2 = f(x_2)$ and $f(x_1) \neq f(x_2)$, i.e., $y_1 \neq y_2$.

We have, $Z = (\mu_Z, \vartheta_Z) \in (s_1 \cup s_2)$ such that $Z = (\mu_Z, \vartheta_Z) \in (s_1 \cup s_2)$ such that $Z = f(W)$, i.e., $(\mu_Z, \vartheta_Z) = \left(f(\mu_W, \vartheta_W)\right)$ as f is Intuitionistic Fuzzy-continuous. Now we write,

$Z(y_1) = \{\left(f(\mu_W)\right)(y_1) = \mu_W\left(f^{-1}(y_1)\right) = \mu_W(x_1), \left(f(\vartheta_W)\right)(y_1) = \vartheta_W\left(f^{-1}(y_1)\right) = \vartheta_W(x_1)\}$ and $\{Z(y_2) = \{\left(f(\mu_W)\right)(y_2) = \mu_W\left(f^{-1}(y_2)\right) = \mu_W(x_2), \left(f(\vartheta_W)\right)(y_2) = \vartheta_W\left(f^{-1}(y_2)\right) = \vartheta_W(x_2)\}$.

Therefore, $Z(y_1) \neq Z(y_2)$ since $W(x_1) \neq W(x_2)$.

Since (Y, s_1, s_2) is IFB-T_2(i), then there exist $A = (\mu_A, \vartheta_A), B = (\mu_B, \vartheta_B) \in (s_1 \cup s_2)$ such that $\mu_A(y_1) = 1$, $\vartheta_A(y_1) = 0$; $\mu_B(y_2) = 1$, $\vartheta_b(y_2) = 0$ and $A \cap B = 0_\sim$.

Now, let us put $M = f^{-1}(A)$ and $N = f^{-1}(B)$ where $M = (\mu_M, \vartheta_M), N = (\mu_N, \vartheta_N) \in (t_1 \cup t_2)$ as f is Intuitionistic Fuzzy-continuous. Now we write, $\{\left(f^{-1}(\mu_A)\right)(x_1) = \mu_A\left(f(x_1)\right) = \mu_A(y_1) = 1, (f^{-1}(\vartheta_A))(x_1) = \vartheta_A\left(f(x_1)\right) = \vartheta_A(y_1) = 0\}$;$\left(f^{-1}(\mu_B)\right)(x_2) = \mu_B\left(f(x_2)\right) = \mu_B(y_2) = 1, (f^{-1}(\vartheta_B))(x_2) = \vartheta_B\left(f(x_2)\right) = \vartheta_B(y_2) = 0\}$ and $M \cap N = 0_\sim$.

Hence $(M, N) \in (t_1 \cup t_2)$.

Therefore, (X, t_1, t_2) is IFB-T_2(i).

Hence)(X, t_1, t_2) is IFB-T_2(i) ⇔ (Y, s_1, s_2) is IFB-T_2(i).

Similarly, we can easily prove (b), (c), (d), (e), (f), and (g).

Conclusion

The main contribution of this paper is the establishment of some new concepts of intuitionistic fuzzy Hausdorff bitopological spaces. We discuss some of these concepts and show that the mappings, hereditary, and good extension properties hold among them. All of our results have the purpose of helping the researchers to establish an extensive framework for the expansion of intuitionistic fuzzy Hausdorff bitopology, which is currently being researched by others and will help advance this aspect of modern mathematics.

References

Ahmed E, Hossain S and Ali MM. On intuitionistic fuzzy T_2-Spaces. *IOSR J. Math.*, 2014; 10(6): 26-30.

Amin MR, Ali DM and Hossain MS. T_2 concepts in fuzzy bitopological spaces. *J. Math. Comput. Sci.*, 2014; 4(6): 1055-1063.

Atanassov K. Review and new results on intuitionistic fuzzy sets. *Int. J. Bioautomation,* 2016; 20(S1): S7-S16.

Atanassov KT and Stoeva S. Intuitionistic fuzzy sets. *Fuzzy sets Syst.*, 1986; 20(1): 87-96.

Bayhan S and Coker D. On fuzzy separation axioms in intuitionistic fuzzy topological spaces. *BUSEFAL*, 1996; 67: 77-87.

Bayhan S and Çoker D. On separation axioms in intuitionistic topological spaces. *Int. J. Math. Math. Sci.*, 2001; 27: 621-630.

Bayhan S and Coker D. On T_1 and T_2 separation axioms in intuitionistic fuzzy topological spaces. *J. Fuzzy Math.*, 2003; 11(3): 581-592.

Chang CL. Fuzzy topological spaces. *J. Math. Analy. Appli.*, 1968; 24(1): 182-190.

Coker D. A note on intuitionistic sets and intuitionistic points. *Turkish J. Math.*, 1996a; 20(3): 343-351.

Coker D. An introduction to fuzzy subspaces in intuitionistic fuzzy topological spaces. *J. Fuzzy Math.*, 1996b; 4: 749-764.

Çoker D. An introduction to intuitionistic fuzzy topological spaces. *Fuzzy sets. syste.*, 1997; 88(1): 81-89.

Coker D. An introduction to intuitionistic topological spaces. *BUSEFAL*, 2000; 81: 51-56.

Coker D and Demirci M. On intuitionistic fuzzy points. *Notes I.F.S.*, 1995; 1(2): 79-84.

Coker D and Haydar Es A. On fuzzy compactness in intuitionistic fuzzy topological spaces. *J. Fuzzy Math.*, 1995; 3: 899-910.

Kandil A and El-Shafee ME. Biproximities and fuzzy bitopological spaces. *Simon Stevin*, 1989; 63(1): 45-66.

Kelly J. *Bitopological spaces*. Proceedings of the London Mathematical Society, 1963; 13: 71-89.

Miah SS, Amin MR and Jahan M. Mappings fuzzy T_0 topological spaces in quasi-coincidence sense. *J. Math. Comput. Sci.*, 2017; 7(5): 883-894.

Miah SS, Amin MR and Rana S., Fuzzy normal topological spaces in quasi-coincidence sense, *J. Bangladesh Acad. Sci*., 2018; 42(2): 201-205.

Miah SS and Amin MR. Mappings in fuzzy Hausdorff spaces in quasi-coincidence sense. *J. Bangladesh Acad. Sci.* 2017; 41(1): 47-56.

Nouh AA. On separation axioms in fuzzy bitopological spaces. *Fuzzy sets syst.*, 1996; 80(2): 225-236.

Sufiya AS A, Fora AA and Warner MW. Fuzzy separation axioms and fuzzy continuity in fuzzy bitopological spaces. *Fuzzy sets syst.*, 1994; 62(3): 367-373.

Zadeh LA. Fuzzy sets. Information and control. 1965; 8(3): 338-353.

J. Bangladesh Acad. Sci. 48(1); 61-74: June 2024 DOI:https://doi.org/10.3329/jbas.v48i1.69379

Journal of Bangladesh Academy of Sciences

Journal homepage: http://www.bas.org.bd/publications/jbas.html

Research Article

Bacterial profiles and multi-drug resistance patterns in bacterial isolates associated with freshwater fish infections

Mohammad Zakerin Abedin*, Laila Jarin[1], Md. Easin Arfat[2], Md. Sadiqur Rahman[3]
and Rasheda Yasmin Shilpi[1]

Department of Microbiology, School of Biomedical Sciences, Khwaja Yunus Ali University, Sirajganj, Bangladesh

ARTICLE INFO

Article History

Received: 15 October 2023
Revised: 24 December 2023
Accepted: 10 January 2024

Keywords: Antimicrobial resistance patterns, Fish pathogens, Indigenous freshwater fishes, Multi-drugs resistance (MDR).

ABSTRACT

Fish and fish products can support 40% of world diets, which meets 60% of the animal protein requisites in Bangladesh. Infections of fishes, along with the continuously elevated emergence of microbial resistance, are the major drawbacks to the massive milestone forward. This investigation aimed to reveal the antimicrobial resistance patterns of the pathogens associated with diverse fish infections. According to Bergey's manual of bacteriological classification, isolated pathogens were provisionally identified at genera levels based on their cultural, morphological, and biochemical characteristics. The Kirby-Bauer (Cockerill and CLSI, 2013) disc diffusion method was exploited to determine the antimicrobial resistance. Pathogenic growths were found in 150 (83.34%) out of 180 samples by *Aeromonas* spp. (39.33%), *Vibrio* spp. (16.67%), *Flavobacter* spp. (14.67%), *Edwardsiell* spp (12.67%), *Pseudomonas* spp. (9.33%), *Streptococcus* spp. (5.55%), and *Citrobacter* spp. (2%) in Shing (*Heteropneustes* spp.), Pangus (*Pangasius* spp.), Pabda (*Ompok* spp.), Gulsha (*Mystus cavasius*), Tilapia (*Oreochromis niloticus*), Koi (*Cyprinus* spp.), Magur (*Clarias batrachus*), and Tengra (*Mystus tengara*). Pathogens showed resistance against Amoxicillin (136/150; 90.67%), Chlortetracycline (135/150; 90%), and Erythromycin (134/150; 89.33%), whereas Levofloxacin (138/150; 92%), Ciprofloxacin (123/150; 82%), Neomycin (120/150; 80%), and Colistin (117/150; 78%), exhibited potential effectiveness. A huge frequency of 60% (90 out of 150) of pathogens exhibited as high as 21 antimicrobial resistance patterns towards a minimum of 4 antibiotics and a maximum of 8 antibiotics, whereas *Aeromonas spp.* isolates were the most prominent. The investigation would provide substantial guidance to veterinarians and animal husbandmen involved in fish cultivation to design therapeutics against infections. Regular and vigorous investigation and implementation of the acquired knowledge would be the only possible solution to halt the rapid increase of antimicrobial resistance.

Introduction

The increasing population of today's world demands significantly augmented production of diverse food substances to satisfy nutritional requirements. Fisheries and aquaculture are major contributors to the nutritional requisites providing animal protein with a substantial frequency of 20% of the human diet covering the world's 40% with a remarkable increase in global fish production to 156.4 million tonnes in 2018 from 21.8 million tonnes in 1960, 69% of which has been provided by Asian countries

---

*Corresponding author:<zakerin.abedin.mb.@kyau.edu.bd>

[1] *Dept. of Botany, Microbiology Laboratory, Jahangirnagar University, Savar, Dhaka, Bangladesh;*
[2] *Dept. of Microbiology, University of Chittagong, Chittagong, Bangladesh*
[3] *Dept. of Microbiology, Aqua Laboratory Quality Feeds Limited, Mymensingh, Bangladesh*

(FAO, 2020). Countries of the Indian subcontinent, such as Bangladesh, India, Nepal, and Pakistan, comprise a major contributing group in this aquaculture production industry, significantly increasing yearly (Nayak, 2020).

Bangladesh, a realm of diversified wetlands of various open water bodies, facilitates in attaining an irrevocable resource of fisheries production to accomplish 60% of the animal protein requirement of her vast population's diet, attaining fifth position in overall aquatic production and ranking third in freshwater fisheries production in inland areas all over the world (DoF, 2018; FAO, 2020). Bangladesh is home to 265 freshwater indigenous fish species under 55 families and 154 genera inhabiting various rivers, canals, haors, baods, beels, lakes, ponds, and floodplains, which corroborates the ancient proverb '*Mache Vate Bangali*,' meaning 'fish and rice make a Bengali', delivered after the fish and rice dominance and irreplaceability in their regular daily diets (Rahman, 2005). The most common indigenous freshwater fishes include Shing (*H. fossilis*), Pangus (*Pangasius* spp.), Shol (*Channa striata*), Pabda (*Ompok* spp.), Gulsha (*Mystus cavasius*), Tilapia (*O. niloticus*), Koi (*Cyprinus* spp.), Magur (*C. batrachus*), Tengra (*M. tengara*) and so on, which is considered as one of the most inexpensive sources of protein production (Pandit *et al.*, 2021).

However, this three-penny protein production has encountered considerable drawbacks in infections by diverse pathogens. *Aeromonas spp., Edwardsiella spp., Flavobacterium spp., Pseudomonas* spp., *Streptococcus spp., Vibrio* spp., *Yersinia ruckeri,* etc. are the most frequent bacterial fish pathogens (Miller and Harbottle, 2018). To control those pathogens, various chemotherapeutics are involved by applying antimicrobial agents to fish species' habitats and food supplements. Unapparent application of such antimicrobials with little or no expertise in selecting antibiotics and determining dose concentrations by veterinarians is enumerated as an affair of egregious perturbation, as it might potentially lead to the attainment of antimicrobial resistance by the pathogens, resulting in further therapeutic failure of certain antibiotics. Genetic exchange of those fish pathogens with terrestrial pathogens might support the potential transfer of determinants of resistance to human and animal pathogens, resulting in antimicrobial resistance (AMR) strains, which might also be facilitated by the antimicrobial leaching into the surroundings from the cultivated area, providing enormously diluted agents to the zoonotic and animal pathogens, resulting in the development of antimicrobial resistance (AMR).

Taking the concerns of infections and therapeutic measures of indigenous fish species into account, this current project was designed in particular to perform thorough research to unearth the frequent pathogens causing abnormalities in cultivated local fish species by isolating and identifying the etiological agents, and to determine the reliable responsiveness patterns of those pathogens against commonly applied antimicrobials as therapeutics for selecting substantially effective antibiotics against the pathogens meticulously.

Materials and Methods

Sampling and transport

A total of 180 infected randomly selected fishes of different species, including 83 Shing (*H. fossilis*), 33 Pangus (*Pangasius* spp.), 18 Pabda (*Ompok* spp.), 17 Gulsha (*M. cavasius*), 16 Tilapia (*O. niloticus*), 5 Koi (*Cyprinus* spp.), 5 Magur (*C. batrachus*), and 3 Tengra (*M. tengara),* with diverse infections, were collected along with water samples from different cultivated areas (Figure 1). All the precautions were maintained during the collection of both water and fish samples. The specimens were preserved within an ice box to provide a cool chain and transported to the Quality Aqua Laboratory, Quality Feeds Limited, Mymensingh, for further exploration of the samples.

(a) Pangus (*Pangasius* spp.)

(b) Shing (*H. fossilis*)

(c) Koi (*Cyprinus* spp.)

(d) Pabda (*Ompok* spp.)

Fig. 1. Deep ulcerative lesions in different indigenous freshwater fishes (a) Pangus at the top left, (b) Shing at the top right, (c) Koi at the bottom left, and (d) Pabda at the bottom right.

Processing, enrichment, and isolation of bacteria

The solid specimens, i.e., infected fishes, potentially needed to be processed and made suitable for the enrichment culture method. Three different parts of the sampled fish species, such as skin, gill, and intestine, were separated and collected aseptically to avoid potential contamination. Those specimens were placed on a sterile, clean chopping board to mince and grind together. After mincing and grinding, 10 gm of the processed samples were added and mixed homogeneously with 90 ml of freshly prepared 0.1% (w/v) peptone water. The homogeneous mixture samples were exploited for further investigation of isolating bacterial pathogens by inoculating 0.1 ml of those blend compositions onto various selective and non-selective media, including Rimler Shotts Medium Base Agar (selective for *Aeromonas spp.*), Thiosulfate Citrate Bile Salt Sucrose (TCBS) Agar (selective for *Vibrio* spp.), *Pseudomonas* Base Agar (selective for *Pseudomonas* spp.), Tryptic Soy Agar (TSA) (for enrichment of bacterial isolates), Brain Heart Infusion (BHI) Agar (for fastidious organisms), Blood Agar, and MacConkey Agar following standard microbiological technique and procedure, and finally incubated for 24 h at 37°C.

Identification of bacterial isolates

Cultural, morphological, and biochemical characteristics of the isolated pathogens were taken into account to detect and identify the species of the pathogens. Colony characteristics, including color, size, shape, texture, and surface appearance on culture media, namely chromogenic agar, MacConkey agar, TCBS agar, SS agar, and Manitol salt agar, were recorded to use further for identification. Bacterial pathogens isolated from selective and non-selective media were exploited for microscopic study to determine cellular shapes and arrangements. The bacterial isolates were differentiated into gram-positives and gram-negatives via a staining technique. Biochemical tests including acid-alkaline reaction, hydrogen sulfide (H_2S) production test, TSI (Triple Sugar Iron) test, MIU (motility, indole, urease) test, gas production test, catalase test, oxidase test, Simmons citrate test, MR (Methyl Red)-VP (Voges-Proskauer) test were performed to determine the biochemical characteristics of the isolated pathogens. Combining all the cultural, morphological, and biochemical characteristics, the genus of the pathogens was identified according to Bergey's manual of bacteriological classification (Chauhan and Jindal, 2020).

Determination of antimicrobial resistance patterns

The disc diffusion method by Kirby-Bauer (Cockerill and CLSI, 2013) was exploited to determine the antimicrobial resistance patterns of the fish pathogen isolates against Amoxicillin (10 µg), Erythromycin (15 µg), Enrofloxacin (5 µg), Chlortetracycline (30 µg), Ciprofloxacin (5 µg), Neomycin (30 µg), Colistin (25 µg), Cotrimoxazole (25 µg), Levofloxacin (5 µg), Doxycycline (30 µg). Bacterial cultures were homogeneously mixed with phosphate buffer saline (PBS) to obtain a bacterial suspension, and the suspensions were adjusted to 0.5 MacFarland's turbidity standard. Following the standard microbiological method, the suspensions of bacterial cultures were inoculated by streaking with sterile cotton swab steak, and the plates were supplied with various antibiotic discs. The disc-containing plates were subjected to a 40°C temperature for 1 hour to facilitate proper diffusion of antimicrobials, followed by a 24-hour incubation period at 37°C. The overnight culture plates were investigated to observe and measure the diameter of the clear zone of inhibition by the antibiotics, and the antimicrobials were interpreted as resistant, sensitive, and intermediate in their activity against all bacterial isolates. For quality control of bacterial culture studies and antimicrobial sensitivity testing, standard cultures of *Aeromonas hydrophila* (ATCC 7966), *Flavobacterium columnare* (ATCC 23463), *Pseudomonas aeruginosa* (ATCC 27853), *Staphylococcus aureus* (ATCC 25923), and *Vibrio cholerae* (ATCC 14035) were exploited throughout the study.

Result

A total of 180 infected fish of different species were collected as specimens. In this study, 6 (3.33%) of the samples were found to be growth negative, while 174 (96.67%) were found to be growth positive, including 150 (83.34%) pathogenic growths and 24 (13.33%) normal florae (Fig. 2).

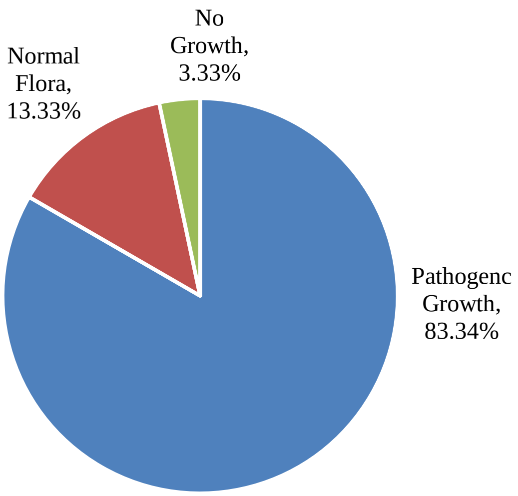

Fig. 2. Bacterial growth pattern of collected specimens.

Diverse species of fish with deleterious infections were randomly sampled for the study. Among the wide range of fish species available in the sampling area, Shing (*H. fossilis*) was vindicated to be widely susceptible to pernicious infections with an exceedingly elevated frequency of 46.1% (83 infected species), followed respectively by Pangus (*Pangasius* spp.) with 18.33% (33), Pabda (*Ompok* spp.) with 10% (18), Gulsha (*M. cavasius*) with 9.44% (17), Tilapia (*O. niloticus*) including 8.89% (16), Koi (*Cyprinus* spp.) and Magur (*C. batrachus*) both sharing a harmonious frequency of 2.78% (5), and Tengra (*M. tengara*) accommodating 1.67% (3) infections (Fig. 3**).**

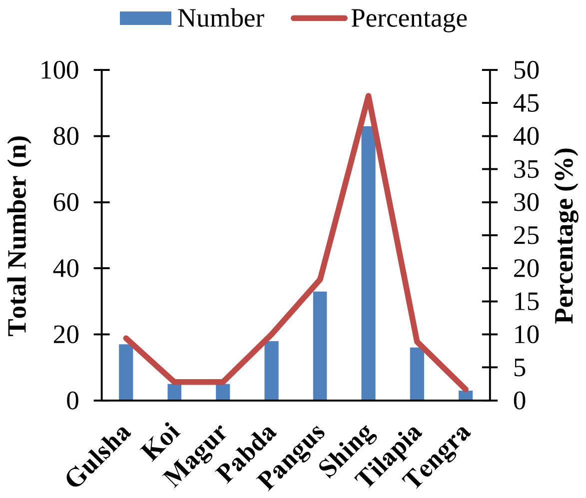

Fig. 3. Frequency of infected fish species.

All the multiplex fish species had remarkably pathogenic microbial communities. *Aeromonas spp.* was unearthed as the most frequent pathogen to infect the fish with a considerably high frequency of 39.33% (59 infections), sequentially followed by *Vibrio* spp., *Flavobacterium spp.*, *Edwardsiella spp.*, *Pseudomonas spp.*, *Streptococcus* spp., and *Citrobacter spp.*, inhabiting 16.67% (25), 14.67% (22), 12.67% (19), 9.33% (14), 5.33% (8), and 2% (3) of the pathogen contaminated fishes respectively **(**Fig. 4**).**

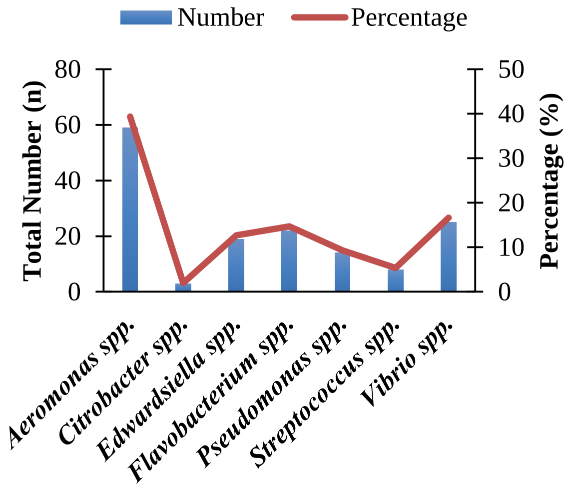

Fig. 4. Frequency of the pathogens contaminating the fish species.

Further exploration of the host-pathogen relation ships in our current investigation revealed a convincing specificity of host contamination by the pathogens. *According to the statistics, Aeromonas spp.*, the most prevalent etiological agent infecting 59 fish species, exhibited the highest frequency of 76.27% (45 infections) of poisoning Shing (*H. fossilis*), whereas its proclivity to pollute other fishes was significantly subordinate with a steeply low frequency of 11.86% (7 infections) in Pangus (*Pangasius* spp.), sequentially succeeded by Tilapia (*O. niloticus*), Pabda (*Ompok* spp.), Gulsha (*M. cavasius*), and Magur (*C. batrachus*) covering a recurrence of 5.08% (3), 3.39% (2), and 1.69% (1), respectively. Moreover, the extremely common pathogen *Aeromonas spp.* caused no harm to Koi (*Cyprinus* spp.) or Tengra (*M. tengara*). *Vibrio* spp., second in the catalog of etiological agents contaminating 25 fish species, manifested its towering infectivity towards Gulsha and Pabda with a parallel incidence of 36%(9 infections). Furthermore, *Flavobacterium spp.* colonized 22 fish species to develop diseases, among which Pangus was supremely infected by the pathogen with an occurrence consistency of 45.45% (10 infections). Nineteen infections of *Edwardsiella spp.* were recorded to populate the Pangus with an excellent frequency of 73.68% (14 infections).

Shing was the most susceptible to *Pseudomonas spp.*, exhibiting a high prevalence of 64.29% (9 infections out of 14). Only 8 *Streptococcus* spp. were isolated from infected pond-cultivated fishes, displaying the highest infection rate against Tilapia, with a frequency of 62.5% (5 infections). *In our current findings*, *Citrobacter spp.* was the least prevalent pathogen of pond-cultivated fish infections (3 infections). The pathogen was manifested to disease Gulsha and Pabda, obtaining a frequency of 66.67% (2 infections) and 33.33% (1 infection). In contrast, no pathogen contamination was observed against Koi, Magur, Shing, Pangus, Tengra, and Tilapia **(**Fig. 5, Table 1**).**

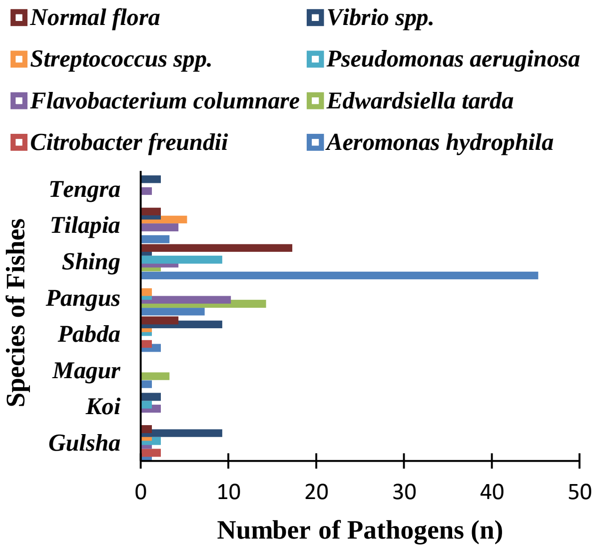

Fig. 5. Allocation of pathogens among diverse fish species

Table 1. Distribution of pathogens among infected fishes.

Pathogens	Total infections (%)	Infected fishes (150 out of 180)	Frequency (%)
Aeromonas spp.	59 (33.91)	Shing (*Heteropneustes fossilis*)	45 (76.27)
		Pangus (*Pangasius* spp.)	7 (11.86)
		Tilapia (*Oreochromis niloticus*)	3 (5.09)
		Pabda (*Ompok* spp.)	2 (3.40)
		Gulsha (*Mystus cavasius*)	1 (1.69)
		Magur (*Clarias batrachus*)	1 (1.69)
Vibrio spp.	25 (14.37)	Gulsha (*Mystus cavasius*)	9 (36.00)
		Pabda (*Ompok* spp.)	9 (36.00)
		Koi (*Cyprinus* spp.)	2 (8.00)
		Tilapia (*Oreochromi sniloticus*)	2 (8.00)
		Tengra (*Mystus tengara*)	2 (8.00)
		Shing (*Heteropneustes fossilis*)	1 (4.00)
Flavobacterium spp.	22 (12.64)	Pangus (*Pangasius* spp.)	10 (45.45)
		Shing (*Heteropneustes fossilis*)	4 (18.18)
		Tilapia (*Oreochromis niloticus*)	4 (18.18)
		Koi (*Cyprinus* spp.)	2 (9.09)
		Gulsha (*Mystus cavasius*)	1 (4.55)
		Tengra (*Mystus tengara*)	1 (4.55)
Edwardsiella spp.	19 (10.92)	Pangus (*Pangasius* spp.)	14 (73.68)
		Magur (*Clarias batrachus*)	3 (15.79)
		Shing (*Heteropneustes fossilis*)	2 (10.53)
Pseudomonas spp.	14 (8.05)	Shing (*Heteropneustes fossilis*)	9 (64.29)
		Gulsha (*Mystus cavasius*)	2 (14.29)
		Koi (*Cyprinus* spp.)	1 (7.14)
		Pabda (*Ompok* spp.)	1 (7.14)
		Pangus (*Pangasius* spp.)	1 (7.14)
Streptococcus spp.	8 (4.6)	Tilapia (*Oreochromis niloticus*)	5 (62.50)
		Gulsha (*Mystus cavasius*)	1 (12.50)
		Pabda (*Ompok* spp.)	1 (12.50)
		Pangus (*Pangasius* spp.)	1 (12.50)
Citrobacter spp.	3 (1.72)	Gulsha (*Mystus cavasius*)	2 (66.67)
		Pabda (*Ompok* spp.)	1 (33.33)
Normal flora	24 (13.79)	Shing (*Heteropneustes fossilis*)	17 (70.83)
		Pabda (*Ompok* spp.)	4 (16.67)
		Tilapia (*Oreochromis niloticus*)	2 (8.33)
		Gulsha (*Mystus cavasius*)	1 (4.17)

Amoxicillin, Chlortetracycline, Ciprofloxacin, Colistin, Cotrimoxazole, Doxycycline, Enrofloxacin, Erythromycin, Levofloxacin, and Neomycin were used for antibiotic responsiveness testing. Aeromonas *spp.* exhibited the peaked resistance against Amoxicillin(96.61%), sequentially succeeded by Chlortetracycline (91.53%), Erythromycin (91.53%), Cotrimoxazole (62.71%) (Fig. 6).

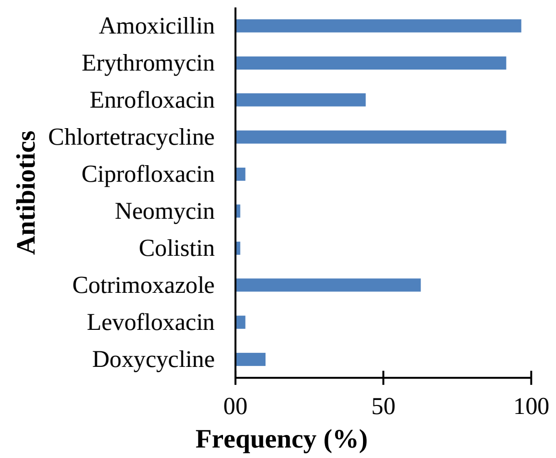

Fig. 6. Antibiotic resistance pattern of *Aeromonas* spp.

Vibrio spp. possessed resistance against Erythromycin (88%), Amoxicillin (80%), Chlortetracycline (72%), and Cotrimoxazole (56%), whereas no resistance was developed against Ciprofloxacin, Colistin, Levofloxacin, or Neomycin (Fig. 7).

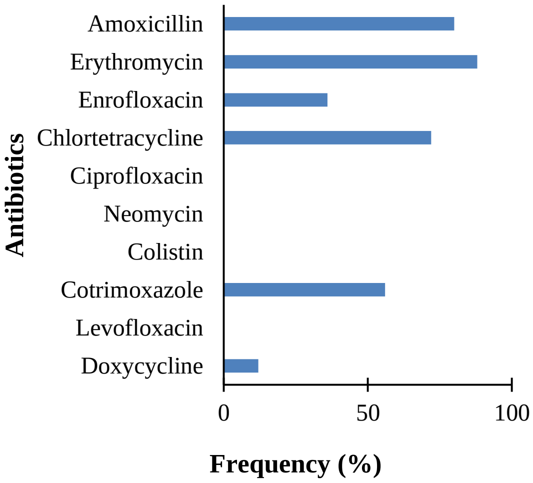

Fig. 7. Antibiotic resistance pattern of *Vibrio*

Flavobacterium spp. was discovered to be resistant to Chlortetracycline (90.91%), Erythromycin (90.91%), Amoxicillin (72.73%), and Cotrimoxazole (54.55%), but not to Colistin, Doxycycline, Levofloxacin, or Neomycin. Doxycycline and Levofloxacin exhibited a uniform effectiveness of 95.45% against *Flavobacterium spp*. **(**Fig. 8**)**.

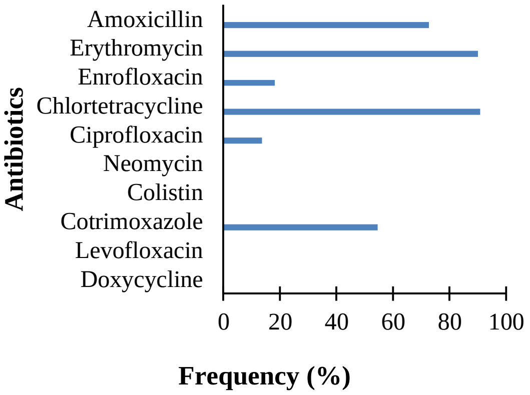

Fig. 8. Antibiotic resistance pattern of *Flavobacterium* spp.

Edwardsiella spp. exhibited supreme resistance to Amoxicillin (100%) and Chlortetracycline (100%), followed sequentially by Erythromycin (94.74%) and Cotrimoxazole (57.89%), whereas no resistance was recorded against Ciprofloxacin, Doxycycline, Levofloxacin, and Neomycin (Fig. 9).

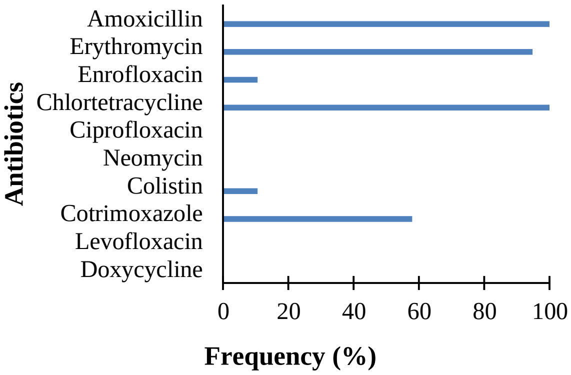

Fig. 9. Antibiotic resistance pattern of *Edwardsiella* spp.

During the treatment of *Pseudomonas spp.* infections, there was a massive resistance to Chlortetracycline (100%), Amoxicillin (92.86%), and Erythromycin (78.57%), but no resistance to

Ciprofloxacin, Colistin, Doxycycline, or Levofloxacin was observed. *Pseudomonas spp.* exhibited considerable susceptibility against Ciprofloxacin (100%), Levofloxacin (100%), Doxycycline (85.71%), Colistin (64.29%), and Neomycin (57.14%) (Fig.10).

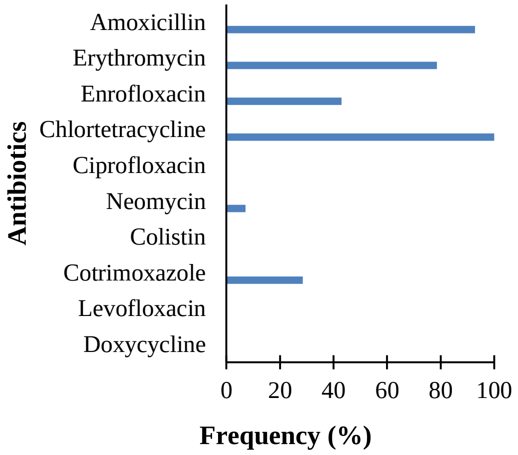

Fig. 10. Antibiotic resistance pattern of *Pseudomonas* spp.

Streptococcus spp. was recorded to have resistance to Amoxicillin (100%), Chlortetracycline (100%), Cotrimoxazole (75%), and Erythromycin (75%), whereas no resistance was displayed against Colistin and Neomycin **(**Fig. 11).

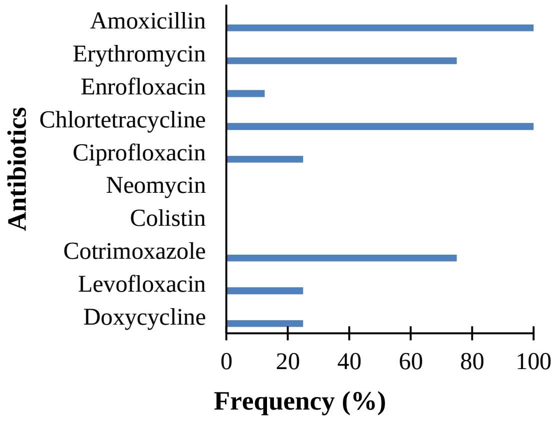

Fig. 11. Antibiotic resistance pattern of *Streptococcus* spp.

The least prevalent pathogen isolated in our study, *Citrobacter* spp., exhibited resistance against Amoxicillin (100%), Erythromycin (100%), Chlortetracycline (66.67%), and Cotrimoxazole (66.67%), whereas no resistance was found against Ciprofloxacin, Colistin, Doxycycline, Levofloxacin, and Neomycin. On the other hand, supreme effectiveness (100%) was possessed against the pathogen by Ciprofloxacin, Colistin, and Levofloxacin separately **(**Fig. 12**)**.

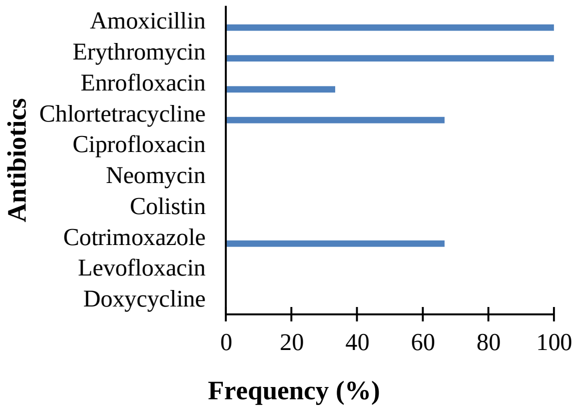

Fig. 12. Antibiotic resistance pattern of *Citrobacter* spp.

The entire pathogen communities were recorded to show resistance mostly to Amoxicillin (90.67%), Chlortetracycline (90%), Erythromycin (89.33%), and Cotrimoxazole (57.33%)**.** On the contrary, the effectiveness of the antibiotics was led by Levofloxacin (92%), subsequently succeeded by Ciprofloxacin (82%), Neomycin (80%), Colistin (78%), and Doxycycline (65.34%) **(**Fig. 13**)**.

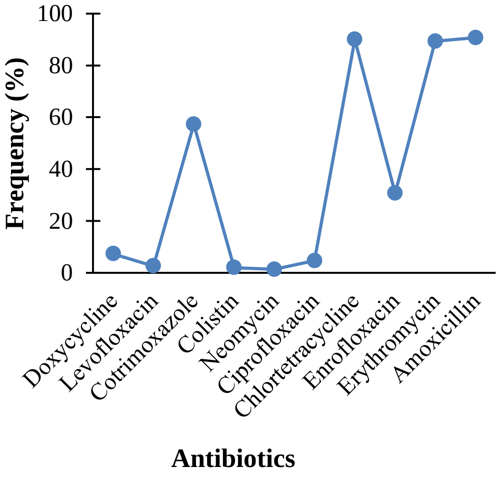

Fig. 13. Overall antibiotic resistance pattern of fish pathogens.

The antimicrobial resistance patterns exhibited by the pathogens isolated from various fish infections were enormously diverse. Patterns of resistance to single, double, triple, and up to eight different antibiotics were observed. Twenty-one types of patterns of resistance were established, taking a limit of a minimum of 4 antibiotics into account, where a single isolate of *Aeromonas spp. was* found resistant to 8 antibiotics (AMX-CIP-COT-CT-DO-ERY-LEV) and another isolate of the same species evolved resistance mechanisms to 7 antibiotics (AMX-CIP-COT-CT-ENR-ERY-LEV). Fourteen isolates of *Aeromonas spp.* were uncovered to be resistant to AMX-COT-CT-ENR-ERY (5 antibiotics), and 12 isolates of the same species were found to be resistant to AMX-COT-CT-ERY (4 antibiotics), which was undoubtedly imitated by ten isolates of *Edwardsiella spp.* Moreover, a total of 90 out of 150 pathogenic isolates (60%) shared those 21 types of resistance patterns towards a minimum of 4 different antimicrobial agents (Table 2).

Discussion

Fish are major contributors to the production of required animal protein worldwide. Freshwater fish culture facilitates the enormous growth and supply of animal protein through vast fish production. One of the most serious drawbacks of that process is the frequent infection of freshwater fish species. Our current project uncovered 83.33% (150 fish samples) of fish out of 180 randomly selected fish species with visible physical impurities being infected by diverse types of pathogens, which would be substantial evidence of the significance of that drawback. The study by Abedin et al. (2021a) also exhibited a higher frequency of 92.16% of fish infections by pathogenic bacteria. Another study on wild, small freshwater fish stated 66.2% of positive cases of infections (Labony et al., 2020). 70% of 500 samples of Nile Tilapia fish were found to be infected by *Aeromonas* spp. (Saleh et al., 2021).

A total of 180 infected fish species were randomly sampled as hosts of diverse pathogens where Shing, Pangus, Pabda, Gulsha, Tilapia, Koi, Magur, and Tengra were found to be contaminated by disease signs with a respective frequency of 46.1%, 18.33%, 10%, 9.44%, 8.89%, 2.78%, 2.78%, 1.67%. A similar pattern of infected fish host sequence in the context of prevalence was observed by Abedin *et al.* (2020a), who exhibited the Shing as the most frequently poisoned fish species, followed by Pangus and Pabda with a respective frequency of 56.9%, 14.7%, and 7.3%. Thai Koi, Shol, Magur, Tilapia, and Tengara fish were also found to be infected in that investigation.

Aeromonas spp., Vibrio spp., Flavobacterium spp., Edwardsiella spp., Pseudomonas spp., Streptococcus spp., and Citrobacter spp. were identified as etiological agents that contaminated and infected fish at rates of 39.33% (59 infections), 16.67%(25), 14.67%(22), 12.67%(19), 9.33%(14), 5.33%(8), and 2%(3), respectively. Among 36(42.9%) *Aeromonas spp.*, 15(17.9%) *Pseudomonas* spp., 7(8.3%) *Vibrio* spp., 9(10.7%) *Staphylococcus* spp., 7(8.3%) *Flavobacterium* spp., 7(8.3%) *Edwardsiella* spp., and 3(3.6%) *Citobacter* spp. and *Enterobacter* spp. were documented as fish pathogens by Abedin et al. (2020a), which is closely related to our investigation with *Aeromonas* spp. as the most frequent source of impurities in fish species. Another study by Saleh *et al.* (2021) displayed 53.4% (187 out of 350 positive growths) *Aeromonas spp.* infections, which elucidates the towering prevalence of *Aeromonas spp.* infections in fish. Miller and Harbottle (2018) described *Aeromonas spp.*, *Edwardsiella spp.*, *F. branchiophilum*, *Mycobacterium* spp., and *Pseudomonas* spp., *as* the most typical and most frequent bacterial fish pathogens, which showed significant resemblance to our analyzed pathogens. Austin and Austin (2012) and Pridgeon and Klesius (2012) stated the pathogenicity of *Aeromonas spp.*, *Edwardsiella spp.*, *Flavobacterium spp.*, *Francisella spp.*, *Photobacterium spp.*, *Piscirickettsia*, *Pseudomonas*, *Vibrio*, *Yersinia*, *Lactococcus*, and *Streptococcus* towards fish species in distinct studies. Unlike ours, *M. marinum* was described as a well-known pathogen of fish skin and soft tissue infection by Aubry et al. (2017). *Aeromonas spp.*, *Edwardsiella spp.*, *Enterobacter cloacae, and Acinetobacter junii* exhibited pathogenicity towards Koi. Goldfish were revealed to be infected by pathogenic bacterial isolates, including *Klebsiella aerogenes, Enterobacter cancerogenus, Citrobacter freundii, Edwardsiella tarda, and Acinetobacter nosocomial's*, which corroborate our current research in the context of pathogens with a high percentage of resemblance (Preena et al., 2019).

Table 2. Multi-antibiotic resistance (MAR) patterns of pathogenic isolates exhibit tolerance to at least four antibiotics.

Pattern Type	Antibiotic (Minimum 4) Resistance Pattern	Pathogens	No of Isolates
I	AMX-CL-CT-ERY	*Edwardsiella spp.*	1
II	AMX-COT-CT-ENR	*Aeromonas spp.*	1
III	AMX-COT-CT-ERY	*Aeromonas spp.*	12
		Edwardsiella spp.	10
		Flavobacterium spp.	6
		Vibrio spp.	5
		Pseudomonas spp.	4
		Streptococcus spp.	3
		Citrobacter spp.	1
IV	AMX-COT-ENR-ERY	*Vibrio spp.*	3
V	AMX-CT-ENR-ERY	*Pseudomonas spp.*	2
		Vibrio spp.	2
		Aeromonas spp.	2
		Citrobacter spp.	1
		Edwardsiella spp.	1
VI	AMX-CT-ERY-NEO	*Pseudomonas spp.*	1
VII	COT-CIP-CT-ERY	*Flavobacterium spp.*	1
VIII	COT-CT-ENR-ERY	*Aeromonas spp.*	1
IX	COT-DO-ENR-ERY	*Vibrio spp.*	1
X	AMX-COT-CT-ENR-ERY	*Aeromonas spp.*	14
		Streptococcus spp.	1
		Vibrio spp.	1
XI	AMX-COT-CT-DO-ENR	*Vibrio spp.*	1
XII	AMX-CIP-COT-CT-ERY	*Flavobacterium spp.*	2
XIII	AMX-CIP-CT-DO-LEV	*Streptococcus spp.*	1
XIV	AMX-COT-CT-DO-ERY	*Aeromonas spp.*	2
XV	AMX-CL-CT-ENR-ERY	*Aeromonas spp.*	1
		Edwardsiella spp.	1
XVI	AMX-CT-DO-ENR-ERY	*Aeromonas spp.*	2
XVII	AMX-CIP-COT-CT-DO-LEV	*Streptococcus spp.*	1
XVIII	AMX-COT-CT-DO-ENR-ERY	*Aeromonas spp.*	1
		Vibrio spp.	1
XIX	AMX-COT-CT-ENR-ERY-NEO	*Aeromonas spp.*	1
XX	AMX-CIP-COT-CT-ENR-ERY-LEV	*Aeromonas spp.*	1
XXI	AMX-CIP-COT-CT-DO-ENR-ERY-LEV	*Aeromonas spp.*	1
		Total isolates	**90 (60%)**

Note: AMX = Amoxicillin; CIP = Ciprofloxacin; CL = Colistin; COT = Cotrimoxazole; CT = Chlortetracycline; DO= Doxycycline; ENR = Enrofloxacin; ERY= Erythromycin; LEV= Levofloxacin;

The pathogens isolated in our current study revealed no significant host specificity as all the isolates individually showed pathogenicity towards a wide range of fish species. For example, *Aeromonas spp.* was parasitic towards a wide range of hosts, including Shing (*H. fossilis*), Pangus (*Pangasius* spp.), Tilapia (*O. niloticus*), Pabda (*Ompok spp.*), Gulsha (*M. cavasius*), and Magur (*C. batrachus*), and analogous features in the context of a wide variety of hosts were exhibited by the whole pathogenic communities. Individual hosts were also susceptible to a wide range of pathogens. Resemblance to our study on host-pathogen interaction was previously described in several studies by Preena et al., (2019), Abedin *et al.* (2020a), Abedin et al. (2020b), Abedin et al. (2021a). Further exploration of the host-pathogen relationships in our current investigation revealed a convincing specificity of contaminating the hosts by the pathogens, where *Aeromonas spp.* displayed significantly high pathogenicity towards Shing (*H. fossilis*), *Vibrio* spp. towards Gulsha (*M. cavasius*) and Pabda (*Ompok* spp.), *Flavobacterium spp.*towards Pangus (*Pangasius* spp.), *Edwardsiella spp.*towards Pangus (*Pangasius* spp.), *Pseudomonas spp.* towards Shing (*H. fossilis*), *Streptococcus* spp. towards Tilapia (*O. niloticus*), and normal flora towards Shing (*H. fossilis*).

The most common isolate, *Aeromonas spp.*, was resistant to Amoxicillin (96.61%), Chlortetracycline (91.53%), and Erythromycin (91.53%) but susceptible to Levofloxacin (91.53%) and Ciprofloxacin (83.05%). Likewise, *Aeromonas spp.* was found supremely resistant to Amoxicillin (100%) and sensitive to Levofloxacin (57%) through an investigation by Abedin et al. (2021b) with the highest intermediate activity towards Chlortetracycline. The highest resistance of 67.4% towards Chloramphenicol and a maximum susceptibility of 90.9% to Meropenem were conferred by *Aeromonas spp.*, whereas the highest intermediate efficiency of 32.6% was shown by Ceftriaxome (Saleh et al., 2021). A total of 12 varieties of resistance patterns (resistant to a minimum of 4 antibiotics) were revealed in *Aeromonas spp.*, where specific isolates were found tolerant to a maximum of 8 different antibiotics. Saleh et al. (2021) stated about 9 different antibiotic resistance patterns along with 10 resistant isolates of *Aeromonas spp.* against 8 different antibiotics. Erythromycin (88%) and Amoxicillin (80%) were resistant to *Vibrio* spp., whereas Levofloxacin (92%), Ciprofloxacin (88%), Colistin (84%), and Neomycin (80%) were found effective to treat *Vibrio spp.* infections and Enrofloxacin (44%) with an intermediate response. In a study by Deng et al. (2020), they described Vancomycin (95.71%) as the highest and Chloramphenicol (4.29%) as the lowest resistant antibiotic against *Vibrio* spp. isolated from marine fish infections in the South China Sea. Chlortetracycline (90.91%) and Erythromycin (90.91%) were resistant, whereas Doxycycline (95.45%) and Levofloxacin (95.45%) were sensitive to *Flavobacterium spp.* Besides, Enrofloxacin (81.82%) was uncovered as an intermediately effective agent against the pathogen. In a particular study by Declercq et al. (2021), *Flavobacterium spp.* isolated from Koi fish exhibited resistance towards both 1st and 2nd generation Quinolone in a certain way. *Edwardsiella spp. had complete resistance to Amoxicillin (100%) and Chlortetracycline (100%) but complete susceptibility to Ciprofloxacin (100%) and Levofloxacin* (94.74%). Moreover, tolerable intermediate activity against the pathogen was recorded in Enrofloxacin (89.47%). Like ours, a study by Abedin et al. (2021b) stated Ciprofloxacin (67%) was the most effective and Amoxicillin (100%) was ineffective against *Edwardsiella* spp. infections in Pangas (*P. pangasius*). Chlortetracycline (100%) and Amoxicillin (92.86%) possessed resistance towards *Pseudomonas spp.*, whereas Ciprofloxacin (100%), Levofloxacin (100%), and Doxycycline (85.71%) were sensitive. A past study by Abedin et al. (2021c) described Amoxicillin (100%), Ciprofloxacin (100%), and Erythromycin (100%) as resistant, and Enrofloxacin (100%) as the most effective antibiotic against *Pseudomonas* spp. fish infections. *Streptococcus* spp. was resistant to Amoxicillin (100%), Chlortetracycline (100%), and Chlortetracycline (100%) and was sensitive to Colistin (100%). *Citrobacter spp.* exhibited 100% resistance against Amoxicillin and Erythromycin, whereas 100% effectiveness against the pathogen was by Ciprofloxacin, Colistin, and Levofloxacin.

In this study, Amoxicillin (90.67%), Chlortetracycline (90%), and Erythromycin (89.33%) exhibited resistance toward entire fish pathogen communities. Divyashree et al. (2020) described Ampicillin (40.78%), Tetracycline (40.22%), and Nitrofurantoin (29.05%) as resistant to pathogens isolated from fish processing effluent. Wu et al. (2019a) found fish pathogens isolated from marine fish farming areas resistant to Oxytetracycline. Amoxicillin (76.47%) and Erythromycin (54.9%) were resistant to fish pathogens, according to Abedin et al. (2021a), which displayed a resemblance to our current study. Pathogens isolated from fish cage culture were exhibited by Wu et al. (2019b) with resistance towards Amoxicillin (27.67%), Erythromycin (23.31%), and Gentamicin (37.32%). As resembling our research, Abedin et al. *(*2020a) stated that Amoxicillin (100%) exhibits supreme resistance towards the pathogens, followed by Erythromycin (64.3%). On the contrary, Levofloxacin (92%), Ciprofloxacin (82%), Neomycin (80%), and Colistin (78%) were effective against fish pathogens, according to our current study. We found that Enrofloxacin (97.8%), Cotrimoxazole (97.3%), and Ciprofloxacin (77%) were potent against the fish pathogens (Abedin et al., 2021c), which displayed some resemblance to our investigation with a huge imparity as Enrofloxacin was noticed to be intermediately effective (62.67%) against the fish pathogens in our study. Twenty-one resistance patterns (resistant to a minimum of 4 antibiotics) were displayed by 90 out of 150 (60%) pathogens isolated in our current study, with the considerable participation of almost every pathogen. *Aeromonas spp. exhibited a wide range of resistance patterns, including tolerance to up to eight antibiotics (AMX-CIP-COT-CT-DO-ENR-ERY-LEV).* Fourteen isolates of *Aeromonas spp.* were uncovered to be resistant towards AMX-COT-CT-ENR-ERY (5 antibiotics), and 12 isolates of the same species were found to be resistant against AMX-COT-CT-ERY (4 antibiotics), which was undoubtedly imitated by 10 isolates of *Edwardsiella spp.* Saleh et al. (2021) also stated that *Aeromonas spp.* has 9 different antibiotic resistance patterns and 10 tolerant isolates towards 8 different antibiotics.

Conclusion

Fish production, the major contributor to animal protein supply worldwide, encounters a massive hindrance of infection by a wide range of pathogens of viruses, bacteria, and fungi, gradually worsening due to the rampant development of resistance towards antimicrobials by the pathogens. Among 180 randomly sampled infected fishes, 6 (3.33%) showed no growth, and 174 (96.67%) displayed culture positivity, including 150 (83.34%) pathogenic growth and 24 (13.33%) normal flora. The presence of *Aeromonas spp.*, *Vibrio spp.*, *Flavobacterium spp.*, *Edwardsiella spp.*, *Pseudomonas spp.*, *Streptococcus spp*., and *Citrobacter spp.* in bacterial communities was linked to 39.33%(59), 16.67%(25), 14.67%(22), 12.67%(19), 9.33%(14), 5.33%(8), and 2%(3) infections in Shing (*H. fossilis*), Pangus (*Pangasius* spp.), Pabda (*Ompok* spp.), Gulsha (*M. cavasius*), Tilapia (*O. niloticus*), Koi (*Cyprinus spp.*), Magur (*C. batrachus*), Tengra (*M. tengara*) accommodating a frequency of 46.1%(83), 18.33%(33), 10%(18), 9.44%(17), 8.89%(16), 2.78%(5), 2.78%(5), and 1.67%(3) fish species respectively as hosts with no particular host-pathogen specificity. The entire communities of pathogens were resistant to Amoxicillin (90.67%), Chlortetracycline (90%), Erythromycin (89.33%), and Cotrimoxazole (57.33%). On the contrary, Levofloxacin (92%), Ciprofloxacin (82%), Neomycin (80%), Colistin (78%), and Doxycycline (65.34%) exhibited potential effectiveness against the pathogens, whereas Enrofloxacin was found to have an intermediate (62.67%) response in our study. A huge frequency of 60% of pathogens exhibited 21 resistance patterns towards a minimum of 4 antibiotics and a maximum of 8 antibiotics, whereas *Aeromonas spp.* isolates were the most prominent. The discoveries about fish pathogens, their prevalence, and antimicrobial responsiveness patterns to pathogens would be a valuable guide to veterinarians in treating a wide range of infections in aquaculture. Elevated resistance towards antimicrobials by fish pathogens might be an alarming issue as the potential pathogenic gene transfer can drive the environmental isolates into a potential threat. Further studies on the resistance genes or transposons of the pathogenic isolates are required, as well as regular investigations into fish pathogens and their responses to antimicrobials.

References

Abedin MZ, Aktar MB, Zaman MS, Hasan R, Jarin L, Karim MR, Rahman MS, Islam R and Uddin ME. Occurrence and antimicrobial susceptibility profiling of bacteria isolated from cultured Pangas Catfish (Pangasius pangasius) and Climbing Perch (Anabas testudineus) Fishes. *J. Mar. Biol. Aquac.* 2020a; 6(1): 7-12.

Abedin MZ, Rahman MS, Hasan R, Shathi JH, Jarin L and Zaman MS. Isolation, identification, and antimicrobial profiling of bacteria from aquaculture fishes in pond water of Bangladesh. *Amer. J. Pure Appli. BioSci.* 2020b; 2(3): 39-50.

Abedin MZ, Yeasmin F, Mehfuz A, Koly FA, Arfat ME, Farnaz NEK, Sadiqur R, Khairujjaman, Islam MI, and Emdadul HM. Enumeration of emergent bacterial pathogen isolated from small indigenous fish species: Pabda (*Ompok* spp) and Gulsha (*Mystus cavasious). Int. J. Oceanogra. Aquacu.* 2021a; 5(4): 000213.

Abedin MZ and Islam MI. Microbiological screening and antibiotics responsiveness of pathogenic bacteria isolated from pond cultivated pangas fishes (Pangasius hypothallus) in Bangladesh. *Sci. Arch.* 2021b; 2(3): 238-244.

Abedin MZ, Hasan R, Rahman MS, Jarin L, Shilpi RY, Islam R and Rahman MA. 2021c. Detachment, distinguishing proof of bacterial pathogens from infected Shing (*Heteropneustes fossilis*) cultured in freshwater ponds in Bangladesh. *Int. J. Biomo. Biome.* 2021c; 12(3): 10-16

Aubry A, Mougari F, Reibel F and Cambau E. Mycobacterium marinum. In: *Tuberculosis and Nontuberculous Mycobacterial Infections*. Schlossberg D (ed.), 7th edition, Chap. 43. John Willy & Sons, 2017. pp. 735-752.

Austin B and Austin DA. Bacterial Fish Pathogens: Diseases of Farmed and Wild Fish. 4th edition, Springer, Dordrecht, The Netherlands, 2012. p. 552.

Chauhan A and Jindal T. Microbiological methods for environment, food and pharmaceutical analysis. *Springer Nature,* 2020; p. 487.

Cockerill FR. Clinical and Laboratory Standards Institute. Performance standards for antimicrobial susceptibility testing: twenty-third informational supplement; [... provides updated tables for... M02-A11, M07-A9, and M11-A8]. National Committee for Clinical Laboratory Standards; 2013.

Declercq AM, Tilleman L, Gansemans Y, De Witte C, Haesebrouck F, Van Nieuwerburgh F, Smet A and Decostere A. Comparative genomics of Flavobacterium columnare unveils novel insights in virulence and antimicrobial resistance mechanisms. *Vet. Res.* 2021; 52: 18.

Deng Y, Xu L, Chen H, Liu S, Guo Z, Cheng C, Ma H and Feng J. Prevalence, virulence genes, and antimicrobial resistance of Vibrio species isolated from diseased marine fish in South China. *Sci.. Rep.* 2020; 10(1): 14329.

Divyashree M, Kumar DV, Ballamoole KK, Shetty V, Chakraborty A and Karunasagar I. Occurrence of antibiotic resistance among gram-negative bacteria isolated from effluents of fish processing plants in and around Mangalore. *Int. J. Environ. Health Res.* 2019; 30: 653-60.

Divyashree M, Kumar DV, Ballamoole KK, Shetty A V, Chakraborty A and Karunasagar I. Occurrence of antibiotic resistance among Gram negative bacteria isolated from effluents of fish processing plants in and around Mangalore. *Int. J. Environ. Health Res.* 2020; 30(6): 653-660.

DoF. Yearbook of fisheries statistics of Bangladesh 2017-2018. Fisheries Resources Survey System (FRSS), Department of Fisheries, Ministry of Fisheries and Livestock: Dhaka, Bangladesh. 2018; 35: p. 129.

FAO. The state of world fisheries and aquaculture 2020: sustainability in action. In: The State of World Fisheries and Aquaculture (SOFIA); FAO: Rome, Italy. 2020; p. 244.

Labony SS, Alim MA, Hasan MM, Hossain MS, Islam A, Alam MZ, Tsuji N and Anisuzzaman. Fish-borne trematode infections in wild fishes in Bangladesh. *Pathog. Glob. Health.* 2020; 114(2): 91-98.

Miller RA and Harbottle H. Antimicrobial Drug Resistance in Fish Pathogens. *Microbiol. spectr.* 2018; 61: 1-20.

Nayak SK. Current prospects and challenges in fish vaccine development in India with special reference to Aeromonas hydrophila vaccine. *Fish Shellfish Immunol.* 2020; 100: 283-299.

Pandit D, Saha S, Kunda M and Harun-Al-Rashid A. Indigenous freshwater ichthyofauna in the Dhanu River and surrounding wetlands of Bangladesh: species diversity, availability, and conservation perspectives. *Conserv.* 2021; 1(3): 241-257.

Preena PG, Arathi D, Raj NS, Arun Kumar TV, Arun Raja S, Reshma RN and Raja Swaminathan T. Diversity of antimicrobial resistant pathogens from a freshwater ornamental fish farm. *Lett. Appl. Microbiol.*, 2019; 71(1): 108-116.

Pridgeon JW and Klesius PH. Major bacterial diseases in aquaculture and their vaccine development. *CABI Reviews.* 2012; 7: 1-16.

Rahman AKA. Freshwater Fishes of Bangladesh, 2nd ed. Zoological Society of Bangladesh, Department of Zoology, University of Dhaka: *Dhaka, Bangladesh*. 20005; p. 263

Saleh A, Elkenany R and Younis G. Virulent and multiple antimicrobial resistance aeromonas hydrophila isolated from diseased nile tilapia fish (Oreochromis niloticus) in Egypt with sequencing of some virulence-associated genes. *Biocontrol. Sci.*, 2021; 26(3): 167-176.

Sørum H. Antimicrobial drug resistance in fish pathogens. In: *Antimicrobial Resistance in Bacteria of Animal Origin*. Chap. 13, Aarestrup FM (ed.) 2005; 213-238.

Wu J, Su Y, Deng Y, Guo Z, Mao C, Liu G, Xu L, Cheng C, Bei L and Feng J. Prevalence and distribution of antibiotic resistance in marine fish farming areas in Hainan, China. *Sci. Total Environ.*, 2019a; 653: 605-611.

Wu J, Mao C, Deng Y, Guo Z, Liu G, Xu L, Bei L, Su Y, Feng J. Diversity and abundance of antibiotic resistance of bacteria during the seedling period in marine fish cage-culture areas of Hainan, China. Mar. Pollut. Bull. 2019b; 141: 343-349.

J. Bangladesh Acad. Sci. 48(1); 75-83: June 2024 DOI:https://doi.org/10.3329/jbas.v48i1.69481

Journal of Bangladesh Academy of Sciences

Journal homepage: http://www.bas.org.bd/publications/jbas.html

Research Article

Cyclic voltammetric behavior of crystal violet in aqueous solution: Correlation with dissolved states of cetyltrimethylammonium bromide

Neamul H. Khansur[1,2], Iqbal Mahmud[3], A.J.F. Samed[4], Md. Nizam Uddin[4],
Md Abul Kalam[5*] and Md. Abu Bin Hasan Susan[1,6*]

Department of Chemistry, University of Dhaka, Dhaka, Bangladesh

ARTICLE INFO

Article History

Received: 23 October 2023
Revised: 10 December 2023
Accepted: 22 December 2023

Keywords: Cyclic voltammetry, Crystal violet, Platinum electrode, CTAB, Micelle, pH.

ABSTRACT

The cyclic voltammetric method was employed to study the electrochemical behavior of aqueous crystal violet in the presence of cetyltrimethylammonium bromide, both below and above the critical micelle concentration. The cyclic voltammograms were highly sensitive to solution pH, exhibiting well-defined oxidation and reduction peaks within the pH range of 1.76 to 2.29. The electrochemical potentials and currents indicate the involvement of a set of reactions responsible for the observed voltammograms. The fully oxidized diquinoid of N, N, N', N'- tetramethylbenzidine (TMBOx) was formed, which was reduced to N, N, N', N'- tetramethylbenzidine (TMB). The presence of CTAB profoundly influenced the electrochemical behavior, and responses were found to depend on the dissolved states of CTAB. The electrochemical process was diffusion-controlled and followed a chemical-electrochemical-chemical (CEC) mechanism.

Introduction

Triphenylmethane (TPM) dyes including malachite green (MG), ethyl violet, crystal violet (CV), and victoria blue B exhibit unique electrochemical activity (Perekotii et al., 2002; Xu et al., 2007; Song et al., 2010) and are extensively used in applications as antibacterial agents, antiseptics, and in industries like silk, textile, and paper (Arsalan et al., 2013). However, TPM dyes are recognized as potential environmental pollutants, prompting considerable research efforts to understand their physiochemical characteristics and devise effective strategies to mitigate their impact (Pillai et al., 2011; Petcu et al., 2016). In addition, they have gained attention in nontraditional usages, particularly in developing molecular devices by exploiting electrochemical switching (Ariga, 2006; Selvakumar, 2017; Toma, 2008; Ge et al., 2022).

Researchers have conducted studies under different electrochemical environments in pursuit of a deeper understanding of the electrochemical characteristics of TPM dyes and how to manipulate them. Perekotii et al. explored the electrochemical properties of CV using a glassy carbon electrode (GCE) to support electrolytes such as potassium salts of nitrate, chloride, and iodide. In KI solution, an electroactive complex with iodide forms on the surface of the electrode (Perekotii et al., 2002). Galus and Adams (1964) unveiled the complex nature of the electrochemical process of CV in acidic environments. They reported that the two phenyl fragments intramolecularly couple when the TPM moiety experiences expulsion of the central carbon residue. This sequence of reactions yielded fully oxidized a diquinoid of N, N, N`, N`-

---

*Corresponding author:<mkalam@tamut.edu;susan@du.ac.bd>

[1]*Department of Chemistry, University of Dhaka, Dhaka, Bangladesh;* [2]*Institute of Glass and Ceramics, Department of Materials Science and Engineering, Friedrich-Alexander-Universität Erlangen-Nürnberg, Martensstraße, Erlangen, Germany;* [3]*Department of Electrical and Electronic Engineering, Eastern University, Dhaka, Bangladesh;* [4]*Department of Chemistry, Shahjalal University of Science and Technology, Sylhet, Bangladesh;* [5]*Department of Natural Sciences, Texas A&M University-Texarkana, Texarkana, USA;* [6] *Dhaka University Nanotechnology Centre (DUNC), University of Dhaka, Dhaka, Bangladesh*

tetramethyl-benzidine (TMBOx). TMBOx is subsequently transformed into the reduced form, N, N, N`, N`- tetramethyl-benzidine (TMB) through a redox process involving a two-electron reduction process (Galus and Adams, 1964; Galas and Adams, 1962). When comparing the oxidation of TPM dyes in liquid SO_2 to that in the aqueous solution under acidic conditions, Hall et al. (1966) observed that the two environments showed very distinct redox activity. They proposed that the redox couple responsible for the voltammogram involved the carbonium ion and the free radical generation.

It would be interesting to find out if the distinct electrochemical activity of TMP dyes persists in surfactant-based organized media and to establish a correlation between dissolved states of the amphiphile and electrochemical responses. The surge in interest in redox-active species, especially TPM dyes in micellar systems, stems from the fact that a systematic change in the concentration of surfactants can control the electrochemical behavior of electroactive probes (Saji et al., 1985; Takeoka et al., 1996). The concept of switching by exploiting electrochemical changes of redox-active surfactants was pioneered by Saji et al. (1991, 1994) and Gokel and coworkers (Munoz and Gokel, 1993; Wang et al., 1996). Their work demonstrated that micelles can be disrupted into monomers through redox reactions, offering an efficient means for preparing thin films of water-insoluble organic dyes. Takeoka et al. investigated the electrochemical behavior of a nonionic surfactant containing a ferrocenyl group (Takeoka et al., 1995, 1996). They revealed that the oxidation state of the redox-active group and the dissolved states of the surfactant affect the features of the cyclic voltammograms of the surfactant solutions. According to Kozlecki et al. (1997), introducing an azo group to the hydrophobic tail of alkane carboxylates and linear alkane sulfonates improves their solubility in water, micellization, and adsorption. Susan et al. conducted extensive research on anthraquinonyl and phenothiazinyl nonionic surfactants (Susan et al., 2000a, 2000b, 2004). Their work demonstrated that these redox-active surfactants exhibit fascinating responses to electrochemical changes, with controllable (electrochemical) behavior achieved by manipulating factors such as the structure of the surfactants, concentration, pH, and redox potential.

Rusling (1994) reviewed earlier research on the redox behavior of electrochemical probes in electro-inactive surfactants. Susan and his team used ferrocene, anthraquinone, and phenothiazine to explore their electrochemical behavior in various surfactant solutions. Their results demonstrated that redox probes, when dissolved in organized systems containing electro-inactive surfactants, can also be administered using the principle of electrochemical switching (Haque et al., 2011; Mahmud et al., 2011; Haque et al., 2012; Keya et al., 2014; Roy et al., 2020). Yeh (1976) also solubilized a redox probe in micelles to estimate micellar diffusion coefficients of Tween 20 (Yeh, 1976). Rahman et al. (2013) examined the electrochemical behavior of MG in an aqueous solution with cetyltrimethylammonium bromide (CTAB), a cationic surfactant, and sodium dodecyl sulfate (SDS), an anionic surfactant. Using a GCE in the experiments, they observed important interactions between MG and various surfactants. They demonstrated that, under ambient conditions, the redox process of MG is irreversible and diffusion-controlled.

Despite extensive studies, research on the redox behavior of TPM dyes in surfactant systems remains in its infancy; in particular, comprehensive studies on CV are still lacking. The CV in a surfactant system is of immense interest due to its unusual yet tunable electrochemical behavior (Galus and Adams, 1964) for the construction of electrochemical switchable molecular devices. To address this gap, Mahmud and coworkers documented the electrochemical characteristics of aqueous CV in the presence and absence of Triton X-100, a nonionic surfactant (Mahmud et al., 2023). Using platinum electrodes in the cyclic voltammetry method, they found the characteristics of the voltammograms of CV were complex and very sensitive to solution pH.

According to the literature (Galus and Adams, 1964, 1962), CV can exist in different forms in solution and give rise to different voltammograms based on the solution pH (Fig. 1). In acidic aqueous buffered solutions, Structure I could undergo complex reactions leading to TMBOx compounds, which, through a two-electron transfer process, form TMB (Fig. 1) (Galus and Adams, 1964). Mahmud and coworkers verified that the electrochemical reaction of the redox pair, TMBOx/TMB, is the basis of the shapes of the cyclic voltammograms at pH 1.76-2.29.

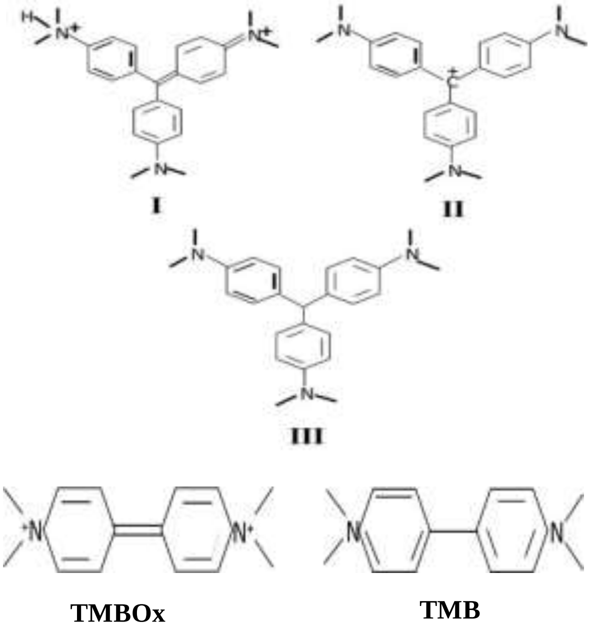

Fig. 1. Different forms of crystal violet in the aqueous electrochemical system at different pH values. Structure I, TMBOx, and TMB are present at low pH, and Structure II and III are at high pH.

The voltammogram changes shape at high pH (alkaline condition) because TMBOx is not formed under this condition, and leucocrystal violet is produced via an electrochemical reduction reaction involving the carbocationic form (Structure II) of CV (Structure III), which is then oxidized to CV. Although complex, the redox process did not change in Triton X-100 in aqueous medium. It is, therefore, interesting to investigate whether the electrochemical behavior is unique for a nonionic surfactant system and whether electrostatic interactions of an ionic surfactant influence the electrochemical behavior similarly. In this study, to correlate the available knowledge of the electrochemical reaction of CV with the dissolved states of a surfactant, we investigated the cyclic voltammetric behavior of the aqueous solution of CV in the presence of a cationic surfactant, CTAB.

Materials and Methods

Sodium chloride (NaCl), CTAB, and crystal violet were purchased from BDH and used without further purification. Puric-S (Organo Co., Tokyo) grade deionized water with a specific resistance of 2.00 MΩ cm was used to prepare all of the stock solutions. The concentration of CV was maintained at 1.00×10^{-6} M for all experiments conducted to investigate its electrochemistry, regardless of the presence of CTAB. The stock solution was properly diluted to produce CTAB solutions in different concentrations.

A pH meter (Model HM-26S; TOA Electronics, Japan) measured the solution pH. The cyclic voltammograms were recorded using a computer-controlled electrochemical analyzer (model HQ 2040; Advanced Analytics, USA). 0.16 M NaCl aqueous solution was used as the supporting electrolyte. A single-compartment three-electrode cell was used. A platinum electrode (area of 0.021 cm^2) served as the working electrode, while a Pt-wire was the counter electrode, and an Ag/AgCl was the reference electrode. Before each measurement, the surface of the working electrode was cleaned and polished with 0.05 µm alumina (Buehler) to render it mirror-polished. The potential was scanned at a scan rate (v) ranging from 10 to 500 mVs^{-1}. To remove the influence of ambient CO_2 and dissolved oxygen, all the pH and electrochemical measurements experiments were performed in an inert atmosphere by purging the solution with N_2 gas at 25°C.

Results and Discussion

Electrochemical responses of crystal violet in a micellar solution of CTAB: The cyclic voltammetric behavior of CV was studied in CTAB with 0.16 M aqueous NaCl solution as the supporting electrolyte.

CTAB concentration varied in a wide range, including concentrations below, above, and far above the CMC, with the CMC value of CTAB being 9.2 $\times 10^{-4}$ M at 25.0 ºC (Rahman et al., 2013). Due to the salting out effect (Shahid et al., 2009), the addition of NaCl brings about a decrease in the CMC of CTAB in aqueous solutions, and the concentrations of 1.5×10^{-3} M or above of CTAB used in this work can be regarded as concentrations above the CMC (Haque et al., 2011).

Fig. 2 presents the characteristics of the shape, potentials, and current of the cyclic voltammograms of 1×10^{-6} M CV at different CTAB concentrations at the v of 10 $\mathrm{mVs^{-1}}$. The cyclic voltammograms in aqueous solution maintain their shape when CTAB is present, as demonstrated in Fig. 2(a). As reported earlier, the electrochemical reaction involves a two-electron transfer process (Mahmud et al., 2023). One reduction peak and its corresponding oxidation peak are observed in these voltammograms. Nonetheless, it has been revealed that the electrochemical reactions rely on the CTAB concentration. The potential data presented in Fig. 2(b) shows the change in half-wave potential ($E_{1/2}$) and cathodic peak potential (E_{pc}) with [CTAB]. While the $E_{1/2}$ is minimally affected, the E_{pc} increases with the concentration of CTAB. This increase in the E_{pc} with CTAB concentration suggests that the formation of TMBOx may be favored in the micellar core or enhanced by the surface activity of CTAB. Figure 2(c) depicts the change in the cathodic peak current, i_{pc}, with [CTAB]. As demonstrated in Fig. 2(c), the i_{pc} decreases as the concentration of CTAB rises, followed by a minimum before increasing again.

Surfactant species exist as free monomers at concentrations lower than the CMC, allowing reducible TMBOx to diffuse freely to the electrode interface. This results in relatively high i_{pc} at low surfactant concentrations. Micelles, in other words, thermodynamically stable aggregates of colloidal dimension, are formed by the aggregation of surfactant species above the CMC. The decrease in the i_{pc} is caused by the solubilization of CV inside the micellar core and the ensuing decreased diffusion to the electrode interface. As the concentration of CTAB reaches far above CMC, the i_{pc} is found to increase. This could be attributed to the solubilization effect, where all the electroactive species are trapped in the micellar cores.

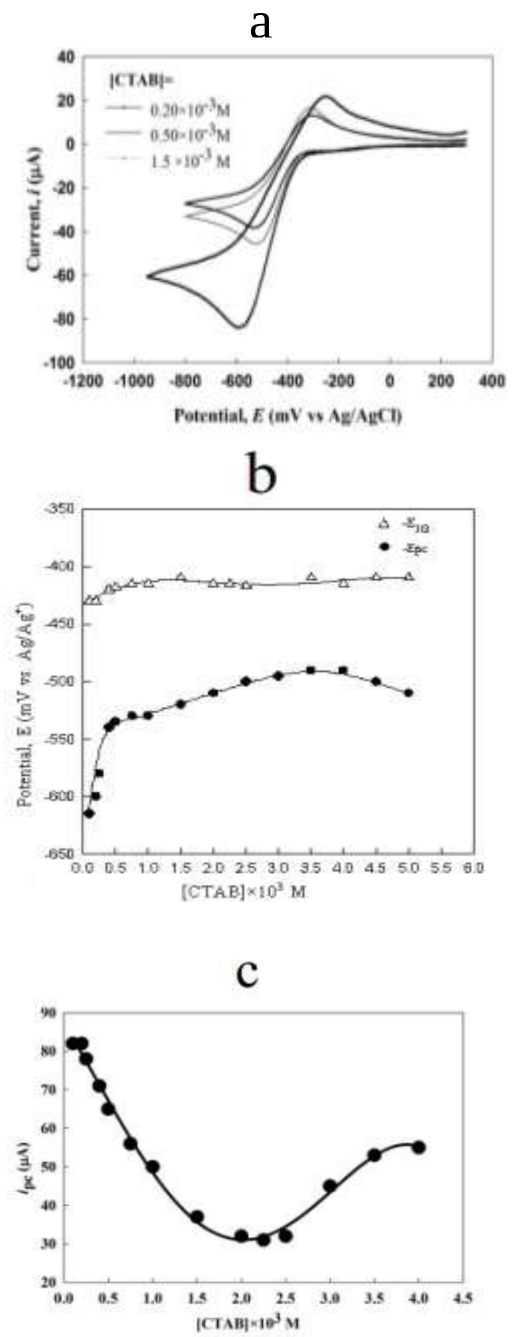

Fig. 2. Cyclic voltammetric results for 1×10^{-6} M crystal violet at various CTAB concentrations at the v of 10 $\mathrm{mVs^{-1}}$ in 0.16 M NaCl aqueous solution: a. characteristic shape of the voltammograms, b. E_{pc} and $E_{1/2}$ vs. [CTAB] plots, and c. i_{pc} vs. [CTAB] plots.

The concentration of CV in the micellar pseudo phase decreases as surfactant concentration rises since more micelles are produced. Since micelles are in dynamic equilibrium with their monomers, diffusion of CV becomes higher to the electrode interface to cause an increase in the i_{pc}. The observations are reminiscent of those for CV in an aqueous solution of TX-100, and the overall trend of the electrochemical behavior is not changed for the cationic surfactant.

To diagnose if diffusion regulates the entire electrochemical process or if the change in CTAB concentration impacts adsorption at the electrode surface, the i_{pc} of 1×10^{-6} M CV at 10 mVs^{-1} was further examined.

a.

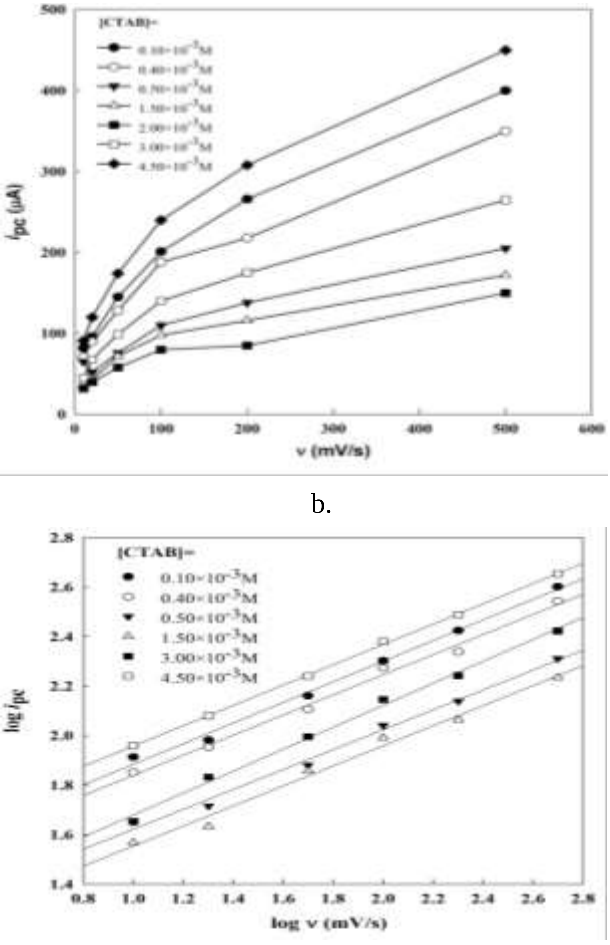

b.

Fig. 3. The variation of the i_{pc} with v for various CTAB concentrations for 1×10^{-6} M crystal violet solution in the presence of 0.16 M NaCl aqueous solution; a. i_{pc} vs. v; b. log i_{pc} vs. log v.

Table 1. Slopes of the plots of log i_{pc} vs. log v at various CTAB concentrations for 1×10^{-6} M CV in 0.16 M NaCl aqueous solution.

[CTAB]×10^3 (M)	Slope
0.10	0.42
0.40	0.41
0.50	0.41
1.50	0.40
3.00	0.44
4.50	0.41

Fig. 3 provides insight into the v dependence of the i_{pc}, revealing that the i_{pc} increases in a non-linear fashion with the v, which indicates a *quasi-reversible* process. It is apparent [Fig. 3(a)] that some other process significantly influences the electrochemical process instead of adsorption. When log i_{pc} vs. log v is plotted, the slopes [Fig. 3(b)] at all CTAB concentrations have values closer to 0.5 than 1 (Table 1), suggesting a diffusion-controlled process (Bard et al., 2022). Furthermore, given that the slope is somewhat less than 0.5, a chemical reaction likely precedes the electrochemical reaction, in this instance, the generation of TMBOx from CV and protonation of the carbocationic dye, even in the presence of CTAB.

a.

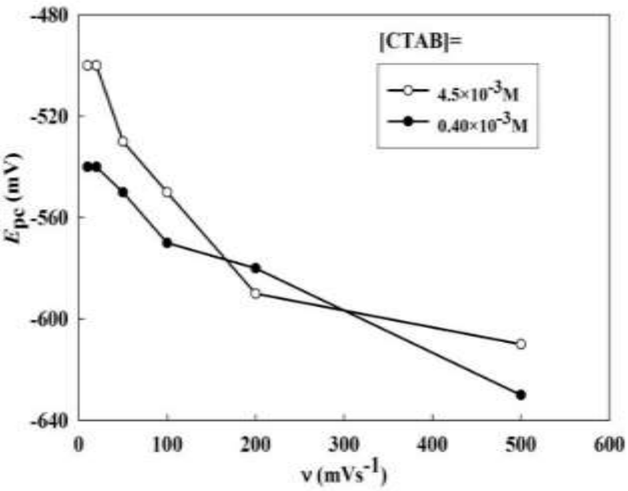

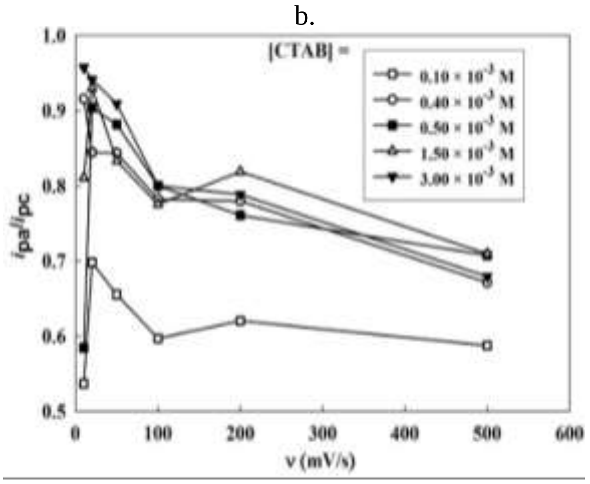

Fig. 4. Variation of the peak potential and currents with *v* for 1×10^{-6} M CV at various concentrations of CTAB in 0.16 M NaCl aqueous solution; a. E_{pc} vs. *v*; b. i_{pa}/i_{pc} vs. *v*.

Fig. 4(a) displays a negative shift in the cathodic peak potential with increasing *v*, implying again that the system is likely *quasi*-reversible (Greef et al., 1985). Meanwhile, Fig. 4(b) displays the ratio of the anodic peak current (i_{pa}) to the i_{pc} (i_{pa}/i_{pc}) as a function of *v* at varying concentrations of CTAB. In Fig. 4(b), it can be observed that the i_{pa}/i_{pc} values are smaller than 1 at all experimental concentrations of CTAB, indicating that other processes, such as a following chemical reaction, complicate the electrochemical reaction (Nicholson and Shain, 1964). The i_{pa}/i_{pc} value initially increases, reaches a maximum, and then decreases with increasing *v*. At lower *v* values, an increase in the ratio with increasing *v* is apparent, supporting the existence of a following reaction (Susan et al., 2000b). At higher *v* values, the decrease in the i_{pa}/i_{pc} with *v* corresponds to the property of a reversible electrochemical reaction coupled with a preceding chemical reaction. This behavior is similar to what is observed with CV in the aqueous solution without any CTAB (Mahmud et al., 2023). During the cathodic scan, the Pt electrode interface exhibits H_2 gas evolution in the presence of CTAB, leading to pH change at the interface. As a result, all TMB produced from the reduction of TMBOx may not be reoxidized, resulting in a decrease in the i_{pa} and hence in the i_{pa}/i_{pc}.

In CTAB solutions, the apparent diffusion coefficient (D_{app}) of CV could be estimated using the Randles-Sevcick equation (Eq. 1).

$$i_{pc} = (2.69\times10^5)n^{3/2}AD_{app}^{1/2}v^{1/2}C \qquad (1)$$

Here, A is the geometric area of the electrode surface in cm^2, D_{app} is in cm^{2}s^{-1}, *v* is in Vs^{-1}, *C* is the concentration of the reactive species in the bulk of the solution in mol cm^{-3}, and i_{pc} is in ampere. The number of electrons participating in the electrochemical reaction is represented by *n*.

Fig. 5 illustrates D_{app} versus [CTAB] for 1×10^{-6} M aqueous CV solution. The D_{app} decreases, reaches a minimum, and then increases with increasing [CTAB]. The D_{app} is expected to decrease above the CMC since the solubilization of CV within the micelle core upon micelle formation reduces the rate of diffusion of CV or TMBOx to the interface. The D_{app} increased as the surfactant concentration decreased at concentrations lower than the CMC, eventually reaching the same diffusivity as CV when CTAB was absent. The diffusivity increased with increasing [CTAB] after reaching a minimum because increasing micelle concentration reduces CV concentration in the micellar pseudo phase, making it easier for CV or its counterpart TMBOx to diffuse to the electrode interface.

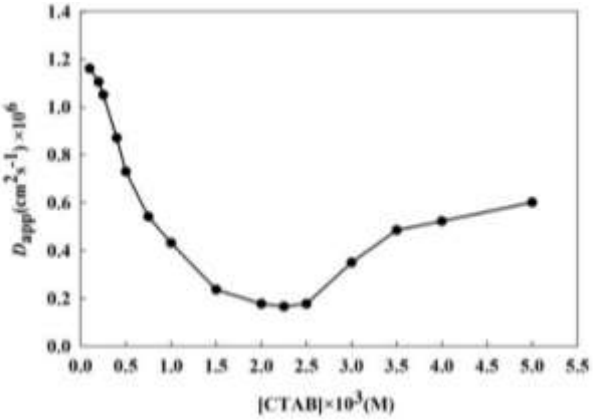

Fig. 5. Electrochemically estimated D_{app} plotted against the concentration of CTAB for 1×10^{-6} M CV aqueous solution.

Electrochemistry of aqueous crystal violet: The electrochemical behavior of aqueous CV solution was examined without CTAB while maintaining other conditions identical to the experiments conducted in the presence of CTAB at pH 2.29. The primary objective was to compare the results obtained in the presence of CTAB with those obtained in its absence. Under the current experimental conditions, cyclic voltammograms showed single reduction waves and their corresponding oxidation waves, similar to those recorded in the presence of CTAB (*vide supra*). These findings were consistent with the works of Galus and Adams (1964) and Mahmud and coworkers (2023). The separation of potentials for the cathodic and anodic peaks (ΔE) for the cyclic voltammograms was greater than $59/n$ mV (where $n = 2$), indicating that the electrochemical process was not entirely reversible under the experimental conditions. The greater ΔE is likely attributed to the sluggish transfer of electrons, which is accompanied by a chemical reaction. Furthermore, the logarithmic relationship between peak current and v exhibits a linear relationship with an acceptable regression coefficient (>0.9997) (Fig. not shown). The slope is 0.44, which suggests that the electrochemical process under the current experimental condition is also controlled by diffusion, as observed in the presence of CTAB. Furthermore, reduction current and v were evaluated using Eq. (1), which further supports a diffusion-controlled process.

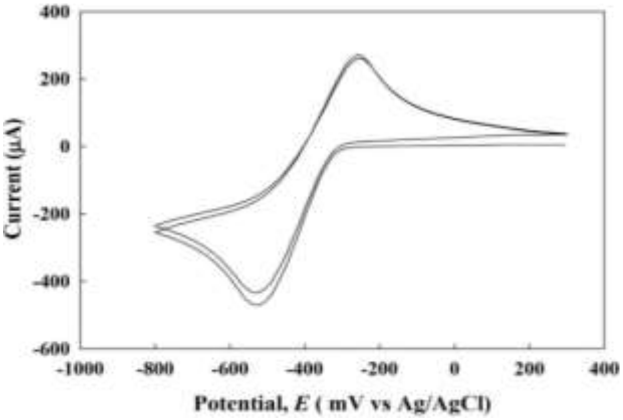

Fig. 6. Cyclic voltammograms of 1×10^{-6} M CV in 0.16 M aqueous NaCl solution during successive scans (pH= 1.86; v = 10 mVs^{-1}).

Cyclic voltammograms were also obtained to measure i_{pa} immediately after cathodic reduction. The system showed a significant current in the ensuing scan, indicating the existence of oxidized species. Notably, however, our observation differs from that reported by Galus and Adams (1964). As the potentials were scanned to obtain multiple cyclic voltammograms consecutively, the i_{pc} increased in the subsequent scan, as depicted in Figure 6. This increase suggests a rise in the relative number of reducible species at the electrode surface during the subsequent scan, suggesting that TMBOx, i.e., the reducible species, will diffuse faster to the interface.

Conclusion

Crystal violet demonstrates pH-dependent electrochemical responses in an aqueous solution, showing distinct cyclic voltammograms between 1.76 and 2.29. The TMBOx/TMB redox couple is primarily accountable for the voltammograms and resembles a diffusion-controlled process. The electrochemical process involves two-electron transfer, and a preceding chemical reaction is coupled with it. In the prior reaction, TMBOx is formed from the dication form of CV. Similar to a nonionic surfactant, CTAB does not affect the shapes of the voltammograms.

Nonetheless, an alteration in CTAB concentration has a major impact on the electrochemical behavior of CV since it results in a change of the surfactant from monomeric to self-assembled species. The voltammogram displays a relatively high peak current at concentrations lower than the CMC since CTAB is a free monomer, allowing the reducible TMBOx to diffuse freely to the electrode interface. However, increasing the concentration of CTAB leads to greater micelle formation, reducing the diffusivity of CV and causing a decrease in peak current. The electrochemical process is coupled with a preceding chemical reaction and a following reaction in the presence of CTAB. These findings contribute to the understanding of the electrochemical properties of CV in the presence of a cationic surfactant. They may have implications in diverse fields, including electrochemistry and molecular switching. These results advance our knowledge of the electrochemistry of triphenylmethane dyes in the presence of cationic surfactants and may find applications in molecular switching and electrochemistry, among other areas.

Conflict of Interests

The authors declare no conflicts of interest.

Acknowledgments

The research grant under DU-UGC from the University of Dhaka is gratefully acknowledged.

References

Ariga K. *Supramolecular Chemistry - Fundamen-tals and Applications*. Springer-Verlag, Berlin/ Heidelberg; 2006. p 208.

Arsalan S, Ahmed G, Hamiz-ul-Fawwad S, Waqar SA and Saleem A. Gentian violet - A blessing in disguise for the developing world. *Burns*. 2013; 39(6): 1326-1327.

Bard AJ, Faulkner LR and White HS. *Electrochemical Methods: Fundamentals and Applications,* 3rd Edition, Wiley, 2022. p. 1104.

Galus Z and Adams RN. The anodic oxidation of triphenylmethane dyes. *J. Am. Chem. Soc.* 1964; 86(9): 1666-1671.

Galus Z and Adams RN. The anodic oxidation of triphenylmethane dyes. *J. Am. Chem. Soc.* 1962; 84(16): 3207-3208.

Ge W, Chen Y, Fan Y, Zhu Y, Liu H, Song L, Liu Z, Lian C, Jiang H and Li C. Dynamically formed surfactant assembly at the electrified electrode–electrolyte interface boosting CO_2 electroreduction. *J. Am. Chem. Soc.* 2022; 144(14): 6613-6622.

Greef R, Peat R, Peter LM, Pletcher D and Robinson J. *Instrumental Methods in Electrochemistry*, John Wiley and Sons, New York, 1985.

Hall DA, Sakuma M and Elving PJ. Voltammetric oxidation of triphenylmethane dyes at platinum in liquid sulphur dioxide. *Electrochim. Acta*. 1966; 11(3): 337-350.

Haque MA, Rahman MM and Susan M. Aqueous electrochemistry of anthraquinone and its correlation with the dissolved states of a cationic surfactant. *J. Solut. Chem.* 2011; 40: 861-875.

Haque MA, Rahman MM and Susan M. Electrochemical behavior of anthraquinone in reverse micelles and microemulsions of cetyltrimethylammonium bromide. *J. Solut. Chem*. 2012; 41: 447-457.

Keya JJ, Islam MM, Rahman MM, Mollah MYA and Susan MABH. Effect of a water structure modifier on the aqueous electrochemistry of supramolecular systems: Redox-active versus conventional surfactants. *J. Electroanal. Chem.* 2014; 712:161-166.

Kozlecki T, Sokolowski A and Wilk KA. Surface activity and micelle formation of anionic azobenzene-linked surfactants. *Langmuir* 1997; 13(26): 6889-6895.

Mahmud I, Khansur NH, Uddin MN, Samed AJFU, Kalam MA and Susan MABH. Complex electrochemical behavior of crystal violet in aqueous solution in the presence of Triton X-100. *Universal J. Electrochem.* 2023; 1(1), 51-60

Mahmud I, Samed AJF, Haque MA and Susan MABH. Electrochemical behavior of anthraquinone in aqueous solution in presence of a non-ionic surfactant. *J. Saudi Chem. Soc.* 2011; 15(3): 203-208.

Munoz S and Gokel GW. Redox-switched vesicle formation from two novel, structurally distinct metalloamphiphiles. *J. Am. Chem. Soc.* 1993; 115(11): 4899-4900.

Nicholson RS and Shain I. Theory of stationary electrode polarography. single scan and cyclic methods applied to reversible, irreversible, and kinetic systems. *Anal. Chem.* 1964; 36(4): 706-723.

Perekotii VV, Temerdashev ZA, Tsyupko TG and Palenaya EA. Palenaya, Electrochemical behavior of crystal violet on glassy carbon electrodes. *J. Anal. Chem.* 2002; 57(5): 448-451.

Petcu AR, Rogozea EA, Lazar CA, Olteanu NL Meghea A and Mihaly M. Specific interactions within micelle microenvironment in different charged dye/surfactant systems. *Arab. J. Chem.* 2016; 9(1): 9-17.

Pillai IMS, Gupta AK and Sahoo C. Electrochemical oxidation of crystal violet dye (Basic Violet 3) using lead oxide electrodes; In: Proceedings of the IASTED International Conference Environmental Management and Engineering, 2011 July 4-6; Calgary, AB, Canada, 2011. pp. 4-6.

Rahman MM, Mollah MYA, Rahman MM and Susan MABH. Electrochemical behavior of malachite green in aqueous solutions of ionic surfactants. *ISRN Electrochem.* 2013; 2013: 839498.

Roy CK, Saha S and Susan MABH. Control over diffusion of ionic ferrocene species in aqueous solution using surfactant based organized media. *J. Electrochem. Soc.* 2020; 167(11): 116512.

Rusling JF. *Electroanalytical Chemistry*, Marcel Dekker, New York, 1994.

Saji T, Ebata K, Sugawara K, Liu S and Kobayashi K. Electroless plating of organic thin films by reduction of nonionic surfactants containing an Azobenzene group. *J. Am. Chem. Soc.* 1994; 116(13): 6053-6054.

Saji T, Hoshino K and Aoyagui S. Reversible formation and disruption of micelles by control of the redox state of the head group. *J. Am. Chem. Soc.* 1985; 107 (24): 6865-6868.

Saji T, Hoshino K, Ishii Y and Goto M. Formation of organic thin films by electrolysis of surfactants with the ferrocenyl moiety. *J. Am. Chem. Soc.* 1991; 113(2): 450-456.

Selvakumar PM. The art of converting molecules into machines: Supramolecular chemistry. *MOJ Biorg Org. Chem.* 2017; 1(4): 118-120.

Shahed, SMF, Islam, MJ, Choudhuri, MMR and Susan MABH. Effect of Added electrolytes on the critical micelle concentration of sodium dodecyl sulfate in aqueous solution. *J. Bangladesh Chem. Soc.* 2009; 22: 123-130.

Song JP, Guo YJ, Shuang SM and Dong C. Study on the inclusion interaction of ethyl violet with cyclodextrins by MWNTs/Nafion modified glassy carbon electrode. *J. Incl. Phenom. Macrocycl. Chem.* 2010; 68: 467-473

Susan MABH, Begum M, Takeoka Y and Watanabe M. Effect of pH and the extent of micellization on the redox behavior of non-ionic surfactants containing an anthraquinone group. *J. Electroanal. Chem*. 2000b; 481(2): 192-199.

Susan MABH, Begum M, Takeoka Y and Watanabe M. Study of the correlation of the cyclic voltammetric responses of a nonionic surfactant containing an anthraquinone group with the dissolved states. *Langmuir* 2000a; 16(7): 3509-3516.

Susan MABH, Ishibashi A, Takeoka Y and Watanabe M. Surface activity and redox behavior of a non-ionic surfactant containing a phenothiazine group. *Colloids Surf. B.* 2004; 38(3-4): 167-173.

Takeoka Y, Aoki T, Sani K, Ogata N, Yokoyama M, Okano T, Sakurai Y and Watanabe M. Electrochemical control of drug release from redox-active micelles. *J. Control. Release* 1995; 33(1): 79-87.

Takeoka Y, Aoki T, Sanui K, Ogata N and Watanabe M. Electrochemical studies of a redox-active surfactant. Correlation between electrochemical responses and dissolved states. *Langmuir* 1996; 12(2): 487-493.

Toma HE. Supramolecular nanotechnology: from molecules to devices. *Curr. Sci.* 2008; 95(9): 1202-1025.

Wang K, Munoz S, Zhang L, Castro R, Kaifer AE and Gokel GW. Organometallic amphiphiles: Oxidized ferrocene as headgroup for redox-switched bilayer and monolayer membranes. *J. Am. Chem. Soc.* 1996; 118(28): 6707-6715.

Xu B, Jiao K, Sun W and Zhang X. Recognition and determination of DNA using victoria blue b as electrochemical probe. *Int. J. Electrochem. Sci.* 2007; 2: 406-417.

Yeh P. The Electrochemistry of micelle-solubilized ferrocene. *J. Electrochem. Soc.* 1976; 123(9): 1334.

J. Bangladesh Acad. Sci. 48(1); 85-97: June 2024 DOI:https://doi.org/10.3329/jbas.v48i1.69554

Journal of Bangladesh Academy of Sciences

Journal homepage: http://www.bas.org.bd/publications/jbas.html

Research Article

Unveiling the unknown: a butterfly checklist of the Adampur forest in Bangladesh

Mohammad Quamruzzaman Babu[1], Akash Mojumdar[2], Prosenjit Debbarma[3],
Khurshed Alom[4] and Md Ashraf Ul Hasan*

*Department of Biological Sciences, Texas Tech University, Lubbock, Texas, USA

ARTICLE INFO

Article History

Received: 19 September 2023
Revised: 11 December 2023
Accepted: 3 March 2024

Keywords: Butterfly, Checklist, Diversity, Adampur, Lepidoptera, Bangladesh.

ABSTRACT

Our study focuses on the butterfly checklist of the Adampur forest beat, located in the Rajkandi Reserve Forest of Moulvibazar, Bangladesh. The study was conducted between December 2014 and January 2018 and aimed to document butterfly species in the area. A total of 266 butterfly species belong to 149 genera and 6 families (Papilionidae, Pieridae, Nymphalidae, Lycaenidae, Hesperiidae, and Riodinidae) were recorded. The Lycaenidae family exhibited the highest species richness, comprising 33.08% (n = 88) of the recorded species, while the Riodinidae family was the least prevalent, representing 0.38% (n = 1) of the species. In this study, the butterfly species recorded revealed varying conservation status according to the International Union for Conservation of Nature Bangladesh assessment, with 26.69% listed as Endangered, 30.08% Least Concern, 23.68% Vulnerable, 1.50% Data Deficient, and 18.05% Not Evaluated. These findings offer crucial insights for future butterfly research and conservation in the Adampur forest beat.

Introduction

Butterflies, belonging to the Order Lepidoptera in the Class Insecta are exquisite creatures defined by their delicate wings. They experience a four-stage life cycle: eggs, larvae, pupae, and adults, with each stage contributing to their fascinating transformation. As per the available data, approximately 19,500 known species of butterflies are distributed across various ecosystems and regions worldwide (Kawahara et al., 2023). Bangladesh has a rich diversity of butterflies. With remarkable diversity, the country hosts 305 butterfly species are distributed among 6 families (Chowdhury et al., 2021), potentially reaching 400 (Larsen, 2004; Chowdhury and Hossain, 2013).

Bangladesh is divided into seven geographic regions, referenced within the scope of wildlife distribution: South, Southeast, Central, Northeast, North, Northwest, and Southwest. (Khan, 2008). These seven geographical regions represent three distinct forest types (mangrove forest, mixed evergreen forest, and moist deciduous forest). Overpopulation and subsequent transformations of natural landscapes into human settlements, agricultural lands, and monoculture plantations have reduced the country's natural land cover to merely about 6%, thereby compromising a significant portion of its biodiversity (Hasan and Kingston, 2022). However, within the remaining natural landscapes of the country, the northeastern part of Bangladesh showcases a rich

---

*Corresponding author:<md-ashraf.ul-hasan@ttu.edu>

[1] *House: 25, Road: 18, Sector: 11, Uttara, Dhaka 1230, Bangladesh;* [2] *Department of Computer Science and Information Technology, Shanto-Mariam University of Creative Technology, Dhaka, Bangladesh;* [3] *Satchari Village, Satchari National Park, Chunarughat, Habiganj, Sylhet, Bangladesh;* [4] *Department of Zoology, Madanmohan College, Sylhet, Bangladesh*

butterfly diversity, providing a suitable home for species that are either threatened or abundant (Chowdhury et al., 2021). The majority of protected areas in this part of Bangladesh feature mixed evergreen forests, particularly in the Moulvibazar District of the Sylhet Division (Hasan and Kingston, 2022). The Adampur Forest lies within the northeastern region of Bangladesh, located under the Sylhet division (Fig. 1). This mixed evergreen forest is within the Indo-Burma biodiversity hotspot (Myers et al., 2000). Abundant in biodiversity, this forest is a thriving habitat for a diverse range of wild floral and faunal species. A total of 549 species of angiosperms from 412 genera and 123 families have been recorded with their natural distribution (Haque et al., 2016). The region has a rich faunal diversity, housing threatened mammals such as the hoolock gibbon, bengal slow loris, rhesus macaque, black giant squirrel, and barking deer. Bird species occurring in the Adampur beat, including the oriental dwarf kingfisher, kalij pheasant, Indian spotted eagle, and grey-headed parakeet, stand as a threatened category within the country (IUCN Bangladesh, 2015). Reptiles such as the changeable lizard, Pope’s green pit viper, spectacled cobra, and tokay gecko can also be observed. Extensive research efforts have been directed towards the flora of this region, yet the fauna, with a specific focus on butterflies, has remained relatively understudied. A notable gap in research pertains to butterflies, encompassing their habitat dynamics and the extent of species diversity within this ecosystem. Hence, this study's main objective was to create a comprehensive record of the butterfly population inhabiting the Adampur forest. Through synthesizing findings from prior research endeavors and our current study, we aimed to conduct an inventory study of butterflies in Adampur forest to contribute to the butterflies of Bangladesh. This study was designed to serve as a cornerstone for unveiling the intricate dynamics of butterfly populations, thereby making a significant contribution to the documentation of the exceptional biodiversity present within the Adampur forest.

Materials and Methods

Our study centered on constructing a butterfly checklist specifically for northeast Bangladesh. This study was conducted during this scheme between December 2014 and January 2018.

Study Area

The Adampur forest (24.26280 N and 91.91277 E) was selected as the study area based on its well-suited ecological conditions, which create an optimal habitat for a diverse range of butterfly species.

It is located within the Kamalganj upazila in the Moulvibazar district of Bangladesh (Fig. 1), which falls within the jurisdiction of the Rajkandi Reserve Forest range. The Adampur forest spans an extensive expanse of 5295.55 hectares and includes a mixture of deciduous and evergreen forests and hillocks, while the Dhalai River meanders through its neighboring vicinity (Islam et al., 2006).

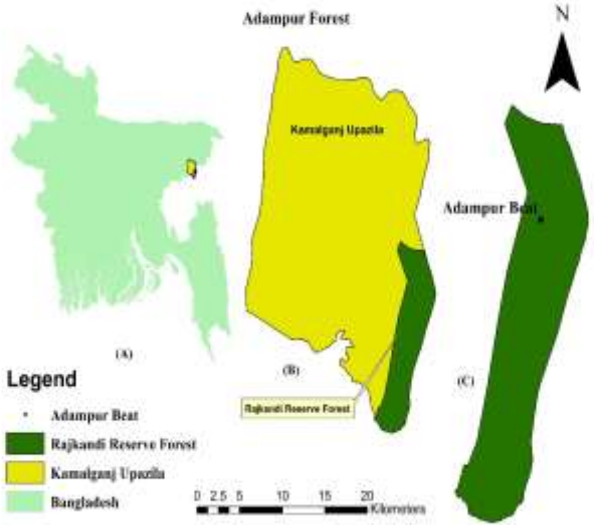

Fig. 1. Map of the study area. A) Bangladesh's political boundary; B) Kamalganj upazila under the Moulvibazar district; C) Adampur forest located within the Rajkandi Reserve Forest range.

The streams (in Bengali: Chara) run through the dense forest and hillocks. The thick foliage and large dipterocarp trees give rise to a verdant canopy above, which permits only intermittent solar irradiance to permeate the ecosystem below. The yearly precipitation averages around 275 centimeters, while the typical humidity is 82% (Tabassum, 2018).

Data collection and identification of butterfly species

The butterflies were observed and recorded, adhering to the established methodology described by Pollard and Yates (1993), as it provides an extensive approach for conducting long-term butterfly surveys (Patterson et al., 2023). Butterflies were observed walking along streams, roads, forest trails, timber plantation areas, villages, and around the forest. We carried out a survey along established transects to collect presence-absence data for butterflies. Each transect was approximately 1-2 kilometers long and 12 meters wide. These transects were randomly selected to encompass diverse habitat types, and consistent observations were carried out under suitable weather conditions to document butterfly species (Hasan et al., 2018), as butterfly diversity is strongly affected by severe weather conditions (Robinson et al., 2012).

The identification process of butterflies involved the utilization of field guides such as Kunte (2000), Chowdhury and Hossain (2013), and Kehimkar (2016). These guides provided valuable information regarding taxonomic and common names per the standards of Larsen (2004) and Kehimkar (2016). Digital and mobile phone cameras were employed to photograph the specimens to aid identification. The photographs of the individuals were then compared to the field guides (mentioned above) and extensive databases available on websites, such as https://www.ifoundbutterflies.org/, https://www.inaturalist.org/, and https://yutaka.it-n.jp/. These online resources proved to be valuable references during the identification process. To further clarify, we contacted the butterfly taxonomy experts from home and abroad. Finally, the classification system utilized to categorize the butterflies followed the guidelines that Larsen (2004) outlined. Information was gathered from IUCN Bangladesh (2015) to evaluate the local status of butterflies. The collected data was managed using Microsoft Excel (2016).

Result and Discussion

A total of 266 species of butterflies, comprising a range of 149 genera and 6 families, namely Papilionidae, Pieridae, Nymphalidae, Lycaenidae, Hesperiidae, and Riodinidae, were recorded throughout the study. In the realm of identified species, Lycaenidae exhibited the most species, which was 33.08%(n = 88), followed by Nymphalidae (29.32%, n =78), Hesperiidae (23.31%, n =62), Papilionidae (7.14%, n=19), Pieridae (6.77%, n=18), and Riodinidae (0.38%, n =1) (Fig. 2).

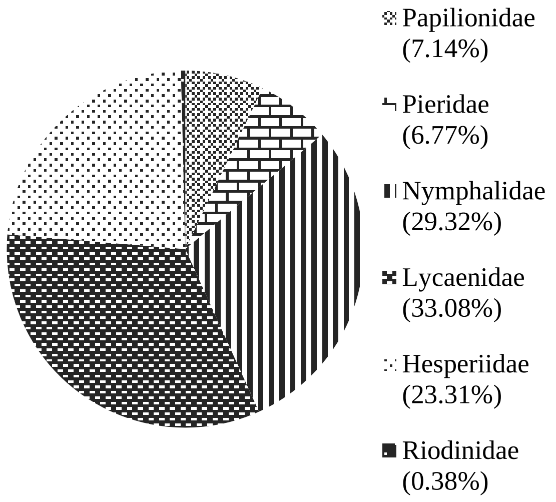

Fig. 2. Family-wise percentage of the recorded butterfly species.

Based on the information provided by IUCN Bangladesh (2015), it was found that 71 (26.69%) out of the total 266 species fell under the category of Endangered (EN), 63 species (23.68%) were identified as Vulnerable (VU), 80 species (30.08%) were listed as Least Concern (LC), and 4 species (1.50%) were included as Data Deficient (DD). Additionally, 48 species (18.05%) remained unassessed and were categorized as Not Evaluated (NE), thus not yet included in the country's red list (Fig. 3).

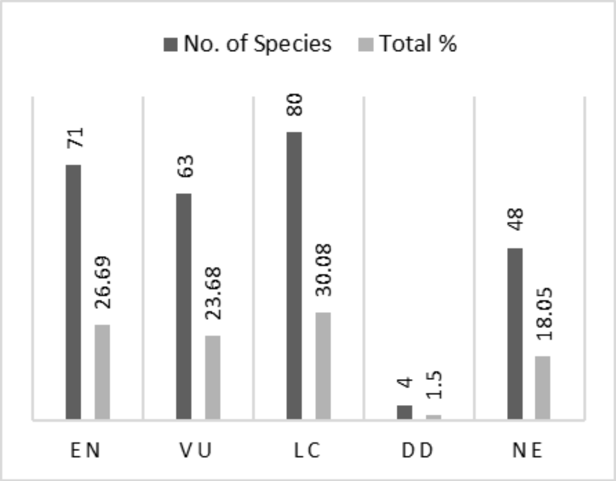

Fig. 3. Status of butterflies found in the Adampur forest (following IUCN Red List status, IUCN Bangladesh 2015).

Table 1. A checklist of butterfly species recorded in Adampur Beat within the Rajkandi Reserve Forest from December 2014 to January 2018 with their local status.

SL No.	Common Name	Scientific Name	Local Status
Family Papilionidae			
1	Common Batwing	*Atrophaneura varuna* (White, 1842)	EN
2	Common Mime	*Chilasa clytia* (Linnaeus, 1758)	LC
3	Tailed Jay	*Graphium agamemnon* (Linnaeus, 1758)	LC
4	Common Jay	*Graphium doson* (C. & R. Felder, 1864)	LC
5	Common Bluebottle	*Graphium sarpedon* (Linnaeus, 1758)	VU
6	White Dragontail	*Lamproptera curius* (Fabricius, 1787)	EN
7	Common Rose	*Pachliopta aristolochiae* (Fabricius, 1775)	LC
8	Common Raven	*Papilio castor* (Westwood, 1842)	EN
9	Yellow Helen	*Papilio chaon* (Westwood, 1845)	VU
10	Red Helen	*Papilio helenus* (Linnaeus, 1758)	VU
11	Lime Swallowtail	*Papilio demoleus* (Linnaeus, 1758)	LC
12	Great Mormon	*Papilio memnon* (Linnaeus, 1758)	LC
13	Blue Mormon	*Papilio polymnestor* (Cramer, 1775)	LC
14	Common Mormon	*Papilio polytes* (Linnaeus, 1758)	LC
15	Great Zebra	*Graphium xenocles* (Doubleday, 1842)	EN
16	Five-Bar Swordtail	*Graphium antiphates* (Cramer, 1775)	VU
17	Spot Swordtail	*Graphium nomius* (Esper, 1799)	EN
18	Common Birdwing	*Troides helena* (Linnaeus, 1758)	VU
19	Golden Birdwing	*Troides aeacus* (C. & R. Felder, 1860)	EN
Family Pieridae			
20	Common Albatross	*Appias albina* (Boisduval, 1836)	EN
21	Chocolate Albatross	*Appias lyncida* (Cramer, 1777)	LC
22	Striped Albatross	*Appias libythea* (Fabricius, 1775)	LC
23	Plain Puffin	*Appias indra* (Moore, 1858)	VU
24	Indian Cabbage White	*Pieris canidia* (Linnaeus, 1768)	LC
25	Common Emigrant	*Catopsilia pomona* (Fabricius, 1775)	LC
26	Mottled Emigrant	*Catopsilia pyranthe* (Linnaeus, 1758)	LC

27	Common Gull	*Cepora nerissa* (Fabricius, 1775)	LC
28	Red-Spot Jezebel	*Delias descombesi* (Boisduval, 1836)	LC
29	Common Jezebel	*Delias eucharis* (Drury, 1773)	LC
30	Painted Jezebel	*Delias hyparete* (Linnaeus, 1758)	LC
31	Red-Base Jezebel	*Delias pasithoe* (Linnaeus, 1767)	LC
32	One-Spot Grass Yellow	*Eurema andersonii* (Moore, 1886)	LC
33	Three-Spot Grass Yellow	*Eurema blanda* (Boisduval, 1836)	LC
34	Common Grass Yellow	*Eurema hecabe* (Linnaeus, 1758)	LC
35	Tree Yellow	*Gandaca harina* (Horsfield, 1829)	EN
36	Great Orange Tip	*Hebomoia glaucippe* (Linnaeus, 1758)	VU
37	Psyche	*Leptosia nina* (Fabricius, 1793)	LC
Family Nymphalidae			
38	Tawny Coster	*Acraea terpsicore* (Linnaeus, 1758)	LC
39	Constable	*Dichorragia nesimachus* (Doyère, 1840)	LC
40	Angled Castor	*Ariadne ariadne* (Linnaeus, 1763)	LC
41	Common Castor	*Ariadne merione* (Cramer, 1777)	LC
42	Common Sergeant	*Athyma perius* (Linnaeus, 1758)	LC
43	Color Sergeant	*Athyma inara* (Westwood, 1850)	VU
44	Blackvein Sergeant	*Athyma ranga* (Moore, 1858)	VU
45	Orange Staff Sergeant	*Athyma cama* (Moore, 1858)	EN
46	Leopard Lacewing	*Cethosia cyane* (Drury, 1773)	LC
47	Tawny Rajah	*Charaxes bernardus* (Fabricius, 1793)	EN
48	Black Rajah	*Charaxes solon* (Fabricius, 1793)	VU
49	Common Maplet	*Chersonesia risa* (Doubleday, 1848)	EN
50	Common Yeoman	*Cirrochroa tyche* (C. & R. Felder, 1861)	EN
51	Rustic	*Cupha erymanthis* (Drury, 1773)	LC
52	Common Map	*Cyrestis thyodamas* (Doyère, 1840)	EN
53	Plain Tiger	*Danaus chrysippus* (Linnaeus, 1758)	LC
54	Striped Tiger	*Danaus genutia* (Cramer, 1779)	LC
55	Blue Tiger	*Tirumala limniace* (Cramer, 1775)	LC
56	Dark Blue Tiger	*Tirumala septentrionis* (Butler, 1874)	VU
57	Glassy Tiger	*Parantica aglea* (Stoll, 1782)	VU
58	Common Duffer	*Discophora sondaica* (Boisduval, 1836)	LC
59	Red-Spot Duke	*Dophla evelina* (Stoll, 1790)	EN
60	Common Palmfly	*Elymnias hypermnestra* (Linnaeus, 1763)	LC
61	Spotted Palmfly	*Elymnias malelas* (Hewitson, 1863)	EN
62	Tiger Palmfly	*Elymnias nesaea* (Linnaeus, 1764)	EN
63	Long - Branded Blue Crow	*Euploea algea* (Godart, 1819)	EN
64	Common Crow	*Euploea core* (Cramer, 1780)	LC
65	Blue King Crow	*Euploea klugii* (Moore, 1858)	VU

66	Blue Spotted Crow	*Euploea midamus* (Linnaeus, 1758)	EN
67	Striped Blue Crow	*Euploea mulciber* (Cramer, 1777)	VU
68	Double Branded Blue Crow	*Euploea sylvester* (Fabricius, 1793)	EN
69	Common Baron	*Euthalia aconthea* (Cramer, 1777)	LC
70	Gaudy Baron	*Euthalia lubentina* (Cramer, 1777)	EN
71	Powdered Baron	*Euthalia monina* (Fabricius, 1787)	EN
72	White-Edged Blue Baron	*Euthalia phemius* (Doubleday, 1848)	EN
73	Great Eggfly	*Hypolimnas bolina* (Linnaeus, 1758)	LC
74	Danaid Eggfly	*Hypolimnas misippus* (Linnaeus, 1764)	VU
75	Peacock Pansy	*Junonia almana* (Linnaeus, 1758)	LC
76	Grey Pansy	*Junonia atlites* (Linnaeus, 1763)	LC
77	Yellow Pansy	*Junonia hierta* (Fabricius, 1798)	LC
78	Chocolate Pansy	*Junonia iphita* (Cramer, 1779)	LC
79	Lemon Pansy	*Junonia lemonias* (Linnaeus, 1758)	LC
80	Blue Pansy	*Junonia orithya* (Linnaeus, 1758)	VU
81	Orange Oakleaf	*Kallima inachus* (Doyère, 1840)	EN
82	Knight	*Lebadea martha* (Fabricius, 1787)	VU
83	Bamboo Treebrown	*Lethe europa* (Fabricius, 1775)	VU
84	Common Red Forester	*Lethe mekara* (Moore, 1858)	EN
85	Dark Archduke	*Lexias dirtea* (Fabricius, 1793)	EN
86	Common Evening Brown	*Melanitis leda* (Linnaeus, 1758)	LC
87	Commander	*Moduza procris* (Cramer, 1777)	LC
88	White-Bar Bushbrown	*Mycalesis anaxias* (Hewitson, 1862)	EN
89	Dark-brand Bushbrown	*Mycalesis mineus* (Linnaeus, 1758)	LC
90	Common Bushbrown	*Mycalesis perseus* (Fabricius, 1775)	VU
91	Long-Brand Bushbrown	*Mycalesis visala* (Moore, 1858)	VU
92	Chinese Bushbrown	*Mycalesis gotama* (Moore, 1858)	VU
93	Common Sailer	*Neptis hylas* (Linnaeus, 1758)	LC
94	Chestnut-Streaked Sailer	*Neptis jumbah* (Moore, 1858)	LC
95	Clear Sailer	*Neptis nata* (Moore, 1858)	VU
96	Nigger	*Orsotriaena medus* (Fabricius, 1775)	VU
97	Common Lascar	*Pantoporia hordonia* (Stoll, 1790)	VU
98	Perak Lascar	*Pantoporia paraka* (Butler, 1879)	EN
99	Clipper	*Parthenos sylvia* (Cramer, 1775)	VU
100	Common Leopard	*Phalanta phalantha* (Drury, 1773)	LC
101	Common Nawab	*Polyura athamas* (Drury, 1773)	LC
102	Jewelled Nawab	*Charaxes delphis* (Doubleday, 1843)	EN
103	Blue Nawab	*Charaxes schreiber* (Godart, 1824)	EN
104	Pallid Nawab	*Charaxes arja* (C. & R. Felder, 1867)	EN
105	Black Prince	*Rohana parisatis* (Westwood, 1851)	EN

106	Popinjay	*Stibochiona nicea* (Gray, 1846)	VU
107	Common Jester	*Symbrenthia lilaea* (Hewitson, 1864)	EN
108	Courtesan	*Euripus nyctelius* (Doubleday, 1845)	EN
109	Common Earl	*Tanaecia julii* (Lesson, 1837)	VU
110	Plain Earl	*Tanaecia jahnu* (Moore, 1858)	EN
111	Vagrant	*Vagrans egista* (Cramer, 1780)	VU
112	Cruiser	*Vindula erota* (Fabricius, 1793)	EN
113	Common Five-Ring	*Ypthima baldus* (Fabricius, 1775)	VU
114	Common Four-Ring	*Ypthima huebneri* (Kirby, 1871)	LC
115	Grey Count	*Tanaecia lepidea* (Butler, 1868)	VU
Family Lycaenidae			
116	Red Imperial	*Suasa lisides* (Hewitson, 1863)	NE
117	Plane	*Bindahara phocides* (Fabricius, 1793)	NE
118	Harlequin	*Taxila haquinus* (Fabricius, 1793)	EN
119	Blue Imperial	*Ticherra acte* (Moore, 1858)	NE
120	Common Imperial	*Cheritra freja* (Fabricius, 1793)	VU
121	Silver-streaked Acacia Blue	*Zinaspa todara* (Moore, 1884)	NE
122	Common Acacia Blue	*Surendra quercetorum* (Moore, 1858)	EN
123	Dark Oakblue	*Arhopala rama* (Kollar, 1844)	NE
124	Aberrant Oakblue	*Arhopala abseus* (Hewitson, 1862)	NE
125	Centaur Oakblue	*Arhopala centaurus* (Fabricius, 1775)	LC
126	Doherty‟s Dull Oakblue	*Arhopala khamti* (Doherty, 1891)	NE
127	Dusted Oakblue	*Arhopala bazaloides* (Hewitson, 1878)	DD
128	Falcate Oakblue	*Mahathala ameria* (Hewitson, 1862)	VU
129	Green Oakblue	*Arhopala eumolphus* (Cramer, 1780)	VU
130	Hewitson's Dull Oakblue	*Arhopala oenea* (Hewitson, 1869)	NE
131	Large Oakblue	*Arhopala amantes* (Hewitson, 1862)	VU
132	Spot Less Oakblue	*Arhopala fulla* (Hewitson, 1862)	NE
133	Tamil Oakblue	*Arhopala bazaloides* (Hewitson, 1878)	DD
134	Vinous Oakblue	*Arhopala athada* (Staudinger, 1889)	NE
135	Yellowdisc Tailless Oakblue	*Arhopala perimuta* (Moore, 1858)	EN
136	Indian Oakblue	*Arhopala atrax* (Hewitson, 1862)	NE
137	Assam Flash	*Rapala tara* (de Nicéville, 1889)	NE
138	Common Red Flash	*Rapala iarbus* (Fabricius, 1787)	VU
139	Copper Flash	*Rapala pheretima* (Hewitson, 1863)	VU
140	Indigo Flash	*Rapala varuna* (Horsfield, 1829)	VU
141	Scarlet Flash	*Rapala dieneces* (Hewitson, 1878)	EN
142	Slate Flash	*Rapala manea* (Hewitson, 1863)	LC
143	Suffused Flash	*Rapala suffusa* (Moore, 1878)	NE
144	Common Onyx	*Horaga onyx* (Moore, 1858)	NE
145	Witch	*Araotes lapithis* (Moore, 1858)	NE

146	Dingy Lineblue	*Petrelaea dana* (de Nicéville, 1884)	EN
147	Brown Lineblue	*Prosotas lutea* (Martin, 1895)	EN
148	Common Lineblue	*Prosotas nora* (C. Felder, 1860)	LC
149	Pointed Lineblue	*Ionolyce helicon* (Felder, 1860)	DD
150	Tailless Lineblue	*Prosotas dubiosa* (Semper, 1879)	VU
151	Transparent Six Lineblue	*Nacaduba kurava* (Moore, 1858)	NE
152	Teesta Brown Lineblue	*Prosotas lutea sivoka* (Evans, 1910)	EN
153	Pale Four-Lineblue	*Nacaduba hermus* (C. Felder, 1860)	NE
154	Common Hedgeblue	*Acytolepis puspa* (Horsfield, 1828)	VU
155	Pale Hedge Blue	*Udara dilecta* (Moore, 1879)	NE
156	White-Disc Hedge Blue	*Celatoxia albidisca* (Moore, 1884)	NE
157	Common Brownie	*Miletus chinensis* (C. Felder, 1862)	EN
158	Purple Leaf Blue	*Amblypodia anita* (Hewitson, 1862)	EN
159	Common Ciliate Blue	*Anthene emolus* (Godart, 1824)	VU
160	Pointed Ciliate Blue	*Anthene lycaenina* (R. Felder, 1868)	EN
161	Angled Pierrot	*Caleta decidia* (Hewitson, 1876)	LC
162	Banded Blue Pierrot	*Discolampa ethion* (Westwood, 1851)	VU
163	Black-spotted Pierrot	*Tarucus balkanica nigra* (Bethune-Baker, 1918)	NE
164	Common Pierrot	*Castalius rosimon* (Fabricius, 1775)	LC
165	Dark Pierrot	*Tarucus ananda* (de Nicéville, 1884)	NE
166	Himalayan Pierrot	*Tarucus venosus* (Moore, 1882)	NE
167	Striped Pierrot	*Tarucus nara* (Kollar, 1848)	EN
168	Common Tinsel	*Catapaecilma major* (Druce, 1895)	EN
169	Forget-me-not	*Catochrysops strabo* (Fabricius, 1793)	VU
170	Silver Forget-me-not	*Catochrysops panormus* (C. Felder, 1860)	NE
171	Lime Blue	*Chilades lajus* (Stoll, 1780)	LC
172	Orchid Tit	*Hypolycaena othona* (Hewitson, 1865)	VU
173	Toothed Sunbeam	*Curetis acuta* (Moore, 1877)	DD
174	Indian sunbeam	*Curetis thetis* (Drury, 1773)	LC
175	Double-Tufted Royal	*Dacalana penicilligera* (de Nicéville, 1890)	EN
176	Cornelian	*Deudorix epijarbas* (Moore, 1858)	NE
177	Gram Blue	*Euchrysops cnejus* (Fabricius, 1798)	LC
178	Indian Cupid	*Everes lacturnus* (Godart, 1824)	EN
179	Purple Sapphire	*Heliophorus epicles* (Godart, 1824)	VU
180	Common Tit	*Hypolycaena erylus* (Godart, 1824)	VU
181	Silverstreak Blue	*Iraota timoleon* (Stoll, 1790)	EN
182	Common Cerulean	*Jamides celeno* (Cramer, 1775)	LC
183	Dark Cerulean	*Jamides bochus* (Stoll, 1782)	VU
184	Metallic Cerulean	*Jamides alecto* (C. Felder, 1860)	LC

185	White Cerulean	*Jamides pura* (Moore, 1886)	EN
186	Pea Blue	*Lampides boeticus* (Linnaeus, 1767)	LC
187	Zebra Blue	*Leptotes plinius* (Fabricius, 1793)	LC
188	Yamfly	*Loxura atymnus* (Stoll, 1780)	VU
189	Malayan	*Megisba malaya* (Horsfield, 1828)	EN
190	Opaque Six-Lineblue	*Nacaduba beroe* (C. Felder & R. Felder, 1865)	LC
191	Small Four-Lineblue	*Nacaduba pavana* (Horsfield, 1828)	NE
192	Common Quaker	*Neopithecops zalmora* (Butler, 1870)	LC
193	Common Gem	*Poritia hewitsoni* (Moore, 1866)	EN
194	Bhutia Lineblue	*Prosotas bhutea* (de Nicéville, 1884)	NE
195	Pale Grass Blue	*Pseudozizeeria maha* (Kollar, 1844)	LC
196	Banded Royal	*Rachana jalindra* (Horsfield, 1829)	EN
197	Scarce Slate Flash	*Rapala scintilla* (de Nicéville, 1890)	NE
198	Chocolate Royal	*Remelana jangala* (Horsfield, 1829)	VU
199	Apefly	*Spalgis epius* (Westwood, 1851)	EN
200	Club Silverline	*Spindasis syama* (Horsfield, 1829)	VU
201	Long Branded Silverline	*Spindasis lohita* (Horsfield, 1829)	VU
202	Lesser Grass Blue	*Zizina otis* (Fabricius, 1787)	LC
203	Dark Grass Blue	*Zizeeria karsandra* (Moore, 1865)	LC
Family Hesperiidae			
204	Pygmy Scrub Hopper	*Aeromachus pygmaeus* (Fabricius, 1775)	VU
205	Bush Hopper	*Ampittia dioscorides* (Fabricius, 1793)	NE
206	Forest Hopper	*Astictopterus jama* (C. & R. Felder, 1860)	LC
207	Common Banded Demon	*Notocrypta paralysos* (Wood-Mason & de Nicéville, 1881)	LC
208	Grass Demon	*Udaspes folus* (Cramer, 1775)	LC
209	Restricted Demon	*Notocrypta curvifascia* (C. & R. Felder, 1862)	EN
210	Spotted Demon	*Notocrypta feisthamelii* (Boisduval, 1832)	NE
211	Chocolate Demon	*Ancistroides nigrita* (Latreille, 1824)	NE
212	Tree Flitter	*Hyarotis adrastus* (Stoll, 1780)	VU
213	Bengal Swift	*Pelopidas agna* (Moore, 1866)	LC
214	Black Paint-brush Swift	*Baoris unicolor* (Moore, 1884)	EN
215	Ceylon Swift	*Parnara bada* (Moore, 1878)	EN
216	Paintbrush Swift	*Baoris farri* (Moore, 1878)	NE
217	Conjoined Swift	*Pelopidas conjuncta* (Herrich-Schäffer, 1869)	LC
218	Contiguous swift	*Polytremis lubricans* (Herrich-Schäffer, 1869)	EN
219	Continental Swift	*Parnara ganga* (Evans, 1937)	NE
220	Dark Straight Swift	*Parnara apostate* (Chiba & Eliot, 1991)	NE
221	Great swift	*Pelopidas*	EN

		assamensis (de Nicéville, 1882)	
222	Rice Swift	*Borbo cinnara* (Wallace, 1866)	LC
223	Small Branded Swift	*Pelopidas mathias* (Fabricius, 1798)	VU
224	Straight Swift	*Parnara guttatus* (Bremer & Grey, 1852)	LC
225	Large Bengal Swift	*Pelopidas subochracea* (Moore, 1878)	NE
226	Dark Yellow-Banded Flat	*Celaenorrhinus aurivittata* (Moore, 1879)	EN
227	Common Small Flat	*Sarangesa dasahara* (Moore, 1866)	VU
228	Common Snow Flat	*Tagiades japetus* (Stoll, 1781)	VU
229	Common Spotted Flat	*Celaenorrhinus leucocera* (Kollar, 1848)	NE
230	Fulvous Pied flat	*Pseudocolade-nia dan* (Fabricius, 1787)	EN
231	Suffused Snow Flat	*Tagiades gana* (Moore, 1866)	VU
232	Tricolor Pied Flat	*Coladenia indrani* (Moore, 1866)	NE
233	Water Snow Flat	*Tagiades litigiosa* (Möschler, 1878)	EN
234	Indian Ace	*Halpe homolea* (Hewitson, 1868)	NE
235	Light Straw Ace	*Pithauria stramineipennis* (Wood-Mason & de Nicéville, 1887)	NE
236	Moore's Ace	*Halpe porus* (Mabille, 1877)	VU
237	Shorthorn Ace	*Halpe veluvana* (Evans, 1932)	NE
238	Banded Ace	*Halpe zema* (Hewitson, 1877)	NE
239	Common Awl	*Hasora badra* (Moore, 1858)	VU
240	Common Banded awl	*Hasora chromus* (Cramer, 1780)	EN
241	Brown Awl	*Badamia exclamationis* (Fabricius, 1775)	VU
242	Banded Orange Awlet	*Burara oedipodea* (Swainson, 1820)	NE
243	Indian Awl King	*Choaspes benjaminii* (Guérin-Méneville, 1843)	EN
244	Small Green Awlet	*Burara amara* (Moore, 1866)	EN
245	Chestnut Bob	*Iambrix salsala* (Moore, 1866)	LC
246	Grass Bob	*Suada swerga* (de Nicéville, 1895)	NE
247	Indian Palm Bob	*Suastus gremius* (Fabricius, 1798)	EN
248	Narrow-banded Velvet Bob	*Koruthaialos rubecula cachara* (Evans, 1949)	EN
249	Small Palm Bob	*Suastus minuta* (Moore, 1877)	NE
250	Dark Velvet Bob	*Koruthaialos butleri* (de Nicéville, 1884)	NE
251	Common Wight	*Iton semamora* (Moore, 1866)	NE
252	Common Redeye	*Matapa aria* (Moore, 1866)	LC
253	Black Veined Branded Redeye	*Matapa sasivarna* (Moore, 1866)	VU
254	Giant Redeye	*Gangara thyrsis* (Fabricius, 1775)	VU
255	Fringed Redeye	*Matapa cresta* (Evans, 1949)	NE
256	Chestnut Angle	*Odontoptilum angulata* (C. Felder, 1862)	LC
257	Common Dartlet	*Oriens gola* (Moore, 1877)	LC
258	Smaller Dartlet	*Oriens goloides* (Moore, 1881)	VU

259	Common Grass Dart	*Taractrocera maevius* (Fabricius, 1793)	NE
260	Dark Palm Dart	*Telicota bambusae* (Moore, 1878)	VU
261	Wax Dart	*Cupitha purreea* (Moore, 1877)	EN
262	Pale Palm Dart	*Telicota colon* (Fabricius, 1775)	NE
263	Tufted Ace	*Sebastonyma dolopia* (Hewitson, 1868)	EN
264	Indian Grizzled Skipper	*Spialia galba* (Fabricius, 1793)	LC
265	Banana Skipper	*Erionota torus* (Evans, 1941)	EN
Family Riodinidae			
266	Punchinello	*Zemeros flegyas* (Cramer, 1780)	LC

A total of 266 butterfly species have been identified in the study area, showcasing a notably extensive array of butterfly fauna. This stark disparity in richness becomes evident when comparing the butterfly fauna of the study area with that of diverse protected areas situated in northeast Bangladesh: 195 butterfly species were recorded in Satchari National Park (Hasan et al., 2018), 159 species in Lawachara National Park (Khandokar et al., 2013), and 74 species in Rema-Kalenga Wildlife Sanctuary (Shihan and Prodhan, 2014). In addition, numerous previously undocumented species have been newly recorded in Bangladesh, with their discoveries originating from the Adampur forest. Notable instances include *Graphium megarus* (Westwood, 1844) observed in March 2013 (Khan et al., 2014), *Logania distanti massalia* (Doherty, 1891) encountered in December 2014 (Sadat et al., 2016), *Zinaspa todara distorta* (de Nicéville, 1887) sighted in March 2016 (Khan et al., 2017), *Arhopala rama ramosa* (Evans, 1925) documented in April 2016 (Khan et al., 2017), and *Kaniska canace* (Linnaeus, 1763) identified in March 2017 (Neogi et al., 2018). Furthermore, *Chersonesia intermedia* (Martin, 1895) was added to the roster in September 2022 (Rashid et al., 2022). However, the species listed, namely *Graphium megarus*, *Logania distanti massalia*, *Kaniska canace*, and *Chersonesia intermedia*, have not been encountered in our research endeavors or other investigations. These findings underscore the dynamic biodiversity of the Adampur forest and its contribution to expanding the known butterfly species repertoire within Bangladesh. Hence, a compelling need emerges to escalate our efforts, encompassing a comprehensive array of fauna, to undertake supplementary research initiatives dedicated to the conservation of the mentioned species and all other coexisting fauna.

The extensive range of butterfly species reflects a healthy environment, as butterflies act as sensitive indicators of environmental and habitat changes (Thomas, 2005; Gross et al., 2007). A higher presence of herbaceous plants creates favorable conditions and sustenance for butterfly species.

In the study area, there were 266 identified butterfly species, and out of these, 134 species (50.37%, EN = 26.69%, and VU = 23.68%) accounted for and fell into the threatened category (IUCN Bangladesh, 2015). The prevailing ecological factor responsible for this situation predominantly involves habitat deterioration, primarily initiated by the alteration of natural land covers into agricultural lands, which includes timber plantations, human settlements, and the expansion of infrastructure (buildings, roads, and bridges) in the area (Hasan and Kingston, 2022). A group of 48 species constituted 18.05% of the total 266 species that are Not Evaluated species (IUCN Bangladesh, 2015). To gain a comprehensive understanding of the ecology and potential threats to these unassessed species, it is imperative to undertake ecological research, evaluate their distribution, monitor population dynamics, and identify specific endangerment factors.

The current butterfly checklist will serve as a baseline, reinforcing the need for further ecological research. Undertaking this inventory will play a pivotal role in refining the checklist, cataloging the butterflies' host plants, and enabling a more precise and effective conservation strategy for the Adampur Forest's butterfly population.

Conclusions

The study of Adampur Forest's butterfly diversity highlighted its role as a vital habitat for 266 species across six families. The distribution percentages among families emphasize the ecosystem's complexity. Conservation urgency is evident. Half of the recorded species are threatened. The discovery of previously undocumented species underscores the significance of the biodiversity of this forest. Butterflies' sensitivity to environmental changes and their ecological roles emphasizes the need for continued conservation. The existing butterfly checklist was a fundamental reference, yet its limitations underscore the vital need for continuous ecological studies. Updating the checklist, documenting host plants, and refining conservation strategies will be pivotal in preserving the butterfly population within the Adampur Forest, particularly amidst changing environmental conditions. This study is a cornerstone for understanding the forest's biodiversity and significant contribution to the broader ecosystem.

Acknowledgment

The authors would like to thank the field assistants and the local community for helping in conducting the study. The taxonomic identification of butterfly species was made possible with the assistance of experts from Bangladesh and abroad. We thank Md. Naim Ur Rashid for creating the study area map.

Author contributions

Conceptualization: MQB, PD, MAUH; methodology: MAUH, MQB; data collection and curation: MQB, MAUH, PD, KA, AM; original draft preparation: AM, MAUH; draft review and editing: MAUH, AM; supervision: MAUH. Following revisions, all authors approved the manuscript.

References

Chowdhury S, Alam S, Chowdhury SU, Rokonuzzaman M, Shahriar SA, Shome AR and Fuller RA. Butterflies are weakly protected in Bangladesh, a mega-populated country. *Glob. Ecol. Conserv.* 2021; 26: e01484.

Chowdhury SH and Hossain M. *Butterflies of Bangladesh: A Pictorial Handbook.* 2nd ed. Dhaka, Bangladesh: Skylark Printers; 2013. p.260.

Gross K, Kalendra EJ, Hudgens BR and Haddad NM. Robustness and uncertainty in estimates of butterfly abundance from transect counts. *Popul. Ecol.* 2007; 49: 191-200.

Haque AKMK, Khan SA, Uddin SN and Rahim MA. Taxonomic checklist of the pteridophytes of Rajkandi Reserve Forest, Moulvibazar, Bangladesh. *Jahangirnagar University J. Biol. Sci.* 2016; 5(2): 27-40.

Hasan MAU and Kingston T. Bats of Bangladesh-A systematic review of the diversity and distribution with recommendations for future research. *Diversity,* 2022; 14(12): 1042.

Hasan MAU, Neha SA, Baki MA and Babu MQ. An inventory of butterfly species in relation to food sources and climatic factors influencing their diversity and richness in a semievergreen forest of Bangladesh. *Arthropods,* 2018; 7(3): 53-68.

Islam MA, Feeroz MM, Muzaffar SB, Kabir MM and Begum S. *Conservation of the Hoolock Gibbons (Hoolock hoolock) of Bangladesh: Population estimates, habitat suitability and management options.* Report to United States, Fish and Wildlife Service. Washington D.C. Mincograph, 2006. P. 48.

IUCN Bangladesh. *Red List of Bangladesh, Volume 7: Butterflies,* IUCN (International Union for Conservation of Nature Bangladesh) Bangladesh Country Office Dhaka, Bangladesh; 2015, p. 400.

Kawahara AY, Storer C, Carvalho APS, Plotkin DM, Condamine FL and Braga MP, et al. A global phylogeny of butterflies reveals their evolutionary history, ancestral hosts, and biogeographic origins. *Nat. Ecol. Evol.* 2023; 7: 903-913.

Kehimkar ID. *Butterflies of India.* BNHS Field Guides. Mumbai Bombay Natural History Society; 2016, p. 505.

Khan AKMMA, Khan T and Khan MK. Three new records of Butterflies from the northeastern region of Bangladesh. *The Festschrift on the 50th Anniversary of the IUCN Red List of Threatened Species, IUCN Bangladesh*, 2014; pp. 35-38.

Khan MMH. *Protected Areas of Bangladesh – A Guide to Wildlife.* Dhaka, Bangladesh: Nishorgo Program, Wildlife Management and Nature Conservation Circle, Bangladesh Forest Department; 2008, p. 304.

Khan T, Babu MQ, Hasan MAU, Shihan TR and Debbarma P. First records of *Zinaspa todara distorta* de Nicéville, 1887 and *Arhopala rama ramose* Evans, 1925 (Lycaenidae: Theclinae) butterflies in Bangladesh. *J. Threat. Taxa.* 2017; 9(8): 10581-10584.

Khandokar F, Rashid M, Das DK and Hossain M. Species diversity and abundance of Butterflies in the Lawachara National Park, Bangladesh. *Jahangirnagar Univ. J. Biol. Sci.* 2013; 2(2): 121-127.

Kunte K. *Indian-A lifescape butterflies of peninsular India.* India: Universities Press (India) Private Limited; 2000, p. 254.

Larsen TB. *An annotated checklist of the butterflies of Bangladesh (Lepidoptera, Rhopalocera).* Dhaka, Bangladesh: IUCN (International Union for Conservation of Nature Bangladesh) Bangladesh Country Office; 2004, p. 158.

Myers N, Mittermeier RA, Mittermeier CG, Fonseca GAB and Kent J. Biodiversity hotspots for conservation priorities. *Nature* 2000; 403: 853-858.

Neogi AK, Islam MJ, Shalauddin M, Mondal AC and Hossain S. The first record of the Blue Admiral *Kaniska canace* Linnaeus, 1763 (Nymphalidae: Lepidoptera) from Bangladesh. *J. Threat. Taxa.* 2018; 10(10): 12429-12431.

Patterson S, Harris J, Dinsmore S and Kinkead K. Evaluating differences in density estimation for central Iowa butterflies using two methodologies. *Peer J.* 2023; 11: e16165.

Pollard E and Yates V. *Monitoring Butterflies for Ecology and Conservation.* Chapman and Hall, London, UK: Springer Dordrecht; 1993, p. 292.

Rashid NU, Kayes MI, Oli MH and Kadija U. A new record of *Chersonesia intermedia* (Martin, 1895) for Bangladesh. *J. Entomol. Zool. Stud.* 2022; 10(6): 19-21.

Robinson N, Armstead S and Bowers MD. Butterfly community ecology: the influences of habitat type, weather patterns, and dominant species in a temperate ecosystem. *Entomol. Exp. Appl.* 2012; 145(1): 50-60.

Sadat MN, Neogi AK, Rahman MS, and Mondal AC. Notes on Two Lycaenid Butterflies Confirm to Bangladesh. *Biolife*, 2016; 4(1): 213-215.

Shihan TR and Prodhan MAH. Butterflies of Rema-Kalenga wildlife sanctuary, Habiganj, Bangladesh. *Int. J. Fauna Biol.* 2014; 1(6): 96-100.

Tabassum N. A taxonomic account of pteridophytic flora of Adampur forest, Moulvibazar district, Bangladesh. *Dhaka Univ. J. Biol. Sci.* 2018; 27(1): 101-111.

Thomas JA. The ecology and conservation of Maculinea arion and other European species of large blue butterfly. Ecology and Conservation of Butterflies. *Chapman and Hall.* 1995, pp. 180-210.

J. Bangladesh Acad. Sci. 48(1); 99-109: June 2024 DOI:https://doi.org/10.3329/jbas.v48i1.71278

Journal of Bangladesh Academy of Sciences

Journal homepage: http://www.bas.org.bd/publications/jbas.html

Research Article

Comparison of non-monotonic and monotonic potentials for cross-sections and analyzing powers of ^{6}Li elastic scattering on ^{12}C at 30 MeV

M. Sujan Islam*, M. Rubel Alamin[1], M. A. Sattar, Shefael K Joarder[2], A. S. B. Tariq[2] and A. K. Basak[2]

Department of Physics, Hajee Mohammad Danesh Science and Technology University, Dinajpur, Bangladesh

ARTICLE INFO

Article History

Received: 30 January 2024
Revised: 19 March 2024
Accepted: 28 March 2024

Keywords: Elastic scattering, Optical model, Energy density function, Non-monotonic, Monotonic

ABSTRACT

The experimental angular distributions of differential cross-section (CS), vector analyzing power (iT_{11}) and tensor analyzing powers (T_{20}, T_{21}, and T_{22}) for the ^{12}C(^{6}Li, ^{6}Li)^{12}C elastic scattering at laboratory energy of 30 MeV are simultaneously analyzed in the structure of simple optical model (OM) using shallow Non-Monotonic (NM) and deep Monotonic Woods-Saxon (MWS) potentials. The Pauli-laden energy density functional (EDF) theory, which results in NM potentials, is also discussed. Equally good fits to the CS, T_{20}, T_{21}, and T_{22} data are obtained using both NM and MWS potentials. But iT_{11} data is only reproduced well using NM potentials in OM. The shallow NM potentials seem better than the deep MWS for simultaneous description of the CS, iT_{11}, T_{20}, T_{21}, and T_{22} data.

Introduction

The best choice of the nuclear interaction potential between two nuclei is a long-standing and challenging problem (Brandan and Satchler, 1997). The study of nucleus-nucleus (NN) potentials is essential not only to understand the structure of the nucleus (Basak et al., 2022) but also for the burning of stars (Duarte et al., 2015) and dynamics of the nucleosynthesis for astrophysics (Thomas, 2020). The exact and reliable NN potential can only lead us to the deep learning of nuclear matter and its structures in the whole universe. The elastic scattering, including diffractive and refractive structures, is significant in obtaining the true nature of NN potentials (Hussain and McVoy, 1948; Hussain and Satchler, 1994; Khoa et al., 2007). The elastic ^{6}Li+^{12}C scattering system also shows diffractive and refractive structures in a wide range of incident energies (Trcka et al., 1990). A few numbers of simultaneous studies are done with the interaction of polarized ^{6}Li on ^{12}C to reproduce the experimental cross section *(CS)*, vector analyzing power (VAP) (iT_{11}), and tensor analyzing power (TAP) (T_{20}, T_{21}, and T_{22}) data (Reber et al.,1994; Kerr et al., 1996; Kerr et al., 1995) but none of them have reproduced the data well. Reber et al. (1994) using Woods-Saxon (WS) potentials, showed that the description of the iT_{11} data needs an angular momentum (*J*)-dependent absorption interaction. Kerr et al. (1995) performed an optical model (OM) analysis of the ^{6}Li+^{12}C elastic scattering at 30 MeV using phenomenological WS potentials, including a *J*-dependent absorption term. They found that T_{21} arises mainly from the tensor interaction, T_{20} from coupling the *J*-dependent and tensor interactions, and the most complicated iT_{11} stems from a combination of the spin-orbit, tensor, and *J*-dependent interactions.

---

*Corresponding author:<sujan4367@gmail.com>

[1] *Bangladesh Atomic Energy Commission, Dhaka, Bangladesh*

[2] *Department of Physics, University of Rajshahi - Rajshahi, Bangladesh*

There are two types of nuclear potentials used in OM for the real part: the phenomenological optical potential (OP) and the microscopically derived one. The phenomenological OPs directly obtained from the analysis of elastic scattering data are found to suffer from discrete and continuous potential ambiguities (Mohr et al., 1997; Satchler, 1983; Islam et al., 2021a; Islam et al., 2021b; Islam et al., 2021c). It is very challenging to remove ambiguities of potential parameters. The discrete potential ambiguity can only be eliminated in the refractive angular structure at higher energies for all kinds of OPs (Goldberg and Smith, 1972; Goldberg et al., 1973; Khoa et al., 2007; Islam et al., 2021a; Islam et al., 2021b) where the CS maximum of the primary nuclear rainbow is followed by an exponential type falloff pattern in the shadow region classically. The microscopic nuclear potentials such as Double Folding (DF) (Satchler and Love, 1979) and Non-Monotonic (NM) (Basak et al., 2011) are directly derived from the microscopic theories. The DF potentials for the Li-nucleus elastic scattering need a significant renormalization factor of $N_R 0.5-0.6$ (Pakou, 2008) in the simple OM to reproduce the CS data and lead to a complete failure to explain the opposite signs of vector analyzing power (iT_{11}) for the ^{6,7}Li elastic scattering. However, all nuclear potentials can be grouped into Monotonic and Non-Monotonic (NM), respectively, without and with repulsive potential at the core. The schematic difference between Monotonic and NM potentials is shown in Fig. 1. The NM potentials are derived from the EDF theory of Brueckner et al. (1968) which incorporates appropriately the Pauli-principle and the derived potentials become shallow in terms of volume integral per nucleon pair (J_R/A_PA_T), A_P and A_T being the mass numbers of the projectile and target nuclei, respectively. Familiar Woods-Saxon (WS) (Woods and Saxon, 1954), Squared Woods-Saxon (SWS) (Michel et al., 1983), and widely used double folding (DF) (Satchler and Love, 1979) potentials are monotonic and deep.

The microscopic NM potential with a repulsive core derived from the EDF theory of (Brueckner et al., 1968a; Brueckner et al., 1969) (BCD) which incorporates appropriately the Pauli principle enjoyed several successes in recent years which include: (i) the alpha-elastic scattering (Tariq et al., 1999), (ii) alpha-inelastic scattering (Basak et al., 2001), (iii) one- (Das et al., 1999), two- (Das et. al., 2000a; Das et al., 2001), three-nucleon (Das et al., 2000b) transfer reactions, (iv) band-mixing of band heads $I^\pi = 1/2^+$ and $I^\pi = 3/2^+$in the Nilsson model (Hossain et al., 2005), (v) verification of the Goldberg criterion (Goldberg and Smith, 1972) of the ^{16}O+^{16}O (Islam et al., 2021a) and ^{12}C+^{12}C (Islam et al., 2021b) elastic scattering with discussion on the intriguing aspect at potential families at lower energies, (vi) ^{16}O+^{16}O cluster states and their fusion to ^{32}S (Basak et al., 2022), (vii) a novel method (Hossain et al., 2015) for determining the nuclear incompressibility K for cold nuclear matter using the ^{16}O+^{16}O elastic scattering. (viii) The opposite signs of the vector analyzing power (VAP) of ^{6,7}Li elastic scattering by ^{58}Ni at 20 MeV (Basak et al., 2011) and ^{120}Sn at 44 MeV (Basak et al., 2011) are reproduced successfully using NM potentials in the OM. This result eliminates a long-standing puzzle. (ix) The NM potential also reveals explicitly the multiple potential families (Islam et al., 2021a; Islam et al., 2021b) at low energies, which can produce an excellent description of elastic experimental data over an extensive angular range.

In the present investigation, the elastic ^{6}Li+^{12}C experimental differential CS, iT_{11}, T_{20}, T_{21}, and T_{22} data at the incident laboratory energy of 30 MeV are analyzed within the structure of the OM using shallow NM and deep Monotonic Woods-Saxon (MWS) (Woods and Saxon, 1954) OPs without including J-dependent absorption term. The present article also discusses the Pauli-laden BCD's EDF (Brueckner et al., 1968a) for deriving the NM potentials. The results obtained using both the NM and MWS potentials are compared. The latter uses the Woods-Saxon form factor (Woods and Saxon, 1954).

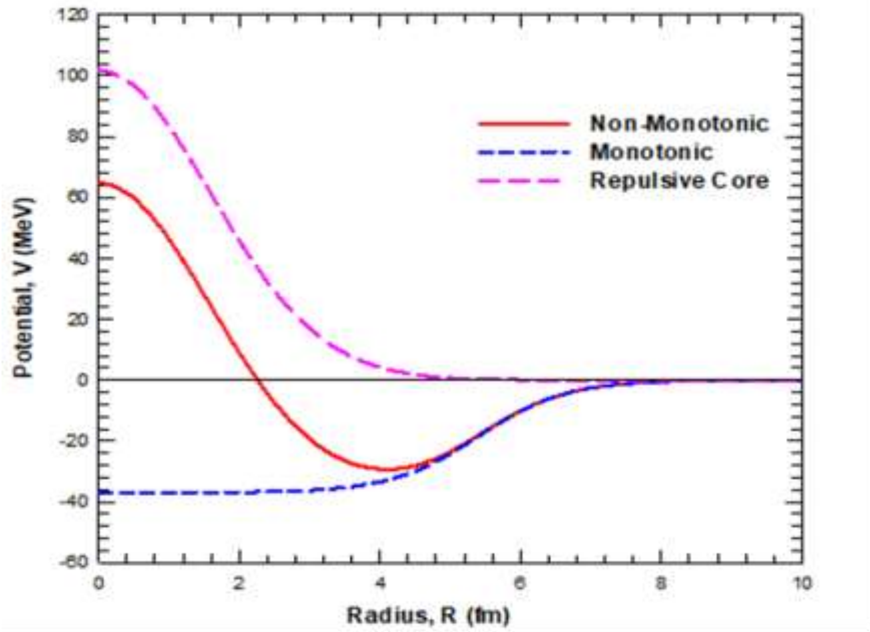

Fig. 1. A schematic difference between Monotonic (dashed blue line) and Non-Monotonic (solid red line) potentials, respectively, without and with repulsive core (pink medium dashed line).

Optical Model Potentials

Energy Density Functional (EDF) Theory

The energy of a nucleus in the EDF theory (Brueckner et al., 1968a) is expressed in terms of density distribution $\rho(r)$ as

$$E = \int \varepsilon[\rho(\boldsymbol{r})]\mathrm{d}^3\boldsymbol{r} \tag{1}$$

where, the energy density $\boldsymbol{\epsilon}[\boldsymbol{\rho}(\boldsymbol{r})]$ is given by

$$\boldsymbol{\epsilon}[\boldsymbol{\rho}(\boldsymbol{r})] = \mathbf{0.3}\left(\frac{\hbar}{2M}\right)\left(\frac{3\pi^2}{2}\right)^{\frac{2}{3}}[\mathbf{1}-\boldsymbol{\xi})^{\frac{5}{3}} + (\mathbf{1}+\boldsymbol{\xi})^{\frac{5}{3}}] \times \boldsymbol{\rho}^{\frac{5}{3}} + \boldsymbol{\nu}(\boldsymbol{\rho},\boldsymbol{\xi})\boldsymbol{\rho} + \frac{e}{2}\emptyset_C(\boldsymbol{r})\boldsymbol{\rho}_p - \mathbf{0.739}e^2\boldsymbol{\rho}_p^{\frac{4}{3}} + \left(\frac{\hbar^2}{8M}\right) \tag{2}$$

Here, M represents the mass of a nucleon, and $\xi = (N - Z)/A$ represents the neutron excess parameter. The first term in (2) arises from the nucleon kinetic energy in nuclear matter. The second term is determined from the Gammel-Christian-Thaler (GCT) nucleon-nucleon (n-n) potential (Brueckner and Gammel,1958) in the Brueckner-Hartree-Fock (BHF) theory. The GCT potential is formed by the combination of central, spin-orbit, and tensor potential parts of the realistic n-n potential, which can describe all the properties of deuteron and the n-n scattering data up to the pion threshold (~137 MeV). In the BHF theory, the mean-field relates the matrix elements of the n-n potential (Brueckner et al., 1968a) to those of the scattering operator with full consideration of the Pauli principle among the nucleons of the same type in the nuclear and nucleonic matter approximations, i.e., using the plane wave for nucleonic wave functions. The third term represents the Coulomb energy, and the fourth term is the correction of Coulomb energy due to the consideration of the Pauli principle among protons (Brueckner et al., 1968b; Hossain et al., 2015). The last term arises due to the inhomogeneity correction (Brueckner et al.,1968b; Hossain et al., 2015) to the kinetic energy due to the finite size and correlation effect among nucleons. The density dependence of the energy per nucleon, *E/A*, in the nuclear and nucleonic matter using the BGT n-n potential with full consideration of the Pauli principle has been calculated in (Brueckner et al. 1968a, Hossain et al., 2015).

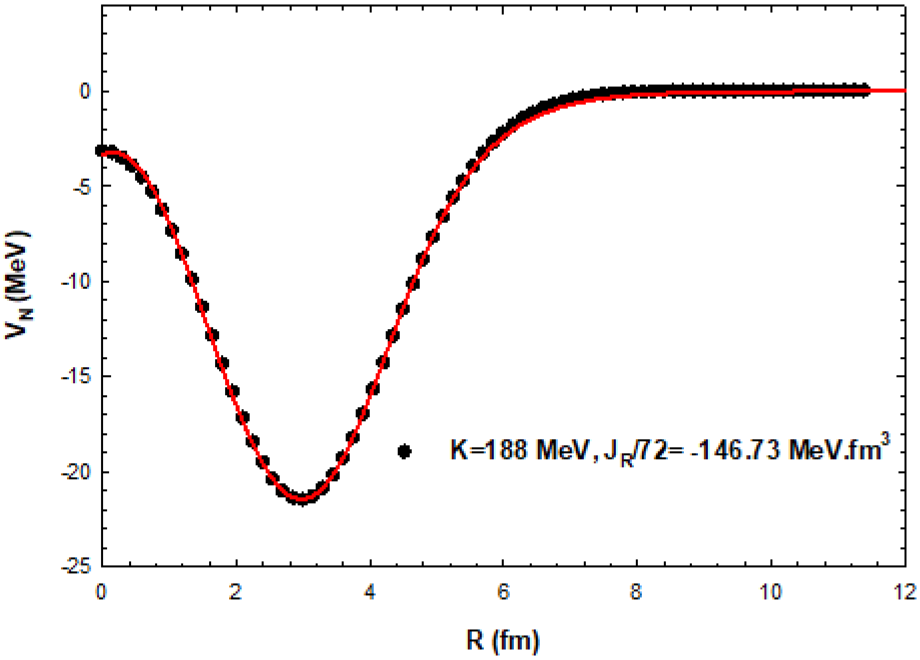

Fig. 2. Parameterization of EDF-generated nuclear potential points for *K*=188. The parameters are listed in Table 1.

Table 1. The equivalent 2pF DDFs parameters for ^{6}Li and ^{12}C.

Nucleus	**2pF DD Function parameters**			**Binding Energy**	
	c (fm)	*z* (fm)	ρ_0 (fm^{-3})	Calculated (MeV)	Experimental (MeV)
^{6}Li	1.333	0.577	0.2118	33.2	32.0
^{12}C	2.294	0.434	0.1752	92.0	92.2

The density dependence of the mean-field $v(\rho,\xi)$ for a symmetric (ξ=0) and homogeneous part of a finite nucleus has been parameterized analytically (Hossain et al., 2015) as

$$v(\rho,\xi=0)=\lambda_1\rho+\lambda_2\rho^{4/3}+\lambda_3\rho^{5/3} \qquad (3)$$

Here, the values of the mean-field parameters for *K*= 188 MeV are

$\lambda_1=-741.28, \lambda_2=+1179.55$, and $\lambda_3=-467.54$, as given in (Hossain et al., 2015).

The EDF potential *V(R)* between the projectile and the target at an interaction distance of *R* is given by

$$V(R)=E[\rho(\boldsymbol{r},R)]-E[\rho_P(\boldsymbol{r},R=\infty)]-E[\rho_T(\boldsymbol{r},R=\infty)] \qquad (4)$$

Here, ρ represents the composite nucleus's density distribution function (DDF). And ρ_P and ρ_T represents the DDFs for the projectile and the target at *R*= ∞, respectively. The DDF of the composite nucleus in the sudden approximation is given as

$$\rho(\boldsymbol{r})=\rho_P(\boldsymbol{r})+\rho_T(\boldsymbol{r}) \qquad (5)$$

The sources of density distribution functions (DDFs) are for ^{6}Li from (Bray et al., 1972) and ^{12}C from (Sick, 1974). These DDFs are re-parametrized by the two-parameter Fermi (2pF) function for application to the EDF calculation as

$$\rho(\boldsymbol{r})=\rho_0[1+\exp\left(\frac{r-c}{z}\right)]^{-1} \qquad (6)$$

Table 1 shows the obtained parameters from the equivalent 2pF DDFs for ^{6}Li and ^{12}C and the calculated and experimental binding energies. The calculated EDF potentials are depicted as points in Fig. 2.

Non-monotonic (NM) Potentials Forms

The EDF-derived NM nuclear part of the ^{6}Li-^{12}C potential points has been parameterized with the following functional forms:

$$V_{NM}(R) = -V_0\left[1 + exp\left(\frac{R-R_0}{a_0}\right)\right]^{-1} + V_1\, exp\left[-\left(\frac{R-D_1}{R_1}\right)^2\right] \qquad (7)$$

The imaginary part of the ^{6}Li+^{12}C OP is taken phenomenologically (Hossain et al., 2015) as

$$W_{NM}(R) = -W_0 exp\left[-\left(\frac{R}{R_W}\right)\right]^2 - W_S\, exp\left[-\left(\frac{R-D_S}{R_S}\right)^2\right] \qquad (8)$$

Monotonic Woods-Saxon (MWS) Potentials

The fundamental part of the ^{6}Li+^{12}C MWS (Woods and Saxon, 1954) potential is taken phenomenologically to be composed of only attractive parts as

$$V_{MWS}(R) = -V_0\left[1 + exp\left(\frac{R-R_0}{a_0}\right)\right]^{-1} \qquad (9)$$

The phenomenological imaginary part of the MWS potential is assumed to be composed of a WS-shaped (Woods and Saxon, 1954) volume term and a surface term in the shifted Gaussian form (Hossain et al., 2015) as:

$$W_{MWS}(R) = -W_0[1 + \exp(\frac{R - R_W}{a_w})]^{-1} - W_S exp\left[-\left(\frac{R-D_S}{R_S}\right)^2\right] \qquad (10)$$

Spin-orbit, Tensor, and Coulomb Potentials used in OM potentials

An effective spin-orbit, U_{SO}(R) part, and a tensor part, U_T(R) in OPs following Reber et al., (1994) and Kerr et al., (1995) are taken in the standard WS as:

$$U_{so}(R) = 2.0\frac{V_{so}}{R}\frac{d}{dR}[1 + \exp\left(\frac{\mathrm{R}-\mathrm{R_{so}}}{\mathrm{a_{so}}}\right)]^{-1}\, l.I \qquad (11)$$

$$U_T(R) = 8\left[V_T a_{RT}^2 \frac{d^2}{dR^2}[1\ + \exp\left(\frac{R-R_{RT}}{a_{RT}}\right)]^{-1}\right] \times \left[\left(\boldsymbol{I}.\check{\mathrm{R}}\right)^2 - \frac{2}{3}\right] \qquad (12)$$

In equations (11 and 12), ℓ**,** ***I***, and Ř refer, respectively, to the partial wave angular momentum, ^{6}Li-spin operators, and a unit vector along increasing *R*. The factor 2.0 in equation (11) stems from $(\hbar/m_\pi c)^2 = 2.0$ fm^2, and a factor $6\sqrt{3}$ in equation (12) has been omitted to conform to the algorithm in the code FRESCO (Thompson, 1988).

The Coulomb potential V_C(R) is taken as,

$$V_C(R) = \begin{cases} \frac{1}{4\pi\epsilon_0}\frac{Z_P Z_T e^2}{R}, & R \geq R_C \\ \frac{1}{4\pi\epsilon_0}\frac{Z_P Z_T e^2}{2R_C}\left(3 - \frac{R^2}{R_C^2}\right), & R < R_C \end{cases} \qquad (13)$$

Here, R_C is the Coulomb radius of a uniformly charged sphere.

The resultant forms of the NM and MSW OPs stand, respectively, as

$$U^{NM}(R) = V_C(R) + V_{NM}(R) + W_{NM}(R) + U_{so}(R) + U_T(R) \qquad (14)$$

and

$$U^{MWS}(R) = V_C(R) + V_{MWS}(R) + W_{MWS}(R) + U_{so}(R) + U_T(R) \qquad (15)$$

Analysis and Results

The data of experimental CS and analyzing powers (iT_{11}, T_{20}, T_{21}, and T_{22}) for the ^{6}Li+^{12}C elastic scattering at 30 MeV are taken from (Kerr et al., 1995). A systematic error of 15% is considered for the experimental data points. The Coulomb radius R_C = 3.92 fm is taken to calculate the Coulomb potential in equation (13). All calculations of OM are performed using the code SFRESCO, which includes the coupled-channels code FRESCO2.9 (Thompson,

1988) and the χ^2-minimization code MINUIT (James and Roos, 1975). The fitting parameters are determined by minimizing the χ^2 expressed by.

$$\chi^2 = \frac{1}{N-F}\sum_i \left[\frac{\sigma_{exp}(\theta_i)-\sigma_{th}(\theta_i)}{\Delta\sigma_{exp}(\theta_i)}\right]^2 \tag{16}$$

Here $\sigma(\theta)$ and $\Delta\sigma(\theta)$ represent the cross-section and the corresponding error at the scattering angle θ. F represents the number of experimental data points, and N is the number of adjusted parameters. N-F denotes the degrees of freedom in minimizing the χ^2 for the data fitting.

In the initial step of the OM analysis, the EDF-derived NM potential parameters for the real part listed in Table 2 were fixed. The parameters of the imaginary parameters of W_{NM} in equation (8) were searched to obtain the best fit to the CS data only with χ^2=388. The EDF potential is valid at the zero-excitation energy $E_x = 0$ (Islam et al., 2021a; Islam et al., 2021b) of the composite nucleus ^{18}Ar. No energy dependency parameter is found from the derivation of NM potential from EDF theory. Hence, the EDF-generated NM potential parameters needed to be readjusted for a good description of the CS data at 30 MeV. Therefore, successive grid and global searches on both the EDF–generated V_{NM} parameters in Table 2 and the previously optimized W_{NM} parameter were employed to describe the *CS* data accurately.

In the next step, the spin-orbit potential parameters (V_{SO}, R_{SO}, and a_{SO}) in equation (11) and the central imaginary parameters optimized in the previous step were adjusted empirically on the iT_{11} data employing a successive number of grid searches. In the third step, the tensor potential parameters (V_T, R_T, and a_T) were employed in a successive number of grid searches to reproduce the T_{21} data.

In the final step, all parameters of equation (14), except the constancy of R_C=3.92 fm, were tuned in values with a successive number of grid searches to reproduce well the experimental CS and analyzing powers (iT_{11}, T_{20}, T_{21}, and T_{22}) data simultaneously. The final fits are done by visually inspecting the angular structure of the experimental data because it is essential to reproduce the angular distributions when $\chi^2 \gg 1$. (Perey, 1963; Koning and Delaroche, 2003). All the parameters obtained from the best fitting are shown in Tables 2 and 3. The χ^2 and the volume integrals J_R/72 and J_I/72, respectively, for the real and imaginary parts of the OP, are also listed in Tables 2 and 3. The calculated CS and analyzing powers (iT_{11}, T_{20}, T_{21}, and T_{22}) shown in the red solid lines using the NM potentials compare well with the experimental data in Fig. 3.

Table 2. Parameters of the nuclear real and spin-orbit parts of OP at 30 MeV.

Type	V_0 (MeV)	R_0 (fm)	a_0 (fm)	V_1 (MeV)	R_1 (fm)	D_1 (fm)	V_{SO} (MeV)	R_{SO} (fm)	a_{SO} (fm)	$J_R/72$ (MeV.fm3)	χ^2
EDF	39.19	3.94	0.766	-35.72	2.43	0.133	-	-	-	-146.73	-
NM	57.12	3.94	0.710	-198.4	1.92	0.133	0.50	5.26	0.55	-144.83	45.0
MWS	300.0	2.22	0.840	-	-	-	1.30	2.75	0.65	-465.16	146.2

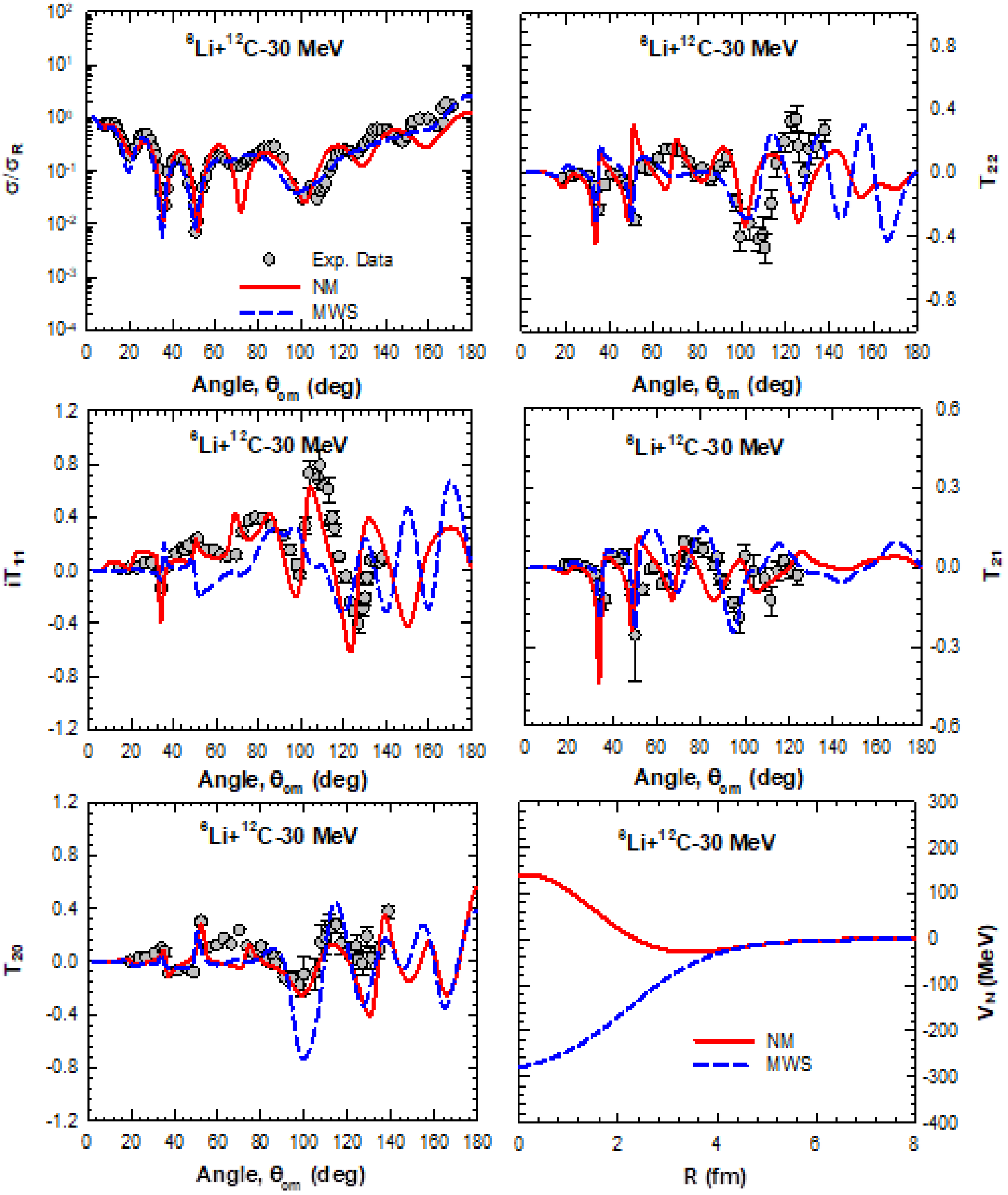

Fig. 3. Optical model (OM) calculations using NM potential (red solid lines) and MWS potential (blue dashed lines) are compared to the experimental *CS* and analyzing powers (iT_{11}, T_{20}, T_{21}, and T_{22}) data of ^{6}Li+^{12}C at 30 MeV using the OP parameters, listed in Table 2 and 3. The radial distributions of nuclear real parts of the two types of OP potential are also displayed in the last inset.

Table 3. Same as Table 2 but for the imaginary and tensor interaction parts.

Type	W_0 (MeV)	R_W (fm)	a_W (fm)	W_S (MeV)	D_S (fm)	R_S (fm)	V_T (fm)	R_T (fm)	a_T (fm)	$J_I/72$ (MeV.fm3)
NM	17.2	3.80	-	15.5	4.40	0.12	2.0	3.94	0.72	-83.92
MWS	17.3	3.11	1.18	0.50	4.92	0.60	2.0	4.58	0.30	-76.25

The above-mentioned fitting procedure was repeated for the U^{MWS} potential in equation (15), with its fundamental part V_{MWS} lacking in the repulsive core (see equation (9)). The initial parameters of the real nuclear part of U^{MWS} were taken from (Kerr et al., 1995). The best-fit parameters using U^{MWS} potentials are also displayed in Tables 2 and 3. The value of χ^2 and the volume integrals $J_R/72$ and $J_I/72$ of equation (15), respectively, for the real and imaginary OP parts, are also listed in Tables 2 and 3. The predicted results of the *CS* and analyzing powers (iT_{11}, T_{20}, T_{21}, and T_{22}) using the U^{MWS} potentials at 30 MeV, shown in the blue dashed lines, are compared to the experimental data in the same Fig. 3. The comparison of nuclear real parts of both the NM and MWS potentials is also shown graphically in Fig. 3.

It is observed from Fig. 3 that the experimental data on the elastic ^{6}Li+^{12}C scattering *CS* along with T_{20}, T_{21}, and T_{22} are reproduced overall successfully at energy 30 MeV in the framework of the simple optical model using both the shallow NM and deep MWS potentials without the J-dependent absorption. However, the iT_{11} data is only well reproduced using shallow NM potential. The MWS potential cannot produce the exact angular shape and position of iT_{11} data well at the mid and higher angular regions. The $J_R/72$ value of NM potential is found to be -144.83 MeV.fm^3, slightly lower than the value of -146.73 MeV.fm^3 for the EDF-derived potential. On the other hand, the value of $J_R/72$ =- 465.16 MeV.fm^3 for MWS is found to be very deep compared to the value of the actual volume integral found in NM potential. For the overall fitting value for *CS*, iT_{11}, T_{20}, T_{21}, and T_{22}, the average chi-square is found using NM potentials to be only χ^2 = 45.0, but for MWS potentials, the χ^2 = 146.2, which is much larger than the NM description. The higher value of $J_R/72$ for MWS compared to the NM potentials suggests the MWS potential is very deep. However, based on two observations: (*i*) the visual inspection of the theoretical description of experimental angular structures of *CS*, iT_{11}, T_{20}, T_{21}, and T_{22} in Fig. 3 and (*ii*) a comparison of the χ^2 values found for both NM and MWS potentials in Table 2, we can suggest the following. The simultaneous analysis using a simple OM picture is found to be much better for the shallow NM potential than the deep MWS potential.

Discussions and Conclusions

The investigation reports the comparative and simultaneous description of the experimental *CS*, iT_{11}, T_{20}, T_{21}, and T_{22} data of the ^{6}Li elastic scattering by ^{12}C at 30 MeV in the structure of simple OM picture using shallow NM and deep MWS potentials. The MWS potential can simultaneously describe the *CS*, T_{20}, T_{21}, and T_{22} data except iT_{11} data in a simple OM picture. On the other hand, the shallow NM potential can successfully describe and also simultaneously all the data sets (*CS*, T_{20}, iT_{11}, T_{21}, and T_{22}) in OM, as shown in Fig. 3. The overall image of the simultaneous description of CS and all the analyzing powers (APs) using the shallow NM potential seems much better than the description using the MWS one.

Our simple optical model description of the *CS* and APs using NM potentials without a *J*-dependent absorption plays better than the description using the *J*-dependent absorption reported in (Reber et al., 1994; Kerr et al., 1995) and also the findings from the Coupled-Channels (CC) calculations in (Reber et al., 1994; Kerr et al., 1995; Kerr et al., 1996). The present analysis using the simple OM suggests that the *J*-dependent absorption potential is *non-essential* for describing the VAP and TAP data. The present investigation with the NM potential shows that the best choice for simultaneous examination of the vector and tensor effects in NN interactions is the repulsive core arising from the Pauli effect. Moreover, the key to success in the simultaneous analysis of CS and analyzing powers using the shallow NM potential rather than deep MWS potential lies in the appropriate generation of a dynamic polarization potential (DPP) effect (Brandan and Satchler, 1997), even in the framework of OM. The appropriate DPP effect with the NM potentials from BCD's EDF (Brueckner et al., 1968a) stems from the realistic n-n potential of GCT (Brueckner and Gammel, 1958), which involves the spin- and tensor-interactions apart from the central part.

Another essential feature of the EDF-derived NM potentials at low energies is their energy independence (Islam et al., 2021a; Islam et al., 2021b). This aspect of the EDF potentials bears excellent promise in employing the NM potentials for studying the NN fusion at the astrophysical low-energies where reliable potentials are scarce. We are now examining the NM potentials on the ^{16}O+^{16}O, ^{16}O+^{12}C, and ^{12}C+^{12}C fusion reactions at deep sub-Coulomb energies, which play an essential role in stellar evolution and supernovae explosions.

Acknowledgment

The authors wish to thank Dr. Ian J. Thompson for his code FRESCO.

References

Basak AK, Abdullah MNA, Tariq ASB, Das SK, Rahman AFMN, Mondal AS, Sen Gupta HM and Malik FB. Investigation of inelastic α-scattering on ^{24}Mg and ^{28}Si. *The Eur. Phys. J. A.* 2001; 12(4): 387-397.

Basak AK, Billah MM, Kobra MJ, Sarkar MK, Rahman MM, Das PK, S. Hossain S, Abdullah MNA, Tariq ASB and Uddin MA. Non-monotonic potentials and vector analyzing powers of ^{6,7}Li scattering by ^{12}C, ^{26}Mg, ^{58}Ni, and ^{120}Sn. *Europhys. Lett.* 2011; 94(6): 62002.

Basak AK, Merchant AC, Freer M, Islam MS, Ramon RA, Rahman MM, Tariq ASB, Uddin MA and Soylu A. ^{16}O + ^{16}O cluster states and their fusion to ^{32}S: A non-monotonic potential description. *Europhys. Lett.* 2022; 138(4)**:** 44002.

Brandan ME and Satchler GR. The interaction between light heavy-ions and what it tells us. *Phys. Rep.* 1997; 285 (4-5): 143-243.

Bray KH, Mahavir jain, Jayaraman KS, Lobianco G, Moss GA, Van Oers WTH, Wells DO and Petrovich F. Elastic and inelastic scattering of protons from ^{6}Li between 25 and 45 MeV. *Nucl. Phys. A.* 1972; 189(1): 35-64.

Brueckner KA and Gammel JL. Properties of nuclear matter, *Phys. Rev.* 1958; 109(4): 1023-1039.

Brueckner KA, Buchler JR, Clark RC and Lombard RJ. Statistical theory of nuclei. II. Medium and heavy nuclei. *Phys. Rev.*1969; 181(4): 1543-1551.

Brueckner KA, Buchler JR, Jorna S and Lombard RJ. Statistical theory of nuclei, *Phys. Rev.* 1968b; 171(4): 1188-1195.

Brueckner KA, Coon SA, and Dabrowski J. Nuclear symmetry energy. *Phys. Rev.* 1968a; 168(4): 1184-1188.

Das SK, Basak AK, Banu K, Mondal AS, Tariq ASB, Rahman AFMN, Gupta HMS, and Malik FB. Effect of the α-nucleus potential on the ^{28}Si (α, p)^{31}P reaction. *Phys. Rev. C.* 2000b; 62(5): 054606.

Das SK, Tariq ASB, Rahman AFMM, Roy PK, Huda MN, Mondal AS, Basak AK, Gupta HMS and Malik FB. Effect of α-nucleus potential on the ^{27}Al (α, t) ^{28}Si reaction, *Phys. Rev. C.* 1999; 60(4): 044617.

Das SK, Tariq ASB, Rahman AFMN, Hossain S, Mondal AS, Basak AK, Gupta HMS and Malik FB. Effect of the α-nucleus interaction on the ^{29,30}Si (α, d)^{31,32}P reaction. *Phys. Rev. C.* 2001; 64(3): 034605.

Das SK, Tariq ASB, Uddin MA, Mondal AS, Basak AK, Rashid KM, Gupta HMS and Malik FB. Effect of α-nucleus potential on the ^{28}Si (α, d) ^{30}P reaction. *Phys. Rev. C.* 2000a; 62 (5): 054605.

Duarte JG, Gasques LR, Oliveira RB, Zagatto VAB, Chamon LC, Medina NH, Added N, Seale WA, Alcántara-Núñez JA, Rossi Jr ES, Amador-Valenzuela P, Lépine-Szily A, Freitas AS, Scarduelli V, Aguiar VAP[1] and Shorto JMB. Measurement of fusion cross sections for ^{16}O+^{16}O, *Phys. G: Nucl. Part. Phys.* 2015; 42(6): 065102.

Goldberg DA and Smith SM. Criteria for the elimination of discrete ambiguities in nuclear optical potentials. *Phys. Rev. Lett.* 1972; 29(8): 500-503.

Goldberg DA, Smith SM, Pugh HG, Roos PG and Wall NS. Scattering of 139-MeV Alpha Particles by ^{58}Ni and ^{208}Pb. *Phys. Rev. C.* 1973; 7(5): 1938-1950.

Hossain S, Abdullah MNA, Das SK, Uddin MA, Basak AK, Gupta HMS, Thompson IJ and Malik FB. Band mixing in ^{29}Si and ^{29}P. *J. Phys. G: Nucl. Part. Phys.* 2005; 31(5): 309.

Hossain S, Tariq ASB, Nilima A, Islam MS, Majumder R, Sayed MA, Billah MM, Azad MMB, Uddin MA, Reichstein I, Malik FB and Basak AK. Dependence of the ^{16}O+^{16}O nuclear potential on nuclear incompressibility. *Phys. Rev. C.* 2015; 91(6): 064613.

Islam MS, Majumder R, Hossain S, Nilima A, Sayed MA, Islam MS, Billah MM, Azad MMB, Tariq ASB and Uddin MA. Non-monotonic shallow nucleus-nucleus potential for heavy-ion elastic scattering. *J. Phys.: Conf. Ser.* 2021c; 1718: 012009.

Islam MS, Ramon RA, Rahman MM, Islam MS, Azad MMB, Tariq ASB, Uddin MA, Ali S and Basak AK. Primary rainbow and Airy minima in ^{12}C +^{12}C elastic scattering with families of non-monotonic potentials. *J. Phys. G: Nucl. Part. Phys.* 2021b; 48(12): 125108.

Islam MS, Ramon RA, Rahman MM, Majumder R, Sayed MA, Nilima A, Azad MMB, Tariq ASB, Uddin MA and Basak AK. Nature of potential families from elastic ^{16}O +^{16}O rainbow scattering. *J. Phys. G: Nucl. Part. Phys.* 2021a; 48(7): 075109.

James F and Roos M. Minuit - a system for function minimization and analysis of the parameter errors and correlations. *Comput. Phys. Comm.*1975; 10: 343-367.

Kerr PL, Kemper KW, Green PV, Mohajeri K, Myers EG, Robson D and Schmidt BG. Tensor effects in ^{6}Li→+^{12}C scattering. *Phys. Rev. C.* 1995; 52(4):1924-1933.

Kerr PL, Kemper KW, Green PV, Mohajeri K, Myers EG, Schmidt BG and Hnizdo V. ^{6}Li→+^{12}C inelastic scattering at 30 and 50 MeV. *Phys. Rev. C* 1996; 54(3): 1267-1281.

Khoa DT, Oertzen Wv, Bohlen HG and Ohkubo S. Nuclear rainbow scattering and nucleus–nucleus potential. *J. Phys. G: Nucl. Part. Phys.* 2007; 34(3): R111-R164.

Koning AP and Delaroche JP. Local and global nucleon optical models from 1 keV to 200 MeV. *Nucl. Phys. A.* 2003; 713(3-4): 231-310.

Michel F, Albinski J, Belery P, Delbar TH, Grégoire Gh, Tasiaux B and Reidemeister G. Optical model description of α+^{16}O elastic scattering and alpha-cluster structure in ^{20}Ne. *Phys. Rev. C.* 1983; 28: 1904-1917.

Mohr P, Rauscher T, Oberhummer H, Máté Z, Fülöp Zs, Somorjai E, Jaeger M and Staudt G. ^{144}Sm-α optical potential at astrophysically relevant energies derived from ^{144}Sm(α,α)^{144}Sm elastic scattering. *Phys. Rev. C*. 1997; 55(3):1523-1531.

Pakou A. Polarization potential for elastic scattering of ^{6,7}Li + ^{28}Si at near-barrier energies. *Phys. Rev. C*. 2008; 78(6): 067601.

Perey FG. Optical-model analysis of proton elastic scattering in the range of 9 to 22 MeV. *Phys. Rev*. 1963, 131(2):745-763.

Reber EL, Kemper KW, Green PV, Kerr PL, Mendez AJ, Myers EG and Schmidt BG. Spin-orbit and tensor potentials from polarized ^{6}Li scattering. *Phys. Rev. C. Nucl. Phys.* 1994; 49(1): R1-R4.

Reber EL, Kemper KW, Green PV, Kerr PL, Mendez AJ, Myers EG, Schmidt BG and Hnizdo V. Analysing powers for elastic and inelastic scattering of polarized ^{6}Li from ^{12}C at 30 MeV. *Phys. Rev. C. Nucl. Phys.*1994; 50(6):2917-2926.

Satchler GR. Direct nuclear reactions. Clarendon Press: Oxford, UK. 1983. p. 854.

Satchler GR and Love WG. Folding model potentials from realistic interactions for heavy-ion scattering. *Phys. Rep.* 1979; 55(3): 183-254.

Sick I. Model-independent nuclear charge densities from elastic electron scattering. *Nucl. Phys. A.* 1974; 218: 509-541.

Tariq ASB, Rahman AFMM, Das SK, Mondal AS, Uddin MA, Basak AK, Gupta HMS and Malik FB. Potential description of anomalous large angle scattering of α particles. *Phys. Rev. C.* 1999; 59(5): 2558-2566.

Thomas R. Essentials of nucleosynthesis and theoretical nuclear astrophysics. IOP Publishing Ltd. 2020. p. 450.

Thompson IJ. Coupled reaction channels calculations in nuclear physics. *Comput. Phys. Rep*. 1988; 7(4): 167-212.

Trcka DE, Frawley AD, Kemper KW, Robson D, Fox JD and Myers EG. Angular momentum dependent absorption in ^{6}Li scattering. *Phys. Rev. C* 1990; 41: 2134-2146.

Woods RD and Saxon DS. Diffuse surface optical model for nucleon-nuclei scattering. *Phys. Rev*. 1954; 95: 577-578.

J. Bangladesh Acad. Sci. 48(1); 111-119: June 2024 DOI:https://doi.org/10.3329/jbas.v48i1.71538

Journal of Bangladesh Academy of Sciences

Journal homepage: http://www.bas.org.bd/publications/jbas.html

Research Article

Synthesis of some 2-azitidinones (β-lactams) as antibiotic mimics and screening of their antimicrobial activity

Kamrunnahar Happy[1], Sumaiya Khan*, Umme Aiman Liza, Afsana Mimi,
Md Rafikul Islam and Mohammad Mamun Hossain

Department of Chemistry, Jahangirnagar University, Savar, Dhaka, Bangladesh

ARTICLE INFO

Article History

Received: 8 February 2024
Revised: 24 March 2024
Accepted: 2 April 2024

Keywords: 2-Azetidinones, Schiff bases, Microwave, Antimicrobial activity.

ABSTRACT

2-Azetidinones (β-lactams) possess broad and potent bioactivity owing to the presence of lactam rings. As evidence has shown, it is one of the most critical biological frameworks. Some new 2-azetidinones have been synthesized from corresponding Schiff bases using different amines and aldehydes. All compounds (Schiff bases and β- lactams) were synthesized for comparison research using conventional and microwave techniques. The microwave approach has been found to reduce reaction time and boost yield drastically. Analysis combining elemental (C, H, and N) and spectroscopic approaches (NMR, IR, and UV) have been applied to ensure the Schiff bases constitution and corresponding β-lactams constitution. The newly synthesized compound's antibacterial action was estimated opposite to one gram-positive and one gram-negative bacteria. One compound (A-03) among synthesized 2-azitidinones was shown significant activity against the gram-positive bacteria. The other synthesized compounds had no substantial activity on either of the microorganisms.

Introduction

Recently, organic chemists have emphasized finding simple, innovative, non-hazardous ways to synthesize compounds. Growing environmental awareness necessitates the creation of efficient, economical methods where fewer risky consequences are undesirable. Carbon-nitrogen double bond is crucial to the synthesis of organic compounds. This can be done by generating Schiff bases (imines) by reacting aldehydes with amines in an acidic atmosphere. Due to their remarkable biological activity, Schiff bases have gained much attention throughout the organic synthesis field (Abdulla and Fuhr, 1975). It is known that azetidinones, a kind of antibiotic with a *β*-lactam structure, have intriguing biological features. Numerous 3-chloro monocyclic *β*-lactams have potent antimicrobial (Calderon and Sabundayo, 2007), antibacterial (Doherty et al., 1994), antiphlogistic (Durckheimer et al., 1985), antiepileptic (Feigelson et al., 1993), and anti-tubercular (Georg et al., 1992) results. They positively impact the central nervous system and operate as enzyme inhibitors (Vander et al., 1991; Palomo et al., 1999; Singh, 2003). They are azetidinones' carbonyl derivatives with a carbonyl group at position 2. These can, as an alternative, be termed β-lactams or 2-azetidinone (Hossain et al., 2009).

---

*Corresponding author:<sumaiya9@juniv.edu>

[1] *Department of Chemistry, Uttara University, Dhaka*

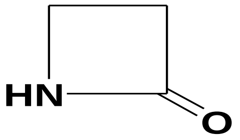

2-Azetidinone, the simplest β-lactam

Utilizing the related strain energy, azetidin-2-one, a four-membered cyclic lactam (*β*-lactam) framework, was identified as an advantageous component for synthesizing numerous chemical substances. One of the most fundamental and adaptable processes for producing a wide range of structurally different 2-azetidinone derivatives is the Staudinger reaction (ketene-imine cycloaddition reaction) (Khalafallah et al., 1995; Nantasenamat et al., 2009). Additionally, the enolate-imine condensation and cyclization reactions can be used to synthesize azetidin-2-ones. Additionally, it produces several *β*-lactam antibiotics (Parikh et al., 2000; Waksman, 1947).

Material and Methods

Physical Measurements

John's electrothermal melting point equipment. IR spectra were captured on a KBr disc using a NICOLET iS10 IR spectrophotometer. The Department of Pharmaceutical Sciences at Tokushima University in Japan recorded ^{1}H-NMR spectra using a 400 MHz AVANCE Bruker NMR spectrometer with $CDCl_3$ (solvent) and TMS (internal standard). The units of change (Chemical) are measured in parts per million (ppm). The device Elementar (Model No.Vario El Cube) carried out the elemental analysis for carbon, hydrogen, and nitrogen. By the Shimadzu UV-1800 UV spectrophotometer, ultraviolet spectrum data were collected. The pure identification of the compounds was verified using TLC and silica gel-G. An iodine chamber produced the spots, and an ultraviolet lamp was used to see them.

Representative procedure for the Synthesis of Schiff Bases (2a-h)

A small amount of glacial acetic acid (a few drops) was added to 30 ml of ethanol to dissolve the 4-methylaniline (0.01 mol). The same reaction mixture added 0.01 mol of the suitable aromatic aldehyde, such as 4-hydroxybenzaldehyde. The mixture for the reaction was then refluxed for 2-4 hours. TLC was used to track the reaction's development at a solvent ratio of 1:4 EtOAc to cyclohexane. It was cooled and neutralized with 5% $NaHCO_3$ (aq. solution) once the reaction was finished. The reaction mixture was then placed onto crushed ice and refrigerated for the following day. A solid compound was filtered, water washed, and vacuum desiccators were used to dry it. The desired compounds (2a-h) were then obtained by recrystallizing the end products with ethyl acetate from the resultant products. Most of the reaction was likewise conducted in a microwave-irradiated environment. Although the other parameters, such as reaction time, solvent quantity, etc., were much better, the yields were comparable (Tables 1 and 2).

The characterization of all Schiff bases was done using spectral methods, which are as follows.

4-Methyl-N-[(4-hydroxyphenyl)methyl-idene] aniline(2a)

Yield: 97% (light brown solid)

Melting point: 250°C

^{1}H- **NMR (ppm)($CDCl_3$): δ** 2.25 (s, 3H, CH_3), 8.32 (s, 1H, -CH=N), 6.79 (d, 2H, J_o = 7.5 Hz, H-2′), 7.02 (d, 2H, J_o = 7.5 Hz, H-3′), 7.10 (d, 2H, J_o = 8.0 Hz, H-3″), 7.66 (d, 2H, J_o = 8.0 Hz, H-2″), 8.68 (s, 1H, Ar-OH).

IR, υ_{max}, KBr (cm^{-1}): ν 3454 (O-H str.), 3025 (Ar. C-H str.), 2916, 2858 (Ali. C-H str.), 1609 (m, C=N str.), 1576, 1509 (m, C=C Ar.), 1286, 1163(s, C-N str.), 839, 818 (substituted phenyl ring).

UV, λ_{max}: 280 nm, 320 nm

Elemental Analysis, $C_{14}H_{13}NO$: Theoretical: C, 79.62; H, 6.16; N, 6.63; Experimental Found: C, 79.52; H, 6.13; N, 6.54.

4-Methyl-N-[(4-dimethylaminophenyl)methyl-dene]aniline(2b)

Yield: 90% (yellow solid)

Melting point:134°C

IR, υ_{max}, KBr (cm^{-1}): 3049 (Ar. C-H str.), 2907, 2853 (Ali. C-H str.), 1614 (m, C=N str.), 1588, 1553, 1532, 1503 (m, C=C str. Ar.), 1314, 1234, 1174 (C-N str.), 884, 821 (substituted phenyl ring).

UV, λ_{max}: 350 nm

Elemental Analysis, $C_{16}H_{18}N_2$: Theoretical:C, 80.67; H, 7.56; N, 11.76; Experimental Found: C, 80.17; H, 7.53; N, 11.66.

4-Methyl-N-[(4-nitrophenyl)methylidene]aniline (2c)

Yield: 92% (pale yellow solid)

Melting point:139°C

IR, υ_{max}, KBr (cm^{-1}): 3099 (Ar. C-H str.), 2951, 2855 (Ali. C-H str.), 1624, 1598 (m, C=N str.), 1584, 1338 (NO_2), 1513, 1504 (s, C=C ring str.), 1189, 1107 (C-N str.), 854, 821 (substituted phenyl ring).

λ_{max}: 294nm, 354 nm

Elemental Analysis, $C_{14}H_{12}N_2O_2$: Theoretical:C, 70.00; H, 5.00; N, 11.67; Experimental Found: C, 69.98; H, 5.03; N, 11.56.

4-Methoxy-N-[(4-hydroxyphenyl)methyldene]aniline (2d)

Yield: 87% (greenish-yellow)

Melting point: 242°C.

^{1}H-NMR ($CDCl_3$) δ_H (ppm):3.78 (s, 3H, OCH_3), 8.39 (s,1H, -CH=N), 6.84 (d, 2H, J_o =7.7Hz, H-2′), 6.91(d, 2H, J_o=7.7Hz, H-3′), 7.16(d, 2H, J_o=8.4Hz, H-3″),7.71(d,2H, J_o=8.4Hz, H-2″),8.79(s,1H, Ar-OH).

IR, υ_{max}, KBr(cm^{-1}): 3447 (O-H str. H-bond), 3043 (Ar. C-H str.), 2922, 2853 (Ali. C H str.), 1605 (s, C=N str.), 1577, 1515, 1503 (s, C=C ring str.), 1283, 1244, 1191, 1163 (s, C-N str.), 841, 823 (substituted phenyl ring).

UV λ_{max}(log ε) (EtOAc): 283 (1.878), 329 (1.715).

Elemental Analysis, $C_{14}H_{13}NO_2$: Theoretical:C, 74.01; H, 5.73; N,6.17; Experimental Found: C, 74.11; H, 5.60; N, 6.22.

4-Methoxy-N- [(4-dimethylamino phenyl) methylidene]aniline (2e)

Yield: 82% (brown solid)

Melting point: 152°C.

^{1}H-NMR ($CDCl_3$) δ_H (ppm): 3.82 (s, 3H, OCH_3), 3.04 (s,6H, $N(CH_3)_2$), 8.34(s,1H-CH=N), 6.73 (d,2H, J_o=7.2Hz, H-2′),6.91(d, 2H, J_o=7.2Hz, H-3′), 7.19 (d, 2H, J_o=8.3Hz, H-3″), 7.75(d, 2H, J_o=8.3 Hz, H-2″).

IR, υ_{max}, KBr (cm^{-1}): 3000(Ar. C-H str.), 2953, 2883(Ali. C-H str.), 1608 (s, C=N str.), 1553, 1524, 1500 (C=C ring str.), 1254, 1298, 1286, 1239, 1177 (C-N str.), 840, 819 (substituted phenyl ring).

UV λ_{max} (log ε) (EtOAc): 355(0.717).

Elemental Analysis, $C_{16}H_{18}N_2O$: Theoretical:C, 75.59; H, 7.09; N, 11.02; Experimental Found: C, 75.60; H, 7.00; N, 11.16.

4-Methoxy-N-[(4-nitrophenyl)methyldene]aniline(2f)

Yield:*98%*

Melting point: 150°C

^{1}H-NMR ($CDCl_3$) δ_H (ppm): 3.80 (s, 3H, OCH_3), 8.58 (s, 1H, -CH=N), 6.97 (d, 2H, J_o =7.9 Hz, H-2′), 7.30 (d, 2H, J_o=7.9Hz, H-3′), 8.06 (d, 2H, J_o=8.8Hz, H-3″), 8.31 (d, 2H, J_o=8.8Hz, H-2″).

IR, υ_{max}, KBr (cm^{-1}): 3081 (Ar. C-H str.), 2957, 2837 (Ali. C-H str.), 1598 (m, C=N str.),

1514 (s, C=C ring str.), 1568(NO_2), 1245, 1191, 1168 (C-N str.), 888, 835 (substituted phenyl ring).

UV λ_{max}(log ε) (EtOAc): 257(1.497), 373(1.650).

Elemental Analysis, $C_{14}H_{12}O_3N_2$: Theoretical:C, 65.63; H, 4.69; N, 10.94; Experimental Found: C, 65.60; H, 4.66; N, 10.88.

4-Methyl-N-anthranylmethylideneaniline (2g)

Yield: 77% (yellowish orange solid),

Melting point: 108°C

IR, υ_{max}, KBr (cm^{-1}): 3046 (Ar. C-H str.), 2917, 2857 (Ali. C-H str.), 1622, 1609 (C=N str.), 1587, 1518, 1498 (C=C ring str.), 1254, 1203, 1157 (C-N str.), 845, 810 (substituted phenyl ring).

λ_{max}: 259nm

Elemental Analysis, $C_{22}H_{17}N_2$: Theoretical:C, 89.49; H, 5.76; N, 4.75; Experimental Found: C, 89.40; H, 5.58; N, 4.60.

4-Methoxy-N-anthranylmethylideneaniline(2h)

Yield: 95%

Melting point: 165°C

^{1}H-NMR ($CDCl_3$) δ_H (ppm): 3.88 (s, 3H, OCH_3), 8.53 (s, 1H, -CH=N), 7.02-8.72 (m,13H, Ar-H).

IR, υ_{max}, KBr (cm^{-1}): 3048 (Ar. C-H str.), 2991, 2830 (Ali. C-H str.),1606(m, C=N str.),

1519, 1503 (C=C ring str.), 1293,1246,1185 (C-N str.), 841, 820 (substituted phenyl ring).

UV λ_{max}(log ε) (EtOAc): 258(1.424).

Elemental Analysis, $C_{22}H_{17}NO$: Theoretical: C, 84.89; H, 5.47; N, 4.50; Experimental Found: C, 84.80; H,5.33; N, 4.56.

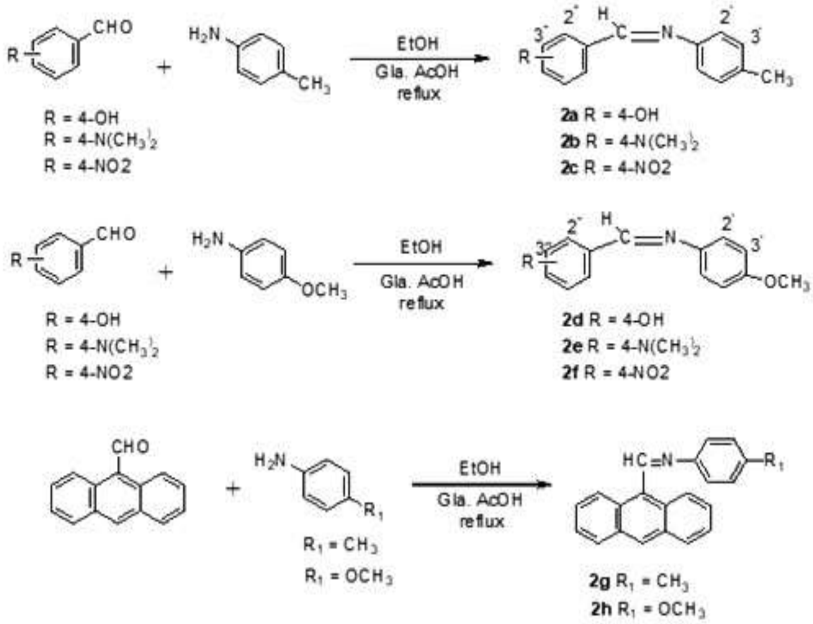

Scheme 1. Synthesis of Schiff-bases.

Synthesis of 2-Azetidinones/β-lactams (1a-h)

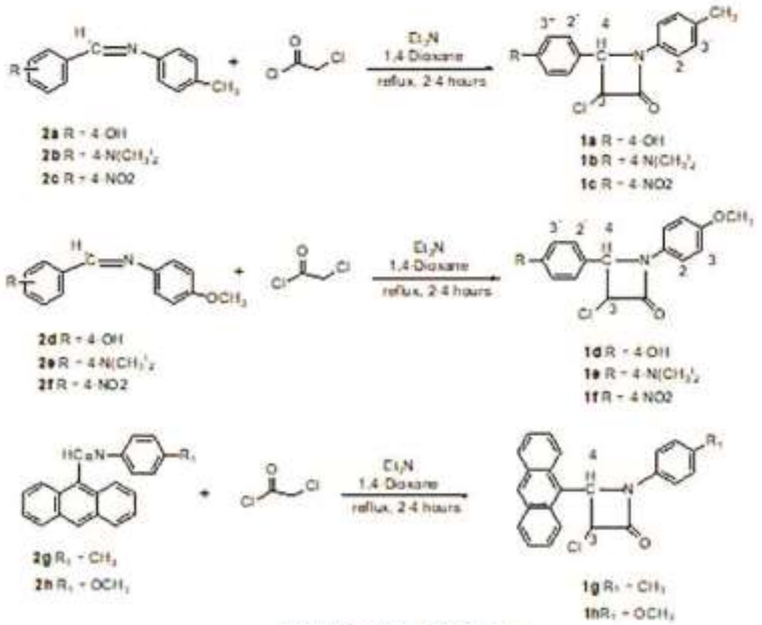

Scheme 2: synthesis oflactams

Table 1. Comparison of conventional and microwave synthesis (2a-c, 2g).

Compound no.	Conventional method		Microwave method	
	Time (hours)	% Yield	Time (minutes)	% yield
2a	4	97	2.5	96
2b	2	90	2	94
2c	2	92	1.5	87
2g	2	77	1.5	75

The representative procedure of lactam synthesis

Between 0°C and 5°C, a well-stirred combination of triethylamine (0.0066 mol) and chloroacetyl chloride (0.0067 mol) was mixed to a solution of compound 2a (0.0033 mol) in 1, 4-dioxane (16.5 ml). After 30 minutes of stirring, the reaction mixture refluxed for three hours. For a whole day, the reaction mixture remained at room temperature. The TLC was used to monitor the reaction's progress, using a solvent ratio of 3:7 (EtOAc:cyclohexane). After using a vacuum evaporator to evaporate the mixture and remove the solvent, the residue was then flooded over cold water containing ice. After filtering, the crude product was dried. The impure solid contains the precursor Schiff-base, separated by column chromatography using a solvent mixture of EtOAc:cyclohexane = 3:7. Evaporating the solvent afforded the desired compounds1a. All other lactams (1b-1h) were obtained through a similar procedure.

The above compounds were also synthesized using the microwave method. Table 2 provides a comparative analysis of yield and reaction time.

The spectral data of the synthesized lactams/ azetidinones are as follows:

3-Chloro-4(4′-hydroxyphenyl)-N(4″-methyl-phenyl)-2-azetidinone (1a)

Yield: 74% (Off-white solid).

Melting point: 184°C

IR, υ_{max}, KBr (cm^{-1}): 3432 (O-H str. H-bond), 3087 (Ar. C-H str.), 2916, 2852 (Ali. C-H str.), 1673 (m, C=O str. lactam), 1617, 1553, 1509 (C=C ring str.), 865, 820 (substituted phenyl ring), 668 (C-Cl str.).

^{1}H-NMR (ppm): 2.33 (s, 3H, CH_3), 4.27 (d, 1H, J = 4.22 Hz, H-4), 5.43 (d, 1H, J = 4.22 Hz, H-3), 7.15-7.43 (m, 8H, Ar-H), 8.18 (s, 1H, Ar-OH).

λ_{max}: 251 nm

Elemental Analysis, $C_{16}H_{14}NO_2Cl$: Theoretical:C 66.90; H, 4.88; N, 4.88; Experimental Found: C, 67.05; H, 4.92; N, 4.18.

3-Chloro-4(4′-dimethylaminophenyl)-N(4″-methylphenyl)-2-azetidinone(1b)

Yield: 58%

Melting point: 124°C

IR, υ_{max}, KBr (cm^{-1}): 3090 (Ar. C-H str.), 2954, 2863 (Ali. C-H str.), 1676 (s, C=O str. lactam), 1599, 1553, 1513 (s, C=C ring str.), 864, 818 (substituted phenyl ring), 668, 596 (C-Clstr.).

^{1}H-NMR (ppm): 2.33 (s, 3H, CH_3), 3.21 (s, 6H, -$N(CH_3)_2$), 4.27 (d, 1H, J = 4.35 Hz, H-4), 5.28 (d, 1H, J = 4.35 Hz, H-3), 6.90 (d, 2H, J_o = 7.7 Hz, H-2′), 6.97 (d, 2H, J_o = 7.7 Hz, H-3′), 7.44 (d, 2H, J_o = 8.5 Hz, H-3″), 7.80 (d, 2H, J_o = 8.5 Hz, H-2″).

λ_{max}: 329 nm

Elemental Analysis, $C_{18}H_{19}N_2OCl$: Theoretical:C 68.79; H, 6.05; N, 8.92; Experimental Found: C, 69.01; H, 5.89; N, 8.68

3-Chloro-4(4′-nitrophenyl)-N(4″-methylphenyl)-2-azetidinone (1c)

Yield: 78% (light brown)

Melting point: 188°C

IR, ʋ$_{max}$, KBr (cm^{-1}): 3093 (Ar. C-H str.), 2951, 2861 (Ali. C-H str.), 1670 (s, C=O str. lactam), 1617, 1513 (s, C=C ring str.), (1558 NO_2), 865, 815 (substituted phenyl ring), 668 (C-Clstr.).

^{1}H-NMR (ppm): 2.33 (s, 3H, CH_3), 4.26 (d, 1H, *J* = 4.33 Hz, H-4), 5.50 (d, 1H, *J* = 4.33 Hz, H-3), 7.15-7.43 (m, 8H, Ar-H).

λ$_{max}$: 253 nm

Elemental Analysis, $C_{16}H_{13}N_2O_3Cl$: Theoretical:C 60.76; H, 4.11; N, 8.86; Experimental Found: C, 59.45; H, 4.42; N, 8.02.

3-Chloro-4(4′-hydroxyphenyl)-N(4″-methoxy-phenyl)-2-azetidinone (1d)

Yield: 52%

Meltingpoint: 96°C

^{1}H-NMR ($CDCl_3$) δH (ppm): 3.80 (s, 3H, OCH_3), 4.31 (d, 1H, *J*=4.55Hz, H-4), 5.54 (d, 1H, *J*=4.55Hz, H-3), 6.89 (d, 2H, J_o=7.8Hz, H-2′), 6.96 (d, 2H, J_o=7.8Hz, H-3′), 7.43 (d, 2H, J_0=8.0 Hz, H-3″), 7.81 (d, 2H, J_o=8.0 Hz, H-2″), 9.86 (s, 1H, Ar-OH)

IR, ʋ$_{max}$, KBr (cm^{-1}): 3295 (O-H str. H-bond), 3066 (Ar. C-H str.), 2957, 2834 (Ali. C-H str.), 1666 (s, C=O str. lactam), 1602, 1548, 1512 (s, C=C ring str.), 832(substituted phenyl ring), 606 (C-Clstr.).

UV λ$_{max}$(log ε) (EtOAc):267(1.724).

Elemental Analysis, $C_{16}H_{14}NO_3Cl$: Theoretical:C 63.37; H, 4.62; N, 4.62; Experimental Found: C,62.89; H, 4.63; N, 4.41

3-chloro-4(4′-dimethylaminophenyl)-N(4″-methoxyphenyl)-2-azetidinone (1e)

Yield:72%

Meltingpoint:125°C

^{1}H-NMR ($CDCl_3$) δ$_H$(ppm): 3.71 (s, 3H, OCH_3), 3.04 (s, 6H, $N(CH_3)_2$), 4.08 (d, 1H, *J*=4.45Hz, H-4), 4.14 (d, 1H, *J*=4.45 Hz, H-3), 6.65-7.71 (m, 8H, Ar-H).

IR, ʋ$_{max}$, KBr (cm^{-1}): 3072 (Ar. C-H, str.), 2957, 2837 (Ali. C-H, str.), 1663 (s, C=O, str. lactam), 1602, 1550, 1511, 1465 (s, C=C ring str.), 830 (substituted phenyl ring), 685 (C- Clstr.).

UV λ$_{max}$(log ε) (EtOAc): 329(0.720).

Elemental Analysis, $C_{18}H_{19}N_2O_2Cl$: Theoretical: C 65.35; H,5.79; N, 8.47; Experimental Found: C, 65.34; H, 5.97; N,8.53.

3-chloro-4(4′-nitrophenyl)-N(4″-methoxy-phenyl)-2-azetidinone(1f)

Yield: 85%

Meltingpoint: 132°C

^{1}H-NMR ($CDCl_3$) δ$_H$ (ppm): 3.80 (s, 3H, OCH_3), 4.19 (d, 1H, *J*=4.75 Hz, H-4), 5.26(d, 1H, *J*=4.75 Hz, H-3), 6.87-7.45 (m, 8H, Ar-H).

IR, ʋ$_{max}$, KBr (cm^{-1}): 3072 (Ar. C-H str.), 2958, 2831 (Ali. C-H str.), 1664 (s, C=O str. lactam), 1607, 1511, 1465 (C=C ring str.), 1549, 1347 (NO_2), 830 (substituted phenyl ring), 685 (C-Clstr.).

UV λ$_{max}$(log ε) (EtOAc): 253(0.876).

Elemental Analysis, $C_{16}H_{13}N_2O_4Cl$: Theoretical:C 57.75; H, 3.94; N, 8.42; Experimental Found: C, 56.97; H, 3.43; N,8.08.

3-Chloro-4-anthranyl-N(4″-methylphenyl)-2-azetidinone (1g)

Yield: 80% (Grey solid)

Melting point: 185°C,

IR, ʋ$_{max}$, KBr (cm^{-1}): 3084 (Ar. C-H str.), 2955, 2857 (Ali. C-H str.), 1672 (s, C=O str. lactam), 1617, 1555, 1512 (s, C=C ring str.), 859, 816 (substituted phenyl ring), 503 (C-Clstr.).

^{1}H-NMR (ppm): 2.33 (s, 3H, CH_3), 4.25 (d, 1H, *J* = 4.65 Hz, H-4), 5.34 (d, 1H, *J* = 4.65 Hz, H-3), 7.16-7.44 (m, 13H, Ar-H).

λ$_{max}$: 250 nm

Elemental Analysis, $C_{24}H_{18}NOCl$: Theoretical:C 77.52; H, 4.88; N, 3.77; Experimental Found: C, 77.01; H, 5.03; N, 3.25.

3-Chloro-4-anthranyl-N(4″-methoxy-phenyl)-2-azetidinone(1h)

Yield: 65%

Meltingpoint: 135°C

^{1}H-NMR ($CDCl_3$) δ_H(ppm): 3.81 (s, 3H, OCH_3), 4.60 (d, 1H, *J*=4.65 Hz, H-4), 5.71(d, 1H, *J*=4.65 Hz, H-3), 6.88-7.45 (m, 13H, Ar-H).

IR, υ_{max}, KBr (cm^{-1}): 3072 (Ar. C-H str.), 2958, 2831(Ali. C-H str.), 1664(s, C=O str. lactam), 1600, 1547, 1511, 1466 (C=C ring str.), 831 (substituted phenyl ring), 685 (C-Clstr.).

UV, λ_{max}(log ε) (EtOAc): 251 (0.364).

Elemental Analysis, $C_{24}H_{18}NO_2Cl$: Theoretical:C 74.32; H, 4.68; N, 3.61; Experimental Found: C,73.99; H, 5.01; N, 3.23.

Antibacterial activity

Antimicrobial agents are substances that work as growth inhibitors or kill agents for microorganisms in treating disease. They can function as virus-killing vermicides, bacteria-killing bactericides, algae-killing algaeecides, or fungal-killing fungicides. The antibacterial activity of newly produced compounds was assessed opposite to one gram-positive (*Staphylococcus aureus*) and one gram-negative (*Escherichia coli*) bacterium using the conventional Kirby-Bauer disk diffusion method. Table 3 describes the findings.

Table 2. Comparison of conventional and microwave synthesis (1a-c, 1g)

Compound no.	Conventional method		Microwave method	
	Time (hours)	%Yield	Time (minute)	% Yield
1a	3	74	3.5	**77**
1b	3	58	3.5	60
1c	3	78	4	80
1g	3	80	3	85

Table 3. Antimicrobial/Antibacterial activity assay of synthesized compounds by disc diffusion method.

Sl.	Compound ID	Zone of inhibition (mm) for *E. coli*			Zone of inhibition(mm) for *S. aureus*		
		256 µg/disc	128 µg/disc	64 µg/disc	256 µg/disc	128 µg/disc	64 µg/disc
1	2a	0	0	0	0	0	0
2	2b	0	0	0	0	0	0
3	2c	0	0	0	0	0	0
4	2g	0	0	0	0	0	0
5	1a	0	0	0	0	0	0
6	1b	0	0	0	0	0	0
7	1c	0	0	0	11.5	9.5	8.5
8	1g	10	0	0	0	0	0

Zone of inhibition (mm) for Reference standard

		E. coli			*S. aureus*		
		i	ii	iii	i	ii	iii
11	Positive Control (Ciprofloxacin 5µg)	18	18	18	18.5	18	18
12	Negative control (100% Acetone)	0	0	0	0	0	0

N.B: Zone of inhibition given in mm (diameter). ‘0’: no inhibitory activity

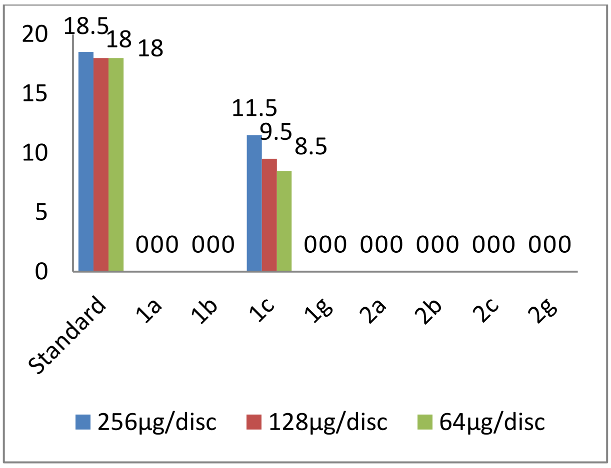

Fig. 1. Graphical representation of zone of inhibition (mm) of synthesized compounds for *S. aureus* in three different concentrations.

Results and Discussion

The special features of the spectroscopic data of the final synthesized compounds (*β*-lactams/azitidinones) can be explained from the general structure of the molecule.

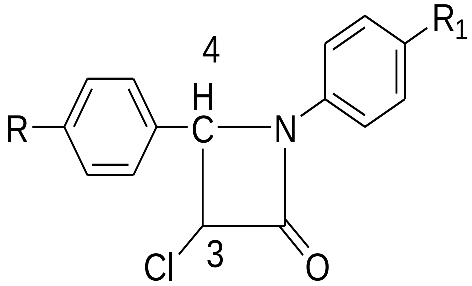

Fig. 2.General structure of synthesized *β*-lactam.

Because the lactam molecule contained an H-bonded O-H group, an unusually strong and broad absorption band was discovered at 3432 cm^{-1} in the infrared spectrum analysis. The NO$_2$ group's existence is the cause of the band at 1558 cm^{-1}. A doublet at δ (4.25-4.27) ppm in the ^{1}H-NMR spectra of produced azitidinone compounds corresponds to an H-4 proton with a coupling constant of J = (4.22-4.65) Hz because of the coupling with an adjacent H-3 proton. Pick is given by the nearby proton H-3 at δ (5.28-5.50) ppm with a J value (4.22-4.65) Hz. A singlet appeared at δ 2.33 ppm for –CH$_3$ protons. Aromatic protons appeared at δ (6.9-8.5) ppm as multiplets. The broad singlet was found to be at δ 8.18 ppm for phenolic –OH proton (compound (**1a**), and a singlet appeared at δ 3.21 ppm for $-N(CH_3)_2$ protons (compound (**1c**). The synthesized compounds show characteristic absorption at (251, 329, 253, 250) nm for the compounds **1a-h**, respectively, in the UV spectrum, which is responsible for a carbonyl chromophoric group. It consists of both $n\rightarrow\pi^*$ and $\pi\rightarrow\pi^*$ transitions. The spectral data of all the synthesized compounds were consistent with their structures., and the microanalyses also supported these structures

Antimicrobial Studies

In the disc diffusion method, Gram-positive and Gram-negative bacteria were used to investigate the antibacterial qualities of the produced compounds. Of all the compounds screened for bacteria, only compound 1c showed action. None of the other chemicals showed robust efficacy against any species at the specified doses. Let's look at the structural variation of compounds. They show antibacterial potency, and the compounds did not show activity at all, which gives a clear idea about the importance of the lactam rings. Compound framework variation conducts bioactivity, and framework modification of molecules commonly changes biological activity.(Vashi et al., 1995; Von Nussbaum et al., 2006) The cyclized products are the *β*-lactams, which showed marked antibacterial activity.

Conclusion

A plethora of β-lactams have been successfully synthesized as antibiotic mimics. A comparison between conventional and microwave techniques provided data on noteworthy reductions in reaction time, eco-friendly nature, and high product yield. The characterizations of newly synthesized compounds were ensured based on IR, UV, and ^{1}H-NMR evidence and were consistent with the desired structure.

Acknowledgments

The authors are grateful to the Department of Chemistry of Jahangirnagar University for supplying laboratory facilities, contributing support, and providing chemicals and reagents. We want to offer our deep gratitude to Kawamura Yasuhiko, PhD, Professor, Department of Chemical Science and Technology, Faculty of Engineering, Tokushima University, Japan, for supplying the ^{1}H-NMR spectral data of the samples. The author is also grateful to the WazedMiah Science Research Centre, Jahangirnagar University, Savar, for measuring the IR spectra and elemental analysis of the samples.

Conflict of interest declaration

The authors declared that there is no conflict of interest.

Author's Contributions

Professor Md. Mamun Hossain and Sumaiya Khan contributed to the idea, supervision, data analysis, and manuscript writing. Kamrunnahar Happy, Sumaiya Khan, Umme Aiman Liza, and Afsana Mimi performed laboratory experiments, data analysis, and literature review and made the table and graphs. M. Rafikul Islam contributed to the Microbial assay of the synthesized compounds.

References

Abdulla RF andFuhr KH., Monocyclic antibiotic beta-lactams. *J. Med. Chem*., 1975; 18(6): 625-627.

Calderon C and Sabundayo BP. Antimicrobial classifications: Drugs for bugs. In: Antimicrobial Susceptibility Testing Protocol, Eds. Schwalbe R, Steele-Moore L and Goodwine AC, 1st edition, CR Press, 2007; p. 46.

Doherty JB, Dorn CP, Durette PL, Finke PE, Mac Coss M, Mills SG, Shah SK, Sahoo SP, Polo SA and Hagmann WK. Substituted azetidinones as anti-inflammatory and antidegenerative agents. US Patent No. 5, 591, 737, Jan 7, 1997.

Durckheimer W, Blumbach J, Lattrell R and Scheunemann KH. Recent developments in the field of β-Lactam antibiotics. Angew. *Chem. Int. Ed.* 1985; 24: 180-202.

Feigelson GB, CurranWV and Ziegler CB.4-Substituted azetidinones as precursors to 2-substituted-3-carboxy carbapenem antibiotics and a method of producing them. US Patent no. 5, 189, 158, Feb. 23, 1993.

Georg GI. The Organic Chemistry of β-Lactams; Wiley Verlag Chemie: New York, 1992; pp. 197-225.

Hossain M, Sukanta S and Foysal A. Antioxidant potential study of some synthesized N-heterocycles. *Bangladesh Med Res. Coun. Bull.*2009; 35: 49-52.

Khalafallah AK, Selim MA, El-Hamd RMA, Elmaghraby MA, Soleiman HA and Raslan MA. Novel synthesis of some new fused/spiro heterocyclic compounds and their biological activity. *Indian J. Chem.* 1995; 34B, 1066-1070.

Nantasenamat C, Isarankura-Na-Ayudhya C, Naenna T and Prachayasittikul V. A practical overview of quantitative structure-activity relationship. *Excli Journal*. 2009; 8: 74-88.

Palomo C, Aizpurua JM, Ganboa I and Oiarbide M Eur. Asymmetric synthesis of β-lactams by staudinger ketene-imine cycloaddition reaction. *J. Org. Chem.* 1999; 12: 3223-3225.

Parikh KA, Oza PS and Parikh AR. Synthesis of some new 2-azetidinones as potential antitubercular agents. *Indian J. Chem*. 2000; 39B: 716-718.

Schwalbe R, Steele-Moore L and Goodwin AC. *Antimicrobial Susceptibility Testing Protocols.* 1st edition, *CRC Press,* 2007; p. 432.

Singh GS. Recent progress in the synthesis and chemistry of azetidinones. *Tetrahedron* 2003; 59(39): 7631-7649.

Vashi BS, Mehta DS and Shah VH. Synthesis and biological activity of 4-thiazolidinones, 2-azetidinones, 4-imidazolinone derivatives having thymol moiety. *Indian J. Chem.* 1995; 26(47): 802-808.

Vashi BS, Mhta DS and Shah VH. Synthesis and biological activity of 4-thiazolidiones, 2-azetodinones, 4-imidazolinone derrivatives having thymol moiety. *Indian j. chem.*1995; 26(47): 802-808

vander Steen FH and van Koten G. Syntheses of 3-amino-2-azetidinones: A literature survey. *Tetrahedron,* 1991; 47(36): 7503-7524.

von Nussbaum F, Brands M, Hinzen B, Weigand S and Häbich D. Antibacterial natural products in medicinal chemistry - exodus or revival?. *Angew. Chem. Int. Ed.,* 2006; 45 (31): 5072-5129.

Waksman SA. What is an antibiotic or an antibiotic substance?. *Mycologia.* 1947; 39 (5): 565-569.

J. Bangladesh Acad. Sci. 48(1); 121-134: June 2024 DOI:https://doi.org/10.3329/jbas.v48i1.70241

Journal of Bangladesh Academy of Sciences

Journal homepage: http://www.bas.org.bd/publications/jbas.html

Research Article

Purification of waste engine oil using raw clay, acid treated clay and clay/activated charcoal

Mahmudur Rahman*, Moni Akter, Abu Bakar Siddik, Md. Waliul Islam[1], Sadia Afrin, Mirola Afroze[2],
Mala Khan[2], Md. Azizul Hoque[3] and Md. Al-Mamun[4]
Department of Chemistry, Jagannath University, Dhaka, Bangladesh

ARTICLE INFO

Article History

Received: 6 December 2023
Revised: 14 April 2024
Accepted: 18 April 2024

Keywords: Waste engine oil, Base oil, Clay, Acid treated clay, Activated charcoal.

ABSTRACT

The purification of waste engine oil was conducted utilizing locally available clay in three different forms: raw, acid-treated, and a mixture of clay with activated charcoal. A 72.6% and 70.12% purification efficiency has been achieved when employing raw and acid-treated clay, respectively. However, the purification yield decreased to 64.35% when utilizing a combination of acid-treated clay and activated charcoal. FTIR analysis confirmed the presence of alkanes and alkenes in the purified oil. The NMR and GC-MS analysis identified the presence of linear and branched alkanes and alkenes, as well as substituted-benzene compounds in the purified oil. The density of waste engine oil and the corresponding purified oil was determined to be 0.929 g/mL and 0.825 g/mL, respectively. After purification, the kinematic viscosity decreased from 192 mm^2/sec to 70 mm^2/sec at 40 °C. The AAS analysis revealed the presence of 13.28 mg/L of lead (Pb) and 91.56 mg/L of chromium (Cr) in the waste engine oil, which significantly decreased to 0.02 mg/L and 0.037 mg/L, respectively, after purification with clay mixed with activated charcoal.

Introduction

Lubricating oil, whether mineral or synthetic, plays crucial roles in minimizing friction, preventing wear and rust, dissipating heat, and purging contaminants from the engine (Kupareva et al., 2013b; Pinheiro et al., 2021; Sarkar et al., 2023). It is commonly referred to as motor or engine oil in vehicle engine applications. Typically, lubricating oil consists of 80–90% base oil and 10-20% additives (Islam et al., 2021). Base oil can be derived from either mineral oil (mineral base oil) or synthesized (synthetic base oil). Due to the lower cost of mineral oil, approximately 85% of the world's lubricant oil supply is obtained from mineral base oil, which is primarily composed of paraffinic hydrocarbons, including saturated linear (n-paraffin) and branched (iso-paraffin) alkanes (Pinheiro et al., 2021).

Lubricating oil typically comprises 86% base oil, 5% viscosity index improver (polyisobutylene, polymethacrylate), 1% oxidation inhibitor (zinc dialkyl, dithiophosphate), 4% detergent (barium and calcium sulphonates or phenates), and 4% multi-functional additives (dispersant and pour point depressant) (Kupareva et al., 2013b). The base oil, primarily composed of mineral hydrocarbons ranging from C_{18} to C_{40} (Prince, 2010; Pinheiro et al., 2021), includes n-paraffin (saturated linear alkanes), iso-paraffin (branched alkanes), naphthenes (cycloalkanes), and aromatics with boiling points ranging from 300 to 565 ^{O}C (Mang and Lingg, 2017; Pinheiro et al., 2021). Synthetic alternatives, such as polyalphaolefins (PAO), synthetic esters, and

---

*Corresponding author:<mm_rahman1978@yahoo.co.uk>

[1]*Trility Solutions Inc., Accolade Avenue, Morisset, Australia;* [2]*Bangladesh Reference Institute for Chemical Measurements, Bangladesh Council of Scientific and Industrial Research (BCSIR), Dhaka, Bangladesh;* [3]*Institute of Energy Research and Development (IERD), Bangladesh Council of Scientific and Industrial Research (BCSIR);* [4]*Materials Science Division, Atomic Energy Center, Dhaka, Bangladesh.*

polyalkylene glycols (PAG), have also been developed (Pinheiro et al., 2021).

Globally, lubricating oil production reached 35.7 million tons in 2017 (Pinheiro et al., 2021). In Europe alone, consumption is approximately 5.7 million tons annually (Kupareva et al., 2013b). However, this consumption generates 2.7 million tons of waste lube oil per year in Europe, with only 0.7 million tons undergoing proper waste oil treatment (Kupareva et al., 2013b). In Bangladesh, a developing country, annual consumption stands at 0.16 million MT tons (Islam et al., 2021), yet only a limited quantity of engine oil is recycled. Unfortunately, a significant portion of used engine oil in Bangladesh is disposed of indiscriminately in drains and soil. This unregulated disposal substantially threatens the local flora and fauna and undermines ecosystem health.

Lubricants used in internal combustion engines degrade over time due to the breakdown of additives and the buildup of sludge and water. However, Mineral-based oil remains stable and resistant to oxidation (Kajdas, 2014). Waste lubricants also contain heavy metals such as lead (Pb), chromium (Cr), iron (Fe), zinc (Zn), calcium (Ca), and organic compounds like polycyclic aromatic hydrocarbons (PAH) and polychlorinated biphenyls (PCB), among others. The environmental impact of waste engine oils is significant as they are non-biodegradable and can hinder plant growth if disposed of in soil, potentially introducing toxic heavy metals such as lead and chromium into the food chain (Morkunas et al., 2018; Pinheiro et al., 2021). Additionally, dumping waste engine oil into water creates an organic film that impedes the oxygenation of aquatic organisms, exacerbating the adverse effects on the environment (Pinheiroet al., 2021).

As base oil remains unchanged in the waste lubricating oil, several methods have been developed to recover base oil from waste lubricant (Kajdas, 2014). A typical refining process comprises four stages: dewatering and defueling (to remove water and light hydrocarbons), de-asphalting (to remove asphalt using sulfuric acid or solvent extraction process), finishing (to improve the oil color and oxidation stability by clay treatment or hydro finishing), and fractionation to obtain base oil (Kupareva et al., 2013b).

The acid/clay process, first introduced in the US during the 1960s (Dang, 1997; Kupareva et al., 2013b; Pinheiro et al., 2021), involves pre-treating waste engine oil through processes like pre-flash or vacuum distillation to separate water and light hydrocarbons. Then, concentrated H_2SO_4 (10-15 wt %) is added to dehydrate waste oil, causing additives and sulfides to precipitate as sludge (deasphalting). Clay treatment is followed by removing organic acids and waxy substances, and the oil undergoes filtration and distillation to yield base oil (Kupareva et al., 2013b). While this process achieves 62-63% purification, the resulting oil is dark in color and has a noticeable odor (Kupareva et al., 2013b). However, challenges associated with the disposal of acid sludge and spent clay (Pinheiro et al., 2021) make this process an unpopular treatment choice. Jafariand Hassanpour(2015) mentioned that acidic sludge, a by-product of the acid/clay process, can be used as a raw material for bitumen production.

To overcome the limitations of the acid/clay process for the purification of the waste lubricant, several alternative technologies have been developed, such as Mineralöl-Raffinerie Dollbergen GmbH (MRD) solvent extraction process, Vaxon process, CEP process, Ecohuile process, Cyclon process (KTI process), Revivoil process, Snamprogetti process/IFP technology, Hylube process, Interline process (Dang, 1997; Audibert, 2006; Kupareva et al., 2013b; Kajdas, 2014; Pinheiro et al., 2021).

The Mineralöl-Raffinerie Dollbergen GmbH (MRD) solvent extraction process employs the liquid-liquid extraction principle. In the Mineralöl-Raffinerie Dollbergen GmbH (MRD) solvent extraction process, water is removed from the waste lubricating oil by dewatering it, and then light hydrocarbon is removed by vacuum distillation. In the following step, the steam-absorption process removes dissolved oxygen (O_2) from the distillate.

The distillate then enters a solvent extraction column, where the distillate combines with N-methyl-2-pyrrolidone (NMP) solvent. The aprotic NMP solvent exhibits a selective affinity for unsaturated hydrocarbons, aromatic hydrocarbons, polycyclic aromatic hydrocarbons (PAH), and sulfur compounds. The solvent containing the raffinate phase is collected at the top of the extraction column. Base oil is recovered after solvent removal in the stripping column. This process achieves an average base oil yield of 84-92% and produces high-quality base oil (Kupareva et al., 2013b; Pinheiro et al., 2021). Re-refining the used lubricating oil by vacuumdistillation/thin wiped film evaporation technique has also been developed (Saleemand Karim, 2020).

In this work, we have replaced the clay/acid process with clay/activated charcoal to avoid the formation of acid sludge. Clay/activated charcoal is effective at adsorbing heavy metals such as lead and chromium and removing degraded additives from waste engine oil.

Materials and methods

Clay was collected fromBijoypur village of Durgapurupazila of Netrokona district, Bangladesh. Activated charcoal was purchased from Loba Chemie PVT. Ltd: India and sulphuric acid from Sigma Aldrich.

2.1 Preparation of acidified clay

A mixture of 40.0 g clay and 400.0 mL sulfuric acid (1 M) was refluxed at 140 °C for 4 hours. The solution was then cooled to room temperature, and the resulting suspended materials were filtered and washed with distilled water to eliminate excess acid and soluble metal salts. Then, the washed suspension was dried at 100 °C for 14 h and calcined at 550 °C for 14.5 h in a muffle furnace. The resultant catalyst weighed 26.9 g of clay.

2.2 Characterization Techniques

Characterization of local clay

The prepared catalyst underwent comprehensive characterization employing various techniques, including X-ray powder diffraction (XRPD), scanning electron microscopy (SEM), x-ray fluorescence (XRF), and Fourier transform infrared (FTIR) spectroscopy. XRD analysis of clay was performed using the GNR Explorer powder X-Ray diffractometer with Cu-Kα1 source at 35 KV and 25 mA and step size of 0.1^o with data integration time 3s per step over an angular range of $5–80^o$ (2θ).The irradiation source was Rh x-ray at 140 mA and 30 kV. SEM images of clay and activated charcoal were obtained using the JEOL-SEM 7600F, sputtered with gold before analysis. Elemental analysis was conducted using the Shimadzu XRF-1800 (Lab Center) instrument, with a 1.0 g sample mixed and ground with 0.25 g of boric acid, followed by palletization. FTIR analysis of engine oil was conducted on the Shimadzu 8400S, Japan, with KBr pellets heated at 100 °C for 1 day before analysis, covering the 400-4000 cm^{-1} range.

Characterization of engine oil

The purified engine oil was comprehensively analyzed through GC-MS, FTIR, and ^{1}H NMR spectroscopy. GC-MS/MS analysis was performed using the Shimadzu GCMS-TQ8040, with a 0.5 µL sample injected in splitless mode on a capillary column Rxi-5ms (30 m × 0.25 mm id). The injection temperature was 250 °C, and the oven temperature program ranged from 50 °C to 300 °C. The column's flow rate and total run time were 1 mL/min and 30 min, respectively, utilizing electron impact ionization for MS detection (full scan mode 50-550 m/z). A quadrupole mass analyzer was used in GC-MS analysis. Hydrocarbon identification was performed using computer-assisted mass spectral search by NIST-MS library 2009.

Additionally, ^{1}H NMR analysis of the engine oil was conducted using the Bruker AVANCE III HD (400 MHz) instrument. A VARIAN AA240FS, atomic absorption spectrometer, was used to determine the amount of lead and chromium. The analysis mode was flame AAS mode. For the analysis of lead (Pb), a single lamp with a maximum current was 12 mA and a slit of 1.0 nm with a wavelength of 217 nm was used. For the analysis of chromium (Cr), a multi-lamp with a slit of 0.2 nm and wavelength was 357.9 nm was used. For the analysis of both metals (Pb and

Cr), the calibration curve was developed in the range of 0.1 to 2.5 ppm, and a new rational regression equation was used for the best fit of the curve.The BET-specific surface area and pore volume were determined by measuring nitrogen adsorption-desorption isotherms atliquid N_2 temperature (-196 °C) with a PMI's BET-Sorptometer (BET-201A, USA) apparatus. Before BET analysis, the samples were degassed at 120 °C under vacuum for 1.5 hours. Data obtained from the BET-Sorptometer were analyzed using BETwin software.

2.3 Purification of waste engine oil

2.3.1 Purification of waste engine oil using raw clay

500 mL waste engine oil and 100 g raw clay were mixed in a 1 L round bottle flask. The mixture was heated on a heating mantle and distilled. The distillate started transferring in the receiving flask at 80 °C and continued transferring until reaching 300 °C. The volume of the purified oil obtained was 440 mL, corresponding to a yield of 72.6%.

2.3.2 Purification of waste engine oil using 1 M H_2SO_4 treated clay

100 mL waste engine oil and 20 g acid-treated clay were mixed in a 1 L round bottle flask. The mixture was heated on a heating mantle and distilled. The distillate started transferring in the receiving flask at 100 °C until reaching 255 °C. The volume of the purified oil obtained was 85 mL, corresponding to a yield of 70.12%.

2.3.3 Purification of waste engine oil using activated charcoal and 1 M H_2SO_4 treated clay

Like the method above, 100 mL waste engine oil, 20 gacid-treated clay, and 20 g activated charcoal were mixed in a 1 L round bottle flask. The mixture was heated on heating mantle and distilled.

The distillate was heated on the heating mantle and distilled. It started to be transferred in the receiving flask at 89 °C and continued transferring until reaching 270 °C. The volume of the purified oil obtained was 78 mL, corresponding to a yield of 64.35%.

2.4 Sample preparation for metal analysis by atomic absorption spectroscopy (AAS)

A 5 g oil sample was heated in a porcelain cup at 105 °C for 3 hours. The oil was further heated in a muffle furnace at 600 °C to convert into ash. The ash was dissolved with 5 mL of concentrated HNO_3 acid and 5 mL of concentrated HCl. The resulting solution was heated until no visible smoke was observed. The solution was transferred to a 100 mL flask, and distilled water was added to achieve a final volume of 100 mL.

Results and Discussion

Characterization of local clay

The chemical compositions of raw clay (Bijoypur) and sulfuric acid-treated clay were determined by XRF (Table 1). The raw clay contains 56.60 % SiO_2 and 38.70 % Al_2O_3. The Si/Al ratio of raw clay is 2.57.

The sulfuric acid treatment increased SiO_2content to 61%, followed by a decrease in Al_2O_3 content to 34.6%. This shift is attributed to the leaching of Al^{3+} ions from the raw clay, resulting from hydrolysis under acidic conditions. The reaction between clay and sulfuric acid is as follows:

$$Al_2O_3.2SiO_2.2H_2O + 3H_2SO_4 \longrightarrow Al_2(SO_4)_3 + 2SiO_2 + 5H_2O$$

Table 1. Compositions (%) of raw clay and 1M H_2SO_4 treated clay by XRF.

Clay (Bijoypur Durgapur)	SiO_2	Al_2O_3	Fe_2O_3	TiO_2	K_2O	Na_2O	MgO	SO_3	Si/Al
Raw clay	56.60	38.70	1.61	1.36	0.81	0.35	0.25	0.14	2.57
1 M H_2SO_4 treated clay	61.00	34.60	0.78	1.26	0.75	0.25	0.24	0.97	3.11

After acid treatment, the Si/Al ratio increased from 2.57 to 3.11. This increase indicates a decrease in the clay's acidity.

The SEM analysis (Fig. 1) provides insights into the morphology of clay and activated charcoal. Particle aggregation is evident in the SEM image of raw clay (1a). Following the 1 M H_2SO_4 treatment of clay (1b), surface roughness increased due to etching, generating smaller particles and an increased inter-particle distance. Notably, the SEM image of activated charcoal (1c) exhibits the presence of numerous voids, indicating the potential for metal adsorption.

The XRD analysis of raw clay (Fig. 2a) reveals that the clay is predominantly composed of silica (quartz) and a small amount of muscovite characterized as potassium aluminum silicate hydroxide, ($KAl_2(AlSi_3O_{10})(OH)_2$). The major 2Ө peaks are 19.83°, 20.93°, 26.72°, 36.61°, 39.54°, 42.51°, 50.20°, 60.02°, 68.19°, and 68.38°. Due to acid treatment of raw clay (Fig. 2b), de-alumination occurred without altering crystallinity. The major 2Ө peaks of acid treated clay were observed at 19.75°, 20.91°, 26.71°, 36.61°, 39.52°, 50.19°, 60.02°, and 68.19°.

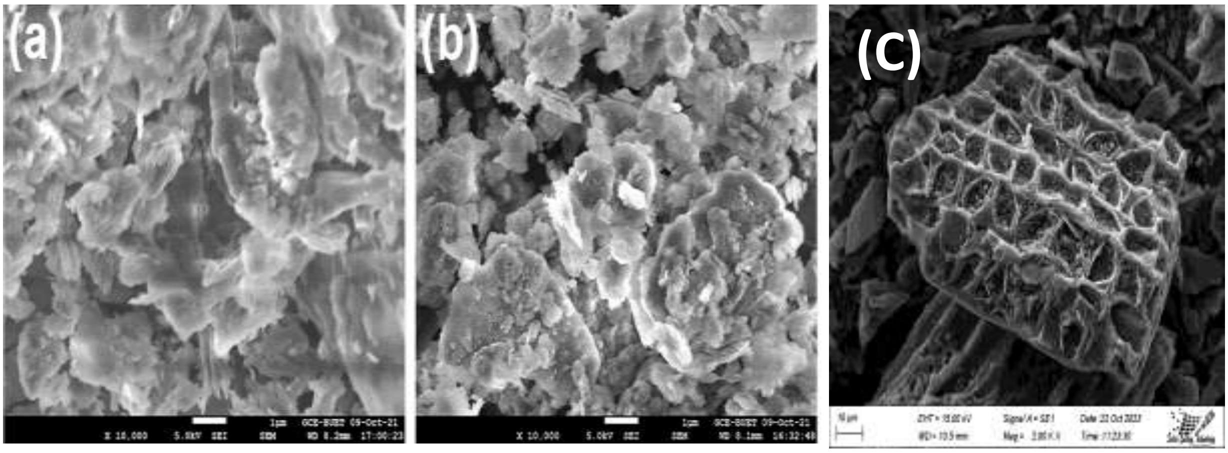

Fig. 1. Scanning electron microscope (SEM) image of (a) raw clay, (b) 1 M H_2SO_4treated clay, and (c) activated charcoal.

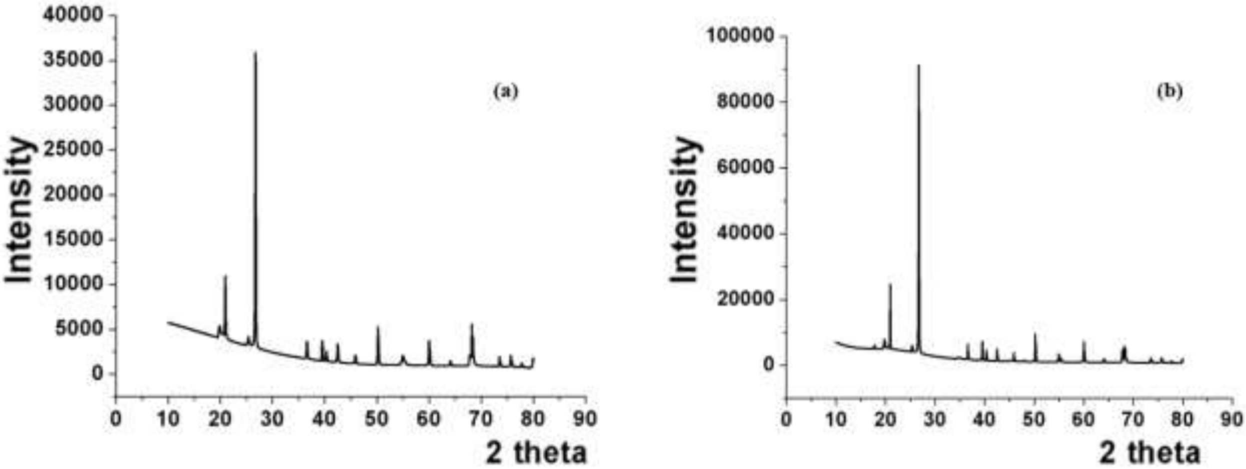

Fig. 2. XRD of raw clay (a) and 1 M acid-treated clay (b).

The BET analysis shows that the specific surface area has increased from 28.38 m^2/g to 576.80 m^2/g due to the mixing of acid-treated clay with the activated charcoal (Table 2). Similarly, the total pore volume of acid-treated clay has risen from 0.0758 cc/g to 0.4074 cc/g after mixing with the activated charcoal. The N_2 adsorption/desorption isotherms of acid-treated clay and a mixture of acid-treated clay and activated charcoal are shown in Fig. 3, displaying a type IV isotherm characteristic of mesoporous materials.

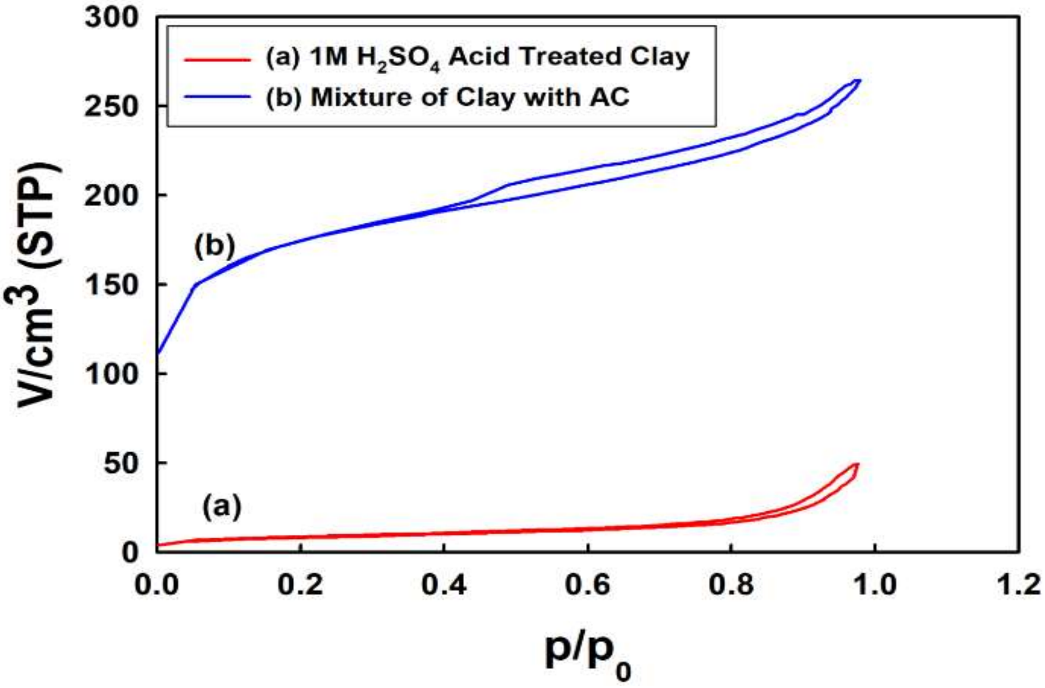

Fig. 3. N_2 adsorption/desorption isotherms of (a) 1 M acid-treated clay and (b) a Mixture of acid-treated clay with activated charcoal (AC).

Table 2. BET results of acid-treated clay and a mixture of acid-treated clay and activated charcoal

Parameter	BET specific surface area (m^2/g)	Total pore volume (scc/g)
Acid treated clay	28.38	0.0758
A mixture of acid-treated clay and activated charcoal	576.80	0.4074

Analysis of purified waste engine oil

Fig. 4 illustrates the color of engine oil before and after the purification process. Note, that the visual analysis indicates an improvement in opacity in the waste engine oil purified by clay/activated charcoal (A) in comparison to the engine oil purified exclusively by acid-treated clay (C). Table 3 outlines the purification outcomes for waste engine oil using raw clay, yielding 72.6% purified oil. Subsequently, applying 1 M sulfuric acid-treated clay resulted in an oil purification of 70.12%. However, the clay/activated charcoal process reduced oil yield, resulting in a 64.35% purified oil.

Fig. 5 represents the FTIR analysis of oil purified by clay/activated charcoal, indicating the presence of alkanes and alkenes in the oil. The C-H stretching of methyl and methylene groups within the alkane structure is discernible at 2959 cm^{-1}, 2931 cm^{-1}, and 2857 cm^{-1}. Additionally, the spectral peak at 1649 cm^{-1} and 1455 cm^{-1} correspond to C=C stretching and C-H scissoring, respectively. Furthermore, the C-H bending is evident at 735cm^{-1}. A similar FTIR spectrum was observed for oil purified by clay only.

Fig. 4. Picture of engine oil purified by clay/ activated charcoal(A), waste engine oil(B), and engine oil purified by acid-treated clay (C).

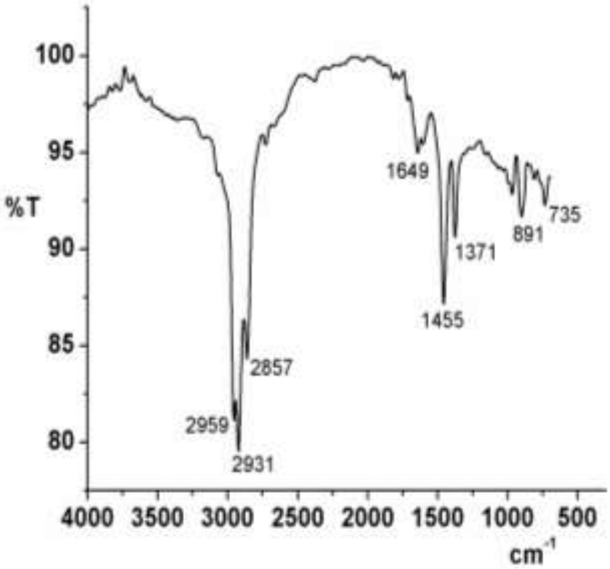

Fig. 5. FTIR of purified engine oil by clay/ activated charcoal.

Table 3. Purified engine oil obtained from raw clay, acid-treated clay, and clay/activated charcoal. The density of purified engine oil is 0.825 g/ml.

Clay	Volume of waste engine oil (mL)	Mass of Clay (g)	Mass of activated charcoal (g)	Purified oil obtained (mL)	Mass of purified oil (g)	%Yield
Untreated clay	500	100	-	440	363	72.6
1M H_2SO_4 treated clay	100	20	-	85	70.12	70.12
1M H_2SO_4 treated clay	100	20	20	78	64.35	64.35

Kupareva et al., 2013a analyzed fresh and used automotive lubricating oil by FTIR spectroscopy. They reported that fresh and used motor oil contained mostly saturated compounds consisting of linear and branched-chain paraffin. Notably, the FTIR spectrum of the fresh and used oil possessed bands at 2954 - 2856 cm^{-1}, an intense band at 1463 cm^{-1}, and a less intense band at 1376 cm^{-1}, attributable to C-H vibrations. Fresh lube oil contains oxygen-containing functional groups used as friction modifiers or lubricity additives. These friction modifiers are generally polar molecules consisting of a polar functional group (ketone, ester, carboxylic acid) and a nonpolar hydrocarbon tail (Kupareva et al., 2013a). Kupareva et al. (2013a) found bands at 1747 and 1701 cm^{-1} in the fresh oil, which arose from carbonyl groups of esters, ketones, or acids. They further inferred that the band at 1747 cm^{-1} originated from five and seven-membered cyclic ketones while that at 1701 cm^{-1} arose from polymethacrylate presented in fresh oil. Polymethacrylate is a viscosity modifier and a pour-point depressant additive in fresh oil. Al-Ghoutiand Al-Atoum (2009) found thatpolymethacrylate typically arose at 1701 cm^{-1} and 1154cm^{-1} in the fresh oil. However, no bands at 1747, 1701 cm^{-1}, and 1154 cm^{-1} were observed in our engine oil purified by clay/activated charcoal. In another study, Dominguez-Rosado andPichtel (2003) investigated used motor oil by FTIR and detected bands at 1704.29 cm^{-1} and 1603.13 cm^{-1} indicating the presence of carbonyl groups of esters, ketones, or acids. They also observed peaks at 869 cm^{-1}, 813cm^{-1}, and 1603 cm^{-1} originating from aromatic hydrocarbons, including polycyclic aromatic hydrocarbons.

Fig. 6 represents the NMR spectrum of the engine oil purified by clay/activated charcoal. The NMR indicates the presence of aromatic protons, as evidenced by the multiplets, at around 7.5 ppm. Multiplets in the 1-2.5 ppm range are attributed to various alkane substituents. A comparable spectrum was observed in the NMR analysis of oil purified using only clay.

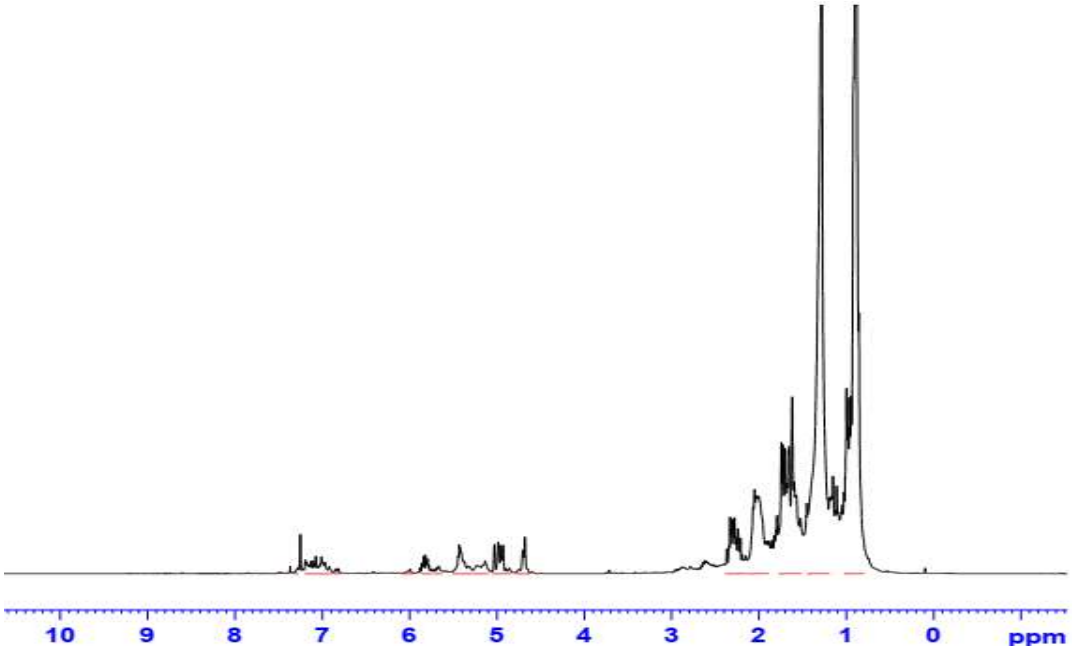

Fig. 6. NMR of purified engine oil by clay/activated charcoal.

Kupareva et al. (2013a) investigated fresh and used automotive lubricating oil by ^{1}H NMR spectroscopy. The authors reported that fresh and used oil showed aromatic protons at δ 6.95-7.05 ppm and 6.75-7.2 ppm, respectively. The olefinic protons arose at 5.65-5.5 ppm in fresh oil and 5.1-5.3 ppm in used oil. The CH_3-C proton was found at 0.9-0.8 ppm in fresh and used oil (Kupareva et al., 2013a). The researchers also reported that the fresh oil contained two high-intensity singlets at δ 5 ppm and 4 ppm and a less intense doublet at δ 4.8 ppm, indicating the presence of esters. However, no high-intensity singlet peak at 5 ppm was observed in the used lube oil. The NMRspectrum of the used lube oil showed a low-intensity singlet at 4ppm, which arosefrom esters. As reported by the study, a higher amount of esters (carbonyl groups) were present in fresh oil than in used oil. The used oil showed a broad peak at δ 2.6 ppm, which originated from organic acids formed via the chemical oxidation process in the used lube oil. In this study, we did not observe any intense singlet peak at δ 5 ppm and 4 ppm in our purified oil by clay/activated charcoal. This indicates the absence of the ester compounds in the purified oil. Aromatic protons and various alkane substituents (CH_3-C protons and –C-CH_2-C protons) were observed in the oil purified by clay/activated charcoal.

The GC-MS analysis of engine oil purified by clay/activated charcoal has been presented in Table 4. The GC-MS results confirm the presence of linear and branched alkane and alkene and substituted benzene compounds. The most notable compounds include octane, 1-octene, 2-methyl octane, 3,3-dimethyl butyl benzene, 1-nonene, 1-decene, 1,2,3-trimethyl benzene, 2-methyl-1-propenyl benzene, octadecane, 1-heptadecene, and 4-propyl heptadecane.

Kupareva et al. (2013a) conducted a comprehensive GC-MS analysis of fresh motor oil and used lube oil without purification. They reported that used lube oil contained gasoline components, short hydrocarbons, cyclic paraffins and aromatics with chain lengths ranging from C_{16} to C_{32}. However, fresh motor oil contains mostly hydrocarbons of longer chains. Both fresh motor oil and used motor oil contained alkylated diphenylamines (such as butyl-diphenylamine and octyl-diphenylamine) which was used as antioxidant additives. However, phenolic antioxidant (such as 4,4´-methylenebis(2,6-di-*tert*-butylphenol)) found in fresh oil was not observed in used motor oil. Naphthalene was found in used oil which is absent in fresh motor oil. In another study, Dominguez-Rosado et al. (2003) analysed fresh and used motor oil by GC/MS. They reported that used motor oil contained some new aliphatic and aromatic hydrocarbon compounds which were not present in the fresh motor oil. The identified new compounds in used motor oil were 1,3,5-trimethyl benzene, p-xylene and methyl ester undecanoic acid. The researchers also reported that substituted-benzene compounds and naphthalene-related compounds are more predominant in the used motor oil. In this study, various substituted-benzene compounds were observed in the purified engine oil. However, methyl ester undecanoic acid was not observed in our purified engine oil. During clay and activated charcoal treatment, some new compounds were observed other than methyl ester undecanoic acid.

To investigate the presence of heavy metals, specifically lead (Pb) and chromium (Cr), in both waste engine oil and purified engine oil, atomic absorption spectroscopy (AAS) was employed. According to the findings from the atomic absorption spectroscopy (AAS) (Table 5), the waste engine oil contained 13.28 mg/L of lead (Pb) and 91.56 mg/L of chromium (Cr). These concentrations were reduced to 4.36 mg/L for lead (Pb) and 0.35 mg/L for chromium (Cr) in the purified engine oil after purification by the acid-treated clay. However, a more significant reduction in lead (Pb) and chromium (Cr) concentrations was observed upon purification with the clay and activated charcoal mixture.The resulting lead (Pb) and chromium (Cr) content in the oil purified by clay mixed with activated charcoal was 0.02 mg/L and 0.037 mg/L, respectively

Table 4. GC-MS of purified engine oil by clay/activated charcoal.

Compound	Retention time	Area (%)
1-Octene	3.251	0.48
Octane	3.375	0.89
1,4-Pentadiene, 2,3,3-trimethyl-	3.502	0.31
Cyclopentane, 1-methyl-2-(2-propenyl)-, trans-	3.957	0.28
1-Heptene, 2,6-dimethyl-	4.195	0.30
Octane, 2-methyl-	4.499	0.28
Benzene, (3,3-dimethylbutyl)-	4.626	1.18
Tridecane, 7-methylene-	4.932	0.47
1-Nonene	5.054	0.39
O-Xylene	5.09	0.47
Hexane, 2,4-dimethyl-	5.244	1.06
Octane, 2,6-dimethyl-	6.034	0.26
1-Decene	7.548	0.54
Benzene, 1,2,3-trimethyl-	7.611	0.51
Decane	7.789	0.92
Cyclopentane, pentyl-	8.785	0.28
4-Decene, 5-methyl-, (E)-	10.202	0.53
1-Undecene	10.406	0.62
Dodecane, 2,6,11-trimethyl-	10.659	1.28
Benzene, (2-methyl-1-propenyl)-	12.032	0.67
Heptane, 4-(1-methylethyl)-	12.238	0.54
Undecane, 4-methyl-	12.408	0.54
Octadecane	12.561	0.45
Cyclohexane, 2-propyl-1,1,3-trimethyl-	13.198	0.47
Cyclopropane, nonyl-	13.377	0.61
Dodecane, 2,6,10-trimethyl-	13.629	1.32
Undecane, 3,6-dimethyl-	13.998	0.44
Tridecane, 2-methyl-	15.666	0.40
3-Tetradecene, (E)-	16.29	0.86
Nonane, 5-butyl-	16.52	1.42

Compound	Retention time	Area (%)
Dodecane	17.908	0.39
2,3-Dimethyldodecane	18.128	0.31
1-Tridecene	19.066	0.56
Octadecane, 5-methyl-	19.284	1.56
Tetradecane, 2-methyl-	20.961	0.36
2-Methyl-1-tetradecene	21.527	0.26
1-Pentadecene	21.702	0.40
Nonadecane	21.905	1.57
Hexadecane, 7,9-dimethyl-	23.058	0.26
Pentadecane, 4-methyl-	23.336	0.42
Pentadecane, 3-methyl-	23.665	0.28
1-Eicosene	25.27	0.37
Pentadecane, 2,6,10-trimethyl-	25.504	1.14
Tetradecane, 5-methyl-	25.6	0.34
Pentadecane, 8-hexyl-	26.75	1.34
1-Heptadecene	28.839	0.42
Nonadecane, 9-methyl-	31.946	0.33
Pentacosane	33.725	0.47
Triacontane	34.064	0.42
Eicosane	34.313	1.31
Heptadecane, 4-propyl-	34.37	0.45
Nonadecane, 4-methyl-	34.47	0.48
Tetratetracontane	34.513	0.72
Eicosane, 2-cyclohexyl-	34.65	0.72
Tetracontane	34.834	0.82
Dodecane, 1-cyclopentyl-4-(3-cyclopentylpropyl)-	34.885	0.76
Undecane, 4-cyclohexyl-	34.92	0.40
Hexadecane, 2,6,10,14-tetramethyl-	34.99	1.01
hexacosane	35.03	2.27
Hexadecane, 4-methyl-	35.155	0.93
Hexacontane	36.144	4.33
Hexadecane	36.73	1.70
Tetracosane	37.042	2.23
Dodecane, 6-cyclohexyl-	38.01	0.25

Activated charcoal effectively adsorbs lead (Pb) and chromium (Cr), reducing their quantity in the purified oil. BET analysis revealed an increase in specific surface area and total pore volume in the clay and activated charcoal mixture, facilitating the effective adsorption of Pb and Cr.

Table 6 presents the fuel parameter values for both waste engine oil and purified engine oil. The density of waste engine oil and the corresponding purified oil was determined to be 0.929 g/mL and 0.825 g/mL, respectively. The initial calorific value of the waste engine oil was 8530.81 KCal/Kg. The purified engine oil exhibited an increased calorific value of 10633 KCal/Kg, as determined by a bomb calorimeter. The kinematic viscosity values at 40 °C decreased from 192 mm²/sec for waste engine oil to 70 mm²/sec for the purified oil. The flash point of the waste engine oil and the purified oil were 109 °C and 158 °C, respectively. The lower value of flash points observed in used oil was attributed to light fuels (Abro et al., 2013; Abdulkareem et al., 2014). Table 7 presents the accepted values of quality assurance of re-refined base oil (Kupareva et al., 2013b; Abdulkareem et al., 2014).

Table 5. Amount of metal contents in waste and purified engine oil *(Data obtained by Absorption spectroscopy* (*AAS*).

Metal	Waste engine oil (mg/L)	Purified engine oil	
		Acid treated Clay (mg/L)	Acid treated clay and activated charcoal (mg/L)
Lead (Pb)	13.28 ± 1.13	4.36 ± 0.37	0.02 ± 0.002
Chromium(Cr)	91.56 ± 8.95	0.35 ± 0.03	0.037 ± 0.004

Table 6. Different parametric values of waste engine oil and purified engine oil

Parameter	Method	Waste engine oil	Purified engine oil with clay/charcoal
Density at 15 °C, g/cc	ASTM D 1298	0.929	0.825
kinematic viscosity, mm^2/sec	ASTM D 445	192 (at 40 °C) 29 (at 100 °C)	70 (at 40 °C) 10 (at 100 °C)
Calorific value, KCal/Kg	Bomb calorimeter	8530.81	10633
Flashpoint,°C	ASTM D 93	109	158
Pour point,°C	ASTM D 97	-13	-20
Ash (%)	ASTM D 482	0.895	0.006

Table 7. Guidelines for quality acceptance of re-refined base oil are as follows (Kupareva et al., 2013b; Abdulkareem et al., 2014).

Parameter	Value
Density at 15 °C, g/cc	0.864 to 0.895
kinematic viscosity, mm^2/sec (CST)	40-45 (at 40 °C) 6-7.5 (at 100 °C)
Viscosity index, cP	90 – 110
Flashpoint, °C	190 to 230
Pour point, °C	0 -9
Ash (%)	0.01

Conclusion

In this study, waste engine oil waspurified by locally available clay mixed with activated charcoal. Different properties were compared before and after the treatment process. A 72.6% and 70.12% purification efficiency could be achieved by employing raw and acid-treated clay, respectively. The introduction of activated charcoal in the acid-treated clay process reduced the oil yield to 64%. Notably, lead and chromium levels decreased significantly in engine oil purified by clay mixed with activated charcoal. The waste engine oil contains 13.28 mg/L of lead and 91.56 mg/L of chromium, whereas the purified oil showed a reduced level of 0.02 mg/L of lead and 0.037 mg/L of chromium when purified by clay mixed with activated charcoal. The FTIR analysis of the purified oil confirmed the presence of alkanes and alkenes. Further, the NMR and GC-MS analyses revealed the presence of linear and branched alkanes and alkenes, along with substituted-benzene compounds in the purified oil. Following the recovery of base oil from waste engine oil, the residual clay mixed with activated charcoal can be used for bitumen production.

References

Abdulkareem AS, Afolabi AS, Ahanonu SO and Mokrani T. Effect of treatment methods on used lubricating oil for recycling purposes. *Energy sources A: Recovery Util. Environ. Eff.* 2014; 36(9): 966-973.

Abro R, Chen X, Harijan K, Dhakan ZA and Ammar MA. Comparative study of used engine oil recycling using extraction by composite solvent, single solvent, and acid treatment methods. *ISRN Chem. Eng.* 2013; 2013: 952589.

Al-Ghouti MA and Al-Atoum L.Virgin and recycled engine oil differentiation: A spectroscopic study. *J. Environ. Manage*. 2009; 90:187-195.

Audibert F. Waste Engine Oils*:* Rerefining and Energy Recovery. 1st edition, *Elsevier*, 2006, p. 91.

Dang GS. Rerefining of Used Oils - a review of commercial processes. *Tribotest* 1997; 3(4): 445-457.

Dominguez-Rosado E andPichtel J. Chemical characterization of fresh, used and weathered motor oil via GC/MS, NMR and FTIR techniques. *Proc. Indiana Acad. Sci*. 2003; 112(2): 109-116.

Islam MS, Sanzida N, Rahman MM andAlam MD. From the value chain to environmental management of used lube oil: A baseline study in Bangladesh. *Case Stud. Chem. Environ. Eng.* 2021; 4: 100159.

Jafari AJ andHassanpour M. Analysis and comparison of used lubricants, regenerative technologies in the world. *Resour. Conserv. Recycl.* 2015; 103: 179-191.

Kajdas C. Re-refining Technologies. In: Encyclopedia of Lubricants and Lubrication. Mang. T. (ed.), Springer, Berlin, Heidelberg, 2014; pp 1554-1569.

Kupareva A, Mäki-Arvela P, Grénman H, Eränen K, Sjöholm R, Reunanen M andMurzin DY. Chemical characterization of lube oils. *Energy Fuel*, 2013a; 27: 27-34.

Kupareva A, Mäki-Arvela P and Murzin DY. Technology for rerefining used lube oils applied in Europe: a review. *J. Chem. Technol. Biotechnol.* 2013b; 88: 1780-1793.

Mang T and Dresel W. Lubricants and Lubrication, 2nd edition, WILEY-VCH Verlag GmbH & Co. KGaA: Weinheim, Germany, 2007, p. 34.

Morkunas I, Woźniak A, Mai VC, Rucińska-Sobkowiak R and Jeandet P. The role of heavy metals in plant response to biotic stress. *Molecules* 2018; 23(9): 2320.

Pinheiro CT, Quina MJ andGando-Ferreira LM. Management of waste lubricant oil in Europe: A circular economy approach. *Crit Rev Environ Sci Technol.* 2021; 51(18): 2015-2050.

Prince RJ. Base Oils from Petroleum. In: Chemistry and Technology of Lubricants. Mortier R, Fox M and Orszulik S. (eds.), *Springer, Netherlands*, 2010; pp 3-33.

Saleem HJ andKarim AR. Re-refining of used lubricating oil by vacuum distillation/thin wiped film evaporation technique. *Pet. Sci. Technol.* 2020; 38(4): 323-330.

Sarkar S, Datta D, Deepak, KS, Mondal BK and Das B. Comprehensive investigation of various re-refining technologies of used lubricating oil: areview. *J. Mater. Cycles Waste Manag.* 2023; 25(4): 1935-1965.

J. Bangladesh Acad. Sci. 48(1); 135-140: June 2024 DOI:https://doi.org/10.3329/jbas.v48i1.68504

Journal of Bangladesh Academy of Sciences

Journal homepage: http://www.bas.org.bd/publications/jbas.html

Research Article

Chromosomal characterization of two medicinal plants from Bangladesh

Ashma Ahmed Warasy

Department of Botany, Jahangirnagar University, Savar, Dhaka, Bangladesh

ARTICLE INFO

Article History

Received: 31 August 2023
Revised: 28 March 2024
Accepted: 24 April 2024

Keywords: Chromosome, Characterization, Medicinal plant, *Oxalis.*

ABSTRACT

Two medicinal plants, *O. corniculata* and *O. triangularis*, were investigated cytogenetically for proper characterization. Both plants had Complex Chromocenter interphase nuclei and Continuous prophase chromosomes. *O. corniculata* was discovered to have 2n=48 chromosomes and 2n=30 in *O. triangularis*. The chromosomal length range was 0.82±0.02-1.61±0.02 in *O. corniculata* and 1.02±0.02-2.52±0.03 in *O. triangularis.* The total length of the 2n chromosome complement was 53.52±1.19 and 46.76±0.41 for *O. corniculat*e and *O. triangular,* respectively. The two species differed in centromeric formulas, such as 48m for *O. corniculata* and 28m+2sm for *O. triangularis*. In their karyotype, no steady decrease in chromosomal length was seen. These characteristics showed that *O. corniculata* and *O. triangularis* could be considered primitive species. Therefore, compiling the cytogenetic features will be helpful to ensure the genuine identification and characterization of the two medicinally important *Oxalis* species.

Introduction

Oxalis is an extensive flowering plant genus that belongs to the Oxalidaceae family, consisting of eight genera with herbaceous plants, shrubs, small trees, and about 570 species (Christenhusz and Byng, 2016). Some species are yellow or pink sorrels, while others are called fake shamrocks or sourgrasses. They are characterized by their divided, palmate leaves that resemble clover leaves-, and funnel- or bowl-shaped flowers that often close at night or in dull weather. Several species, cultivars, and hybrids are popular in rock gardens, raised beds, an alpine house, or as houseplants. Some are considered very invasive weeds. Most of the members of this family are distributed across the world's warmer regions (Mathew, 1958). *Oxalis corniculata* L. is one of these species and possesses well-known traditional medicinal uses like- diarrhea, dysentery, stomachache, Datura poisoning, scorpion sting, giddiness, curing fever, coughs, cold, mouth ulcers, eczema, headache, expulsion of gastrointestinal worms, jaundice, and hepatitis (Muhammad and Mir, 2000). *O. triangularis* are largely used as medicinal plants. Other *Oxalis* spp. are grown as food (tuberous roots of *O. tuberosa* are used as food, leaves of *O. acetosella* are used as salads, and stems of *O. pescaprae* are used as a vegetable), and because of their magnificent pink, purple, and white blooms and lovely leaves, they have potential as an ornamental herb (Sharma and Chatterji, 1960). Different members of this genus contain oxalic acid, giving the leaves and blossoms an acidic flavor that can be refreshing to chew (Ahmed et al., 2009). So, the members of this genus are under threat because of their extreme medicinal uses. The consequences would be worse if they were not managed or conserved at this stage.

---

[*] Corresponding author:<aawarasy@yhoo.com>

In such a situation, genetic diversity analysis is essential in order to achieve appropriate conservation, multiplication and management options for the *Oxalis* spp. that exist in Bangladesh. Authentic characterization of *Oxalis* spp. is required for this purpose. Karyotype analysis is a must for authentic characterization. Other karyotypical criteria, such as heterochromatin distribution, should also be studied to obtain further information about different germplasm. Tanaka (1971) used orcein staining to classify distinct types of heterochromatin distribution. Later, other researchers attempted to describe heterochromatin distribution using different cytogenetical methods (Shahla and Alam, 2011). These investigations found that staining features in interphase nuclei and prophase chromosomes may differentiate distinct taxa, including variations of many germplasm karyotypes, a consistent and dependable characteristic unique to each specimen. Several cytological studies have been done on this genus abroad, but locally, it is very rare. The cytological work in the genus *Oxalis* has revealed several exciting features. Firstly, an aneuploid series of chromosome numbers have been found in this genus, such as x=5, 6, 7, 9, and 11 (Bonna et al., 2017). In addition to direct aneuploid sets, chromosome numbers other than the diploid sets have been recorded, such as 2n=24 chromosomes in *O. corniculata* (Rutland, 1941) and *O. stricta* (Bonna et al., 2017). High polyploidy sets such as 2n=66 and other higher numbers of chromosomes in *O. tuberosa* are also on record. Further, even in the same species, diploid and polyploid individuals are recorded in *O. brasillienses* (2n=14, 28).

The members of this genus are interesting for chromosome study because of their variability in chromosome number. The study of karyotypes is critical in cases where the basic chromosomal number is variable. Such research helps to describe each species and sheds light on how one form evolved from another.

Therefore, a conventional cytogenetic method through karyotype analysis was used to compare the degree of heterochromatic condensation, determine the chromosomal number, create a karyotype, and characterize two *Oxalis* species, *O. corniculata* and *O. triangularis*. This characterization is constructive for improving and conserving these germplasm.

Materials and Methods

Materials

This study investigated the following two *Oxalis* species: *O. corniculata* and *O. triangularis*. The plant materials were obtained from the conservatory and old Arts building of Jahangirnagar University, Savar, Dhaka, Bangladesh.

Methods

Healthy roots were collected. Only cold water at room temperature was used to pre-treat the collected root, followed by a 15-minute fixation in 45% acetic acid at 4°C. The roots were hydrolyzed for 8-9 seconds. These roots were placed on a slide, and the meristematic area was cut. Then, 1% aceto-orcein was added to it. A clean cover glass was applied to the substance and then lightly tapped and squished. Finally, the slides were observed under a microscope and photographed using a digital camera.

Results and Discussion

Orcein-stained interphase nuclei and prophase chromosomes.

Diverse karyomorphological traits were observed in heterochromatin distribution, which aids in characterizing diverse germplasm. In the current investigation, some big heterochromatic areas were found in the interphase nuclei of both cultivars. These were scattered around the nucleus. Few heterochromatic areas grouped together in these two species, generating larger heterozygotic patches in the interphase nucleus. A prominent nucleolus occupying more than 1/3rd of the nucleus was found in both cases (Figs. 1, 2). Both cultivar's prophase chromosomes were stained uniformly along their full length (Figs. 3, 4).

Tanaka (1971) was the first to provide karyomorphological criteria for interphase nuclei and prophase chromosomes. He divided them into five separate types based on each case's staining property. Later, several workers used these criteria to characterize various plant materials. (Sultana and Alam, 2016; Saha and Begum, 2020).

The present study discovered "Complex Chromocenter Type" interphase nuclei and "Continuous Type" prophase chromosomes in both *Oxalis corniculata* and *O. triangularis* (Figs. 1, 2, 3, 4; Table 1). The current findings do not support the common feature of heterochromatin distribution in prophase chromosomes. The observations above suggested the presence of facultative heterochromatin. These features have been limitedly considered as cytological parameters in *Oxalis* spp. Therefore, this is a critical strategy for characterizing the two *Oxalis* species.

Table 1. Types of heterochromatin distribution.

***Oxalis* species**	**Interphase nuclei**	**Prophase chromosomes**
O. corniculata	Complex chromocenter	Continuous
O. triangularis	Complex chromocenter	Continuous

2n chromosomes number

Two *Oxalis* species had distinct 2n chromosome numbers in this investigation. In the current study, *Oxalis corniculata* was discovered to have 2n=48 chromosomes (Fig. 5, 7; Table 2). Another scientist previously reported the same chromosomal number (Mathew, 1958). Furthermore, different chromosomal numbers were reported, including 2n=24 (Rutland, 1941) and 2n=44 (Chatterjee and Sharma, 1970). Several scientists believed that the primary chromosomal number for this species was x=11. Hence, specimens with 2n=44 may be called tetraploid. If x=7 is also included, then 2n=28 and 2n=42 could be tetraploid and hexaploid, respectively. However, the observed 2n=48 in this investigation did not correspond to the basic numbers of x=11 and x=7. In this scenario, aneuploid aberration may have evolved the 2n=48 from a higher ploidy level. In the case of *O. triangularis*, 2n=30 diploid chromosome number was determined in the present investigation (Fig. 6, 8; Table 2). Bonna et al. (2017) reported the same chromosome number for this species. Thus, the present report of 2n=30 chromosomes supports that of Bonna et al. (2017). However, the 2n=30 chromosome number confused the basic chromosome numbers x=11 and x=7. In this case, the 2n=30 might have evolved from a nearer ploidy level by aneuploid aberration. 2n=48 for *Oxalis corniculata* and 2n=30 for *O. triangularis* indicated that the species has octaploid or pentaploid nature if x=6, respectively. 2n=42 for *O. corymbosa*, x=6 is most likely the primary chromosome number for these species.

The cytological work carried out locally (only Bonna et al. (2017) and abroad on the genus *Oxalis* has revealed several interesting features. Several aneuploid series of chromosome numbers have been reported, such as x=5, 6, 7, 9, and 11 (Bonna et al., 2017). In addition, chromosome numbers other than the diploid sets have been recorded, such as 2n=24 chromosomes in *O. corniculata* (Rutland, 1941). High polyploidy sets like 2n=66 and other high diploid chromosome numbers in *O. tuberosa* are also recorded (Bonna et al., 2017). Moreover, Diploid and polyploid individuals in the same species (2n=14, 28 in *O. brasillienses*) were also reported by different scientists (Bonna et al., 2017).

Chromatin length

The chromosomal length range was 0.82±0.02-1.61±0.02 µm for *O. corniculata* and 1.02±0.02-2.52±0.03 for *O. triangularis*, where there was no discernible steady decrease in chromosomal length in either case (Figs. 7, 8, 9, 10; Table 2). The average chromosomal length for *O. corniculata* was 1.12 µm and 1.56 µm for *O. triangularis*. The overall length of the 2n chromosomal complement was determined to be 53.52±1.19 µm for *O. corniculata* and 46.76±0.41 µm for *O. triangularis*. The total length of *O. corniculata* was almost nearer than that of *O. triangularis*. Bonna et al. (2017) did not find this type of observation regarding total chromatin length among the two species. As a result, the current findings clearly demonstrated the variety of chromatin length across the specimens tested in this study.

Centromeric feature

Two *Oxalis* species were discovered to have more or less comparable centromeric index ranges of 45.90-50.00 for *O. corniculata* and 45.63-49.02 μm for *O. triangularis.* In the instance of the centromeric formula, all metacentric chromosomes in *O. corniculata* were shown to be strictly symmetric. Bonna et al. (2017) also found all metacentric chromosomes in this species. As a result, the current findings demonstrate that this species has a strictly symmetric karyotype. On the other hand, *O. triangularis* possessed 28 metacentric and 2 sub-metacentric chromosomes, representing an almost symmetric karyotype. Bonna et al. (2017) observed 26 metacentric and 4 submetacentric chromosomes in this species. There is quite a difference between Bonna et al. (2017) and the present investigation. The reason for this differential observation may be some chromosomal abnormalities, such as terminal deletion, pericentric inversion, unequal translocation, could have resulted in the formation of sub-metacentric chromosomes from metacentric chromosomes.

According to Stebbins (1971), two species of *Oxalis* are primitive plants, while *O. triangularis* is relatively advanced.

Karyotype symmetry and asymmetry index

The Karyotype asymmetry index (AsK %) was 52.90% for *O. corniculata* and 54.60% for *O. triangularis,* as observed in the present study (Table 2). On the other hand, 89.83% karyotype symmetry index (Syi %) was found in case of *O. corniculata* and 83.53 % was found in *O. triangularis* (Table 2). Karyotype symmetry index values decreased with increasing asymmetry, indicating both species' symmetric karyotype nature. No reports about these karyotypic parameters of *Oxalis* were available in earlier studies. So these features are essential for characterization of selected *Oxalis* species.

Therefore, the two medicinal plants, *O. corniculate* and *O. triangular* were karyomorphologically investigated in this study. They showed the above characteristic features after staining with orcein, which is very helpful for improving and conserving this germplasm.

Table 2. Comparative karyotype analysis.

Cytogenetical Parameters	***O. corniculata***	***O. triangularis***
2n	48	30
Total length of chrom. complement (μm)	53.52±1.19	46.76±0.41
Range of individual chromosome length (μm)	0.82±0.02-1.61±0.02	1.02±0.02-2.52±0.03
Range of CI	45.90-50.00	45.63-49.02
Centromeric formula	48m	28m+2sm
Karyotype symmetry index (Syi %)	89.83	83.53
Karyotype Asymmetry index (AsK %)	52.90	54.60

m = metacentric, sm = sub-metacentric chromosome, CI = Centromeric index

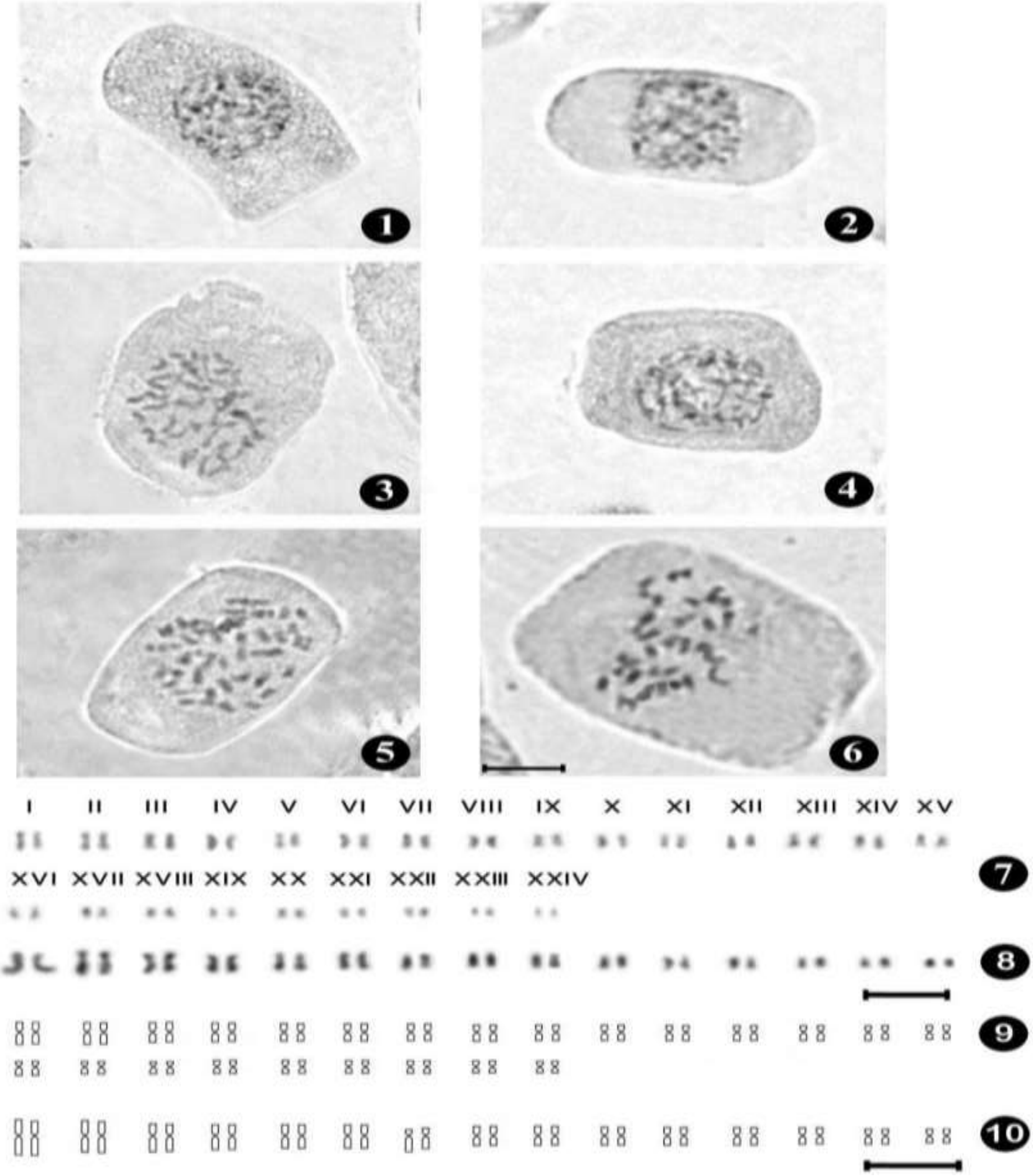

Figs. 1-10. Orcein-stained cytogenetical analysis of two species of *Oxalis* L. 1. Interphase nuclei of *O. corniculata*. 2. Interphase nuclei of *O. triangularis*. 3. Prophase chromosome of *O. corniculata,* 4. Prophase chromosome of *O. triangularis*. 5. Mitotic metaphase of *O. corniculata.* 6. Mitotic metaphase of *O. triangularis*. 7. Karyotype of *O. corniculata*. 8. Karyotype of *O. triangularis*. 9. Idiogram of *O. corniculata*. 10. Idiogram of *O. triangularis*. Bar=5µ.

References

Ahmed ZU, Hassan MA, Begum ZNT, Khondker M, Kabir SMH, Ahmad M, Ahmed ATA, Rahman AKA and Haque EU. In: Encyclopedia of Flora and Fauna of Bangladesh. Angiosperms: Dicotyledons (Fabaceae-Lythraceae). *Asiat. Soc. Bangladesh.* 2009; pp. 305-309.

Bonna IJ, Afroz M, Sultana SS and Alam SS. Comparative karyotype and RAPD analysis of four oxalis L. species. *Cytologia.* 2017; 82(5): 527-533.

Chatterjee A and Sharma AK. Chromosome study in Gera- niales. *Nucleus*. 1970; 13: 179-200.

Christenhusz MJM and Byng JW. The number of known plants species in the world and its annual increase. *Phytotaxa.* 2016; 261(3): 201-217.

Mathew PM. Cytology of Oxalidaceae. *Cytologia.* 1958; 23: 200-210.

Muhammad IS and Mir AK. Folk use of medicinal herbs of Margalla Hills National Park, Islamabad. *J. Ethnopharmacol.* 2000; 69: 45-56.

Rutland JP. The merton catalogue. *New Phytol.* 1941; 40: 210-214.

Saha S and Begum KN. A comparative analysis on mitotic interphase and prophase among twelve varieties of *Brassica* L. from Bangladesh: Brassicaceae. *International J. Bios*. 2020; 17(4):73-82.

Shahla S and Alam SS. Comparative fluorescent banding in two forms of *Leonurus sibiricus* L. *Cytologia*. 2011; 76(3): 361-366.

Sharma AK and Chatterji T. Cytological studies on three species of Oxalis. *Caryologia.* 1960; 13: 755-765.

Stebbins GL. Chromosomal evolution in higher plants. Edward Arnold, London. 1971; p. 216.

Sultana SS and Alam SS. Differential fluorescent banding in 11 varieties of *Gossypium hirsutum* L. from Bangladesh. *Cytologia.* 2016; 81(1): 111-117.

Tanaka R. Type of resting nuclei in Orchidaceae. *Bot. Mag. Tokyo.* 1971; 84: 118-122.

INSTRUCTION FOR AUTHORS

The Journal of Bangladesh Academy of Sciences is published four times a year in March, June, September and December. Original research articles, review articles, and short communications of high standards of all branches of Science and Technology are considered for publication in this journal. Review articles are generally by invited authors; however, the Editor welcomes suggestions of potential topics and potential authors.

The following instructions must be followed while preparing the manuscript intended for publication in this journal:

1. **Research Article:** Manuscripts should be concise and consistent with the style of the journal. The manuscript must be typed using Times New Roman font, size 12 on A4 size page, and wide (1 inch) margins on all four sides. The main text must be typed in a two-column format with 1.5 spacing, and for full papers, it should not exceed 10-20 typed pages, including figures, tables, and references. In general, an article may contain the following sub-titles in sequence: **Title, Abstract, Keywords, Introduction, Materials and Methods, Results and Discussion, Acknowledgement (**if any), and **References.**

A. Title: The first page of the paper, the title page, should have the title and the names of the authors. The title should be brief and specific. Abbreviations and formulae should be avoided where possible. The next line in italics should be the authors' affiliation addresses (where the actual work was done) below the names. Indicate all affiliations with a lowercase superscript letter immediately after the author's name and in front of the appropriate address. The corresponding author, along with email address, should be indicated at the footnote with a proper asterisk.

B. The second page should carry the Title of the paper, Abstract, and Keywords. Author(s) name must not be typed on this page.

(i) Abstract: It should not exceed 150 words and should briefly state the purpose of the research, the significant results, and meaningful conclusions. Nonstandard or uncommon abbreviations should be avoided, but if essential, they must be defined at their first mention in the abstract itself.

(ii) Keywords: Immediately after the abstract, provide a maximum of 6 keywords.

C. The next pages (a maximum of 15 printed pages), will contain the main text of the paper.

(i) Introduction: It should be concise and relevant to the objectives of the study. The importance of the research work described should be pointed out. An appropriate review of the current literature should be made to identify the frontier of existing knowledge and point out the need for further work. The knowledge contributed to the study should be mentioned.

(ii) Materials and Methods: Materials used should be mentioned precisely along with their sources and any pre-treatment undertaken.

The description of methods must be brief but clear enough to enable a reader to reproduce the results. References must be considered sufficient for methods described in earlier publications: only relevant modifications should be described.

It is recommended that authors use the nomenclature and symbols adopted by IUPAC document UIFII (S.U.N. 65-3) 1965, symbols, units, and nomenclature in Physics or by IUPAC Manual of Physiochemical symbols, Terminology and similarly for other disciplines.

(iii) Results and Discussion: This section should include descriptions of results obtained with the help of figures, tables, graphs, and photographs as may be necessary. Tables should have a descriptive title. Large and cumbersome tables should be avoided. Figures and graphs should be prepared and should be properly labelled with bold solid lines such that no further size reduction will be necessary. The paper should contain a minimum number of **Tables, Graphs,** and **Figures.** The same data should not be depicted using both tables and figures. The photographs are to be submitted in JPEG format.

The discussion should include thorough analysis and interpretation of results, and comparison with existing relevant published results, if any, and self-evaluation of the new knowledge contributed, avoiding extensive citations and discussion of published literature.

(iv) Conclusions

The study's main conclusions may be presented in a short Conclusions section, which may stand alone or form a part of the Results and Discussion section.

(v) Acknowledgment: The following support for the research work should be acknowledged:

- Funding by any agency;
- The use of instruments in a laboratory other than those of the authors;
- Individual’s help during the research (e.g., providing an interpretation of results, language help, writing assistance, or proofreading, etc.).

(vi) Author contributions

For transparency, we encourage authors to submit an author contribution statement outlining each author's contributions to the paper. The authors should have participated sufficiently in the work to take public responsibility for appropriate portions of the content.

(vii) References and Text Citations:

In the text, references should be cited within brackets quoting the first author's surname followed by et al. if necessary and the year of publication in the appropriate place, e.g. (Bhuiyan, 2020), Khan et al. (2021) or (Khan et al., 2021). In the case of only two authors, surnames of both need to be mentioned, e.g., (Khan and Rahman, 2021). A semi colon should separate two or more references when putting within the same bracket. At the end of the manuscript, references should be listed and arranged alphabetically according to the first author's surname according to the style described below:

(a) Journal article:

In each reference, names of all authors' will have to be given in the same style, e.g., surname followed by initials, lumped together without using a full stop. The names will be followed by the full title of the article and the journal's abbreviated title (in italics). The year of publication will be given next, followed by volume number (issue number) and page ranges. For abbreviations of the names of journals, authors are advised to follow the *World List of Scientific Periodicals.* For online publications, the URL address must be given. Note: Please list ALL authors’ names in the list of references, do not use (et al.). **Examples:**

Islam S. The Induced Morphological and Root Anatomical Changes in Lentil. *J. Bangladesh Acad. Sci.* 2019; 43(2):107-112.

James BD and Bennett DA. Causes and Patterns of Dementia: An Update in the Era of Redefining

Alzheimer’s Disease. *Annu. Rev. Public Health;* 2019; 40: 65-84.

Moniruzzaman M, Khatoon R and Qamruzzaman AKM. Influence of Plant growth Regulators on Vegetative Growth, Sex Expression and Yield of Summer Bottle Gourd. *Bangladesh J. Agril. Res*. 2019; 44(4): 577-590.

(b) Book or Chapter in a Book:

The place and name of the publisher, year of publication, will have to be given in addition to the name of the author(s), the title of the book (in italics), edition number (if not first), and the number of pages. In the case of an article or chapter in a book or proceedings of a conference, author(s) name and the title of the article or chapter will be followed by the title of the book (in italics), the names of the editors of the book, edition number (if not first), the place and name of the publisher, year of publication and page or page numbers of chapter. **Examples:**

Book:

Carlson BM. *Human Embryology and Developmental Biology*. 4th ed. St. Louis: Mosby; 2009. p. 541.

Cassese A, Acquaviva G, Fan M and Whiting A. *International Criminal Law: Cases and Commentary*. Oxford University Press; 2011, p. 600.

Chapter in an edited book:

Muhammad HFL and Dickinson KM. Nutrients, energy values and health impact of conventional beverages, Chapter 3. In: *The Science of Beverages, Volume 12: Nutrients in Beverages*. Grumezescu AM, Holban AM, eds., Elsevier Science; 2019; pp. 77-109.

Balsam KF, Martell CR, Jones KP, Safren SA. Affirmative cognitive behavior therapy with sexual and gender minority people. In: *Culturally Responsible Cognitive Behavior Therapy: Practice and Supervision*. Iwamasa GY, Hays PA, eds., 2nd edition, American Psychological Association. 2019; p. 287-314.

(c) Proceedings of a Conference:

Luca J and Tarricone P. Does emotional intelligence affect successful teamwork? In: *Meeting at the Crossroads*. Kennedy G, Keppell M, McNaught C (eds.), Proceedings of the 18th Annual Conference of the Australasian Society for Computers in Learning in Tertiary Education, 2001 Dec 9-12; Melbourne: Biomedical Multimedia Unit, The University of Melbourne; 2001. pp. 367-376.

(d) Reports:

Bangladesh Bureau of Statistics (BBS). Population census - 2011. Preliminary report. Bangladesh Bureau of Statistics, Ministry of Planning, Government of the People's Republic of Bangladesh, Dhaka, 2011.

Rowe IL and Carson NE. *Medical manpower in Victoria. East Bentleigh (AU)*: Monash University, Department of Community Practice; 1981. p. 35. Report No.: 4.

2. **Short communication:** Important research findings that may initiate further research in the relevant field may be published in the form of a short communication. This should not exceed three printed pages (900 words), including Graphs, Tables, and Figures. The presentation should be continuous and paragraphed, i.e., without headings like Introduction, Materials, and Methods, etc. A short communication paper should have an **Abstract** containing the gist of the article and should not exceed 60 words, followed by **Keywords.**

3. **Declarations:** While submitting, the corresponding **a**uthor will have to make a declaration mentioning the laboratory/laboratories in which the work was carried out and certifying that the contents of the paper were not published before or submitted for publication in any other journal and that all the co-authors have given their consent for the article to be considered by the Editorial Board for publication in the Journal of Bangladesh Academy of Sciences.

Declaration of conflicting interests

The corresponding author must provide a formal conflict of interest statement for all authors disclosing any financial and personal relationships with other people or organizations that could inappropriately influence (bias) their work. If no conflict exists, please state that 'The author(s) declare(s) that they have no conflicts of interest regarding the publication of this article.'

4. The manuscript should be submitted in pdf or MS Word or LaTex files through online at www.bas.org.bd/publications/jbas.html. Equations generated by using Math Type or Math ML should be incorporated in the text.

   Soft copies of manuscripts with tables, graphs, illustrations, and photographs placed correctly in a printable format are to be submitted. Authors wishing to publish coloured schemes/diagrams/ sketches/photographs in their papers need to pay for the printing charges of one format. This will be charged only after the acceptance of the manuscripts for publication in the JBAS.

   The manuscript submitted should also contain a separate list of tables, figures, illustrations, photographs, and sketches with appropriate captions.

5. Electronic versions of final galley proofs will be sent to authors. No alteration in the title or additions in the text is desirable at this stage.

6. All correspondence for publication should be made on www.bas.org.bd/publications/jbas.html to the **Editor, Journal of Bangladesh Academy of Sciences, National Science and Technology Complex, Agargaon, Dhaka 1207.**

N.B.: No paper will be accepted for publication if it does not conform to the style specified for the journal and approved by the Editorial Board, which has the authority to accept or reject the manuscript of a paper submitted without showing any reason.